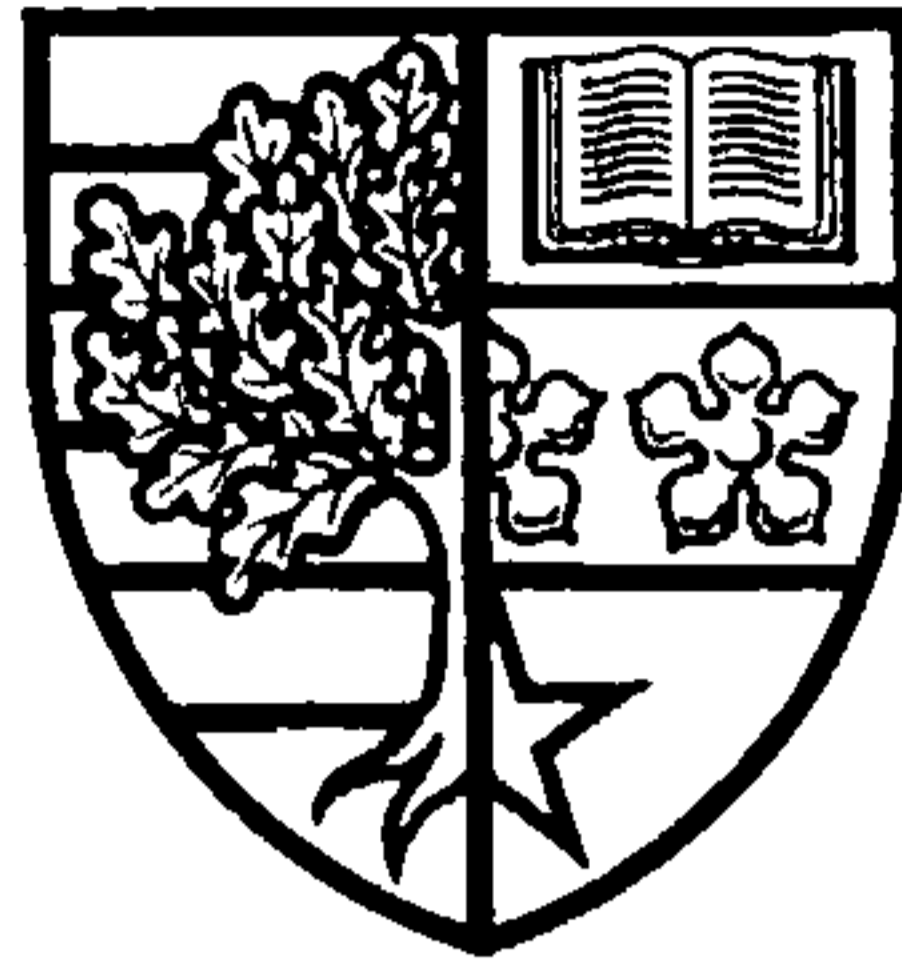


# Bicycle Chain Efficiency



Matthew Donald Kidd BEng

Submitted for the degree of Doctor of Philosophy

in Mechanical Engineering at Heriot-Watt University Edinburgh

May 2000

This copy of the thesis has been supplied on condition that anyone who consults it is understood to recognise that the copyright rests with its author and no information derived from it may be published without the prior written consent of the author or the University (as may be appropriate).

Department of Mechanical & Chemical Engineering  
Heriot-Watt University  
Riccarton  
EDINBURGH  
EH14 4AS

## Acknowledgements

I wish to express my gratitude to numerous people within the university, industry and more personal relations. Thanks must be extended to Heriot-Watt University for awarding me a scholarship, allowing me to continue my work first started as an undergraduate at the University of Edinburgh. The impetus for the research of the cycle chain efficiency came from Fraser Scott and those at Scottoiler Ltd. Much serious and light-hearted encouragement came from Fraser, helping me help him.

From an academic point of view, I wish to thank my supervisors Mr Norman Loch and Professor Bob Reuben for providing me with direction and assistance for the programme of research. Central to the realisation of the torquemeter instrumentation was Andrew Haston the departmental electronics guru. Davie Walker and Mark McCaskey of the workshop also provided much help. As a regular release from academic toil, I should also acknowledge the other residents of the dungeon, both past and present.

Those external to the University who warrant a mention are Pedro Miguel Nunes dos Santos from Transmecca for supplying me with chains and components; the Measurements Group for solving the problems of partiality stemming from strain gauges. Regular exchanges of information also took place across the Internet with interested parties, so thank you to Jobst Brandt, Jim Papadopoulos, and James Spicer amongst others. Closer to home, I am indebted to the support and drive from my girlfriend – finally we have touch down!

## Abstract

Despite its conception by Leonardo Da Vinci<sup>(1)</sup> and its implementation by Hans Renold several hundred years later, the chain has escaped a comprehensive engineering assessment of its efficiency in use. This work examines in detail the efficiency of the chain in its application to the modern bicycle. Improvements in chain design during the past century have made substantial contributions to strength-to-weight ratio, ease of gear shifting in derailleur systems and to reliability. Whilst these changes have led to benefits in bicycle performance, few developments have attempted to improve the transmission of valuable human power *per se*, with efficiency assumed to be high and readily achieved.

Confirmation of the way in which chain tension is distributed around a driving sprocket has been achieved experimentally using a simple strain gauged rig and shows good agreement with previous work. The analysis considered operating conditions unique to the bicycle compared to those chains used in industrial applications.

Since frictional losses in a modern chain are very small, measurement of transmission efficiency demands very accurate means of recording torque. This has been achieved by the successful design and development of novel, non-contacting torque transducers enabling efficiency to be measured with errors less than 0.1%.

Estimation of the coefficient of friction associated with energy losses within a chain has been achieved using a simple pendulum rig and conventional pin-on-plate methods to simulate rolling and sliding action. The coefficient of friction is an important factor in determining efficiency; although small changes in its value between lubricant states may not produce large improvements in efficiency, compared

to other parameters, the overall effect on the competitive cyclist that wins by narrow margins it could be a considerable factor.

The effect of chain offset between the front and rear sprockets (a condition inherent in any bicycle with a derailleur gear system) has been investigated and its contribution to frictional losses and hence efficiency assessed.

The contribution of various proprietary chain lubricants to overall efficiency, together with their short and long term effects, has been tested under simulated running conditions. This has enabled the chemical composition and lubricating mechanism of each lubricant to be assessed on a comparative basis.

Employing a simulated bicycle drive rig, a factorial design set of experiments has revealed how efficiency is influenced by major parameters e.g. power, speed, gear ratio, sprocket size, lubricant, chain alignment and chain wear. Analysis of these results has highlighted the relative contribution and importance of such parameters towards achieving high levels of efficiency.

Analytical work has extended chain modelling strategies of previous works by biasing the studies towards bicycle systems. Finite element stress analysis of chain links, analysis of forces within a chain and estimation of frictional energy losses have provided a further understanding of the chain's mechanisms.

Overall, the results highlight the conditions necessary for achieving high levels of transmission efficiency and provide valuable information for cyclists and manufacturers.

## Table of Contents

<b>1. INTRODUCTION .....</b>	<b>1</b>
1.1 BACKGROUND .....	1
1.2 THESIS OUTLINE.....	6
<b>2. LITERATURE REVIEW .....</b>	<b>9</b>
2.1 INTRODUCTION.....	9
2.2 CHAIN MECHANICS .....	9
2.3 WEAR AND LUBRICATION.....	18
2.4 EFFICIENCY .....	21
2.5 CYCLE CHAIN EFFICIENCY.....	22
2.6 LUBRICATION MECHANISMS.....	28
2.7 TORQUE MEASUREMENTS .....	37
2.7.1 <i>Traditional Methods</i> .....	38
2.7.2 <i>Non-contacting methods</i> .....	42
2.7.2.1 Phase change methods.....	42
2.8 SUMMARY .....	45
<b>3. TORQUEMETER INSTRUMENTATION .....</b>	<b>47</b>
3.1 INTRODUCTION.....	47
3.2 REQUIREMENTS .....	48
3.3 DESIGN.....	50
3.3.1 <i>Physical</i> .....	50
3.3.2 <i>Electrical</i> .....	55
3.4 PERFORMANCE TESTING AND CALIBRATION PROCEDURE.....	67
3.5 CALIBRATION RESULTS .....	71
3.6 SUMMARY .....	76
<b>4. LOAD DISTRIBUTION ANALYSIS .....</b>	<b>77</b>
4.1 INTRODUCTION.....	77

4.2	MISALIGNMENT FROM OUT-OF-PLANE BENDING.....	78
4.3	APPARATUS AND PROCEDURE.....	85
4.4	RESULTS.....	91
4.4.1	<i>In-Plane Loading 0°</i> .....	95
4.4.2	<i>Out-of-plane loading +3.5°</i> .....	95
4.4.3	<i>Out-of-plane loading -3.5°</i> .....	96
4.4.4	<i>Pre-engagement Phenomenon</i> .....	96
4.5	SUMMARY .....	98
5.	COEFFICIENT OF CHAIN FRICTION.....	99
5.1	INTRODUCTION.....	99
5.2	EXAMINATION OF CHAIN COMPONENTS.....	102
5.3	PENDULUM METHOD.....	105
5.3.1	<i>Estimation of <math>\mu</math> from Pendulum Tests</i> .....	109
5.3.2	<i>Analysis of results</i> .....	110
5.3.2.1	Energy Technique.....	111
5.3.2.2	Viscous Technique .....	113
5.3.2.3	Coulomb Technique .....	114
5.3.3	<i>Results</i> .....	116
5.4	PIN ON PLATE METHOD.....	118
5.4.1	<i>Biceri UWM tests</i> .....	121
5.5	RESULTS.....	122
5.5.1	<i>Water</i> .....	124
5.5.2	<i>Lubricant A (Triflow)</i> .....	126
5.5.3	<i>Lubricant B (FinishLine)</i> .....	126
5.5.4	<i>Lubricant C (Weldite)</i> .....	126
5.5.5	<i>Lubricant D (Water and SACI combination)</i> .....	130
5.6	SUMMARY .....	132
6.	LATERAL FORCE ANALYSIS.....	133
6.1	INTRODUCTION.....	133

6.2	APPARATUS .....	133
6.3	THEORY.....	136
6.4	RESULTS.....	137
6.5	SUMMARY .....	138
<b>7.</b>	<b>CHAIN EFFICIENCY .....</b>	<b>141</b>
7.1	INTRODUCTION.....	141
7.2	EXPERIMENTAL APPARATUS AND PROCEDURE.....	144
7.2.1	<i>Mechanical Parameter Details .....</i>	<i>150</i>
7.2.1.1	Sprocket (front) .....	150
7.2.1.2	Sprocket (rear).....	150
7.2.1.3	Chain Type .....	151
7.2.1.4	Lubricant .....	152
7.2.2	<i>Operational effects.....</i>	<i>153</i>
7.2.2.1	Power .....	153
7.2.2.2	Speed.....	154
7.2.2.3	Time .....	154
7.3	TEST PROCEDURE .....	155
7.4	PROCEDURE.....	159
7.5	RESULTS.....	161
7.5.1	<i>Combination and Solitary Effects .....</i>	<i>161</i>
7.5.2	<i>Lubricant.....</i>	<i>167</i>
7.5.3	<i>Time (short term).....</i>	<i>168</i>
7.5.4	<i>Time (long term).....</i>	<i>173</i>
7.5.5	<i>Chain Tension .....</i>	<i>179</i>
7.5.6	<i>Sprocket size.....</i>	<i>182</i>
7.5.7	<i>Chain Alignment .....</i>	<i>185</i>
7.5.8	<i>Chain Length.....</i>	<i>187</i>
7.6	SUMMARY .....	189
<b>8.</b>	<b>CHAIN MECHANICS AND FRICTIONAL LOSS.....</b>	<b>190</b>

8.1	INTRODUCTION.....	190
8.2	FRICTIONAL LOSSES – TIGHT SIDE .....	190
8.2.1	<i>Chain Pin and Bush</i> .....	192
8.2.1.1	Forward pin, pin-link.....	192
8.2.1.2	Rear pin, roller-link.....	194
8.2.2	<i>Bush and roller</i> .....	195
8.2.2.1	Rear roller, roller-link.....	195
8.2.2.2	Forward roller, roller-link.....	196
8.2.3	<i>Chain offset</i> .....	196
8.3	FRICTIONAL LOSSES – SLACK SIDE.....	199
8.3.1.1	Idler sprockets .....	199
8.3.1.2	Driver & Driven Sprockets.....	200
8.4	TRANSMISSION EFFICIENCY .....	200
9.	DISCUSSION.....	203
9.1	INTRODUCTION.....	203
9.2	INSTRUMENTATION AND MEASUREMENT .....	203
9.3	SENSITIVITY OF CHAIN EFFICIENCY TO COMBINED FACTORS .....	208
9.4	CHAIN EFFICIENCY AND SPROCKET SIZE .....	210
9.5	SLACK-SLIDE TENSION .....	214
9.6	SPROCKET ALIGNMENT .....	217
9.7	CHAIN TENSION (TIGHT SIDE) .....	220
9.8	LUBRICATION .....	222
9.9	SUMMARY .....	224
10.	CONCLUSIONS.....	226
	REFERENCES.....	228
	APPENDIX A: ERROR ANALYSIS .....	236
	TORQUEMETER INSTRUMENTATION .....	236
	CHAIN EFFICIENCY .....	236

POWER .....	237
<b>APPENDIX B: HEAT CALCULATIONS OF FRICTION BRAKE SYSTEM .....</b>	<b>238</b>

## Table of Figures

FIGURE 1-1: REAR DERAILLEUR MECHANISM .....	3
FIGURE 2-1: FORCE ANALYSIS AT CHAIN-SPROCKET INTERFACE .....	11
FIGURE 2-2: RESULTS FROM ELDIWANY & MARSHEK <sup>(20)</sup> .....	15
FIGURE 2-3: FOUR-SQUARE RIG DESIGN.....	19
FIGURE 2-4: CRANKED VS. STRAIGHT LINK TYPES.....	20
FIGURE 2-5: STRIBECK DIAGRAM OF LUBRICATION REGIMES .....	30
FIGURE 2-6: TRANSITION MAP OF BOUNDARY AND ASSOCIATED LUBRICATION REGIMES .....	30
FIGURE 2-7: TORQUE MEASUREMENT TECHNIQUES .....	39
FIGURE 2-8: FULL BRIDGE STRAIN GAUGE CONFIGURATION .....	41
FIGURE 3-1: FRONT AND REAR SHAFT ADAPTERS .....	51
FIGURE 3-2: STRAIN GAUGE CONFIGURATION .....	51
FIGURE 3-3: CALCULATED TORQUE SENSITIVITY FOR VARIOUS SHAFT DIAMETERS.....	52
FIGURE 3-4: SHAFT RADIAL LOADING.....	54
FIGURE 3-5: INSTRUMENTATION SCHEMATIC.....	57
FIGURE 3-6: VOLTAGE-FREQUENCY CALIBRATION .....	58
FIGURE 3-7: PULSE CHARACTERISTICS.....	59
FIGURE 3-8: PULSE CHARACTERISTICS (MODIFIED).....	59
FIGURE 3-9: SPECTRUM ANALYSIS OF TORQUEMETER SIGNAL OUTPUT AT 1KHz.....	60
FIGURE 3-10: SPECTRUM ANALYSIS OF TORQUEMETER SIGNAL OUTPUT AT 6KHz.....	60
FIGURE 3-11: SPECTRUM ANALYSIS OF TORQUEMETER SIGNAL OUTPUT AT 1KHz (MODIFIED).....	60
FIGURE 3-12: SPECTRUM ANALYSIS OF TORQUEMETER SIGNAL OUTPUT AT 6KHz (MODIFIED).....	60
FIGURE 3-13: PLL OPERATING PRINCIPLE .....	62
FIGURE 3-14: LABVIEW PROGRAM BLOCKS .....	66
FIGURE 3-15: CALIBRATION RIG.....	67

FIGURE 3-16: FREQUENCY VS. APPLIED TORQUE.....	68
FIGURE 3-17: INPUT SHAFT CALIBRATION .....	73
FIGURE 3-18: OUTPUT SHAFT CALIBRATION.....	74
FIGURE 3-19: DYNAMIC TEST OF TORQUEMETER .....	75
FIGURE 4-1: ACCOMMODATING MISALIGNMENT, EXAGGERATED CHAIN LINK POSITIONS .....	81
FIGURE 4-2: BENDING STRESS RELATIVE TO DIRECT STRESS .....	82
FIGURE 4-3: SPROCKETS INCLINED AT AN ANGLE $\beta$ .....	84
FIGURE 4-4: EXAGGERATED POSSIBLE COMPONENT POSITIONS.....	84
FIGURE 4-5: EXPERIMENTAL APPARATUS.....	87
FIGURE 4-6: ANGULAR TEST PLOT.....	90
FIGURE 4-7: 28 TOOTH SPROCKET RESULTS.....	92
FIGURE 4-8: 38 TOOTH SPROCKET RESULTS.....	93
FIGURE 4-9: 52 TOOTH SPROCKET RESULTS.....	94
FIGURE 5-1: FRICTION POINTS.....	100
FIGURE 5-2: CHAIN CROSS SECTION .....	103
FIGURE 5-3: VISIBLE CHANGES TO CHAIN COMPONENTS FROM WEAR SIMULATION .....	104
FIGURE 5-4: PENDULUM TEST APPARATUS.....	106
FIGURE 5-5: EXAMPLE WAVEFORM.....	107
FIGURE 5-6: EXPONENTIAL DECAY, VISCOUS DAMPING, $\xi < 1.0$ (UNDERDAMPED) .....	108
FIGURE 5-7: LINEAR DECAY, COULOMBIC DAMPING.....	108
FIGURE 5-8: BICERI TEST APPARATUS .....	119
FIGURE 5-9: PIN AND PLATE INTERACTION.....	119
FIGURE 5-10: FORCE VS. TIME FOR PIN-ON-PLATE.....	123
FIGURE 5-11: COEFFICIENT OF FRICTION USING WATER AS A LUBRICANT .....	125
FIGURE 5-12: COEFFICIENT OF FRICTION - LUBRICANT A .....	127
FIGURE 5-13: COEFFICIENT OF FRICTION - LUBRICANT B .....	128
FIGURE 5-14: COEFFICIENT OF FRICTION - LUBRICANT C.....	129
FIGURE 5-15: COEFFICIENT OF FRICTION - WATER/SACI COMBINATION .....	131
FIGURE 6-1: LATERAL FORCE PHOTOGRAPH .....	134
FIGURE 6-2: LATERAL FORCE RIG (SCHEMATIC).....	135

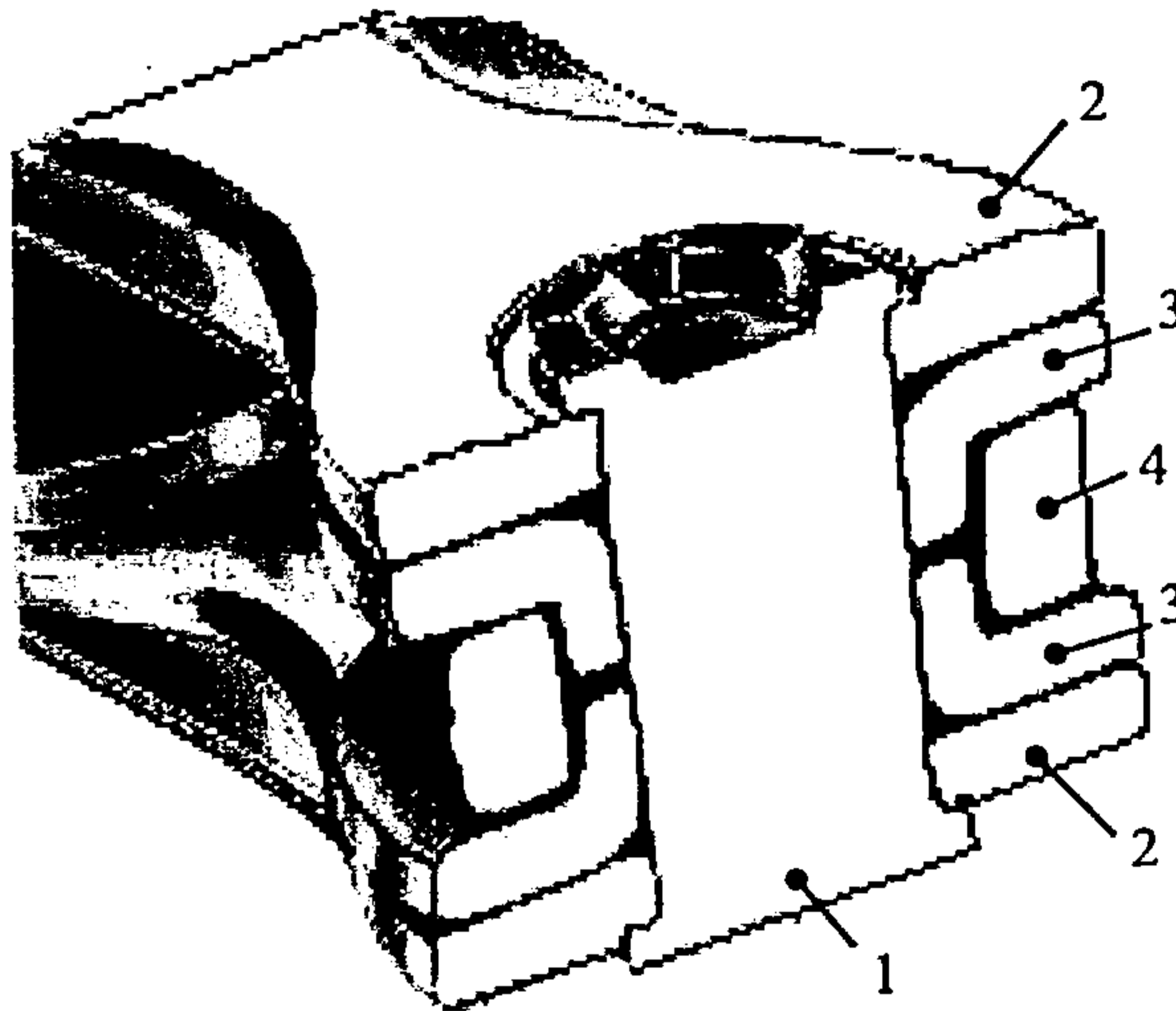
FIGURE 6-3: LATERAL FORCE EXPERIMENTAL DATA.....	139
FIGURE 6-4: NORMALISED LATERAL FORCE .....	140
FIGURE 7-1: PHOTOGRAPH OF CHAIN EFFICIENCY TEST APPARATUS (SIDE) .....	144
FIGURE 7-2: PHOTOGRAPH OF CHAIN EFFICIENCY TEST APPARATUS (PLAN) .....	145
FIGURE 7-3: CHAIN EFFICIENCY APPARATUS SCHEMATIC.....	146
FIGURE 7-4: FREQUENCY INSTABILITY OF HALL-EFFECT SENSOR .....	149
FIGURE 7-5: CHAIN TYPES.....	151
FIGURE 7-6: FRICTION BRAKE HEATING .....	158
FIGURE 7-7: SAMPLE DATA READING .....	160
FIGURE 7-8: RESULTS HYPERCUBE.....	163
FIGURE 7-9: GRAPHICAL STATISTICAL ANALYSIS .....	166
FIGURE 7-10: CHAIN EFFICIENCY AND POWER, VARIOUS LUBRICATION STATES .....	170
FIGURE 7-11: CHAIN EFFICIENCY AND <i>TRIFLOW</i> LUBRICANT.....	171
FIGURE 7-12: CHAIN EFFICIENCY AT POINT OF LUBRICATION INJECTION .....	172
FIGURE 7-13: CHAIN EFFICIENCY DEGRADATION WITH <i>TRIFLOW</i> .....	175
FIGURE 7-14: CHAIN EFFICIENCY DEGRADATION WITH <i>FINISH LINE (1)</i> .....	176
FIGURE 7-15: CHAIN EFFICIENCY DEGRADATION WITH <i>FINISH LINE (2)</i> .....	177
FIGURE 7-16: CHAIN EFFICIENCY DEGRADATION WITH SACI .....	178
FIGURE 7-17: CHAIN EFFICIENCY AND POWER, VARYING TENSION.....	180
FIGURE 7-18: CHAIN EFFICIENCY AND CHAIN TENSION.....	181
FIGURE 7-19: CHAIN EFFICIENCY AND SPROCKET SIZE, 48:21 .....	184
FIGURE 7-20: CHAIN EFFICIENCY AND SPROCKET SIZE, 38:16 .....	184
FIGURE 7-21: CHAIN EFFICIENCY AND SPROCKET SIZE, 28:12 .....	184
FIGURE 7-22: CHAIN EFFICIENCY AND SPROCKET ALIGNMENT.....	186
FIGURE 7-23: CHAIN EFFICIENCY AND LENGTH OF CHAIN .....	188
FIGURE 8-1: CHAIN ARRANGEMENT ON A BICYCLE .....	191
FIGURE 8-2: CHAIN MISALIGNMENT .....	196
FIGURE 8-3: OFFSET FORCES SCHEMATIC.....	197
FIGURE 8-4: POWER LOSS CONSTITUENTS OF TOTAL FRICTION COMPONENT MODELLING.....	202
FIGURE 9-1: THEORETICAL AND EXPERIMENTAL CHAIN EFFICIENCY AT VARIOUS SPROCKET SIZES .....	213

FIGURE 9-2: THEORETICAL CHAIN EFFICIENCY AND SLACK-SIDE TENSION ..... 216

FIGURE 9-3:THEORETICAL CHAIN EFFICIENCY AND ALIGNMENT ..... 219

FIGURE 9-4:THEORETICAL CHAIN EFFICIENCY AND CHAIN TENSION ..... 221

## Bicycle Chain Components



Key:

- 1. Pin
- 2. Outer link (or plate)
- 3. Inner link (or plate) with integral bush
- 4. Roller

# 1. Introduction

## 1.1 Background

For over 100 years, the bicycle has relied on a chain to transfer power from the cyclist's legs to the rear wheel. During this time, significant improvements in such areas as materials, frame structure, brakes, suspension and gears.<sup>(2),(3),(4),(5),(6),(7),(8)</sup> have resulted in greatly enhanced levels of safety, reliability and comfort being associated with the modern bicycle. However, despite being a major component of the bicycle, the chain has attracted relatively little attention and its development has remained static apart from for engineering materials developments. The perception that the chain is a versatile and efficient form of transmission (figures in excess of 98% have been quoted<sup>(9),(10)</sup>) has perhaps contributed to its relative neglect. Such levels of efficiency can be misleading, particularly for the modern bicycle chains which operate under widely varying conditions and this thesis presents a thorough investigation of the many factors influencing chain performance. The work contributes to the understanding of the chain allowing improvements in design and implementation leading to an enhanced performance of the bicycle.

The effects of improved efficiency can be illustrated in a number of ways. Using the theoretical energy requirements for a bicycle and rider given by Whitt and Wilson<sup>(9)</sup> it is possible to observe the sensitivity of chain efficiency on performance. In terms of distance over a given period a 3% improvement in efficiency would increase the distance reached by 1%. The world record of distance covered in 1 hour may be extended by 500m if such a 3% improvement could be made; such a distance is not uncommon for previous record margins. Where the conservation of energy is more important, such as in a stage race, where most riders travel at the same 'peleton'

(group) speed and races are won in a final sprint or breakaway. A typical stage may cover 220km and last for 5½ hours. If a rider can maintain a 3% advantage of chain efficiency over their competitors then the energy conserved over the race would be the reciprocal of 3% e.g. 146kJ less than the peleton mean energy exertion of 5.205MJ.

The origin for the misconception of the bicycle chain's high efficiency comes from the industrial applications of chain drives. The use of chains in industry is widespread, e.g. power transfer, conveyer belts and timing operations. As a result of this, the bulk of research in which efficiency was considered has been centred on these applications where efficiencies may well be around 98%. However, to apply the findings of industrial drive research to the bicycle requires careful adaptation. The working conditions and environment in which the bicycle chain operates are significantly different, as is the power level and the manner in which it is transferred. Additionally, the ideal form of lubrication for the chain is an enclosed oil bath, commonly implemented for industrial applications but impractical for use on the bicycle. Although chain guards were once fitted to for most bicycles, they are not compatible with today's bicycle styles, so leaving the chain exposed to all forms of debris and contaminants. This, combined with infrequent or incorrect lubrication, leaves the modern bicycle chain unlikely to attain the levels of efficiency enjoyed by its industrial counterparts operating in near-perfect conditions. The benefits of greater power throughput with a chain drive are improved efficiency and this can be realised more easily with industrial drives.

Modern bicycle gear trains also have a considerable effect on chain efficiency. The (rear) derailleur gear change mechanism literally de-rails the chain off one sprocket and onto another, either smaller or larger, thereby changing the gear ratio

between the pedals and the rear wheel. The front derailleur operates over two or three sprockets at the crank whilst the rear one covers a larger number at the wheel hub. The rear derailleur gear mechanism consists of a parallel motion linkage with an arm supporting two small (normally 11 teeth) idler sprockets, Figure 1-1. The linkage is moved along the axis of the sprockets such that the idler sprockets are always below, and in the same plane as, the desired sprocket. The idler sprocket arm “holds” the chain and forces it to change onto the sprocket by “de-railing” it from one to another. Another purpose this arm serves is to take up the extra length of chain, arising from the altered ratios between front and rear sprockets, and this is achieved with a torsional spring. It is desirable to have a reasonable magnitude ( $<50\text{N}$ ) of tension such that the “free” chain does not swing about and interfere with the engagement of the front sprocket.

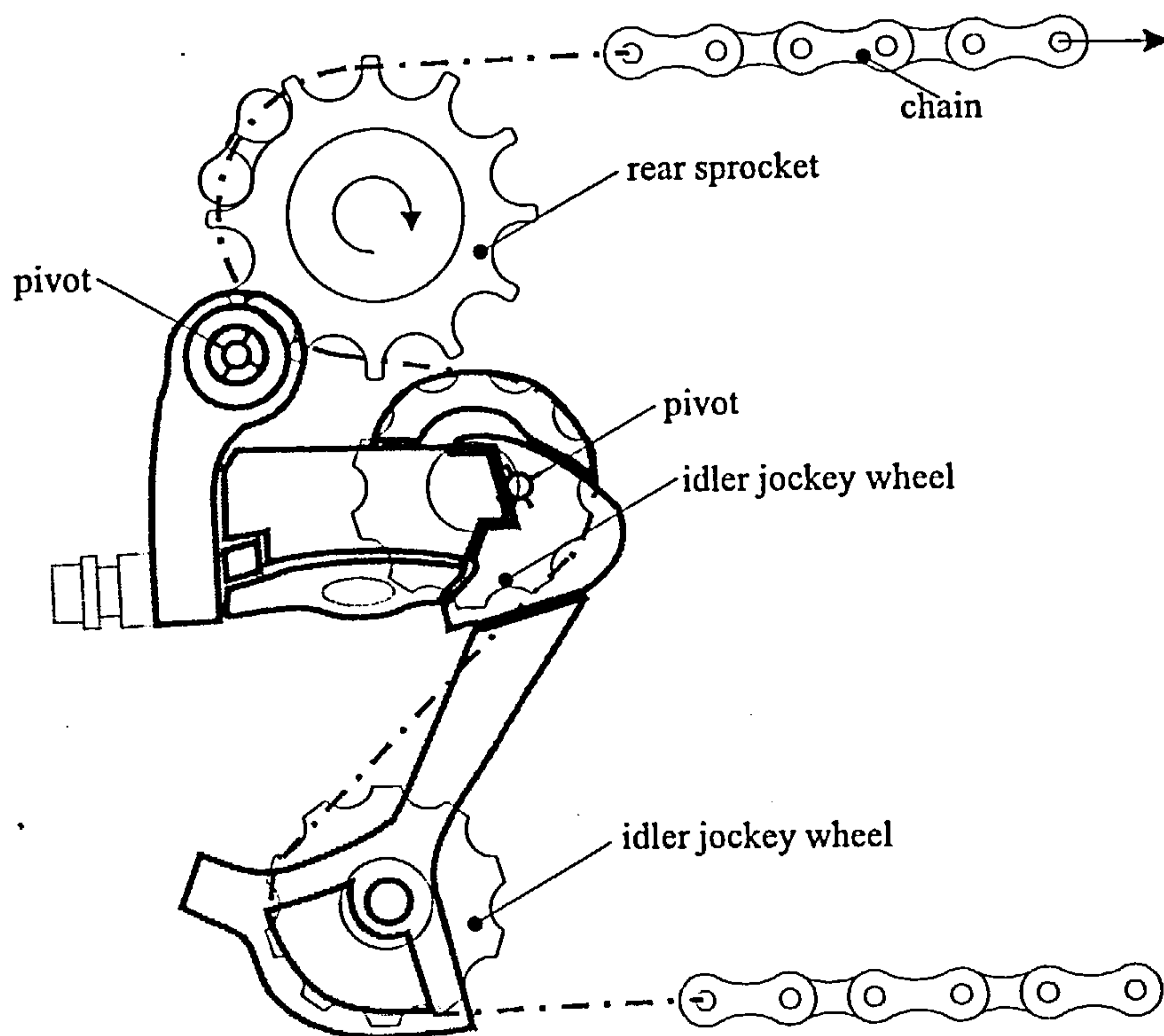


Figure 1-1: Rear derailleur mechanism

In order to operate at peak efficiency in terms of human physiology, having a greater choice of gears available equates to the cyclist going faster or further. The derailleur mechanism is universally popular because it can offer up to nine sprockets, either of closely matched ratios or covering a wide range, out-performing the only other alternative, the hub gear. The penalty for offering such a number of sprockets is that the chain is often running at an angle which is not co-planar with the sprockets. Although designed to cope when operating at angles of “misalignment”, the chain does so with increased friction between side plates when leaving the rear sprockets and engaging with the front sprockets.

Not only does the basic concept of the derailleur system hamper efficiency but further operating characteristics also reduce it. As the chain runs through the two idler sprockets it must go through very tight angles of articulation. Of all the possible movements in a chain, it is articulation that requires the most energy to complete. As well as this, the arm itself imposes a tension in the “slack” side of the chain system thus requiring the cyclist to do work on the return half of the chain’s journey, not normally a factor in industrial applications. A final factor in the derailleur’s operation is that in order to accommodate an increase in the number of sprockets (up to 9), the chain has been made correspondingly narrower. This has increased local bearing pressure at the pins with greater demands placed on the lubricant.

It can be seen that the main differences between the implementation of the cycle chain and those in industry originate from the derailleur gear system. Operating the chain with misalignment, high articulation, a tension on the return side and with high bearing pressures would not arise in a properly designed chain transmission

system. As a further factor militating against high efficiency, the potential for poor and improper lubrication is greater for the bicycle chain.

Such facts serve to illustrate the uniqueness and importance in understanding of how the cycle chain works, what range of efficiency it provides and to what extent the factors identified above affect efficiency. To answer these questions a series of experiments were devised and corresponding models have been developed to predict optimal operation with all the constraints of the long distance cycling competition environment.

## **1.2 Thesis Outline**

The following chapters of this thesis cover a comprehensive literature survey in Chapter 2, instrumentation in Chapter 3, a range of experiments in Chapters 4 to 8 and new theory in Chapter 9. The overall discussion of these chapters and their relationships is given in Chapter 10, with final conclusions in Chapter 11.

Investigating how the force in a chain link varies as it approaches and then engages with a sprocket under a range of conditions is important to the understanding of where the peak bearing pressures occur, their magnitude and for how long they persist. The results of such a load distribution analysis are shown and discussed in Chapter 4. This work extends previous studies applied to industrial chains and the contribution relates specifically to the lighter and narrower type of bushingless bicycle chain which has to accommodate lateral flexure to suit the derailleur mechanism, a requirement not relevant to industrial chain. In particular, a detailed observation of the chain load immediately prior to and beyond engagement with the sprocket is undertaken for different conditions.

Further force analysis, presented in Chapter 6, reveals the lateral loads present on rear sprockets. This helps to isolate the effects of how changing gear ratio alters the forces in the chain. This is necessary because, when the chain is shifted to another sprocket, its lateral position is also moved. Whilst the sprocket causes a change in ratio thus altering the speed and loading characteristics of the chain, it will also give rise to a lateral force on the chain. On a bicycle it is impossible to isolate these related effects, so by changing gear but without the associated lateral shift of the chain, the combined effects can be isolated.

Having gained familiarity with the forces present in the chain, some knowledge must be gained about the lubrication of the load bearing surfaces in order to reduce the frictional effect. Using a proprietary pin-on-plate wear rig, the coefficient of friction for chain component couples including several lubricants was calculated. The results, shown in Chapter 5, indicate how different lubricants react to the regime of boundary lubrication, combined with the effects of time and water ingress. Chapter 5 also covers the frictional forces present in a single link articulation with varying degrees of lubrication and orientation. A metallographic study of some chain components was carried out to obtain information about the friction surfaces.

The main series of experiments was carried out on a bicycle transmission simulator in order to gain realistic data on the characteristics of chain efficiency. The finer details of the rig and the results of the tests are given in Chapter 7. It consists of real bicycle components e.g. sprockets, rear derailleurs and chains arranged to simulate a typical modern bicycle and operated at the levels of power consistent with human operation. The efficiency is measured by recording the magnitude of input and output torques, purely of the chain transmission system (excluding shaft bearing losses) whilst under load. Knowing the overall efficiency of the chain to be high, the torquemeters require to be of very high precision and resolution to detect the small changes expected.

The design, development and commissioning of this instrumentation proved to be a considerable and time-consuming task and is described in Chapter 3. The measurement system comprises two hollow section steel shafts with a pair of strain gauges bonded to each and mounted to experience the principal strain associated with pure torque. Wired to a strain gauge amplifier in-situ on the shaft, the signal is

transformed to a stream of varying frequency infra-red LED pulses. The signal travels from the end of the shaft, along its axis to a PC data acquisition card with a frequency-counting capability.

Having now established how the chain works on both a large and small scale, a detailed model may be constructed. Chapter 8 outlines a mathematical model for the complete chain system to evaluate the theoretical transmission efficiency and also providing a basis for comparison with experimental trends of the results which is completed in Chapter 9.

Overall, the following contributions have been made by this work:

- the theory of chain mechanics has been extended to include lateral flexure commonly experienced by a bicycle chain (Chapter 4).
- an accurate non-contact torque transducer has been designed and constructed, capable of a  $5 \times 10^{-3} \text{Nm}$  resolution, to measure the comparatively small losses inherent in a chain drive (Chapter 3).
- in-situ measurements of chain efficiency have been made over a wide range of operating conditions (Chapter 7).
- the results of dynamic chain efficiency measurements and other ancillary tests (Chapters 4-6) have been combined to provide a lubrication and operation strategy which maximises the efficiency of power transfer for the bicycle chain.

## **2. Literature Review**

### **2.1 *Introduction***

The idea of measuring chain efficiency is not new. Indeed, as much as 100 years ago the first experiments<sup>(11),(12)</sup> were undertaken to investigate bicycle chain efficiency, the aim at the time being to compare different transmission methods and, of course, to satisfy engineering curiosity. A thorough literature survey reveals that such an experiment has only been completed and published twice since then, in 1983<sup>(13)</sup> by a cycle components manufacturer and again in 1998<sup>(14)</sup>. It is unlikely that these few occurrences reflect the true number of investigations, and manufacturers around the world have possibly carried out extensive testing but, for one reason or another, have not made the results public. Consistent with advances made in theories of lubrication and accuracy of measurements over the past century, it is therefore timely to examine chain efficiency in the context of competition cycling where small changes in efficiency can have an appreciable effect. This review examines studies of chain efficiency and mechanics and will encompass theories of boundary and mixed lubrication applicable to the chain. Because a substantial part of the experimental work relies on accurate non-contact torque measurements, the various types of torque measurement available will also be reviewed.

### **2.2 *Chain mechanics***

An understanding of how a chain works is crucial to investigations of force and efficiency measurements. The setting out of the fundamentals of chain mechanics

were completed by Binder in 1956<sup>(15)</sup> and this work is the seminal reference for many published papers years later.

When transmitting power using chains and sprockets, the chain is in contact with a number of sprocket teeth (as an angular proportion to the whole sprocket, this is referred to as 'lap'). Each engaged tooth of the sprocket carries a proportion of the tension of the 'tight' side. The chain tension in the links decreases as links move from the entry to the sprocket on the tight side to the exit on the slack (return) strand. The distribution of this chain tension and corresponding tooth load depends on the number of teeth, chain lap, tooth pressure angles, friction and elastic properties.

To calculate the basic force relations at chain joints, Binder<sup>(15)</sup> made a series of assumptions to aid simplification:

1. no mechanical clearances exist between mating components,
2. chain pitch is exactly equal to sprocket pitch,
3. friction is negligible,
4. the pressure angle is constant,
5. no elastic deformation,
6. no misalignment between chain and sprocket,
7. the chain and sprocket are considered as rigid bodies,
8. the driving strand between sprockets is horizontal,
9. the sprocket tooth reaction line is co-linear with the tooth pressure angle.

The term geometric progressive load distribution or GPLD was coined later to describe the approach taken by Binder. The GPLD analysis is outlined with reference to Figure 2-1.

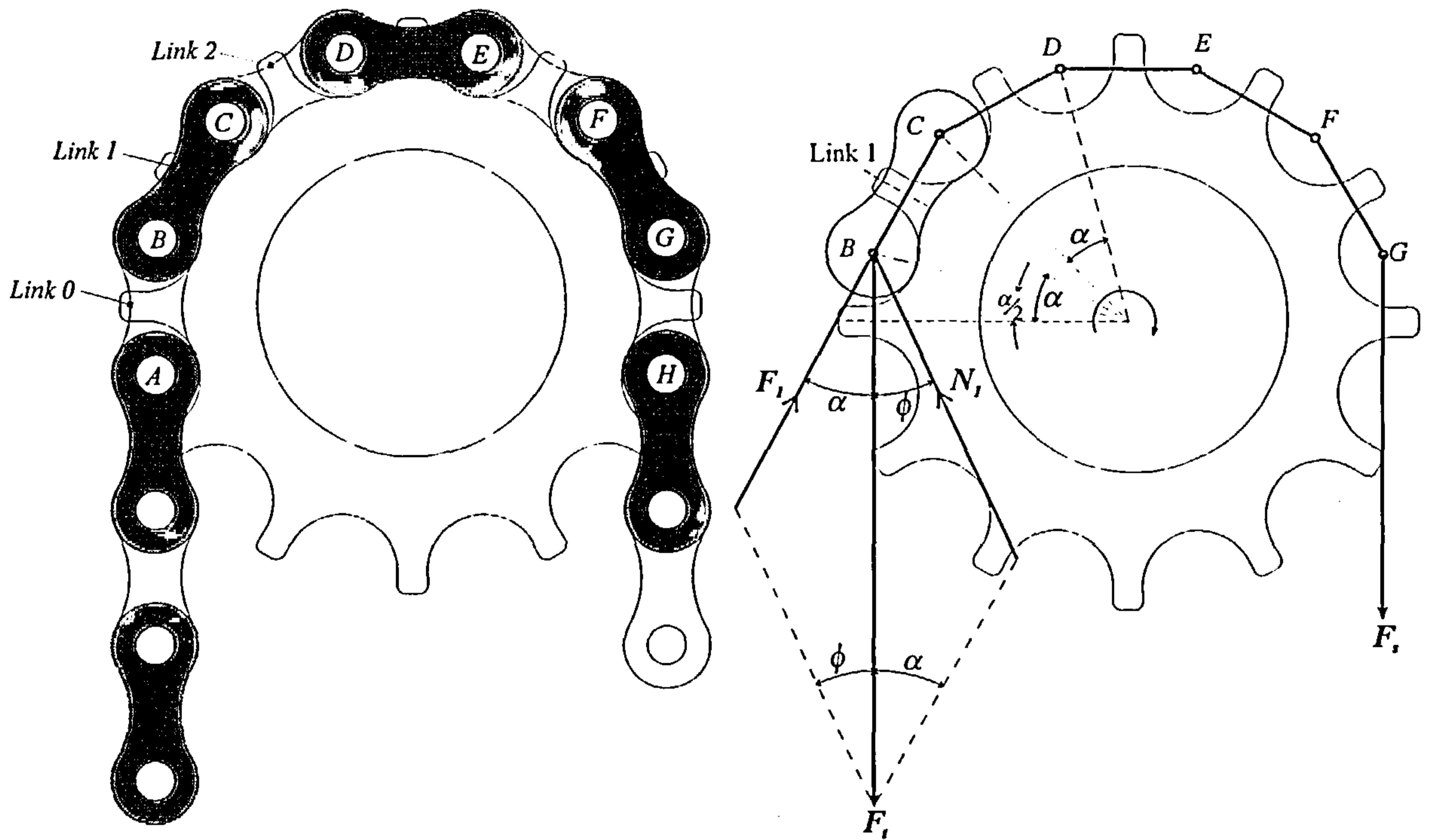


**Figure 2-1: Force Analysis at Chain-Sprocket Interface**

The average tooth pressure angle  $\phi$  and the articulated angle  $\alpha$  for a new chain sprocket combination are defined as:

$$\phi = 35 - \frac{120}{Z} \quad \text{Eq. 2-1}$$

$$\alpha = \frac{360}{Z} \quad \text{Eq. 2-2}$$

Where  $Z$  is the total number of teeth on the sprocket.

Figure 2-1 shows the system of forces acting on a sprocket and a chain at a tension  $F_t$ . The driving strand under tension  $F_t$  is used as a reference force and may or may not be equal to the net sprocket torque force, depending on  $F_s$ . The tension of the chain at the exit of the sprocket is at a slack side tension of  $F_s$ . The tight side tension

is also in link 0 (between rollers  $A$  and  $B$ ),  $F_1$  is the tension in link 1 ( $BC$ ),  $F_2$  is the tension in link 2 ( $CD$ ) thus  $F_n$  is the tension of link ' $n$ '.

Considering link 1 to be fully seated, the tooth between rollers  $A$  and  $B$  exerts a force  $N_1$  on roller  $B$  at a pressure angle  $\phi$ . Equilibrium of the rollers  $B$  and  $C$  result in,

$$F_1 = F_t \frac{\sin \phi}{\sin(\alpha + \phi)} \quad \text{Eq. 2-3}$$

and

$$N_1 = F_t \frac{\sin \alpha}{\sin \phi} \quad \left( = F_t \frac{\sin \alpha}{\sin(\alpha + \phi)} \right) \quad \text{Eq. 2-4}$$

For link 2,

$$F_2 = F_1 \frac{\sin \phi}{\sin(\alpha + \phi)} \quad \text{and} \quad N_2 = \frac{\sin \alpha}{\sin \phi} \quad \text{Eq. 2-5}$$

The equilibrium of roller ' $n$ ' leads to:

$$F_n = F_{n-1} \left( \frac{\sin \phi}{\sin(\alpha + \phi)} \right) = F_t \left\{ \frac{\sin \phi}{\sin(\alpha + \phi)} \right\}^n \quad \text{Eq. 2-6}$$

and

$$N_n = F_n \left( \frac{\sin \alpha}{\sin \phi} \right) \quad \text{Eq. 2-7}$$

The load distributions between driver and driven sprockets arise because of the existence of friction. In the driver sprocket case, the friction between the bushing & roller and between roller & sprocket are different in comparison to the driven sprocket. Conwell<sup>(16)</sup> investigated these differences experimentally and observed how the driven sprocket case reduced chain tension more rapidly than the driver.

When friction is introduced, the effect is to reduce the pressure angle. This allows friction to be considered as an angle,  $\delta$  so changing the equilibrium to:

$$F_n = F_{n-1} \left( \frac{\sin(\phi - \delta)}{\sin(\alpha + \phi - \delta)} \right) \quad \text{Eq. 2-8}$$

The effects of friction were considered further by Naji & Marshek<sup>(17)</sup> who considered the lowest coefficient of static friction ( $\mu_s$ ) to be between roller and sprocket tooth ( $\mu_r$ ) or between roller and bushing ( $\mu_b$ ). For equation 2-8 the friction angle is given by:

$$-\tan^{-1} \mu_s < \delta < \tan^{-1} \mu_s \quad \text{Eq. 2-9}$$

so now the equilibrium can be expressed as:

$$\frac{\sin(\phi + \delta_s)}{\sin(\phi + \alpha - \delta_s)} < \frac{F_n}{F_{n-1}} < \frac{\sin(\phi - \delta_s)}{\sin(\phi + \alpha - \delta_s)} \quad \text{Eq. 2-10}$$

where  $\delta_s$  is the minimum value of  $\tan^{-1} \mu_r$  and  $\tan^{-1} \mu_b$ . For values of the ratio  $F_n / F_{n-1}$  less than the left hand side expression of the inequality, the roller slides up the tooth flank if  $\mu_r < \mu_b$ , but rolls up the tooth flank if  $\mu_r > \mu_b$ .

The inclusion of friction in this manner was one of the many contributions Marshek made to chain mechanics. With Naji<sup>(18)</sup>, sprockets of different elastic modulus and material were tested with the finding that, over a wide range of effective spring constant ratios, the GPLD was independent of this variable. In later work, Marshek and Eldiwany<sup>(19)</sup>, measured stiffness more accurately, and found that it did in fact alter the early stages of the GPLD. As the tooth modulus of elasticity increases so the first teeth of the sprocket take a correspondingly higher proportion of the load, in comparison, less stiff materials lead to deflections with the load carried by more teeth.

Further work from Eldiwany and Marshek<sup>(20)</sup> investigated misalignments between driver sprocket and chain, speed of rotation, and lubrication, although this

last parameter had been reported earlier<sup>(18)</sup> as having no effect. It was found that low speeds (0.2-60 rpm) had no noticeable effect on deviation from the GPLD, and thus no inertia effects were experienced. The results of testing with misalignment are of importance to the bicycle transmission investigation because of the inevitable misalignment in derailleur systems. Eldiwany and Marshek chain load distribution test machine consisted of hanging masses on a chain engaged in a sprocket whose axis was horizontal. The sprocket was rotated slowly and readings from a specially strain gauged link were plotted against angular position. Their results showed a large increase in link load up to 180% (of nominal, well aligned load) with 6° of misalignment, Figure 2-2.

Conwell, Johnson and Petersen<sup>(1)</sup> designed a machine to measure the forces in chain drivers but this time during normal (dynamic) operation. Although the speed range varied around 800-1500rpm, it is somewhat debatable if the results<sup>(16)</sup> from transmitted torques of 2.8-6.7 Nm are useful, since these values are substantially lower than common usage and those investigated in other analyses, e.g.<sup>(20)</sup>. The results did, however, confirm that quasi-static theory models do not work at high speeds (800+ rpm) when inertia effects come into play. A similar but overall more thorough analysis was made by Staments<sup>(21)</sup> in 1951 in an attempt to rate chains for high speed running. Using an optical strain gauge attached to the side of a chain, measurements were made to discover the effects of centrifugal force. It was found that this centrifugal force could be as high as the straight side tension force thereby doubling the overall chain force. Equivalent calculated values for a bicycle chain operating at high speed suggest that the increase to chain tension due to centrifugal force is less

than 4N, around 1% of the chain tension required to pedal at this high speed (120rpm at the front sprocket).

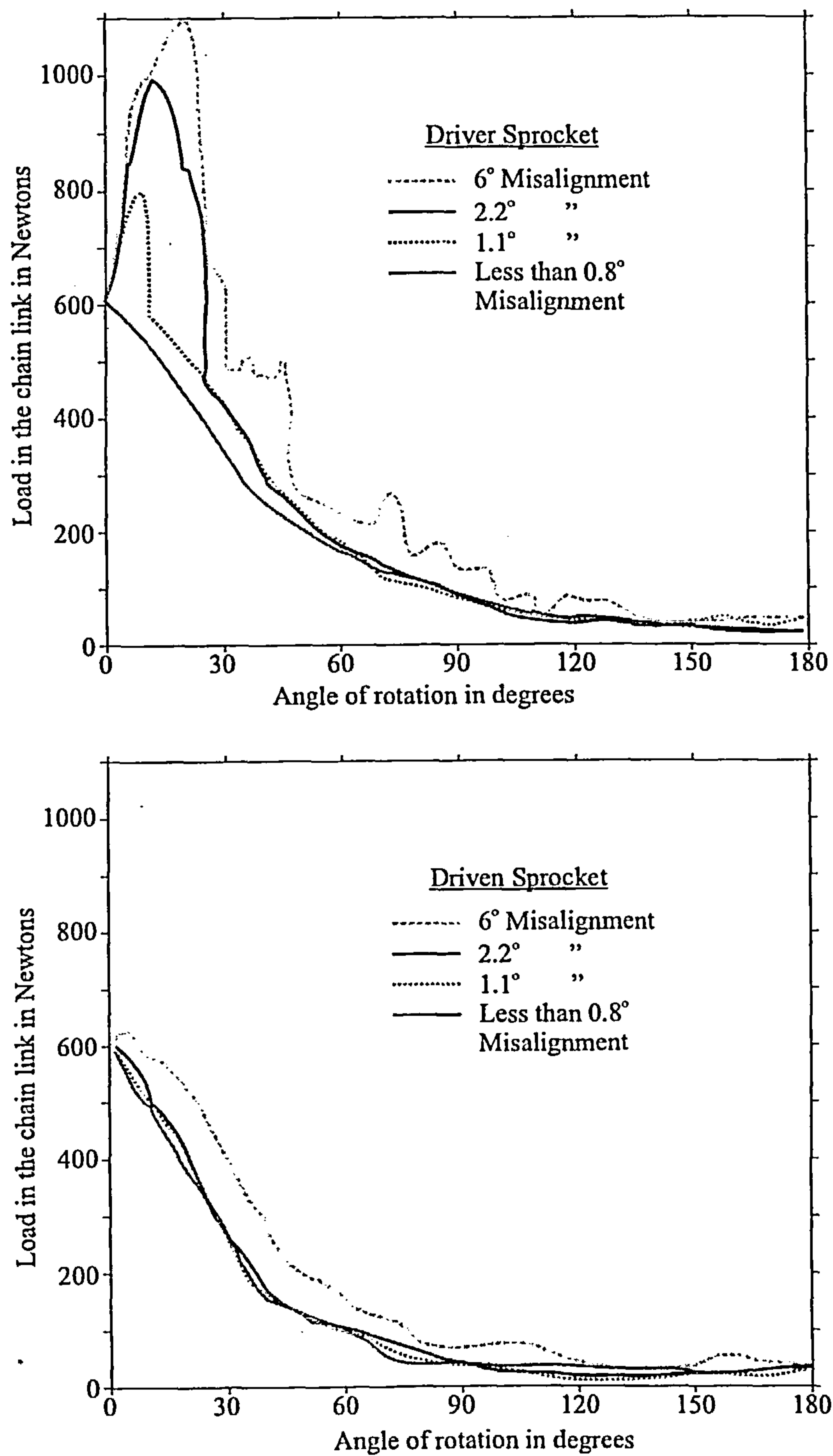


Figure 2-2: Results from Eldiwany & Marshek<sup>(20)</sup>

It is interesting to note that none of the chain force experiments that have taken into account misalignment has been accompanied by any theory to explain the phenomenon of large force increases. Another omission in most analyses is that the stress levels sustained by the chain side-plates are never estimated. This aspect was investigated by Kin and Dubrovsky in 1985<sup>(22)</sup> who attempted to re-design the chain side-plates by reducing local stress concentrations in order to enhance fatigue life. Six basic plate configurations were employed by placing 1mm base strain gauges over the surface of an enlarged model plate. It was found that the traditional bicycle plate form resulted in the poorest performance as far as high stress and low fatigue strength were concerned. The more successful designs included simple straight bar and traditional plate with stress reducing holes. Whilst the straight bar may increase the overall mass of the chain, the plates with the holes would, of course, decrease the mass. It was also noted that all but one of the 300 samples failed in the cross sections located 15° away from the horizontal axis of the holes.

Concentrating on the sprocket-chain interface, there are several models proposed. Marshek and Naji<sup>(23)</sup> completed another GPLD analysis, but this time with worn chains. When considering chains with approximately 2% elongated wear, it was found that the roller teeth of a sprocket are subjected to a higher load level. Furthermore, a driven sprocket suffered to a greater degree when compared to a driver with the same number of teeth, this being due to the different friction characteristics between driver and driven sprockets. The number of teeth and links was also highlighted by the fact that an even number of teeth and an odd number of links (or vice-versa) combination resulted in longer life as the larger roller link loads are distributed evenly over the entire sprocket. If an even-even (or odd-odd) combination

is used, no alternation of loads is experienced. This is recognised in the track cycling world where fixed wheel (no gear) bicycles are the most commonly employed.

Kim and Johnson focused on the actual movements and trajectory of the rollers with respect to the tooth profile and further improved upon Binder's work with a new model. For example, the pressure angle was now calculated as part of the model<sup>(24)</sup>. In testing the new model with their experimental data and that of Naji<sup>(25)</sup>,<sup>(15)</sup> all were found to be in good agreement. A similar approach had been made earlier by Naji and Marshek<sup>(26)</sup> although with a slightly simplified tooth profile and no considerations of friction. For both analyses it can be said that, with a pitch mismatch between sprocket and chain, the pressure and articulated angles vary from roller to roller. When this mismatch is due to chain wear (i.e. old chain on new sprocket), these pressure and articulation angles converge to values dictated by a function of pitch difference and not an assumed contact point for the first roller-tooth engagement.

Further modelling of the chain was completed by Murray and Canfield<sup>(27)</sup> using a 3D rigid body dynamics model. The subject of study was a chain tracked drive system similar to those found on earth moving plant equipment. A numerical model found non-uniform dynamic loading forces on the sprocket load-bearing surface. Peak amplitudes of sprocket load were up to four times greater than that of the mean force. Further, the force varied up to 10 times a second for an 18 tooth sprocket and a chain mean linear velocity of 715mm/s. These dynamic effects provide an indication of the "roughness" of transmitted forces.

### **2.3 Wear and Lubrication**

Whilst previous work had considered wear as one of a number of factors, Hollingworth<sup>(28)</sup> investigated wear specifically using an adoption of a recognised method called the four-square principle. In a conventional four-square arrangement two specimens are tested in a closed power loop. The energy added to the loop to promote movement then equals the losses within the system, Figure 2-3. Whilst stationary the chains (the specimens in this case) are mechanically torqued against each other. When the system is brought up to speed, power is transmitted through the specimens but contained within the loop<sup>(28)</sup>. Ross and Marshek<sup>(29)</sup> also used a novel application of this principle involving only one set of specimens (i.e. only half a square) tensioned by means of a pulley and masses acting on the sprocket's shaft housing. The energy provided by a 20KW variable displacement hydraulic motor then equalled that to overcome articulation frictions at any given power. The wear rate was determined by measuring the loss in chain mass over time. Further analysis was made using a scanning electron microscope (SEM) to examine the pin's surface. Measurements revealed that after an initial running-in period, linear volumetric wear rates were found. Tests on two industrial chains running at 10kN tension between 8 and 12 tooth pairs at  $2\text{ms}^{-1}$  induced wear of between  $0.035$  and  $0.040\text{ mm}^3/1000$  articulations. In terms of the bicycle, two high tension (500N) articulations will occur for every link in the chain for every 20m covered (using a 52:12 ratio) by the bicycle at  $1\text{ms}^{-1}$  chain speed (100 rpm at the pedal crank). It was also found that the number of articulations performed however the drive with the largest articulation angle (i.e. smaller sprockets) gave the highest wear rate. The chain pin wear was found to be

initiated at the outer circumferences, converging towards the middle as wear progressed.

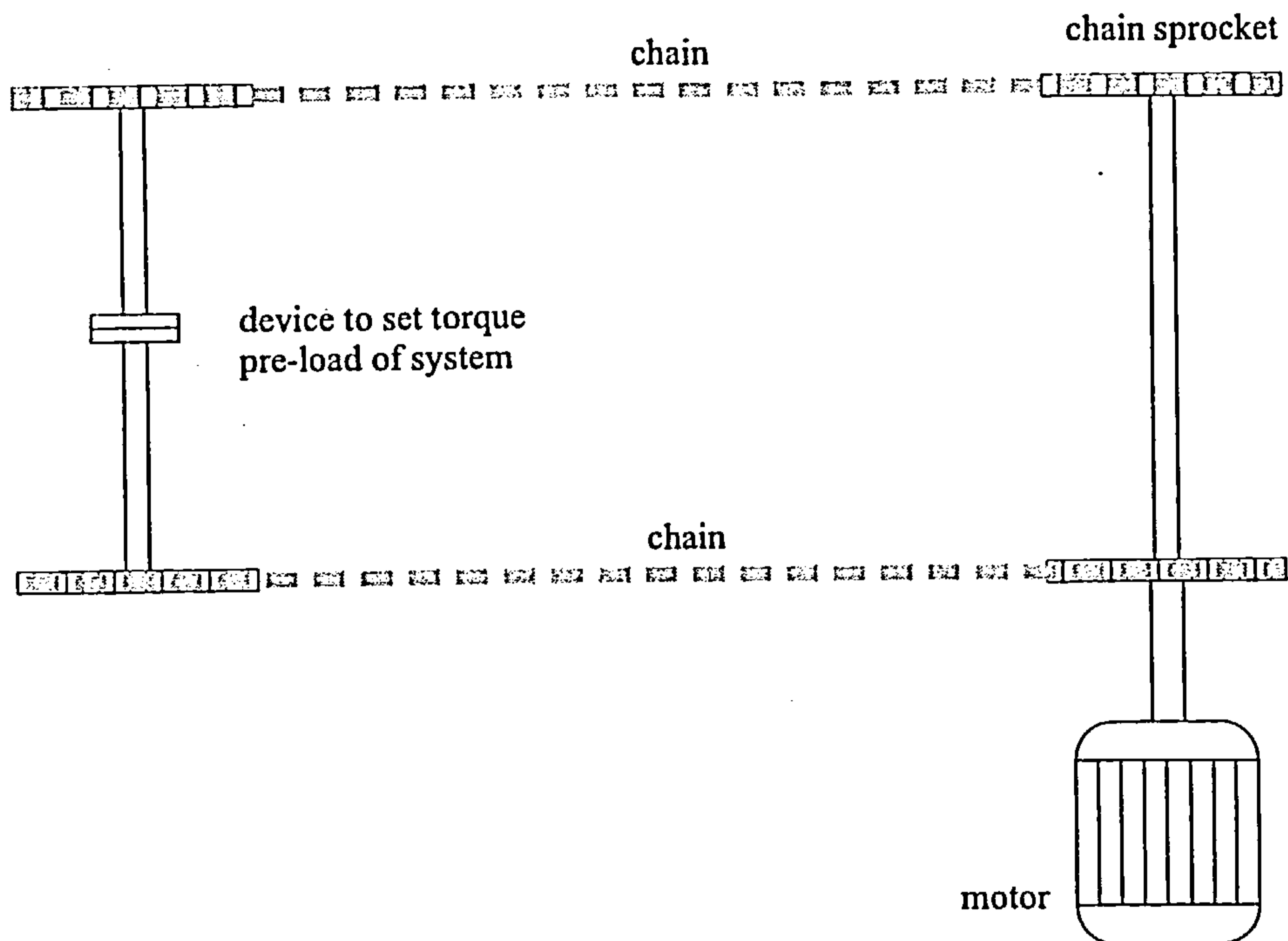


**Figure 2-3: Four-Square rig design**

In 1987 Hollingworth<sup>(28)</sup> noted that 'surprisingly little tribological literature had been published on the subject of driven chain wear', and further commented on how gears had received greater attention in the literature, both theoretically and experimentally. As a result, chain users rely on manuals<sup>(30),(31),(32),(33),(34),(35)</sup> and trade articles<sup>(36),(37)</sup> to provide them with good lubrication practice. However, much manufacturers' data is in turn gleaned from user feedback suggesting little design science and much empiricism.

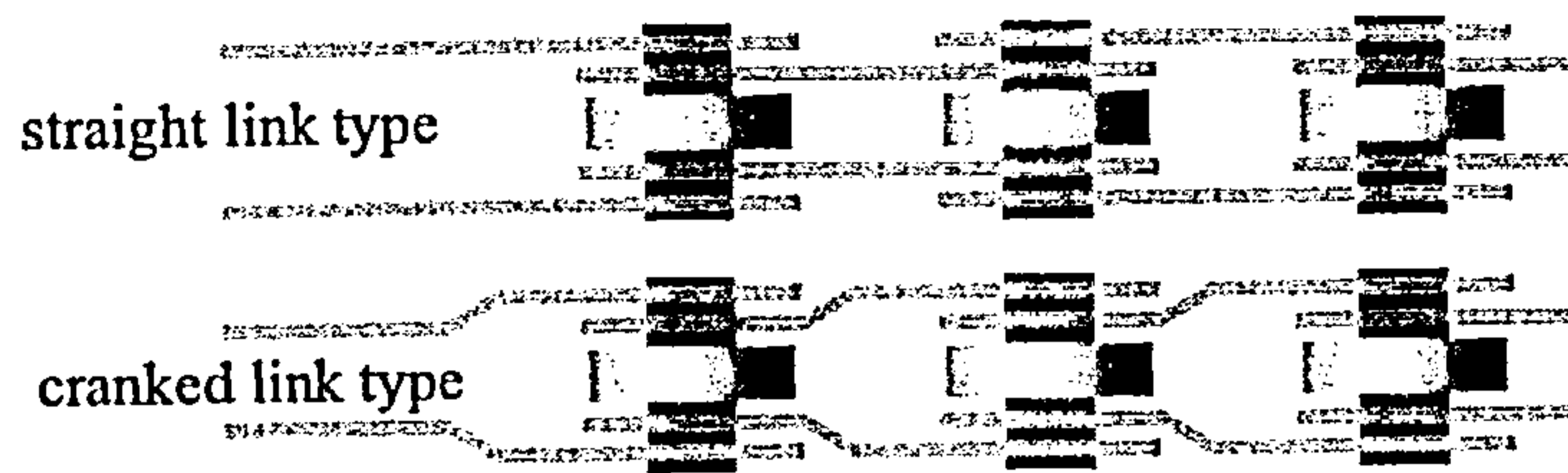


**Figure 2-4: Cranked vs. straight link types**

In 1986 a methodical approach to the lubrication problem of chains was completed by Peeken and Coenen<sup>(38)</sup>. They considered different lubrication conditions such as type of applicator, volume of lubricant, oil viscosity and anti-wear additives, observing how each affected the wear rate of an industrial roller chain. Results showed that the wear rate was lowest when oil was supplied to the inside of the chain drive where the slack span leaves the driving sprocket. When supplying oil at this location it was found that the amount of oil required to maintain a low wear rate was around 20% of that compared to other positions. For a  $\frac{3}{4}$  inch pitch chain transferring 15.1 kW at 1800rpm with a 200ml/min lubricant supply, the wear rate was found to be 0.06%/100 hours. Further reductions in wear rate by using a pressurised oil spray pipe were also shown to occur: for similar conditions using the same quantity of oil wear rates could be reduced from 0.12 to 0.024%/1000hrs. The choice of base oil also made a difference; a higher viscosity oil ( $200\text{mm}^2\text{s}^{-1}$ ) decreased the wear rate by 45%, compared to oil at  $60\text{mm}^2\text{s}^{-1}$  viscosity. Unsurprisingly, antiwear and extreme pressure additives also effect a further reduction in wear. With respect to solid lubricant additives, it was found that molybdenum disulphide was a far more effective wear reducer than graphite.

## 2.4 Efficiency

In an extension to their earlier work<sup>(39)</sup> Hollingworth and Hill formed a model for theoretical efficiency of a cranked link drive<sup>(10)</sup>. The difference between a cranked link (or offset side bar) chain and normal (straight side bar) linked drive is shown schematically in Figure 2-4, where it can be seen that each link in a cranked drive is identical, whereas the straight line design requires alternate pin links and roller links (or outer and inner links).

The result of the model showed increased efficiency for greater numbers of sprocket teeth, both driver and driven, due to reduced articulation angles. When the number of teeth of the driver<sup>(40)</sup> exceeded the driven it was found that the "open end forward" (right to left in Figure 2-4) case yielded greater efficiencies than "narrow end forward". This is the case most commonly found on a bicycle when the driving sprockets (e.g. 28,38,48) exceed in tooth number the driven (12-26). It is already acknowledged<sup>(10)</sup> that chain drivers do not function well below 11 teeth anyway so the results of the model are in accord with practice. The results were obtained by modelling energy losses for the articulations for open end forward and narrow end forward cases, using a value for the coefficient of friction measured previously<sup>(41)</sup>.

Hollingworth also noted that bush-roller wear will generally be smaller than pin-bush wear on account of the larger dimensions and usually greater hardness of components<sup>(41)</sup>. Comparisons between the theoretical results of Coenen and Peeken<sup>(42)</sup> and his experimental data were also made. Coenen and Peeken<sup>(42)</sup> also used an energy method to predict overall efficiencies. They highlighted a total of 6 areas for energy loss, three for pin-bush contact and the rest involving bush-roller contact. These models are considered in more detail in chapter 9.

## **2.5 Cycle chain efficiency**

When Whitt and Wilson produced *Bicycling Science*<sup>(9)</sup> in 1974 it provoked a great deal of interest in the engineering science of the bicycle, from ergonomics to component design. It is disappointing, then, that the references<sup>(43),(44)</sup> provided for the claimed 98.5 % efficiency for the cycle driven chain are insubstantial. These works do indeed mention chain efficiency but do not reference any scientific studies and seem only to be applicable to industrial chains. What Whitt and Wilson missed, as indeed does every other piece of literature uncovered to date, was two independent pieces of work completed in the late 1890s.

In the first published article, Mack<sup>(11)</sup> reported experiments to measure the entire bicycle's efficiency including bearings and tyre rolling resistance. Three bicycles were tested representing the best, intermediate and cheapest construction practices of the time. Efficiencies were found to be less than 50% with small chain tensions (under 50N), increasing as the tension rose; the maximum efficiency of 92% on the best bicycle was some 20% better than the cheapest offering. When considering pure chain transmission, average efficiencies for 7, 8 and 9 tooth rear sprockets were found to be 89.7, 91.5 and 93.4% respectively; the size of the front sprocket was not stated. The measurements were made by lowering and raising masses, thus it was a pseudo-dynamic analysis. In the published discussion following Mack's paper it was asked 'Have any of the members data upon the efficiency of the bicycle as a machine?' In reply, Prof. R.C. Carpenter announced considerable work that had been done in the preceding year. The method used was similar to Mack's but tested the efficiency under full operation (dynamic) conditions. The full description of Carpenter's experiment and his results were published the next year<sup>(12)</sup>.

The results certainly matched those of Mack in form, i.e. low efficiency when little power is transferred, with efficiency improving as power is increased. The best performing chain was of a Morse construction, where the chain acts on the side of the sprocket, and showed no loss in performance when wet sand was introduced as part of a test. The normal roller chain of the time showed very erratic behaviour when exposed to the sand contaminant as it clogged between the sprocket and roller.

At the time of Carpenter's study there was much debate as to the type of transmission the bicycle should have with many advocating the 'chainless' approach, i.e. shaft driven. As part of the test programme Carpenter was completing at Cornell University, shaft drives were found to come very close to matching the chain. The best attainable efficiency for the chain was found (at highest load) to be 99% whereas under the same conditions the shaft and bevel gear combination only reached 97% efficiency.

Comments following Carpenter's publication sparked discussion over how to reduce friction in the drive, with Barr<sup>(11)</sup> proposing that larger sprockets would result in improved efficiency. Further suggestions<sup>(11)</sup> were proposed by correspondents that argued that the coefficient of friction was reduced under extreme pressures and that smaller drivers were better suited for higher efficiency, a hypothesis based on a misconception about the laws of friction. Barr's hypothesis was proven by Burgess<sup>(14)</sup>, who completed a set of static experiments to determine the forces required to overcome friction. Burgess' theory predicted small improvements in efficiency from 98.8% to 99.4% by doubling the size of the sprockets used at 480W input power. These predictions took into account the larger area and sprocket mass but not chain mass. The results showed a similar improvement with sprocket size doubling at an

equivalent crank torque of 48Nm, from 98.4 to 99.3% although the difference between the two values rose from 0.6% to 0.9%. Burgess was the first to consider how these enhancements related to the performance cyclist. Greater efficiencies were expressed as improvements in time for a distance race and *vice versa*. As an example, a doubling of sprocket size from 26 teeth would lead to greater distances achieved by those competing for the 'hour world record' title. The challenge is to cover the greatest distance in a velodrome in exactly 60mins. The doubling effect would amount to around a 100m increase over the current 56km. Such an extended difference is of the same magnitude as incremental new record distances. However such records are already made with sprocket sizes approaching the maximum physically possible in the bicycle configuration.

An attempt to implement a system to apply these potential improvements is hindered by the practicalities of the bicycle. Increasing the size of sprockets much further than existing components would require a major redesign of the transmission system, and it is unlikely that a twofold increase in diameter could be achieved without increase in weight. Current maximum front sprocket sizes are around 60 teeth.

The most recent academic study of bicycle chain efficiency was completed by Spicer et al<sup>(45)</sup>. These authors measured the power input and output of a bicycle drive chain with torquemeters and a speed sensor, providing dynamic efficiency values with a good degree of accuracy. Four areas for investigation were followed. The effects of time on efficiency were observed over a period of 2 hours in order to identify how long a test was required to provide results of good repeatability. The duration of experiments was not found to influence efficiency. Closely related but not identified at

the time are the effects of lubrication. Chains were degreased and re-lubricated with efficiency measurements being made in both states. It was concluded that the lubrication state had no noticeable effect. Spicer et al found that the most significant factors affecting efficiency were the two other conditions examined, namely chain drive configuration and power throughput.

Changes in gear ratio (52:11, 32:15, 52:21) and offset constituted the chain drive configuration variables. It was observed that larger rear sprockets yielded a more efficient transfer of power. Comparing a 52:11 with a 52:21 gear combination at 50W and 60rpm, the larger rear sprocket was found to transmit 85.5% whereas the lower ratio resulted in 81.0% efficiency, the precision being  $\pm 0.3\%$  for both cases. The 3 gear ratios were tested with and without their natural offsets encountered in the bicycle set-up, and it was observed that the chain offset had a negligible effect on efficiency.

The set of variables that had the largest effect on efficiency were input power and angular velocity. Holding all other variables constant, there was a monotonic relationship between power increase and efficiency improved. For example, whilst driven at a constant speed of 60rpm a 52:15 gear combination yielded 83.2% efficiency at 50W but, at 200W, the efficiency was considerably higher at 98.0%. Conversely, increasing the input speed whilst maintaining the input power reduced the drive efficiency. Again, for example, considering the 52:15 sprockets, the efficiency at 30rpm(100W) was 97.8%, but for the same power, and a speed of 90rpm, the efficiency dropped to 87.2%. These effects are explicable in terms of the tension-efficiency relationship. It was found that efficiencies rose with an increase of tension irrespective of speed or input power. A linear relationship is apparent when efficiency

is plotted against the reciprocal of chain tension, with the highest efficiency occurring at high chain tensions.

In an effort to locate the losses in the chain Spicer *et al* used an infrared camera to observe those areas that generated heat from frictional losses. Heat intensity images allowed the following general observations of the chain to be made:

1. chain pins heat rapidly and reach steady state within 45 minutes,
2. the tension pulley (jockey wheel) takes heat in equal amounts from the chain and pulley bearing at low tensions and high rotational rates,
3. at high chain tensions and low rotational rates, the heating of the jockey wheels is mostly from the chain,
4. overall steady-state temperature conditions of the chain drive occur within 15mins of starting a test.

The infrared images could not account fully for the frictional losses for the range of efficiencies observed. A more sensitive and comprehensive thermal imaging analysis may resolve these inconsistencies. Spicer *et al* conclude that friction can only account for a fraction of the overall losses. The remainder, it is suggested, is due to low frequency vibrations that may be damped by the system overall. The efficiency suggests a critical dependence on the chain engagements and disengagements. This would account for higher efficiencies with larger sprockets and also higher chain tensions.

The first manufacturer to publish work which might previously have been considered sensitive was Fichtel and Sachs. Results from their tests were reported in a German cycling magazine in 1983 by Keller<sup>(13)</sup>. The test rig used consisted of transmission components arranged so as to simulate a real bicycle. A front chainring (driver sprocket) was powered by a motor through a torque metering input shaft. The

sprocket was attached to a bicycle wheel, resting on two rollers. The load was imposed on the system by a combination of an axially weighted wheel onto a roller fitted with a bicycle brake. The power output was calculated by measuring the torque generated at the back wheel by means of an arm of known length and a force transducer. The exact details of the measurement system and associated accuracy are unknown. The power range investigated was 25-500W varied by altering the chain tension (300-1,000N) and speed (20-100 rpm); all these values are of magnitudes consistent with human outputs. A variety of transmission methods were tested; shaft, hub gear and derailleur types.

The efficiency-power curves matched those of previous experiments with most efficient power transfer at the highest outputs. The highest attained efficiency was 93% with new clean chain and the derailleur gear set in the middle of the sprockets so that the chain line was straight. Up until this time no efficiency experiments had considered chain line as variable. The results, between 100 and 500W, showed a drop in efficiency of between 2% and 6%, the biggest loss being associated with the smallest (13 teeth) sprocket. Further effects of using the derailleur mechanism were then observed by altering the length of the chain by  $\pm 4$  links from the normal 108. Operating over a power range of 50-400W it became apparent that, below 150W, the most efficient lengths were 104, 108 and 112 links respectively with a maximum difference of 0.8%. Beyond 150W, different effects seem to have come into play and the most efficient chain lengths reversed, the range still being around 0.8%.

Attempts were also made to examine the effects of wear. When transmitting 200W with a worn chain, the efficiency may reach 99%; after 8,000 km of use this

may drop to 97-98% although a well used dry chain may drop to 93%. These findings came from a random sample of 3 employees' chains so the sample size is very low<sup>(46)</sup>.

Certain conclusions can be drawn from this disparate set of observations spread over more than 100 years. Efficiency is certainly high for cycle chain transmission, readily measured to be greater than 90%. The losses from friction remain fairly constant, independent of power and as a proportion of total energy they are small, so the measured efficiency is high and it rises as power throughput increases. This was also observed in preliminary studies by the author<sup>(3)</sup> and other unpublished work<sup>(40)</sup>. The size of the sprockets influences the friction losses, with larger sprockets creating less friction. Further factors which reduce efficiency are using worn chains and operating the chain at an angle. This is why professional cycle competitors have the chain and sprockets cleaned or changed regularly and position the most commonly used sprockets to minimise misalignment.

## **2.6 Lubrication Mechanisms**

Whilst studies of chain efficiency are scarce, studies linking efficiency and lubrication are more so. Peeken and Coenen<sup>(42)</sup> studied the effects of lubrication on chain efficiency by experiments in which they tested two oils of differing viscosities; however there was no statement of hypothesis as to why their tests showed that a lower viscosity increased efficiency. Radcliffe<sup>(47)</sup> used unlubricated chains with only changes in atmospheric gas considered. This work suggested that the debris from chain wear could act as a form of dry, solid lubricant. A similar observation can be seen in high wear, low friction coefficient bearings<sup>(48),(49)</sup>. While this may be true in a controlled experiment, the debris contained in a bicycle chain is of varying size and

material, both of which are highly dependent on the operating environment. Combining solid wear fragments with oil and water is likely to lead to an effect more like that of a grinding paste rather than of a lubricant. What Radcliffe observed may be similar to the running-in of bearings when surfaces with an initially high roughness and high friction coefficient, become polished or ground thereby lowering the resistance to sliding or rolling; this process is accompanied by a wear rate which is higher than in the normal operating condition<sup>(50),(51)</sup>.

Chains operate in the boundary lubrication regime since the relative speed of the rubbing surfaces is slow (less than 10mm/s). At low speeds (or high constant pressures) it is almost impossible to maintain the degree of fluid lubrication present in hydrodynamic lubrication<sup>(52)</sup>. With a non-replenishing lubricant, the thick lubricant layer breaks down and the surfaces are only separated by lubricant films of molecular proportions and there is considerable asperity contact. The contact mechanisms are now governed by the chemical properties of the surface-lubricant interface and the bulk lubricant properties of density and viscosity are much less relevant. The attributes important now are the lubricant and surface chemical compositions, substrate properties and the surface profile geometry. The coefficient of friction is now typically 0.05 - 0.15, which is considerably lower than for chemically clean surfaces, although several magnitudes greater than that with hydrodynamic lubrication. The regimes of boundary lubrication are normally illustrated in a Stribeck diagram, Figure 2-5, derived from generalised experimental data, although the bearing surfaces in the chain do not operate in the manner of a common journal bearing. This chain form shows the coefficient of friction  $\mu$  plotted against the non-dimensional

group  $\eta\omega / p$  (also referred to as the Hersey number) where  $\eta$  is the Newtonian viscosity,  $\omega$  the rotational speed and  $p$  the nominal bearing pressure.

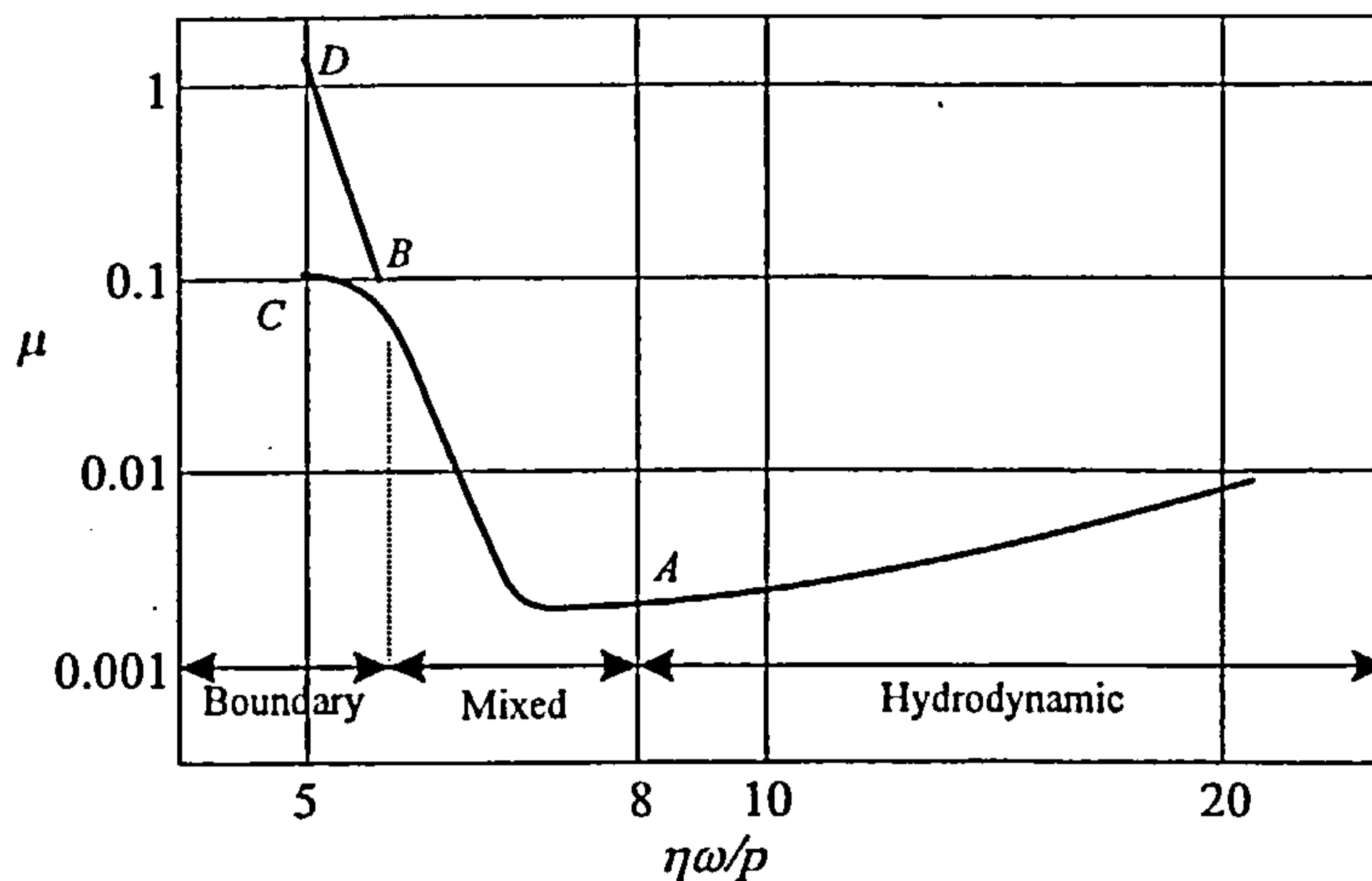


Figure 2-5: Stribeck Diagram of Lubrication Regimes

The regions of hydrodynamic, mixed and boundary lubrication regimes are clearly noted. In the case of boundary lubrication (B-C or B-D) the possible friction coefficients are less predictable and cover a much wider range than in other lubrication types. A more appropriate representation of the regimes of sliding metal-to-metal contact for the chain environment is the transition map used by the OECD International Research Group<sup>(51)</sup>, Figure 2-6.

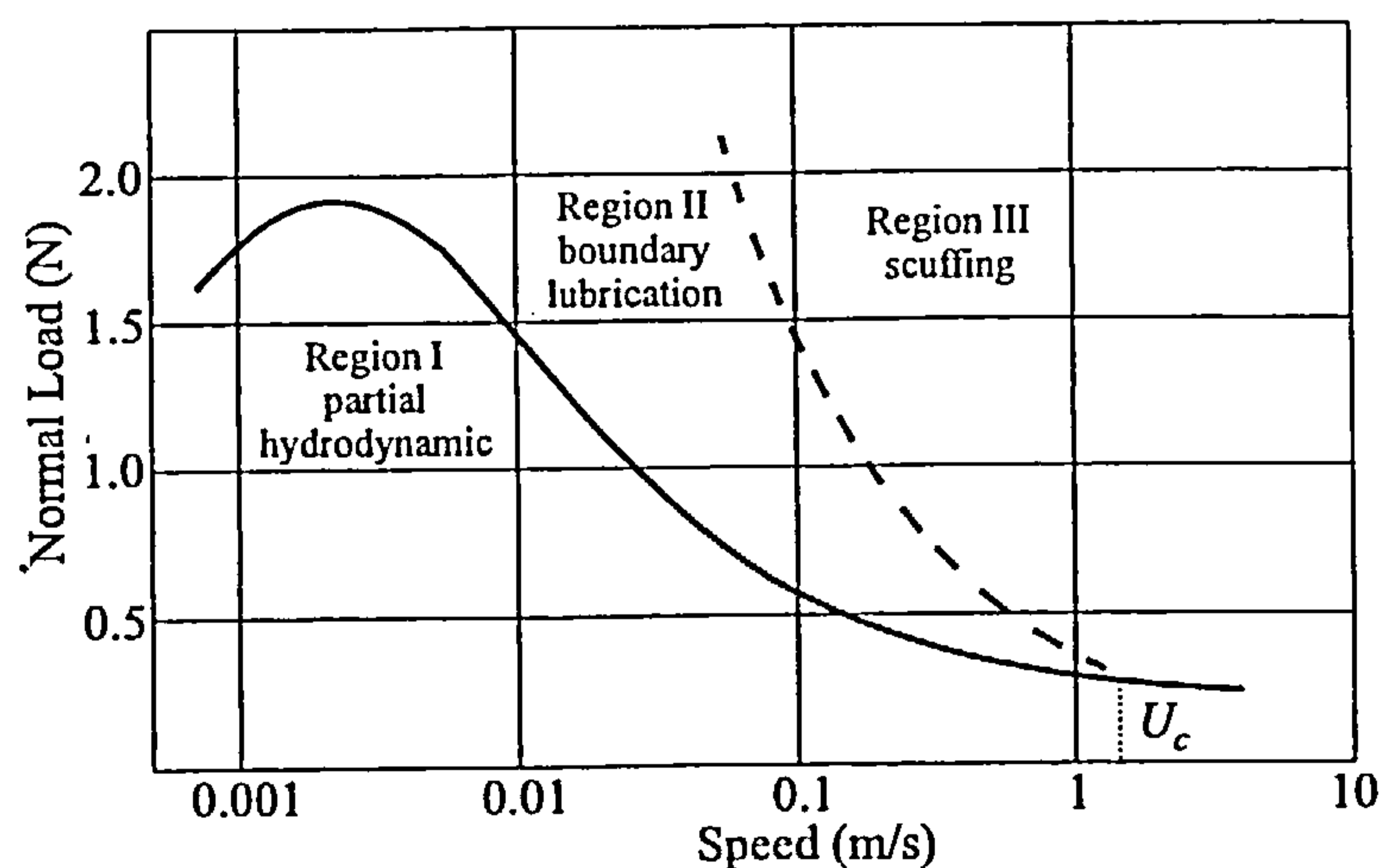


Figure 2-6: Transition map of boundary and associated lubrication regimes

This diagram shows in greater detail the relationship between load and relative sliding velocity for steel. Of interest is the transition of boundary lubrication to scuffing, defined as localised damage caused by the occurrence of solid-phase welding between sliding surfaces, without local surface melting. This transition will not occur at speeds above  $U_c$ , when the bearing state will pass directly from partial to scuffing. The region of scuffing is commonly signified in operation when there is an increase in noise, vibration, temperature and adhesion or material transfer between the surfaces; this is usually manifested in cycle operation as a squeaking chain.

The passage from one lubrication regime to another is also dependent on the relationship between film thickness and surface roughness. The film thickness parameter or lambda ratio,  $\Lambda$  quantifies this relationship and is defined as:

$$\Lambda = \frac{h_{\min}}{\sqrt{R_{q1}^2 + R_{q2}^2}} \quad \text{Eq. 2-11}$$

where  $h_{\min}$  is the minimum lubricant film thickness, and  $R_{q1}$  and  $R_{q2}$  are the respective r.m.s. surface roughnesses of the two solid surfaces. Boundary lubrication occurs at  $\Lambda < 1$  when asperity interactions become the dominant friction factor, rather than the shear properties of the bulk lubricant<sup>(51)</sup>. During an investigation into how  $\Lambda$  changed as bearing surfaces wore and the effect on subsurface stress distribution, Zhou et al<sup>(50)</sup> found large sub-surface von Mises stresses that could lead to crack formation or pitting by a process of contact fatigue.

One of the fundamental problems with the study of surface-surface and lubricant interactions is the inability to observe the interface during operation. Data is gathered from observing the effects of the post-event phenomenon and comparing these with the features beforehand. It is well known that no matter how well machined

or polished mating surfaces are, the actual area of contact will not exceed 2-7% of the apparent area<sup>(53)</sup>. The measurement of surface profiles can be done by a variety of instruments; Sherrington and Smith<sup>(54)</sup> outline the operation of many types and suggested applications, from stylus-based to microscope-based measurements. The resultant measurements give an indication of the actual surface profile, which can be considered, according to Hamrock<sup>(55)</sup>, to be made from three superimposed characteristics:

1. Error of form, where the surface deviates from the designed pattern because of errors inherent in the manufacturing process.
2. Waviness, which is the term characterised by relatively long wavelengths, small amplitude, periodic variations normally attributed to unwanted vibrations occurring during manufacture, for example cutting tools.
3. Roughness, or irregularities inherent in the cutting and polishing process during production.

A number of different measures of surface profile of engineering components are commonly used. Perhaps the most popular are amplitude-based measurements, where roughness is defined in terms of some type of mean distance from a datum, for example:

$$R_a - \text{Centreline average (CLA):} \quad R_a = \frac{1}{N} \sum_{i=1}^N |z_i| \quad \text{Eq. 2-12}$$

$$R_q - \text{Root mean square (rms):} \quad R_q = \left( \frac{1}{N} \sum_{i=1}^N z_i^2 \right)^{1/2} \quad \text{Eq. 2-13}$$

$$R_t - \text{Maximum peak to valley height:} \quad R_t = \max(z) - \min(z) \quad \text{Eq. 2-14}$$

For all of the above cases a reference line is used such that the average of the Z co-ordinate,  $z_i$  values is zero. The  $N$  samples are taken at uniform, small, length intervals,

$\Delta$ , depending on the wavelength of interest and according to Nyquist-like considerations.

Because the lubrication in a bicycle chain is so poorly controlled, it is very hard to formulate a model that comes anywhere close to real observations. Modern theories of friction normally require a detailed description of the asperities. Shape is commonly defined in terms of root cross-sectional area, slope, height and tip curvature and these parameters, along with shape distribution, asperity and density are all important factors for determining the nature of friction and how a lubricant must work. For example, Tripp et al.<sup>(56)</sup> found that asperity slope rather than height was a more important factor in reducing friction. By modelling asperities as paraboloidal protuberances (one of many options as others have considered cantilever beams<sup>(53)</sup> and prisms<sup>(57),(58)</sup>) and using a macro type finite element method, magnitudes of the micro deformations could be found in two cases, dry and lubricated. It was discovered that in the dry condition, the surfaces conformed to each other and in the lubricated condition a parallel conformity occurred with a fluid film separating the surfaces. Asperity contacts between metals of similar hardness have been simulated by Black et al.<sup>(58)</sup> using scaled asperity models made from Woods metal, a soft and ductile material. The model asperities were triangular in cross section but variations in angular dimensions were made that resulted in different interface angles and in turn altered coefficients of friction; the higher the interface angle the greater the friction. Photographs of the model asperities slipping and deforming against each other were also given, providing a visualisation of the modes of surface movements. To investigate couples consisting of metals of different hardness, another macro experiment was conducted, this time by Radchik and Kotlyar<sup>(53)</sup>, who slid three

different metal blocks (aluminium, steel and bronze) against a bronze plate that had strain gauges measuring the surface deformation. This simple test confirmed that the lowest strain occurred with the material of highest modulus of elasticity, steel. However the tests did not extend to examining the wear features of different metal couples. Radchik and Kotlyar<sup>(53)</sup> had acknowledged that with dry friction, increasing the hardness of one material reduces the overall wear of the two surfaces. Furthermore, increased hardness would also result in smaller sheared off particles of both bodies, i.e. less wear irrespective of modulus of elasticity.

Many models of surface contact have been concerned with the plastic deformation or shearing of protuberances but a further consideration must be of a 'ploughing' effect. Azarkhin and Richmond<sup>(57)</sup> analysed the ploughing possibility using an energy method to determine power losses in a variety of asperity cases where density and orientation were varied.

An energy method of modelling friction can be taken from Dashia's<sup>(59)</sup> interpretation of the Kingsbury hypotheses<sup>(60),(61)</sup>, observing how contact friction is influenced by temperature, velocity of sliding and certain molecular properties of the lubricant. The dislodging of the molecules occurs at a surface provided that the time,  $t_z$ , it takes the asperity to slide the distance,  $z$ , between the sites is large compared to the time of residence,  $t_r$ . This time of residence,  $t_r$ , spent by a particular molecule on a site can be related to the thermal energy level of the molecule and to the temperature of the surroundings by:

$$t_r = t_0 \exp\left(\frac{E}{RT}\right) \quad \text{Eq. 2-15}$$

where  $E$  is the energy from the heat of adsorption of the molecule on the surface and  $T$  is the absolute temperature,  $R$  is the universal gas constant and  $t_0$  is the period of thermal vibration of the molecule.

Since the rate of adsorption of the molecules is exponential with time, the area covered can be given by,

$$(1 - \alpha) = \exp\left(-\frac{t_z}{t_r}\right) \quad \text{Eq. 2-16}$$

Where  $\alpha$  is the *fractional film defect*, which is the fraction of the total metal area over which the breakdown (desorption) has occurred. It is an indication of the degree of failure of the lubricant.

When the average time  $t_z$  taken by an asperity to move a distance  $z$ , which is equivalent to the equivalent diameter of cross sectional area of the adsorbed molecule, is expressed using the sliding velocity  $v$ , the fractional film defect can be simplified to the form,

$$\alpha = 1 - \exp\left[-\frac{z}{vt_0} \exp\left(-\frac{E}{RT}\right)\right] \quad \text{Eq. 2-17}$$

where  $T$  is the local temperature of the interface. The molecular properties  $t_0$  and  $z$  are not dependent on load, speed or temperature of a sliding system.

The approach taken by Rabinowicz<sup>(48)</sup> is similar in that it looks at the apparent and real areas of contact but goes further by considering the chemical properties of the surfaces and lubricant. Two models are proposed, single or multiple penetration, depending on the lubricant used. If the lubricant is penetrated at one point only, we have a simple two component system in which there is solid-solid contact over one fraction of the junction, denoted by  $\alpha$ , and the solid film lubrication over the rest of

the junction denoted  $(1-\alpha)$ . The shear strength for the solid contact regime is  $s_m$ , that of the solid film regime is  $s_l$ , and hence the force required to shear the junction of area  $A$  will be,<sup>(62)</sup>

$$F = \alpha A s_m + (1-\alpha) A s_l \quad \text{Eq. 2-18}$$

which is equivalent to  $f = \alpha f_m + (1-\alpha) f_l \quad \text{Eq. 2-19}$

where  $f_m$  and  $f_l$  are the friction forces at the unlubricated and lubricated films<sup>(48)</sup>.

The bearing surfaces in a chain may be considered smooth by engineering standards, perhaps with a peak-to-valley roughness dimension of around  $0.1\mu\text{m}$ . By contrast, the molecular length of paraffinic hydrocarbon chains used in lubricating oils is of the order of  $0.0025\mu\text{m}$ , which, although it represents a large molecular length, is only about 1% of typical asperity heights<sup>(63)</sup>. It may seem unlikely that such thin surface layers can possibly provide any real degree of protection to heavily loaded sliding surfaces, but it has been demonstrated by Bowden and Tabor<sup>(62)</sup>. If a drop of stearic acid (one of the classical boundary lubricants) is floated on the surface on the bath of clear water it will spread until it is everywhere one molecule thick. In addition all the molecules will be oriented with their longest dimension perpendicular to the surface, like a pile on a carpet. Such a film may then be floated off on to a metal plate for friction testing<sup>(62)</sup>. The results of these friction tests show that although a single monolayer of the lubricant was soon worn away (around 5 metal roller traverses) low friction behaviour was maintained for much longer periods if a number of such layers were laid down on top of each other, Williams<sup>(51)</sup>.

The best boundary lubricants are thus those with long chain molecules with an active end group that adheres to the surface. Such polar lubricants as fatty oils, long-

chain acids and greases are suited to the demands required in this environment. Unfortunately with respect to the application as a bicycle chain lubricant, they have the undesirable characteristic of attracting dirt and trapping moisture<sup>(64),(48),(65)</sup>. Theories on boundary lubrication suggest that those lubricants neither based on such molecules nor lacking in active additives would be inferior. An alternative to using a hydrocarbon base for a lubricant has been proposed by a chain lubrication manufacturer. A water soluble surfactant containing long chain hydrocarbons is applied to the chain in conjunction with varying amounts of water. The methodology suggested is that a frequent application of this mixture allows peak efficiency to be maintained. Soluble surfactants are more frequently employed as cutting or grinding fluids<sup>(66)</sup> where the demands on the lubricant are not so great as in bearings. Singer<sup>(26)</sup> has suggested that water itself may act as a sufficient lubricant in comparison to other mineral based oils.

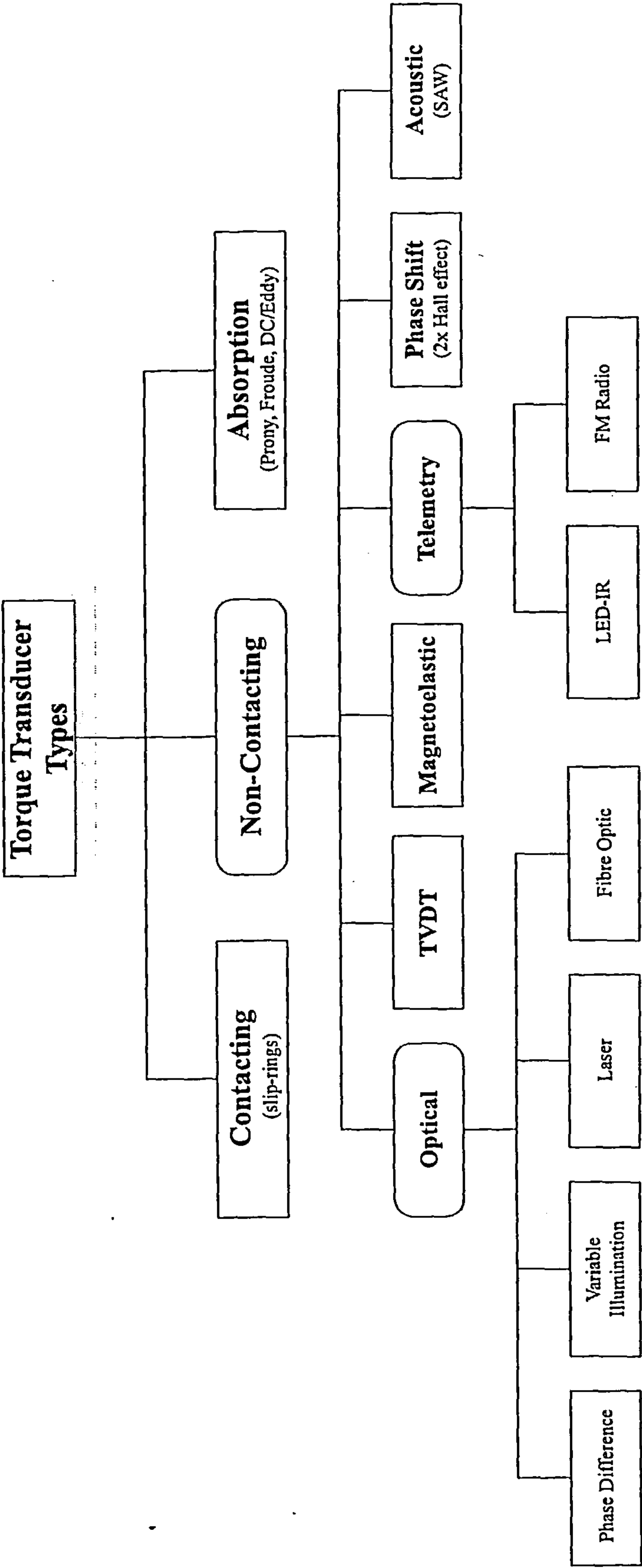
## **2.7 Torque Measurements**

Instrumentation plays a vital role in any experimental research but in the case of measuring absolute values for chain efficiency, let alone detecting small variations between tests, the need for great accuracy is paramount. Consequently, a substantial proportion of this work was spent developing a new torquemeter instrumentation system. The very first attempt to measure chain efficiency by the author<sup>(3)</sup> used an unsuitable radio telemetry system on a rig that later became modified to provide results presented later in the thesis. This section catalogues and briefly evaluates those options considered with the final chosen solution in Chapter 3. Figure 2-7 provides an overview of the methods outlined in the following sections, highlighting the wide range of non-contacting types of transducer.

### 2.7.1 Traditional Methods

The practice of torque measurement is relatively new in comparison with force measurements that can date back over a thousand years<sup>(67)</sup>. Absorption dynamometers that absorb a prime mover's power in order to measure it such as the Prony brake (as used by Carpenter bicycle experiments<sup>(12)</sup>) or Froude's water brake were invented in the 1800s. Brakes based on these designs are still in use today but are more commonly used in large power output devices. For example, fluid friction brakes (Froude type) can absorb up to 18MW and operate up to 10,000rpm; dry friction brakes (like the Prony) can measure as much as 150kW at between 1,000-2,000rpm. Other devices dating back to this time operate with electromotive force as the absorber and indicator. DC brakes or generators may be used to produce electromagnetic fields that can be measured by using an arm projecting from the stator or from the current in the coils. A more recent adaptation of this principle is the eddy-current brake that has a toothed metal rotor. The current in the windings of the stator creates eddy currents in the rotor which produces an electromagnetic force that acts on the stator. The torque is calculated from the counter torque required to stop the stator from moving.

Figure 2-7: Torque Measurement Techniques



Other types of absorbing dynamometer include those which use a similar principle to the Froude brake but use air instead of water as a power dissipater. The speed at which the fan operates for a given type, size and number of vanes is known as is the torque required to do so. The problem with this, the electrical and Froude types is the limited range of speeds under which they can operate. Also, absorbing devices are generally not sufficiently accurate to detect small or brief changes in torque, nor can they operate 'in-line'.

Using the linear elastic properties of metals under small deformations, transmission (in-line) torque transducers open up a wide range of measurement methods. Simple torsional bending theory states that an elastic shaft with an applied torque,  $T$  will twist through an angle  $\theta$  given by:

$$T = \theta \frac{GJ}{L} \quad \text{Eq. 2-20}$$

where  $G$  is the shear modulus of elasticity of the material,  $J$  is its polar moment of inertia and  $L$  the corresponding section length. If all these constants are grouped together to form a torsional stiffness,  $K$ , then the linear relationship becomes:

$$T = K\theta \quad \text{Eq. 2-21}$$

The use of resistive strain gauges as an electrical load cell for stress or strain measurement is now widespread practice in engineering<sup>(68)</sup>. When bonded to a shaft in a certain orientation, strain gauge array can provide a reliable method for torque measurement. The full bridge configuration shown in Figure 2-8 is the most frequently used<sup>(69)</sup>; by using a full bridge with the 'arms' diametrically opposite any effect of bending is theoretically eliminated e.g. T1 and T2 are on opposite sides of the shaft and are oriented to measure a positive moment of the shaft.

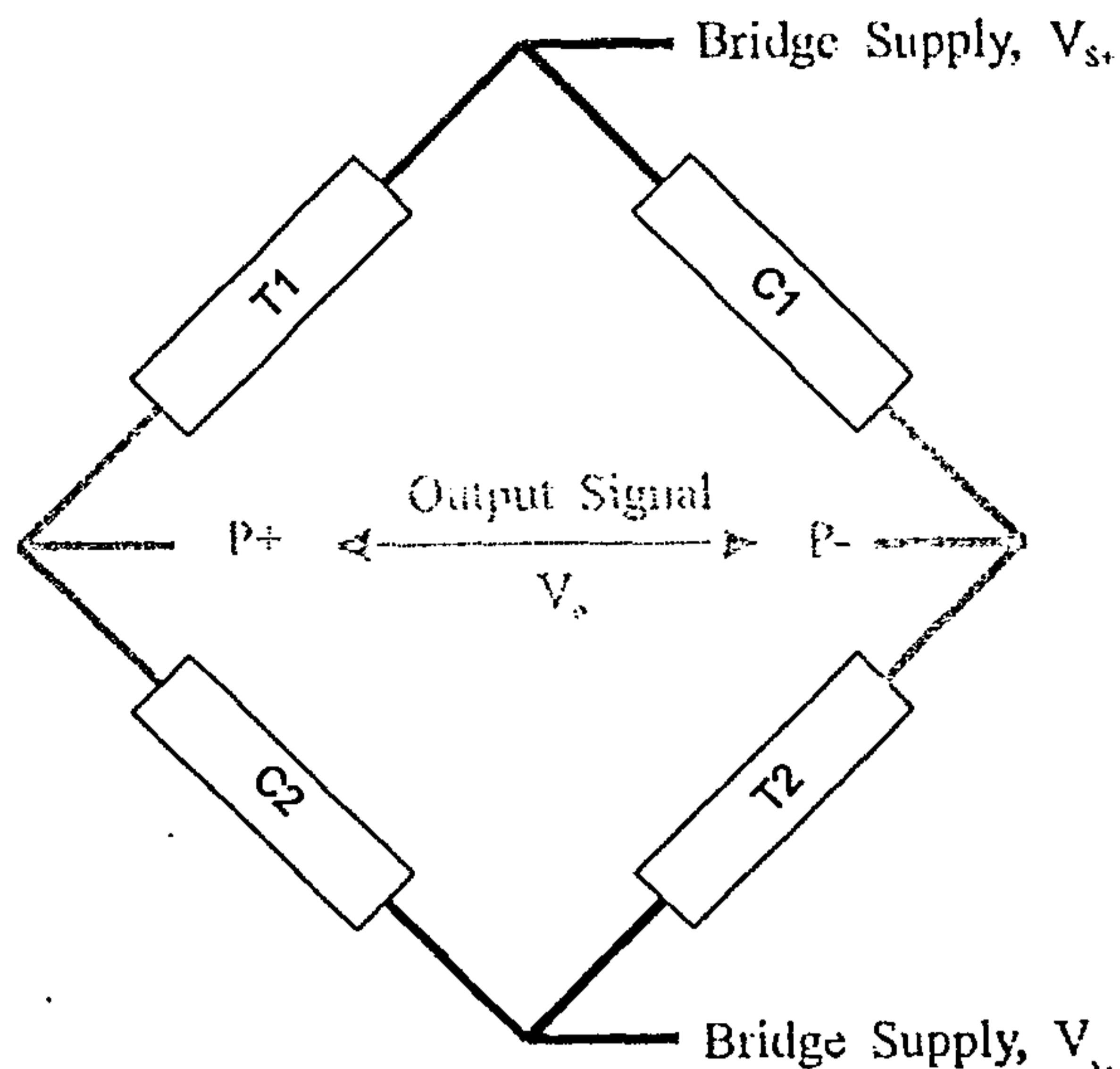


**Figure 2-8: Full bridge strain gauge configuration**

The strain measured by the full bridge configuration,  $\epsilon$ , can be calculated by observing the changes to the output voltage,  $V_o$  due to alterations of the tensile (T1, T2) and compressive (C1, C2) strain gauge resistances. Knowing the supply voltage to be  $V_s$  and the gauges all having an equal gauge factor of  $GF$  then it can be shown that:

$$V_o = V_s \left[ \frac{T2}{T2 + C1} + \frac{C2}{C2 + T1} \right] \quad \text{Eq. 2-22}$$

thus the strain can be given by,

$$\epsilon = -\frac{1}{GF} \frac{V_o}{V_s} \quad \text{Eq. 2-23}$$

Once the positioning on a suitable section of shaft has been determined the only problem remaining is transferring this low power signal off the rotating shaft to record it. There are two classes of method to do this, contacting or non-contacting.

Contacting torque transducers use slip rings to supply power to a bridge amplifier through an input circuit, which in turn sends the now stronger signal back through an output circuit. Spring loaded 'brushes' on the static part of the equipment

make contact with gold or platinum rings on the shaft. The problems associated with this method are cost, complexity and signals prone to noise. If the bush-ring contact is not perfect due to ring or shaft defects dust or oil ingress, then the torque signal becomes swamped by noise. Contacting torque transducers are becoming less frequently used for these reasons and because there are simpler more reliable and more accurate instruments based on the non-contacting principle.

## 2.7.2 Non-contacting methods

There are many methods of torque measurement that use no form of physical contact between rotating shaft and static receiver. Several of these methods detect the actual angular twist along the shaft using magnetic fields or optical measurements, the latter having the advantage that they are immune to electromagnetic interference. Other techniques use acoustic or magnetoelastic measurements.

### 2.7.2.1 *Phase change methods.*

Using the torsional displacement properties of the shaft (Eq. 2-16), if the angle of relative twist between two points along the shaft is known, then the torque can be calculated directly. One method of achieving this is by using two gear teeth and two Hall-effect or magnetic pulse type sensors. By observing the phase shift in the pulses, the angular displacement can be determined. An alternative method of relative angular difference may use photocells and light reflecting marker bands on the shaft<sup>(70)</sup>. Whilst these methods were conceived some years ago, it is only more recently with the introduction of digital circuitry that such approaches are becoming more frequently applied<sup>(71)</sup>. Recent applications of optically measuring the shaft twist use angular encoder disks<sup>(72)</sup>, mounted such that a light source may pass through an aperture to a

photocell that is 50% of the maximum possible when no torque is applied. When the shaft experiences torque and therefore twist, there will be an increase or decrease in the amount of light falling on the photocell, depending on the orientation of the disks and administered torque. The accuracy of this optical transducer is  $\pm 1.56\%$ <sup>(72)</sup>. A more accurate (at least compared to theoretical results) implementation of optically detecting twist of the shaft uses a laser and CCD array<sup>(73)</sup>, or a Moire fringe method that utilises two circular gratings mounted concentrically at separate points on a shaft. The first grating is ruled radially, the other having rulings tangential to a central circle. As angular displacement occurs, circular fringe patterns are formed and read by a 256-element CCD array. The prototype implemented and tested by Spooner *et.al.*<sup>(73)</sup> showed that the principle was valid but required several refinements in operation prior to any industrial applications.

So far, all the methods considered require placement on or access to the outer surface of the shaft. Where this is hard to achieve for physical or environmental constraints, an alternative approach may be necessary. Rudd *et.al.*<sup>(74)</sup> used a method that detected the phase difference of angular position between a point within the length of the shaft and its end surface. Polarised light from an LED was passed down the centre of the measuring shaft and was reflected back through another polariser at the far end. Relative rotation between the polarisers produces maximum light intensity when they are parallel and a minimum signal when perpendicular. A sensor at the near end of the shaft picked up a second modulated light signal from the same source as it was chopped by alternating reflective and non-reflective areas on the end face. Comparison of the near and far end signals yielded the desired measurement of

angular displacement. The signal processing could be carried out remotely by using optical fibres to carry the signal.

Magnetic methods can also be used to obtain torque either by torsional twist or using magnetoelastic material properties. If the shaft is made of a non-magnetic material then a torsional variable differential transformer (TVDT) can be used. Its principle of operation relies on a 45°-slotted gap between three, externally mounted, tubular magnets opening and closing under torsional loads. Electrical coils situated around the magnets show varying voltages as the magnets move in relation to each other, increasing or decreasing the induced voltage in the coils<sup>(69)</sup>.

A system based on the magnetoelastic method has been implemented in an automotive power assisted steering system by Garshelis<sup>(75)</sup>. This novel approach employs a magnetically conditioned sleeve mounted on a shaft. Without external excitation, the magnetic field created by this sleeve changes intensity and polarity according to the torque shared by the sleeve and shaft. A magnetic vector-sensing device positioned sufficiently close to the sleeve will be able to detect such changes and provide an electrical output accordingly. The conditioning of the magnetic sleeve (or ring) is a complex procedure and specific applications may require different magnetic material types. The long-term stability following cyclic stresses is still to be fully investigated before its use becomes more commonplace in mass-produced systems.

An alternative to using electrical resistance strain gauges, although still maintaining their principle of application, has been developed by Hall<sup>(76),(77)</sup>, using quartz slivers of dimension 1 x 3 mm thickness with etched aluminium electrodes and bonded to flat sections of a shaft. The strain in the quartz brought about by changes in

torque create differences in natural frequency. When arranged in a similar manner to strain gauges, aligned at 90° to each other but at 45° to the main shaft axis, changes in torsional load can be measured additively since, as one natural frequency increases, the other drops. It is claimed that a resolution of a few parts per billion is possible and that linearity is better than 0.1%. Figures for the performance of a product based on this principle are likely to be less good however.

## **2.8 Summary**

This chapter has reviewed the results of studies in chain mechanics, chain efficiency, lubrication and torque measurement.

The thoroughness of the search on chain efficiency has located unpublished materials, translations and uncovered articles written in excess of a century ago. This is the first time such a comprehensive review has been carried out in the field of chain efficiency.

Because the main challenges in the field of lubrication are seen as being in the hydrodynamic regime, it is not surprising to find so few published works dealing specifically with the chain. The general literature on boundary lubrication tends to apply to well-controlled efficiency systems and the current work will need to acknowledge the fact that lubrication-state is highly variable and subject to contaminants.

The many methods of determining torque revealed reflect the wide range of torquemeters available for use. The more recent developments in instrumentation allow improved accuracy over more established methods and given time their associated costs of implementation may reduce. It has been concluded, considering the

current status of the various technologies, that a strain-gauge based method of non-contacting torque measurement is likely to be the most successful as their limitations are known and the hurdle of signal transmission from a rotating shaft can be solved using modern electronics.

### 3. Torquemeter Instrumentation

#### 3.1 Introduction

The determination of transmission efficiency requires the input and output power of the system to be known. Although these can be measured without a torquemeter using, for example, indirect measurements of electrical power input or heat output, these methods are not convertible to an accurate measurement of mechanical efficiency. For example, correction factors for bearing or resistive losses must be used and it is therefore desirable to have direct measurement of mechanical power. To make an accurate measurement of the actual torque and thus the power transmitted by the shaft driving the chain requires the use of an in-line transducer. The various types of transducers available and the details of their operation were covered in Chapter 2.

When making two independent observations such as input and output torque measurement, the accuracy of instrumentation is paramount. Any errors in measurement are compounded by the calculation of efficiency which requires the division of the input by the output signals. Due to the high efficiency of the chain system of 90-99%, the differences between power input and output are small. If the system runs at an efficiency of 98%, then calculating the efficiency with a 2% error bound makes comparisons very difficult between operational changes that themselves only change efficiency by  $\pm 1\%$ . Although a differential method based on a four-square principle<sup>(28)</sup> would perhaps result in easier or more accurate detection of small changes between experiments, the actual efficiencies would not be known and this is a primary objective of the experiments.

### **3.2 Requirements**

In order to observe small changes in the efficiency of the chain resulting from alterations in operational parameters, a system with reliable, precise resolution and accuracy is required. A desired torque resolution of 0.1% and accuracy of  $\pm 0.05\%$  at full scale were decided upon based on the requirement to know efficiency to better than 0.1%. The sensitivity of the instrument must be such that brief (2Hz) or slight changes in torque are apparent and known with a degree of confidence. Other types of torquemeter available are unable to match these requirements, especially when cost is a constraint.

As the instrumentation was to be developed and tested within the timescale and resources of the specific project, simplicity in design and cost of components was another important factor to be considered. This process would also facilitate faster development and lead to a greater understanding of operation principle, in particular to track the sources of noise and potential optimisation of accuracy. By making the system simple and low in component count, another requirement would also be met, that of size. For an in-line transducer to be incorporated easily into the skeleton of the efficiency experimental rig, it had to be able to be strapped onto or into a main shaft mounting diameter of 30mm and 100mm long. Provision was also necessary for the power source for the electronics. Although the use of slip rings would not impede the system accuracy, the implementation could be unwieldy and expensive and the potential for noise was unknown. Rechargeable batteries of sufficient amperage hour capacity would be cheap, simple and would allow the system to run for at least 60 minutes without performance being affected.

The ability to acquire measurements automatically and with good time resolution was an important factor. It was felt that this would only be achieved by interfacing the instrumentation with a computer and data acquisition card. As the system would be bespoke, an element of software development would be inevitable but, taking careful consideration of the signal characteristics, the task could be made simpler.

The final requirement to be defined was the operational range. To be representative of the spectrum of cyclists' power output and indeed match the output of the existing rig motor, the torquemeter should be capable of measuring from 0-50Nm. Because the apparatus only operates with the chain going in one direction, the sense needed only to be positive. With respect to the rotational speeds to be encountered, the transmission of the signals should be able to work at speeds up to 540rpm (52:12 at 120rpm). The numerical requirements can be summarised in Table 3-1.

Torque range	0-50Nm
Resolution	$5 \times 10^{-3}$ Nm
Accuracy	$\pm 0.05\%$ at FS

Table 3-1: System requirements

### 3.3 Design

#### 3.3.1 Physical

A one-piece construction steel shaft formed the basis for both input and output shafts, the only difference between the two arising from the attachments fitted to their ends, Figure 3-1. The torque measurement was made using resistance strain gauges mounted outwith the self-aligning double race bearings supporting the shaft; this feature ensures that any bearing losses are eliminated and need not be subtracted from the torque measurements. The gauges were placed on a hollow section of shaft, thereby increasing the system sensitivity and requiring less electrical amplification thus reducing noise. Figure 3-3 shows how the section modulus of  $J_4$  represents the best balance between sensitivity and practicality for production.

The gauge configuration is shown in Figure 3-2. This arrangement is a recognised <sup>(69),(78)</sup> method to eliminate any strain signal produced from pure bending or axial thrust in the shaft. The gauge arms were aligned at 45 degrees to the main axis of the shaft and at 90 degrees to each other. By aligning the gauges in this manner, the principal strain due to torsion is by far the dominant signal and the use of a full Wheatstone bridge configuration improves sensitivity further. Furthermore, by having the gauges in such close proximity to each other and with short lead wires no extra precautions for temperature compensation are required.

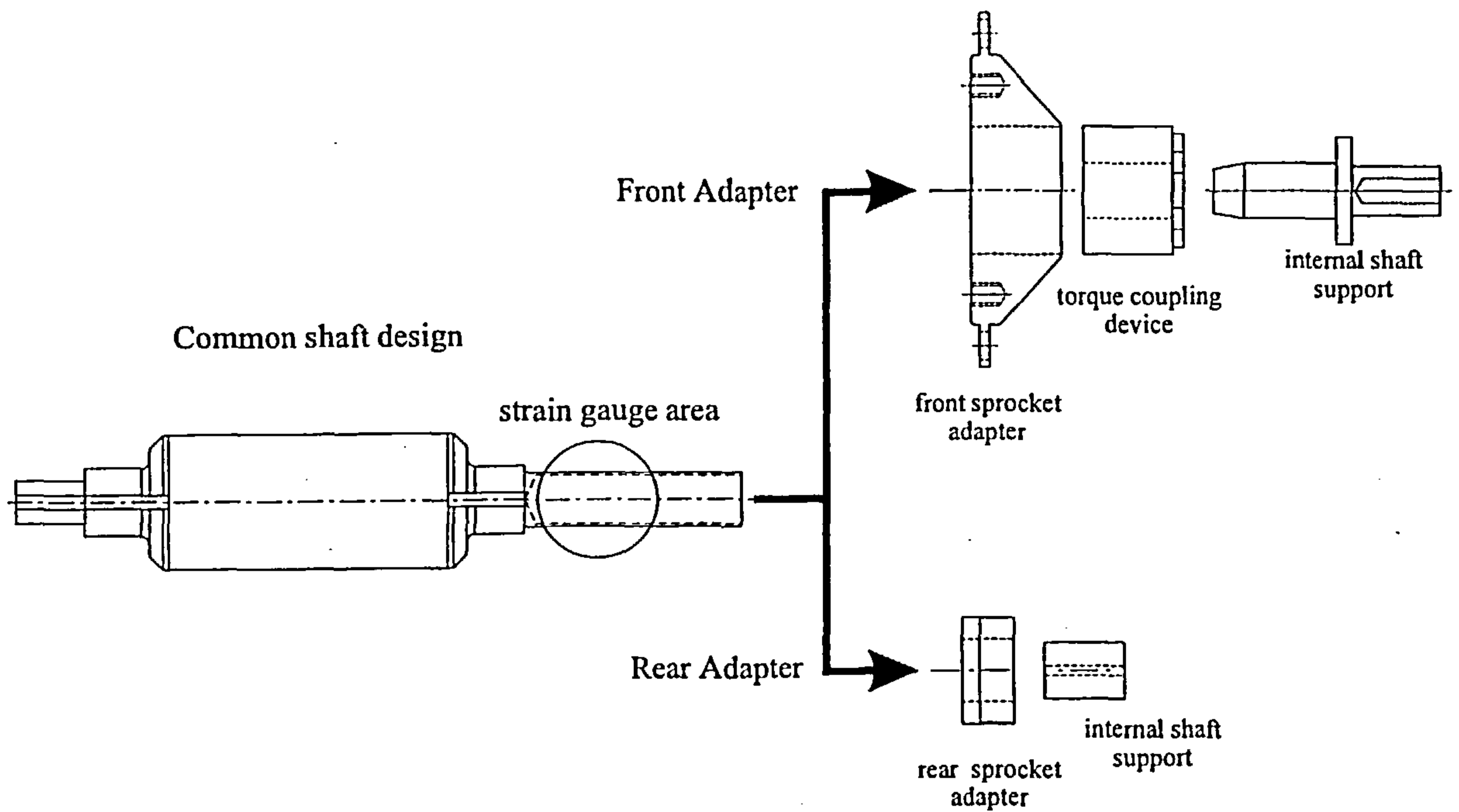


**Figure 3-1: Front and Rear Shaft Adapters**

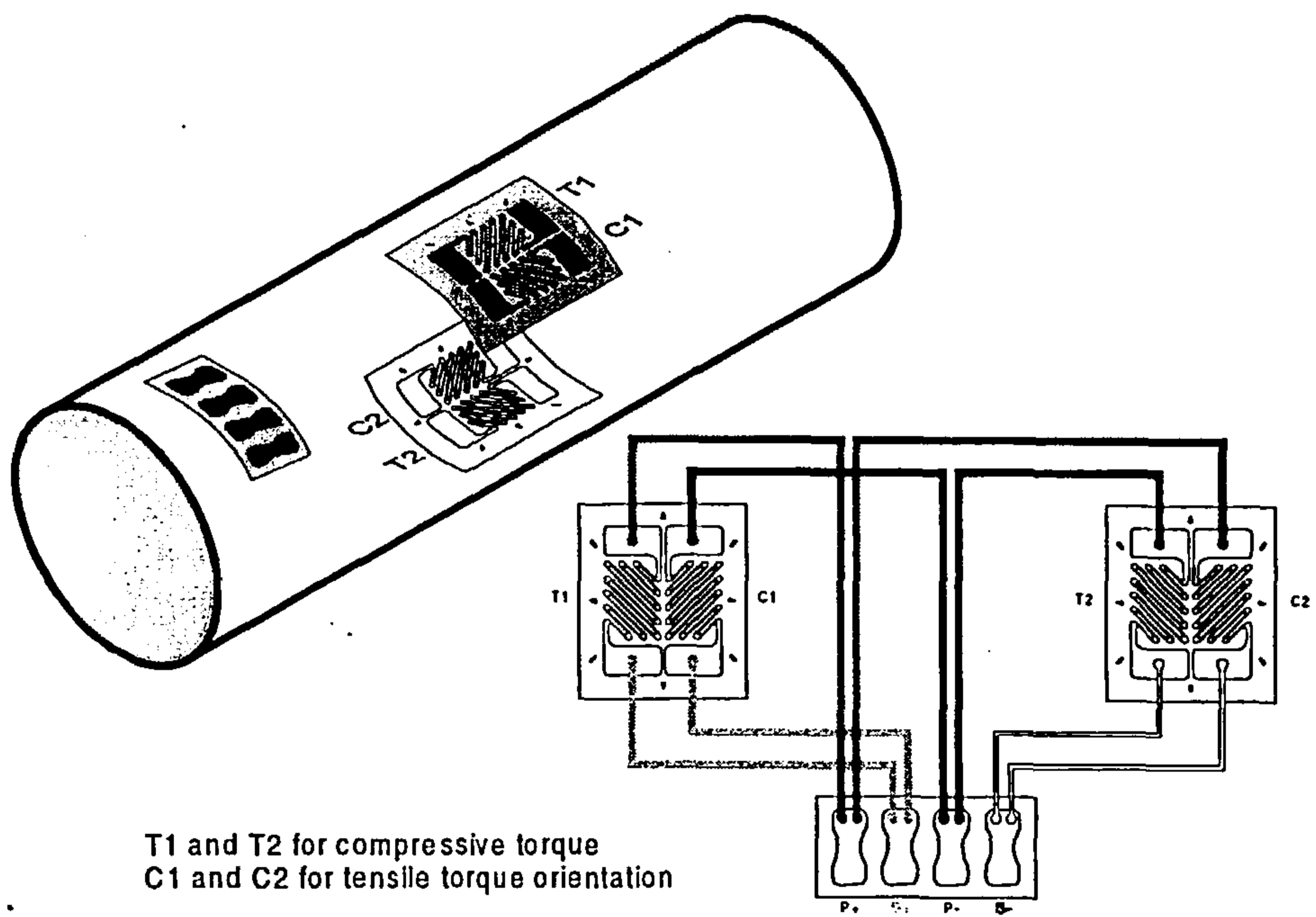
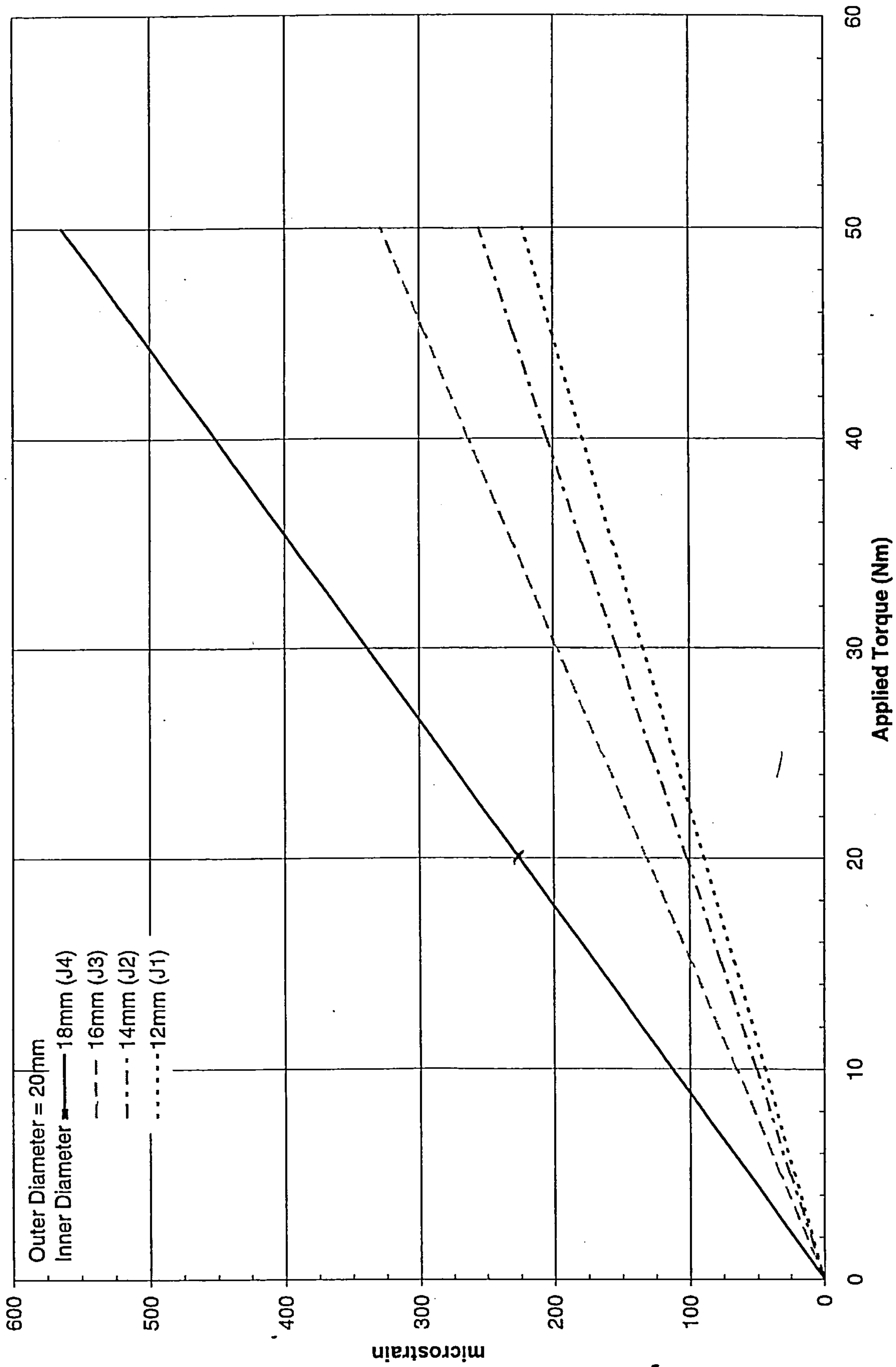


**Figure 3-2: Strain gauge configuration**

Figure 3-3: Calculated Torque Sensitivity for Various Shaft Diameters



The gauges were Micro Measurements N2A-06-T031P-350 transducer class. A simple cyanoacrylate adhesive was used in preliminary testing but problems with reliable installations and doubts over long term stability from creep meant another, more robust solution was required. Using *Mbond* heat cure adhesive and 2 layers of coating, the final method yielded better consistency, confidence in use and better protection for the strain gauges. Before operation, the bridge was balanced whilst gently rubbing the gauge surfaces and a value for zero offset of  $\pm 0.003\text{mV/V}$  for the input shaft and  $\pm 0.01\text{mV/V}$  for the output was recorded. Although these values are not important for the use in the calculation of torque, the fact that they are very close to zero indicates a successful gauge installation.

Two different approaches were taken to mounting the cycle components to the front and rear shafts. Problems of mounting arose from the hollow section feature of the circular shaft, because of the slenderness of a 1mm wall thickness on a 20mm diameter and because the components must remain concentric to the axis of the shaft. An expanding hub device was chosen for the front (or input) shaft, that effectively shrink fit the component onto the shaft. The maximum transmissible torque of this coupling is 170Nm which is at least three times greater than the maximum operational value of 50Nm. The operation of the device ensured concentric placement, allowed quick changing of components and required no modifications to the shaft.

The contact pressure exacted by the torque coupling on the shaft and hub can be up to  $65\text{MNm}^{-2}$  when tightened to 170Nm, but the torque applied for this application was 90Nm. It was necessary to ensure that the contact pressure would not interfere with the strain gauges, which are in close proximity to the clamping region of the coupling.

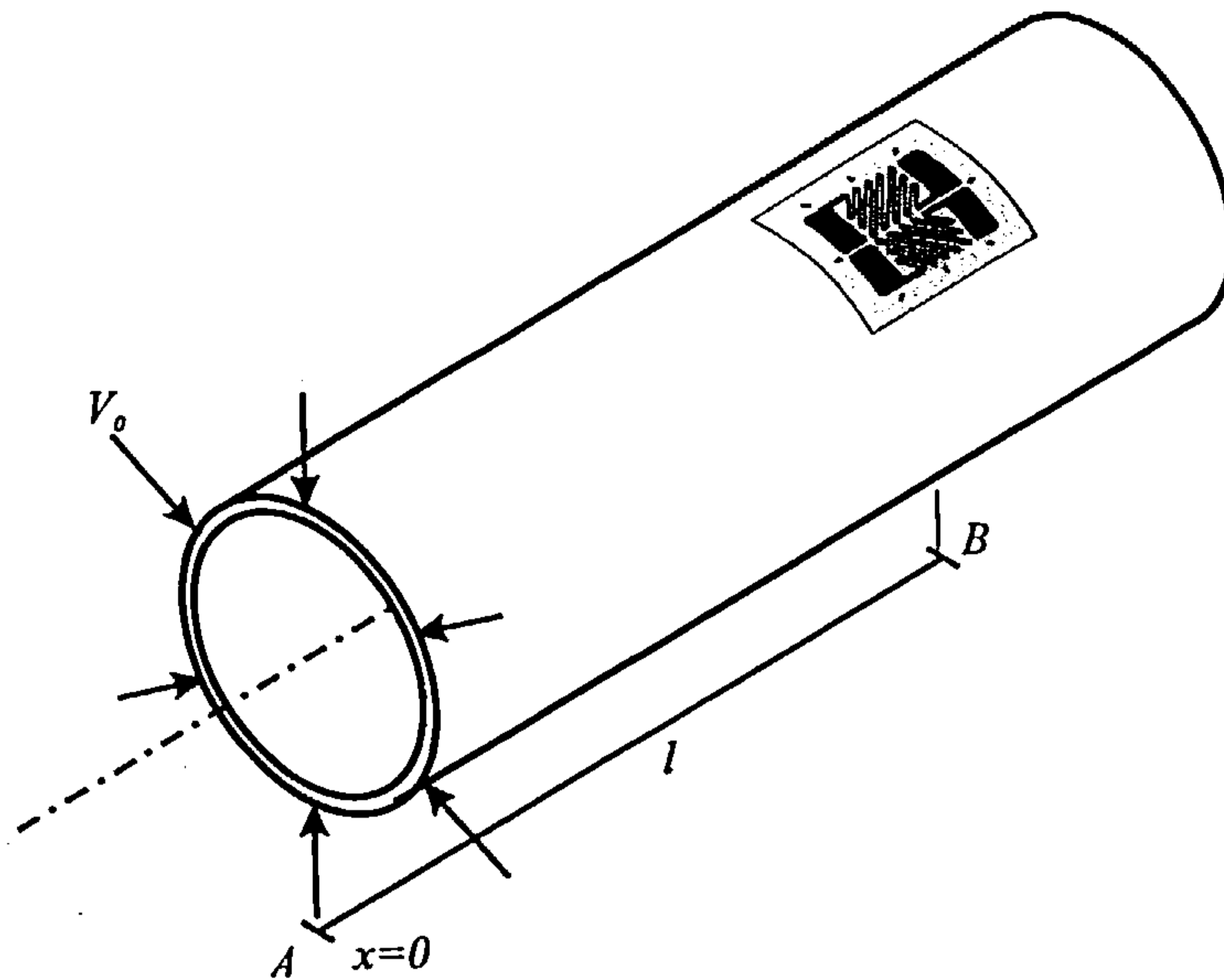


**Figure 3-4: Shaft Radial Loading**

For the dimensions of the shaft used, a standard solution<sup>(79)</sup> determines the case to be a thin walled, long cylinder and when experiencing a radial load a deformation estimate of the effect of the coupling on the strain at the gauge point may be obtained. The radial deflection is given as:

$$y = \frac{-V_0}{2D\lambda^3} e^{-\lambda x} \cos \lambda x \quad \text{Eq. 3-1}$$

If  $y_A$  is the deflection at  $A(x=0)$ , on the circumferential line of radial load  $V_0$ , then  $y_B$  is the deflection at  $B$ , at a distance  $x=l$  along the shaft, see Figure 3-4 ( $l$  was measured to be 10.43mm, the distance from the end of the coupling to the start of the strain gauges).  $\lambda$  and  $D$  are constants derived from geometric and material values:

$$\lambda = \left\{ \frac{3(1-\nu^2)}{R^2 t^2} \right\}^{1/4} \quad \text{Eq. 3-2}$$

$$D = \frac{Et^3}{12(1-\nu^2)} \quad \text{Eq. 3-3}$$

where :  $\nu$  = Poisson's ratio (0.3)

$R$  = mean radius of cylinder (9.5mm)

$t$  = wall thickness (1.0mm)

$E$  = Modulus of Elasticity ( $200 \times 10^3 \text{ Nmm}^{-2}$ )

The deflection ratio,  $\left| \frac{y_A}{y_B} \right|$  for a radial load was calculated to be  $0.915 \times 10^{-5}$ .

This fraction indicates the limited influence on the strain gauges caused by the coupling device. To prevent possible damage from over tightening, and to relieve some stress in the thin walled cylinder, a close fitting pin was inserted into the hollow shaft covering the axial length over which the coupling clamped on the outside.

Whereas the size of the front shaft components allowed the use of the torque coupling, the rear components did not. Instead, a collar was fitted to the end of the shaft and was threaded to the size of a bicycle rear hub, allowing the component to be simply screwed on. The collar was machined such that it fits the shaft with an interference clearance and, to prevent rotation, dog point set screws were driven through the collar, through the shaft wall and into a plug bonded into the end of the shaft. Again, this was designed to exceed the maximum operating torque. *Loctite* 402 adhesive was used and information given in the data sheets predict a static torque limit of 142Nm and dynamic limit of 49.8Nm. With extra load being taken by the three set screws through the shaft, the combination is capable of meeting the maximum operating limits.

### 3.3.2 Electrical

The circuitry on the rotating shaft can be broken down into three functions: strain gauge bridge amplifier, signal conversion and signal transmission (see Figure 3-5 for overview). A strain gauge bridge amplifier can vary in complexity greatly

depending on how versatile, sensitive and accurate the requirements are, but all operate on the same principle that can be condensed into a single integrated circuit. Initial tests of the circuit were based around a 3 chip operational amplifier design, but it was found more practical to combine these stages into one *Burr-Brown* INA125 low power, high accuracy instrumentation amplifier chip. For the signal conversion, a highly linear and accurate voltage to frequency converter, a *Teledyne* CPD9401, was used.

To test the accuracy, drift and sensitivity of this integrated circuit, a voltage calibrator was used to generate a constant, but manually variable, input signal and a frequency counter was used to measure the output. The performance of the circuit proved satisfactory for the requirements of accuracy, Figure 3-6.

Having now converted shaft torque to a linearly proportional frequency of pulses, all that is required is the transmission to a static receiver and data acquisition apparatus (Figure 3-5). This pulse signal was used to drive an infrared LED, mounted at the end of the shaft, emitting along its axis. Positioned between 2 and 5 mm away from the LED was a photodiode, which formed the static receiver for the data. As the photodiode detects the pulses of infrared radiation, a voltage is generated and the signal is regenerated as an analogue voltage.

The measurement of the signal frequency can be performed by different hardware or software techniques. Whilst the system was being developed, a hardware-based counting method was used, based on a reciprocal frequency counting technique. This involves synchronised multiple period measurements followed by computation of the reciprocal value. The use of this hardware frequency counter allowed measurements to be made simply and reliably, with averaging taken over 0.1, 1.0, or

10 seconds. The frequency was displayed on a LCD panel but no provision for storing data was available and, as three units would be required, a multiple software frequency calculation method was required for the later stages of development and operation.

By interfacing the photodiode voltage boosted signal with a PC via a *National Instruments* AT-MIO-16-9L data acquisition card, several channels of data could be analysed at once, Figure 3-5. Applying a Fast Fourier Transform (FFT) to the signal would yield the harmonic frequency of the signal.

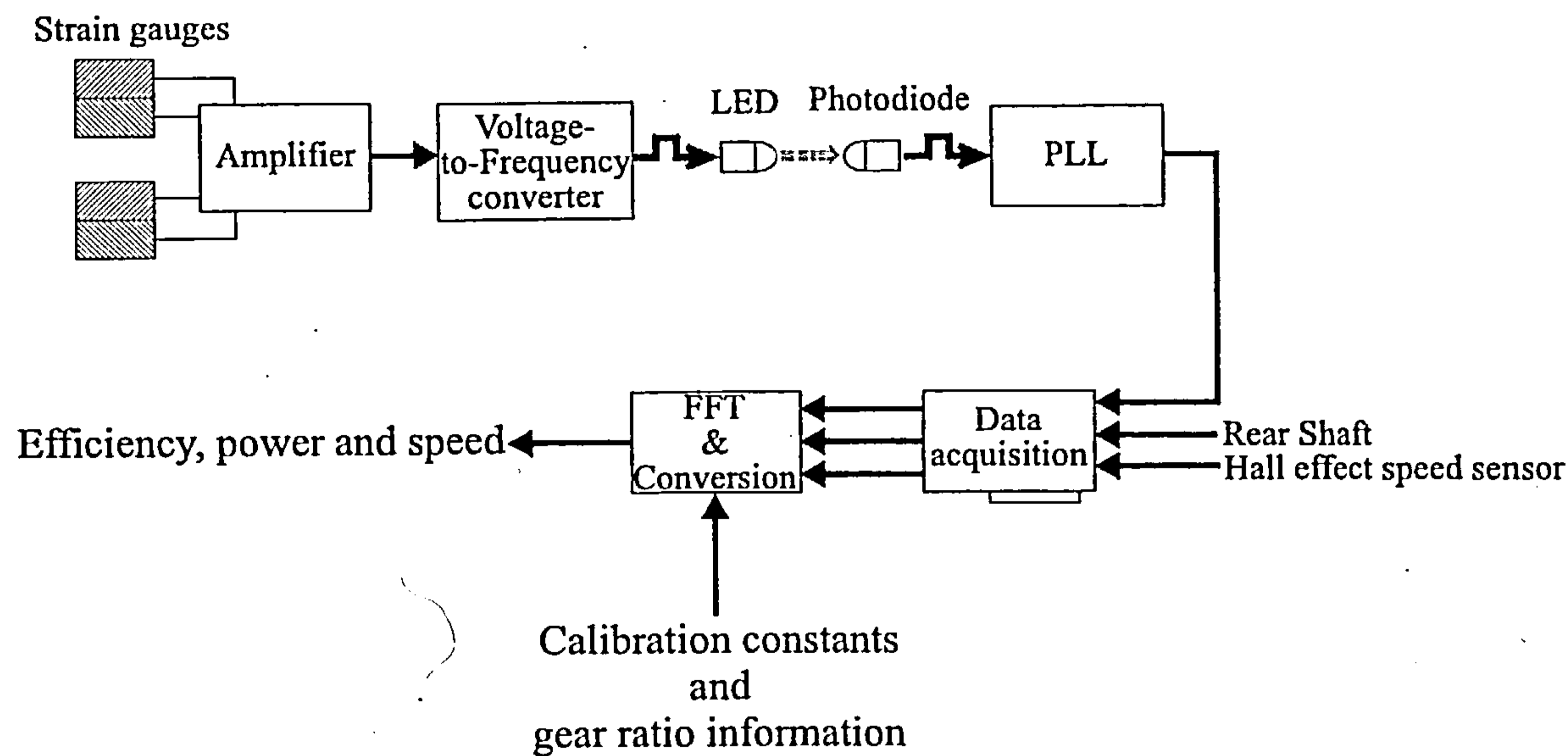
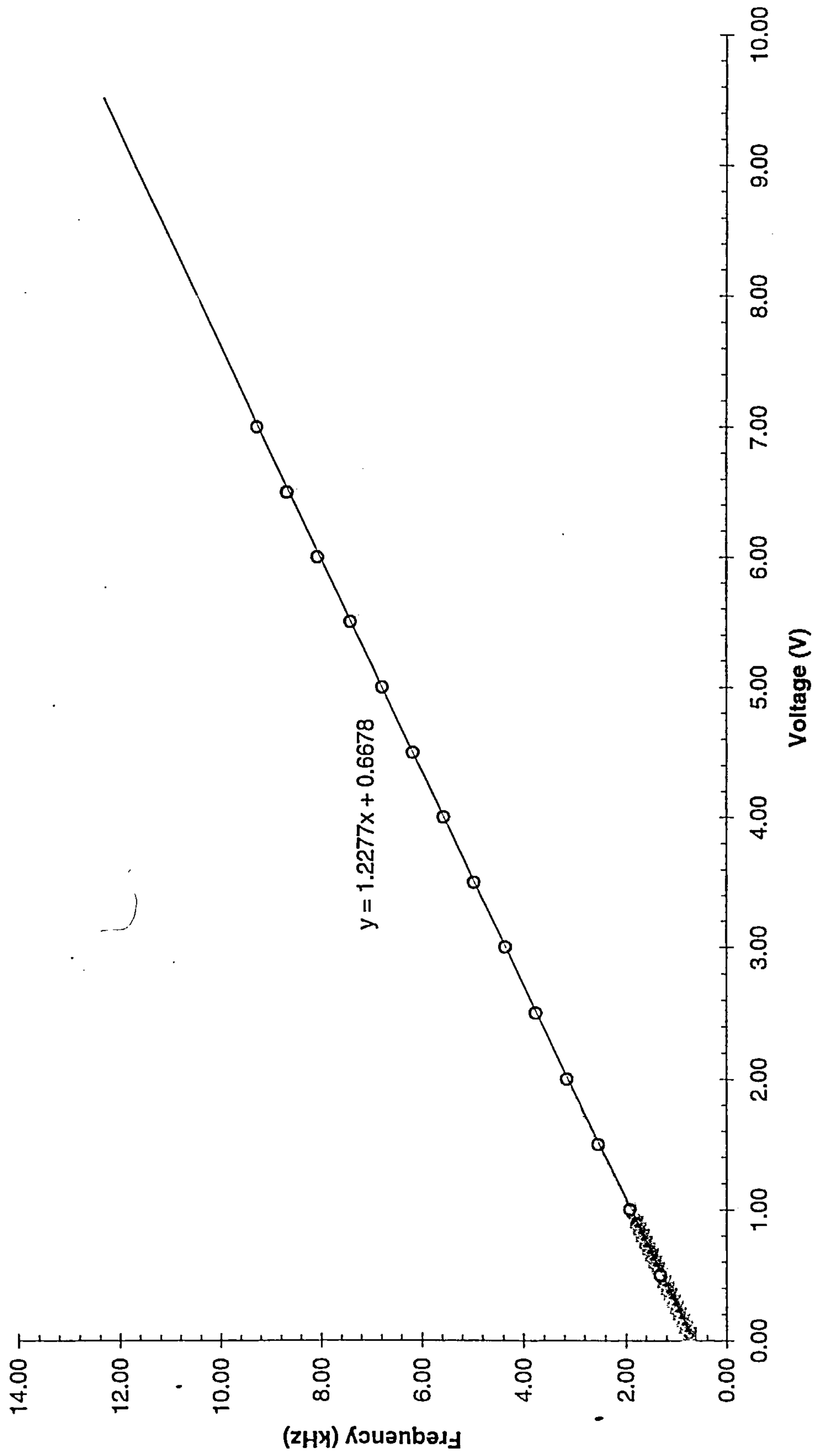
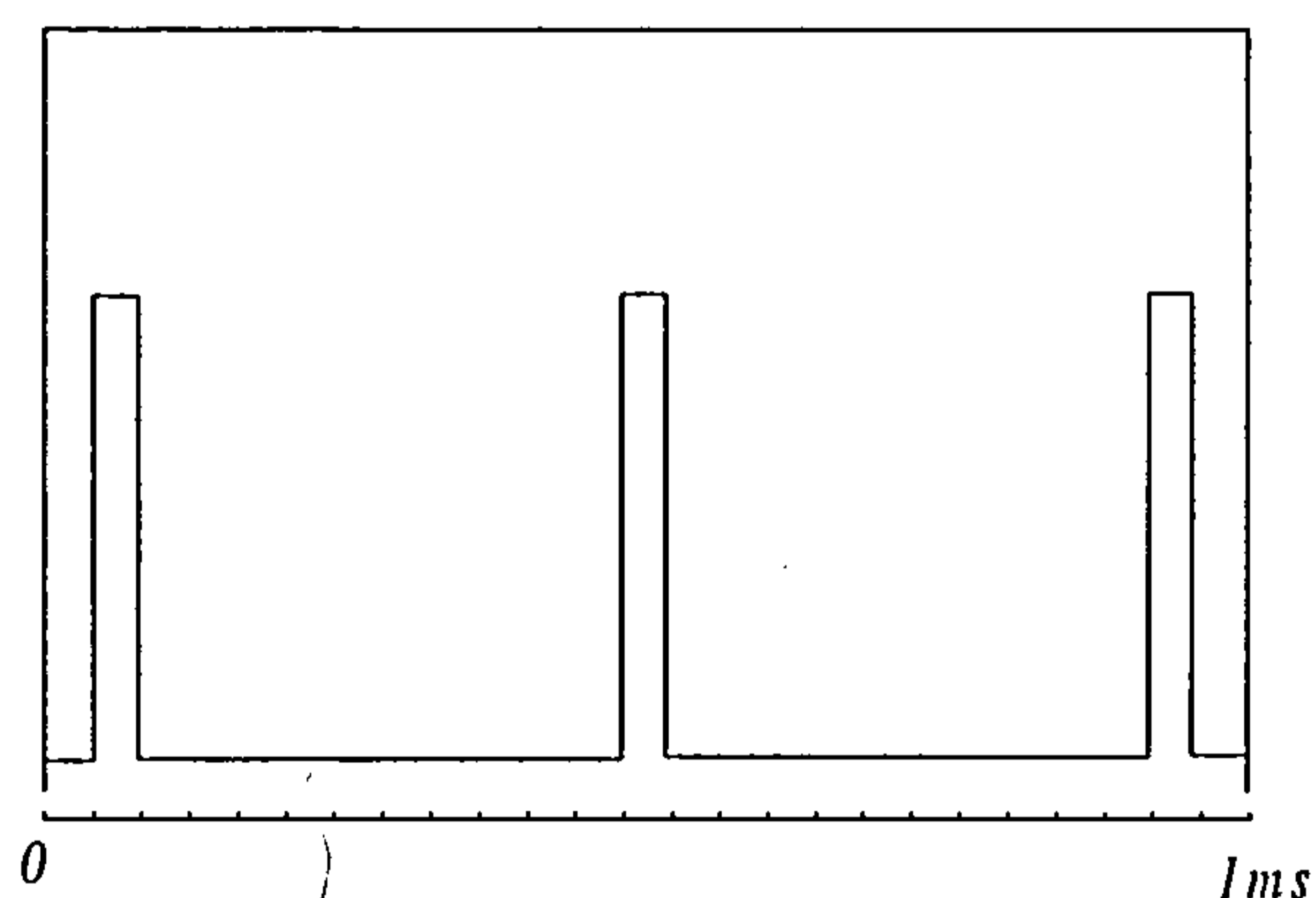


Figure 3-5: Instrumentation schematic

Figure 3-6: Voltage-frequency calibration



Despite having written the software in LabView and successfully tested it with a signal generator over the frequency range of 1kHz to 12 kHz, the system did not initially work with the torquemeter signal. This was due to the characteristics of the signal duty cycle (mark-to-space ratio). In order for the torquemeter electronics to function for as long as possible from its battery power supply, the 'on time' for the LED was kept short and mostly off; this is represented in Figure 3-7. The pulse width, irrespective of frequency, is set by the voltage-to-frequency circuitry and is 20 $\mu$ s. This means that the duty cycle is between 2% and 10%. Since the acquisition card can only operate at 33 kHz with 3 channels, the pulse in the signal could not be reliably detected. This resulted in the generation of strong harmonics, as can be seen in the plots taken using an HP3582A spectrum analyser (Figure 3-9 and Figure 3-10).



**Figure 3-7: Pulse characteristics**

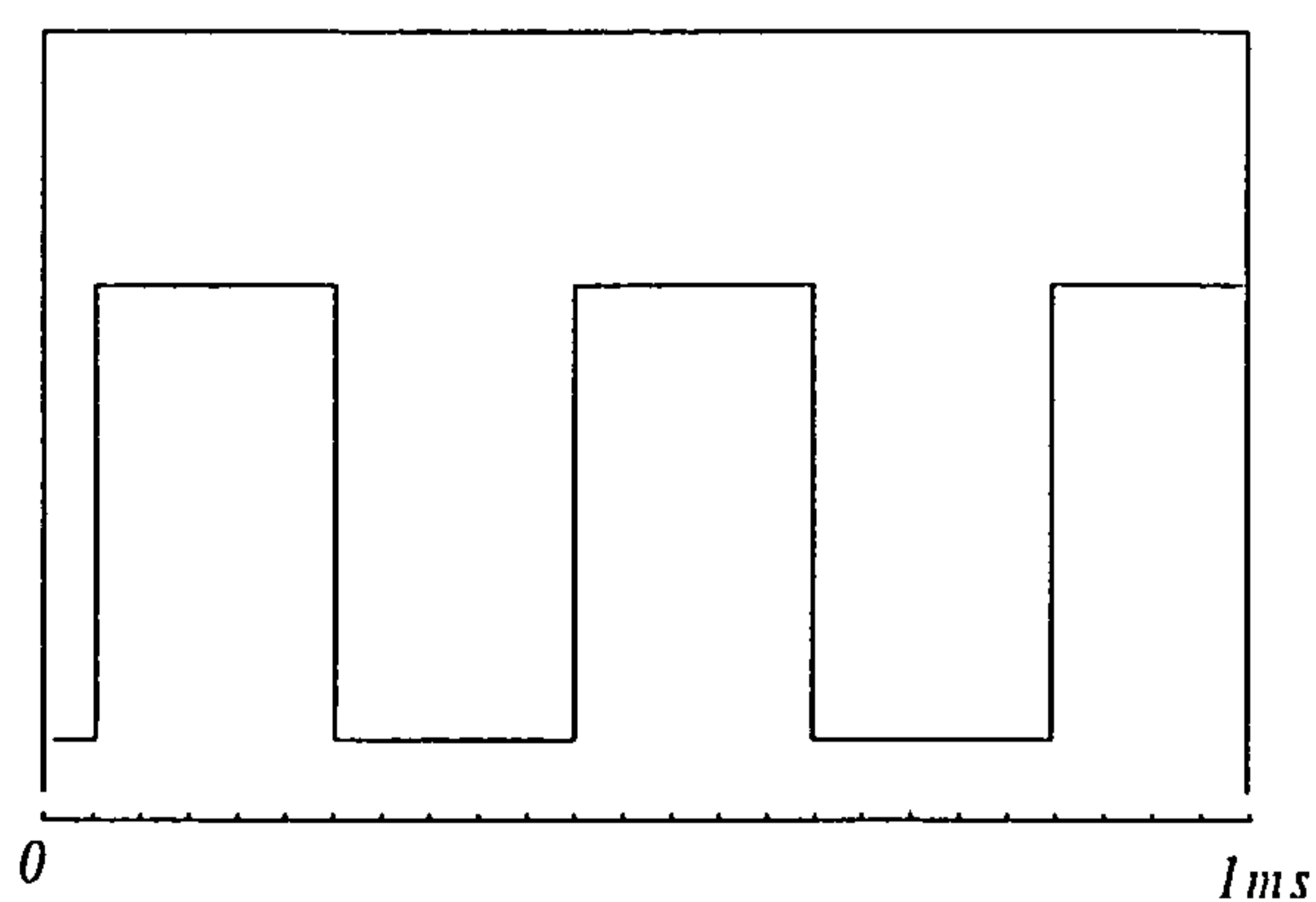


**Figure 3-8: Pulse characteristics (modified)**

Figure 3-9: Spectrum analysis of torquemeter signal output at 1kHz

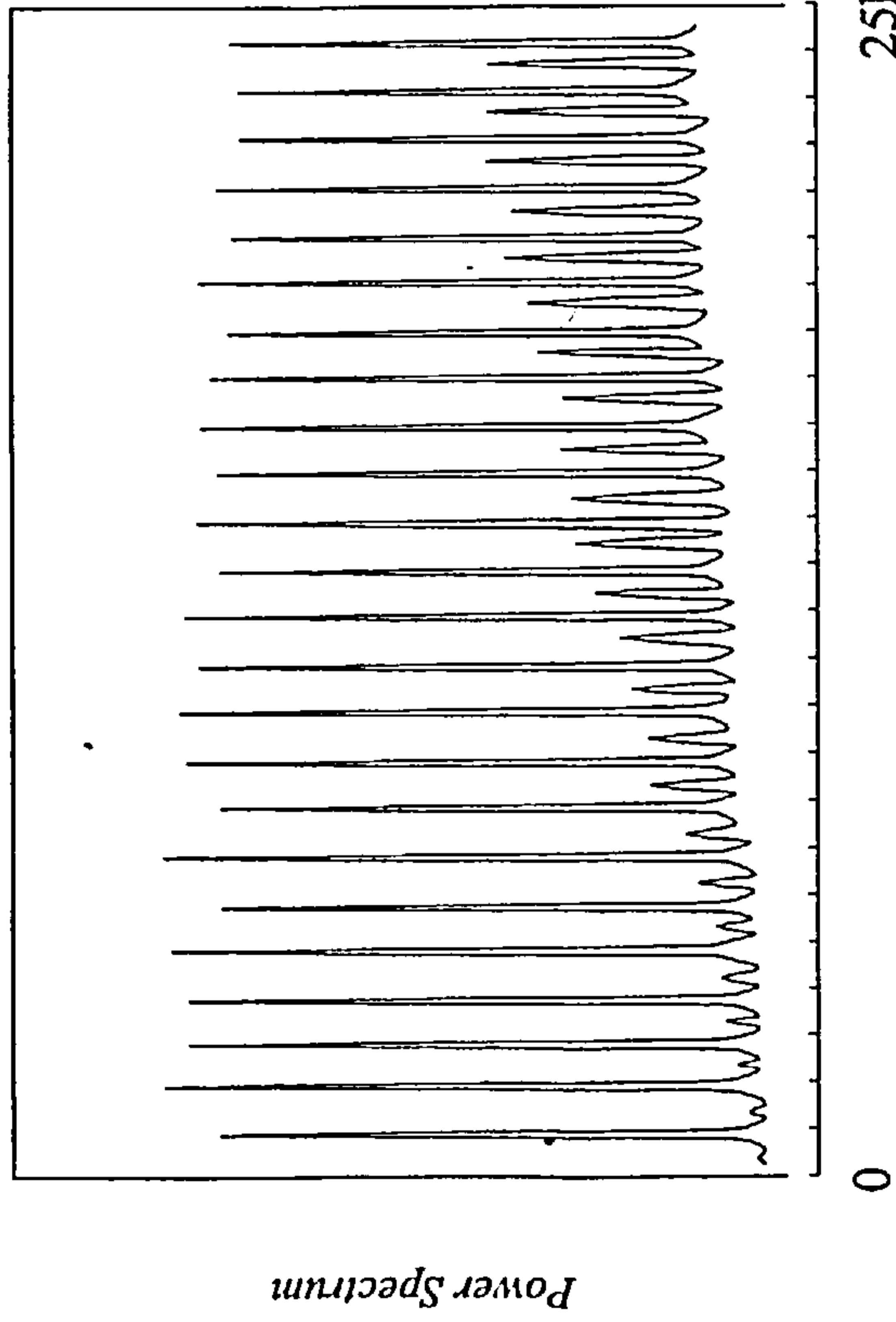


Figure 3-11: Spectrum analysis of torquemeter signal output at 1kHz (modified)

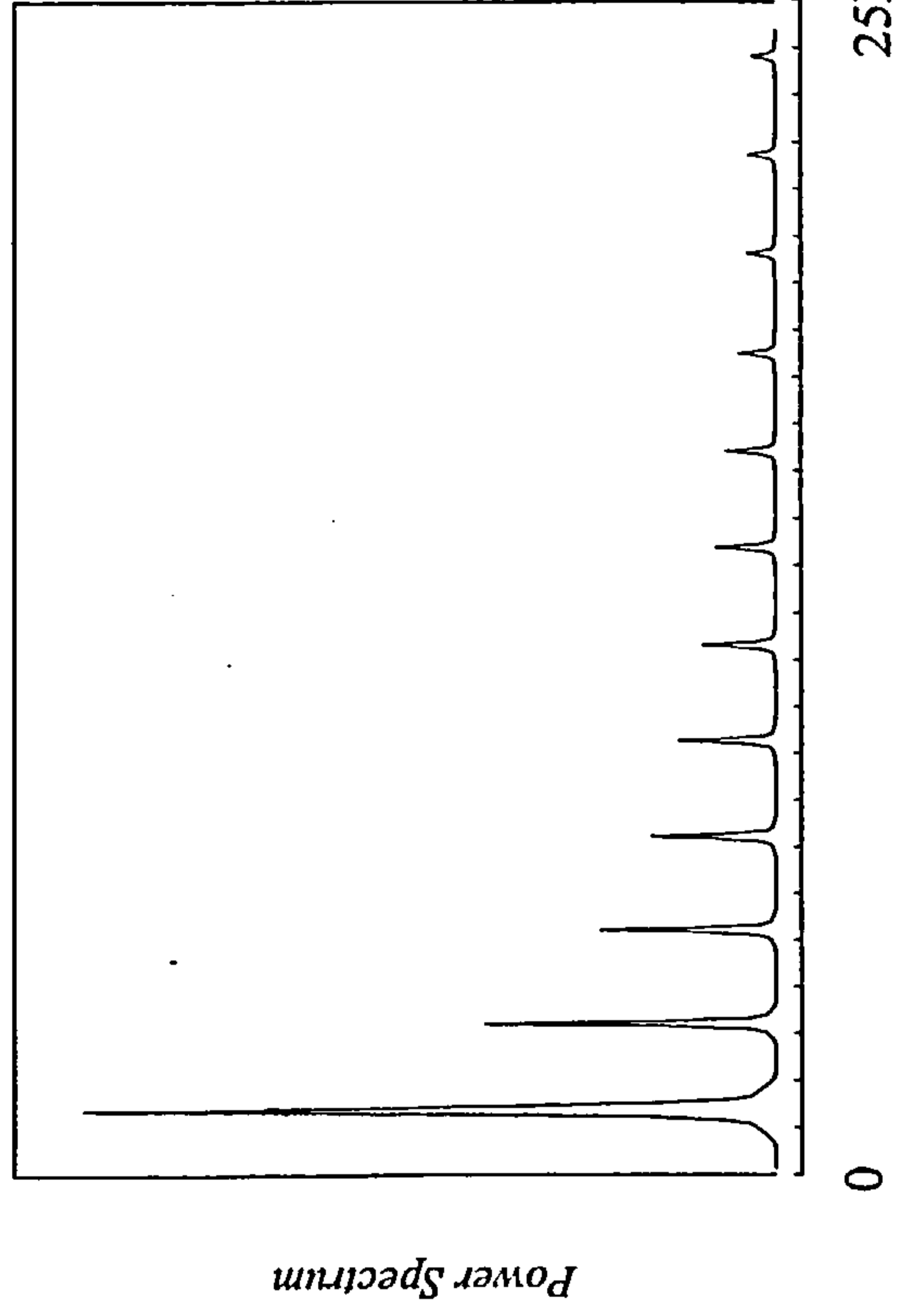


Figure 3-10: Spectrum analysis of torquemeter signal output at 6kHz

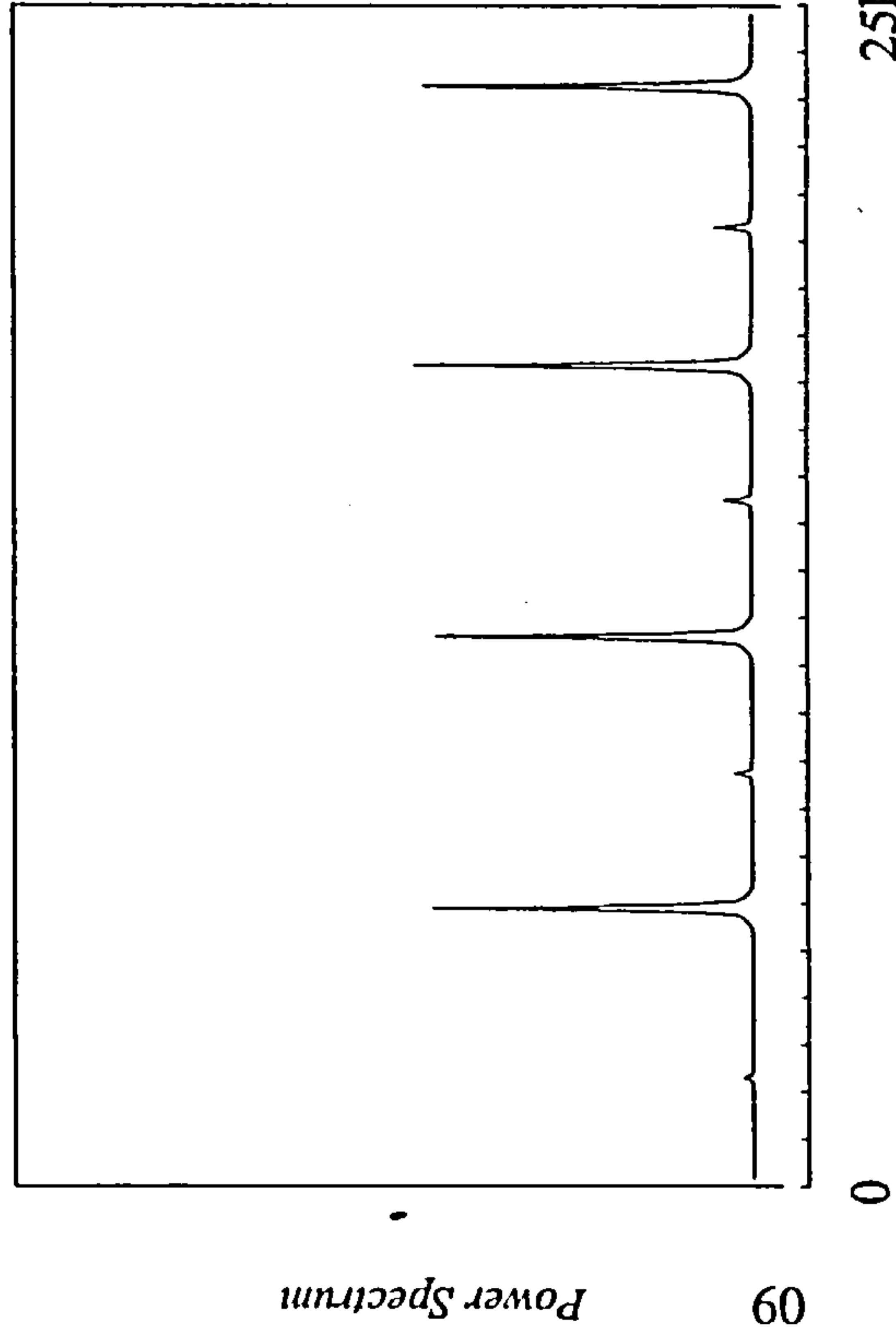
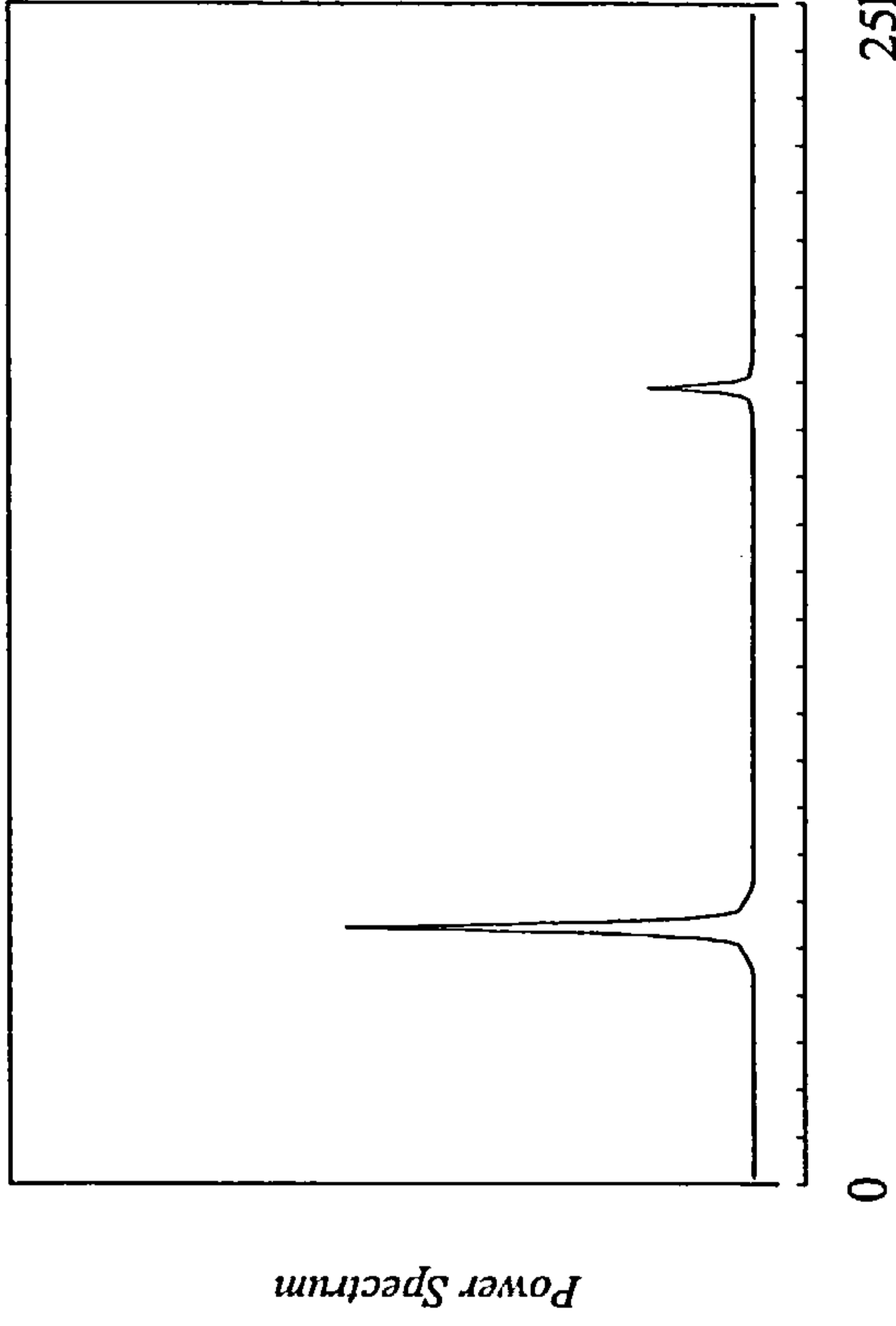


Figure 3-12: Spectrum analysis of torquemeter signal output at 6kHz (modified)



It was decided that it would be more convenient to change the signal characteristics rather than altering the detection and calculation methods. Thus a conversion technique was used, a phase-locked loop (PLL) electronic circuit situated between the photodiode output and the data-acquisition board. The function of this circuit was to alter the frequency signal so that it is detected more accurately and in a more stable manner than the raw signal characteristics from the on-shaft circuit. The components of the PLL circuit are a phase detector, low-pass filter, amplifier and a voltage-controlled oscillator (VCO) and the arrangement is shown in Figure 3-13 (modified from Boylestad<sup>(80)</sup> and de Sa<sup>(81)</sup>). The PLL implementation is common in electronics applications when frequency synthesis is required. The purpose of application in this instance is to track the input frequency from the photodiode and output a signal of equal frequency but with an even mark-to-space ratio (duty cycle). The raw output of the voltage to frequency converter is illustrated in Figure 3-7. By increasing the mark or 'high' state period to equal that of the space or 'low' state, the modified signal is represented by Figure 3-8. To output this new signal, the input frequency is compared to that of the VCO by a phase detector, the difference in phase being output as an error voltage  $V_e$ . In operation,  $V_e$  is proportional to the phase and frequency difference of the incoming frequency and the VCO frequency.  $V_e$  contains 2 components that are the sum and difference of the two compared frequencies, the lower of which is passed through the low pass filter. The filter output is amplified and becomes the input of the VCO. Whilst the error voltage is zero, the VCO output is the free-running frequency. When the two frequencies match, the PLL is said to be in the locked state.

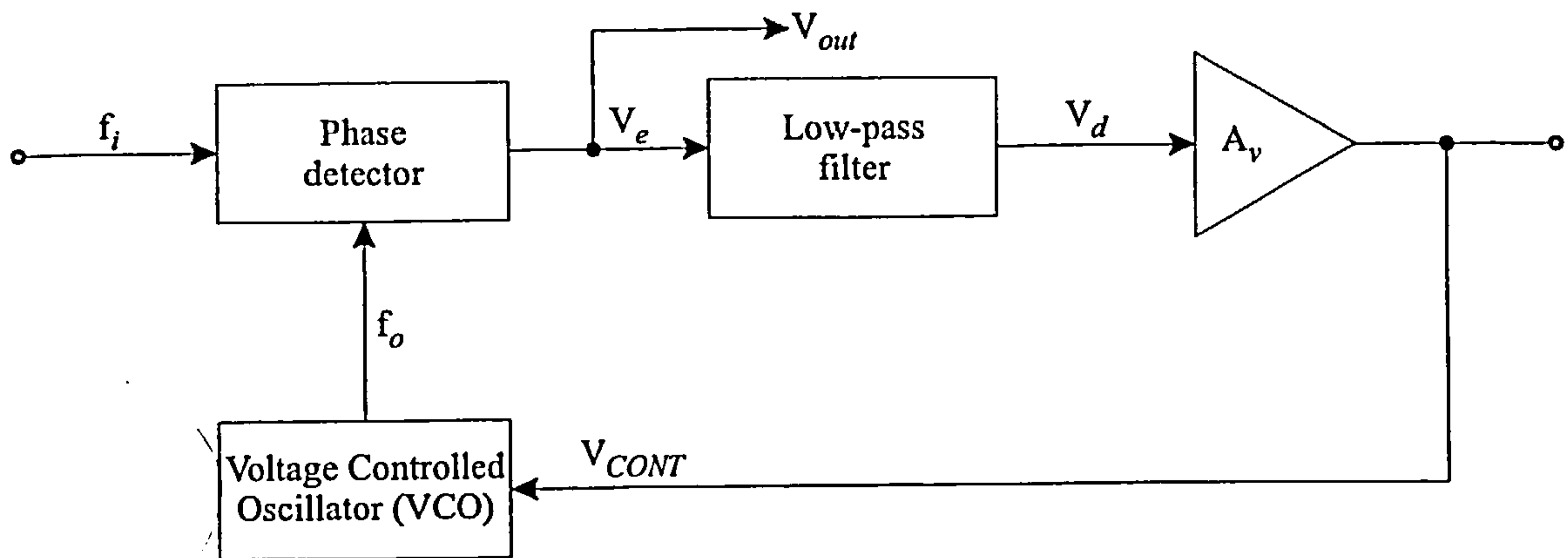


Figure 3-12: PLL operating principle

If the input voltage,  $V_I = V_{ip} \sin 2\pi f_I t$  and the VCO output voltage,

$$V_{VCO} = V_{op} \sin 2\pi f_o t$$

then when multiplied in the phase detector:

$$V_I \times V_{VCO} = V_{ip} V_{op} (\sin 2\pi f_I t)(\sin 2\pi f_o t)$$

and using the trigonometric identity,

$$(\sin A)(\sin B) = \frac{1}{2} [\cos(A - B) - \cos(A + B)]$$

SO NOW:

$$V_I \times V_{VCO} = \frac{V_{ip} V_{op}}{2} \cos 2\pi \underbrace{(f_I - f_o)}_{\text{difference}} t - \frac{V_{ip} V_{op}}{2} \cos 2\pi \underbrace{(f_I + f_o)}_{\text{sum}} t$$

The frequency matching speed at which the circuit can lock, together with the stability of the lock, depends on the free running frequency of the VCO and the damping factor of the circuit. The values chosen for the components provided a circuit with critical damping and good stability for the 1 to 10 kHz operating input frequency range.

The modified waveform produced a reduced magnitude and smaller number of harmonic frequencies, Figure 3-11 and Figure 3-12, illustrating a reliably detectable and measurable FFT frequency calculation.

The process of converting the PLL synthesised frequency signal to a stored value is completed by using the acquisition card and software written in LabView. Figure 3-14 shows, in block diagram form, the operations performed, each module being effectively a sub-program or procedure taken from the routines available from the LabView libraries. The signal is acquired at 33kHz, which is the maximum value allowed by the hardware limitation of 100kHz over the number of channels being sampled. With the input frequency range not likely to exceed 10-12kHz, the signal is being over-sampled at a rate sufficient to eliminate aliasing. Having acquired the signal, it is then passed through a Chebyshev band-pass filter set to allow signals between 0.9-12kHz to pass through. The purpose of the filter is to eliminate any noise and minimise the likelihood of harmonics passing through to the time-to-frequency domain converter. The generation of a power spectrum from the raw data requires a number of parameters to be defined and these are discussed in the following sections.

The calibration program used to determine the offset value for torque was extended for the purpose of displaying real time power and efficiency values. The common front end (user interface) is shown in Figure 3-11a and the individual processes are shown in further detail in Figure 3-11b. The following data are entered by the user; the device number that refers to the data application card and the channels to be read in this case, card 1 and channels 0, 2 and 4 - representing front, rear and speed sensors, the scan rates (a.k.a acquisition rates) (in this case 33000 scans per second rather than the default 100 per second shown in brackets). A large buffer size

must also be allocated to allow for the data processing after acquisition, the amount chosen representing approximately one third of a second. The size of each simultaneous scan was chosen to be 2048 samples as this allows for an accurate measurement of data, yet does not incur too great a memory or time overhead. Each scan is a 12-bit digital conversion of analogue voltage data.

Real time values appear in the right hand column of Figure 3-14, having been processed by the underlying program, this being useful during development as it gave information on how well balanced the acquisition and processing demands were. Figure 3-14b shows the graphical programming steps used to create the program. *AI-config* and *AI-start* prepare the acquisition card for use with the user-defined parameters from the front screen. The box in the centre of the figure represents a 'for' loop during which scans are read from the card and passed to a processing routine labelled "1". The loop continues indefinitely, creating an array of measurement values until the stop button is pressed, upper right hand corner of Figure 3-14a. Once stopped, the array is passed out of the loop to a routine that outputs the data to a text file, normally stored on the hard disk.

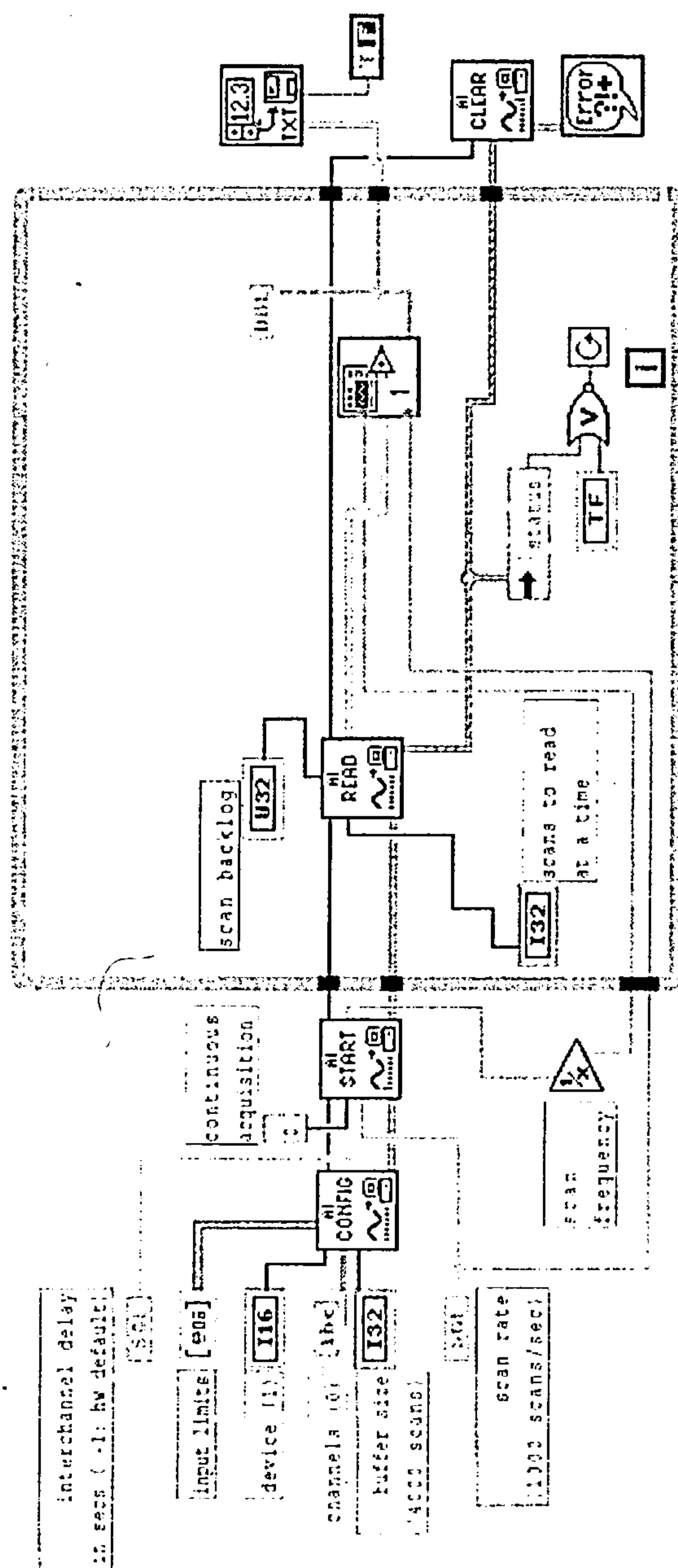
The conversion of frequency data is completed by '*3fcalcs.vi*' shown in Figure 3-14c. The flow of data is generally from left to right and enters at the point signified by 'SGL'. The first step is to break the 3x2048-sized array into the three signals to be examined, input torque, output torque and speed voltages. In a form of processing that simulates parallel processing, each array then gets filtered, windowed and converted into a power spectrum. The input and output torque signals share the same filter cut off frequencies because of the similar signal characteristics, but the frequency output of the data contained in the tachometer signal is much lower and requires different

parameters. The power spectrum arrays are then passed to the FFT routine to determine the peak frequency. As this frequency has already been biased by the PLL circuitry, the value is stable and accurate by comparison with the frequency instrumentation.

The frequency of the speed sensor is simply to equal the input shaft speed in directly. For power calculations, however, the angular velocity in radians per second is required. This numerical value is then multiplied by the gear ratio entered by the user to generate a rear shaft rotational velocity. Once the front and rear frequencies have been determined, they are converted into torque by the constants set by the user on the front screen (Figure 3-14d). The torque value in turn multiplied by the relevant angular velocity thus returning front and rear power values, which are shown on the front screen. Dividing the output by the input torque gives the efficiency. The efficiency value is passed only to the real time graph on the front screen, unlike the two power and one speed values that are converted to a text file for recording.



**Figure 3-14b: LabView program blocks**



Read & chart data until an error occurs, or the stop button pressed.

malicious

City Documental Database

last edited on 3/01/1999 at 16:13

ZC:51 7E 6061/6060 UC FORM 13

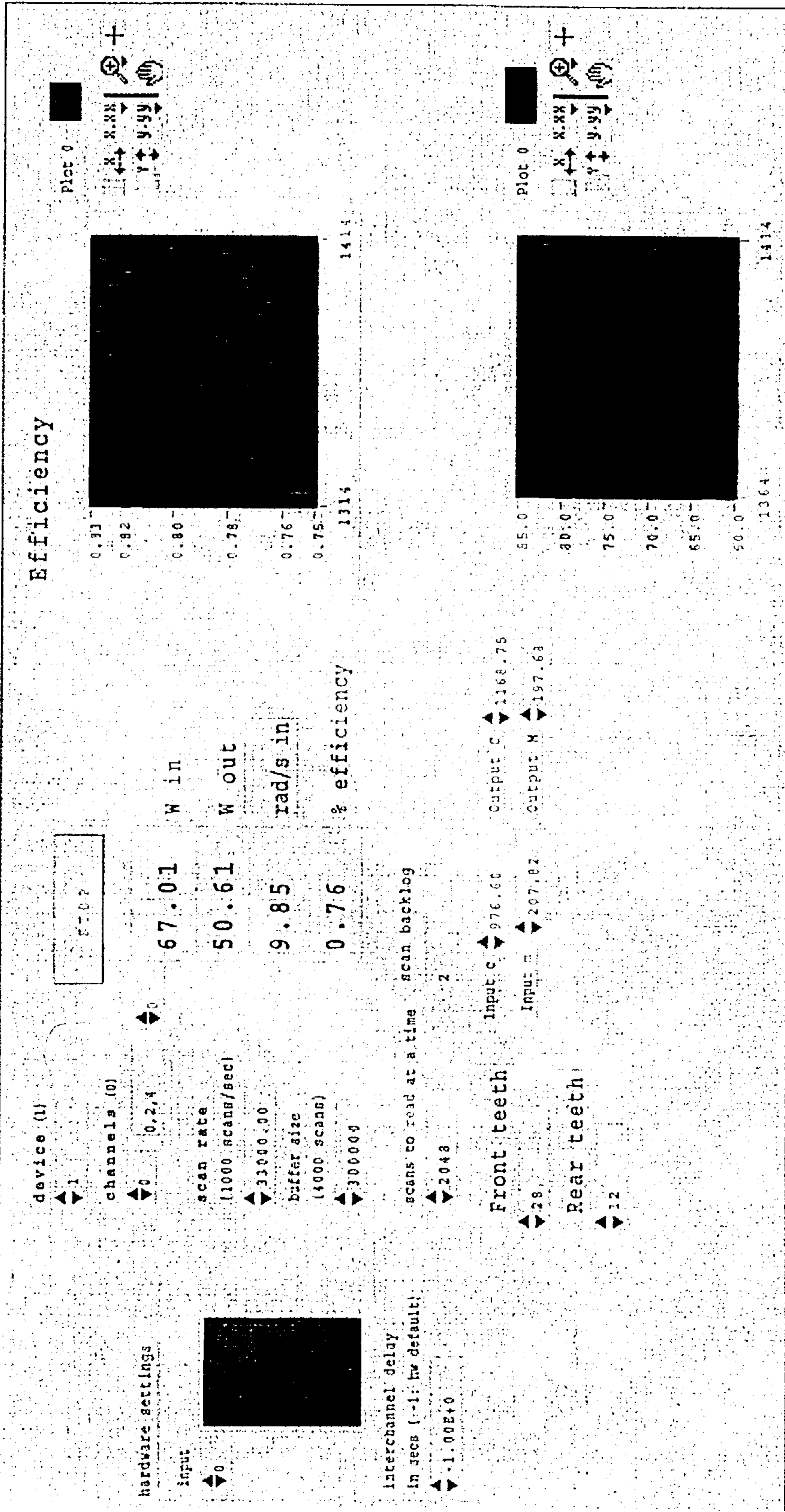
Figure 3-14c: LabView program blocks

new (5).vi

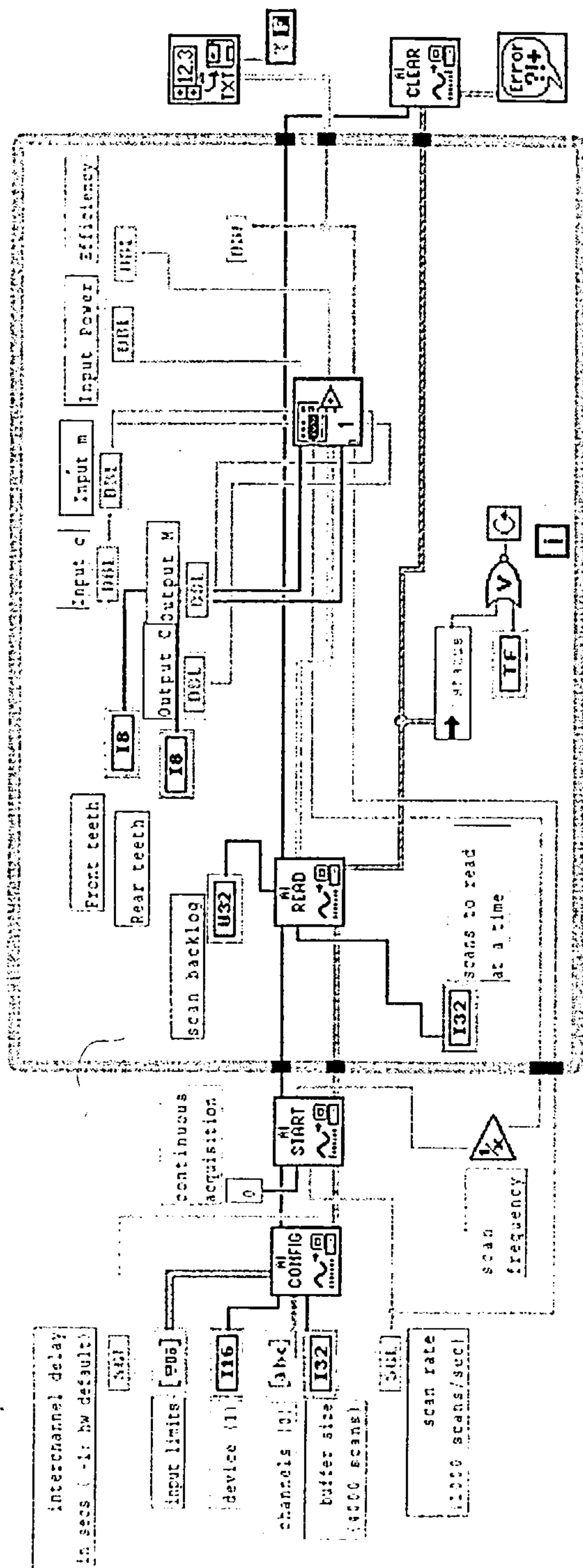
C:\My Documents\Marcelinev (5).vi

Last modified on 27/08/1999 at 09:53

Printed on 03/09/1999 at 15:33



Crummy Documents\Matt\new [11.v]  
Last modified on 27/06/1999 at 09:53  
Printed on 09/03/1999 at 15:32



Read & chart data until an error occurs, or the stop button pressed.

Figure 3-14e: LabView program blocks



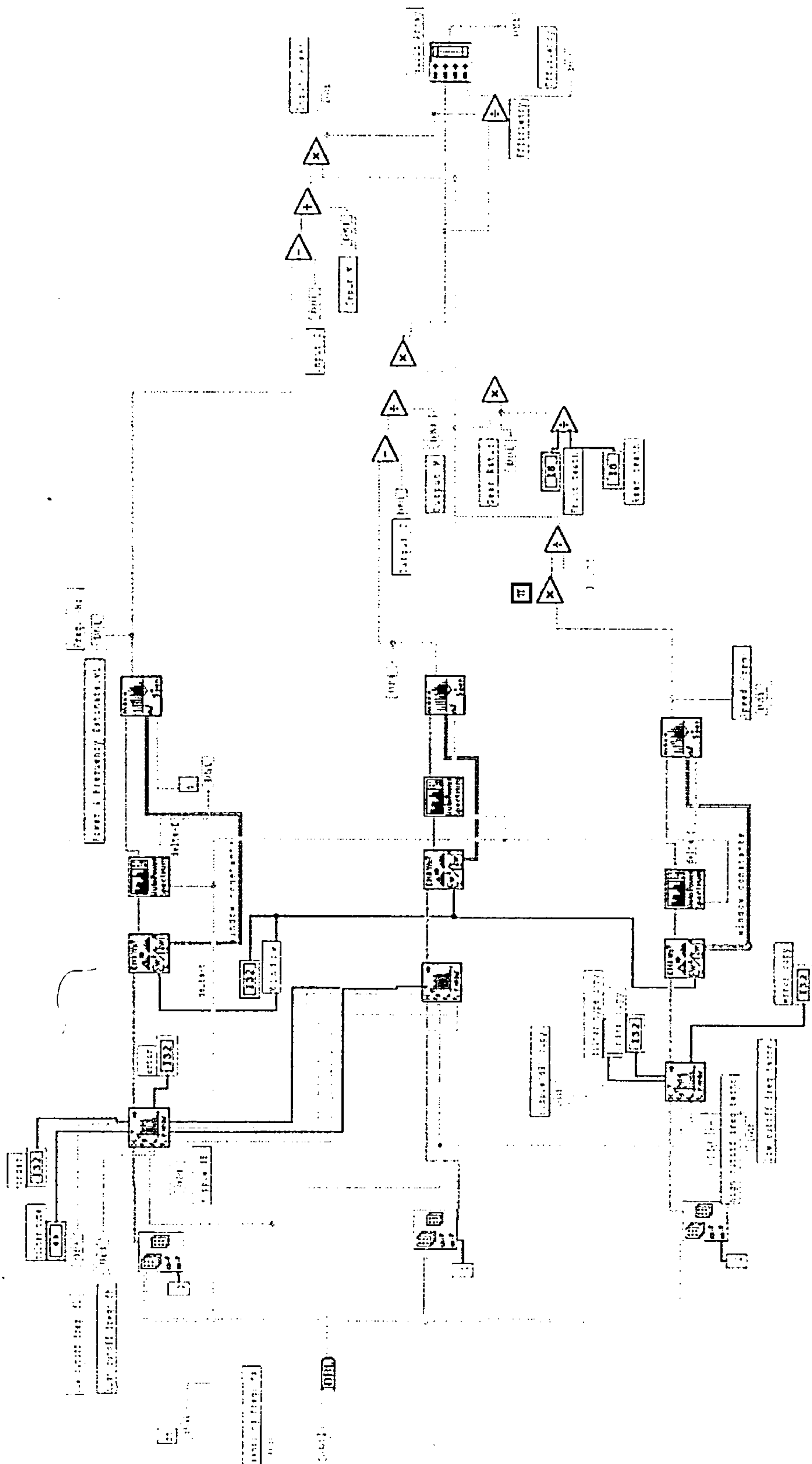
Page 1

3feales.vi

C:\My Documents\Watt\3feales.vi

Last modified on 09/09/1999 at 15:29

Printed on 09/09/1999 at 15:34



### 3.4 Performance testing and calibration procedure

Three parts of the instrumentation required thorough testing to ensure correct operation and then the system as a whole underwent calibration. The strain gauges were tested for correct operation by connecting them to a signal-conditioning amplifier (Micro Measurements 2311) and applying a pure torque to the shaft. This was achieved by mounting the torquemeter shaft in as close to operation conditions as possible in a jig, fixing one end of the shaft and applying a pure torque to the free end. Using the same torque coupling as used for affixing components to the front shaft, an arm could be fitted across the shaft, as in Figure 3-15. The arm is able to rotate under load about the shaft centre, a couple was set up by having equal masses at either end of the arm using a cable and pulley arrangement. This arrangement minimises any strain due to bending of the shaft, although this had already been reduced by using the strain gauge bridge configuration described earlier.

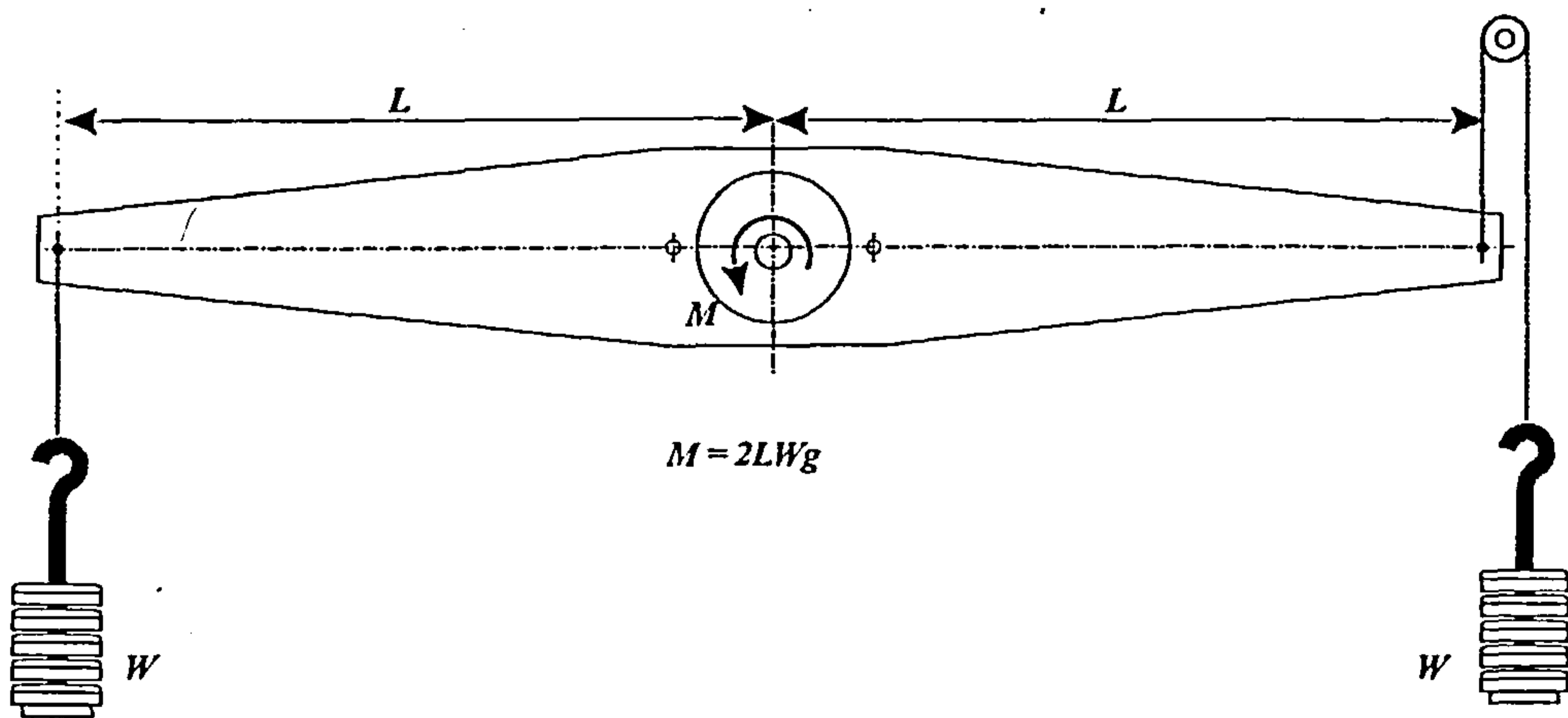
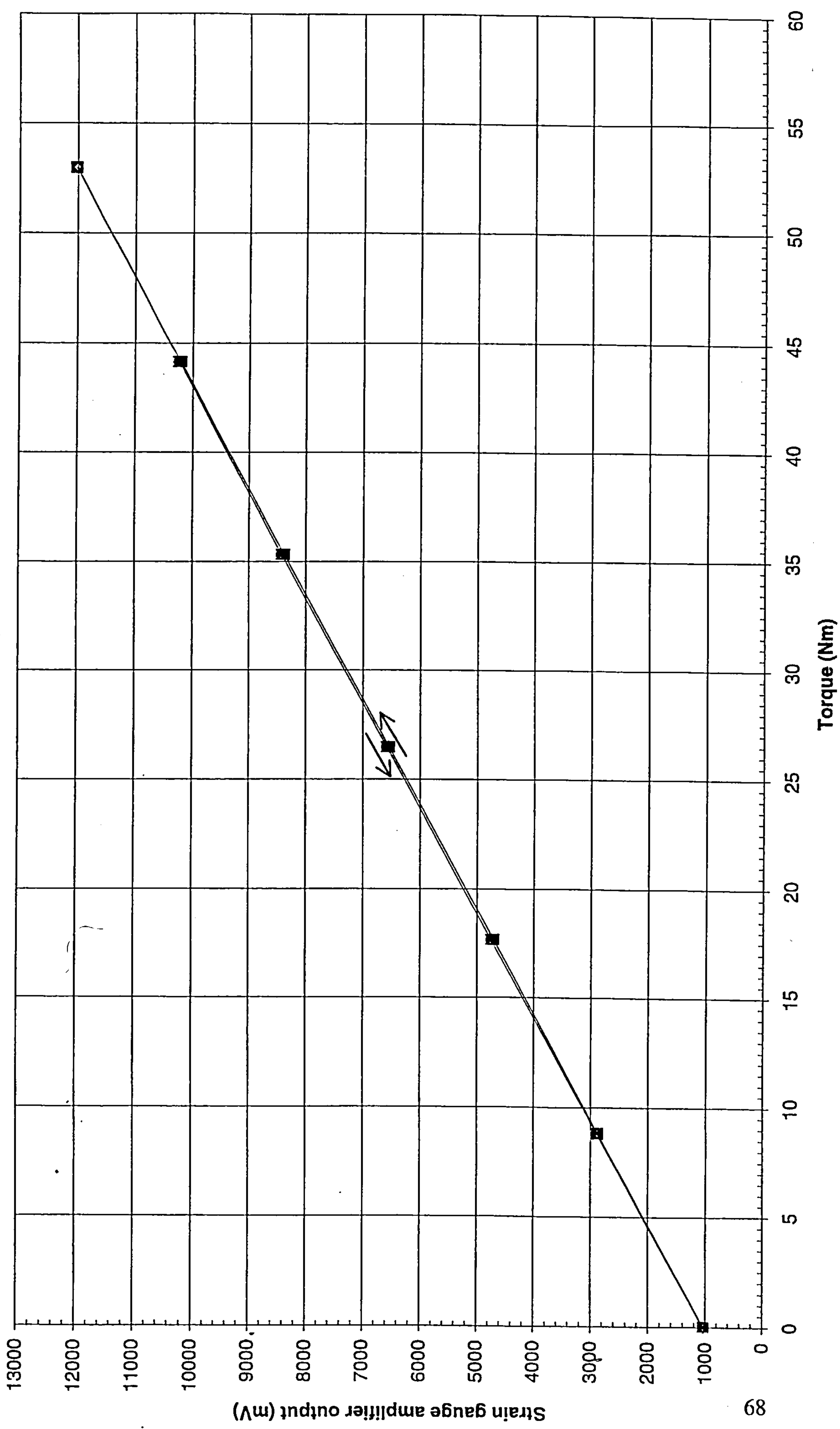


Figure 3-15: Calibration rig

Figure 3-16: Frequency vs. applied torque



The record of strain readings as the applied torque was increased revealed a linear relationship, as shown in Figure 3-16. The sensitivity of the gauges was such that careful application of masses was required to prevent swinging and local vibrations needed to be minimised to stop errors. Now confident of the strain gauge operation in both shafts with respect to linearity and sensitivity, the electronic circuitry and telemetry was next to be tested.

The control of the operational characteristics of the electronics consists of four separate adjustments. Three of these are on the shaft circuit, the remaining are being used to adjust the triggering for the photodiode and PLL circuit. The on-shaft controls adjust two stages of gain and the offset, very similar to a normal strain gauge amplifier. A maximum torque of 54Nm was applied to set the gain and then the offset was adjusted such that the system produced 1KHz with no load and 12kHz at maximum load. Because the offset and gain both change the nature of the signal, several iterations were required to get the desired output.

Adjustments to the receiver side of the telemetry do not affect changes in the frequency attributes of the signal but rather set the level at which the system operates. Just as before when the strain gauge bridge was connected to the 2311 equipment and the torque strain relationship was derived, so loading of the torque arm would now produce a torque-frequency relationship. Frequency measurements were made using the frequency counter described previously and noted against torque. Again a linear response was found. The display resolution of the frequency counter was greater than that of the 2311 apparatus and also appeared to offer a greater bandwidth which led to a test to observe the torque signal resolution. At a load of 27Nm (mid system range), small 1 gram masses were added to the mass hanger and changes noted of the

frequency output. An addition of just 1g representing  $0.3 \times 10^{-3} \text{Nm}$  was visible but the variation due to noise was of a greater magnitude at  $3 \times 10^{-3} \text{Nm}$ .

The final testing required of the system prior to calibration concerned the acquisition hardware and software. Two signal generators were used to simulate the torquemeter frequency signal for the tests. The software was run to adjust various program parameters, such as window type and size, that resulted in the most accurate and reliable readings whilst maintaining sufficient sampling resolution for the purpose of the main efficiency experiments. This was also the opportunity to integrate a third input to the acquisition software from the Hall effect sensor measuring the rotational velocity of the shaft. The software had to be capable of dealing with a total of three frequency determination operations simultaneously, since the Hall effect signal must have its frequency component measured also to recover the shaft r.p.m.

It was found that the software could sample at 33 kHz on all channels, process the data and create a snapshot record every 0.06s. The accuracy at these operating settings was not compromised and agreed well with the frequency counter measurements made in line, one at a time. Manipulation of the frequency data within the program could allow an output not only torque and power data but actually calculate the system efficiency using gear ratio information provided by the user.

When the torquemeter telemetry and PC were connected as a whole, the complete system was operating as it would in the efficiency experiments and was thus ready for calibration.

### 3.5 Calibration Results

The applied torque load was incremented in 8.8Nm steps from 0 to 53Nm as this corresponded to a convenient 3kg mass step. Each step increased the load on both sides of the torque arm. Three sets of readings were taken at each torque value; each reading made from 300 values over 30 seconds. A 60-second interval was left between acquisitions giving a total calibration period of 3½ minutes. A distinction was made between increasing and decreasing the applied load by recording values for 53 to 0Nm in exactly the same manner as loading, in an attempt to identify any creep or relaxation phenomena.

Figure 3-17 and 3-18 show the output frequency versus applied torque for the input and output shafts respectively. Table 3-2 details the mean readings for each applied torque and also gives the standard deviations for each data set. The desired linear relationship of  $T = Kf + c$  is satisfied for both input and output cases e.g.

$$\text{Input torque, } T_i = K_i f_i + c_i$$

and      Output torque,  $T_o = K_o f_o + c_o$

Analysis of the data then yields numerical values for the constants :

$$\text{Input, } K_i = 207.82 \text{ and } c_i = 976.60$$

$$\text{Output, } K_o = 197.68 \text{ and } c_o = 1168.75$$

Table 3-2: Calibration results

	Input		Output	
	$\bar{n}$	$\sigma$	$\bar{n}$	$\sigma$
K	207.82	0.05	197.68	0.05
c	976.60	0.45	1168.75	0.35

To confirm the instrument suitability for dynamic operation, a simple test was performed. Water was poured into a bucket attached to the arm of the apparatus at approximately 0.2l/s whilst acquiring the frequency signal. Analysis of the data represented in Figure 3-19 reveals that the system can cope with a continuously varying load with no measurable instability.

In practice, when the torquemeter shafts were assembled into the experimental apparatus no problems were encountered. Before each set of experiments, however, the output signals were noted for the unloaded state so that an accurate zero reference could be obtained.

Figure 3-17: Calibration of  
INPUT SHAFT

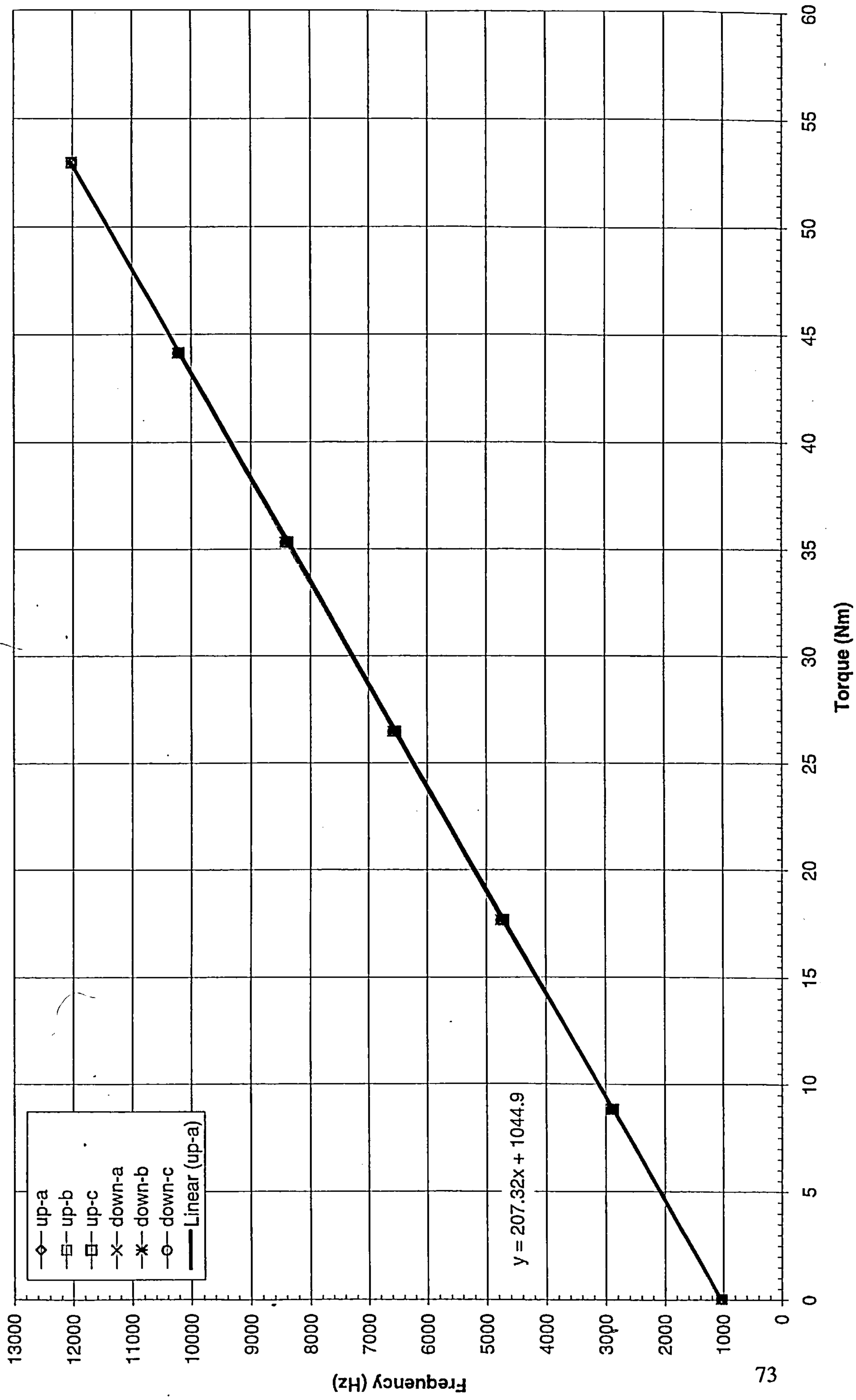


Figure 3-18: Calibration of  
OUTPUT SHAFT

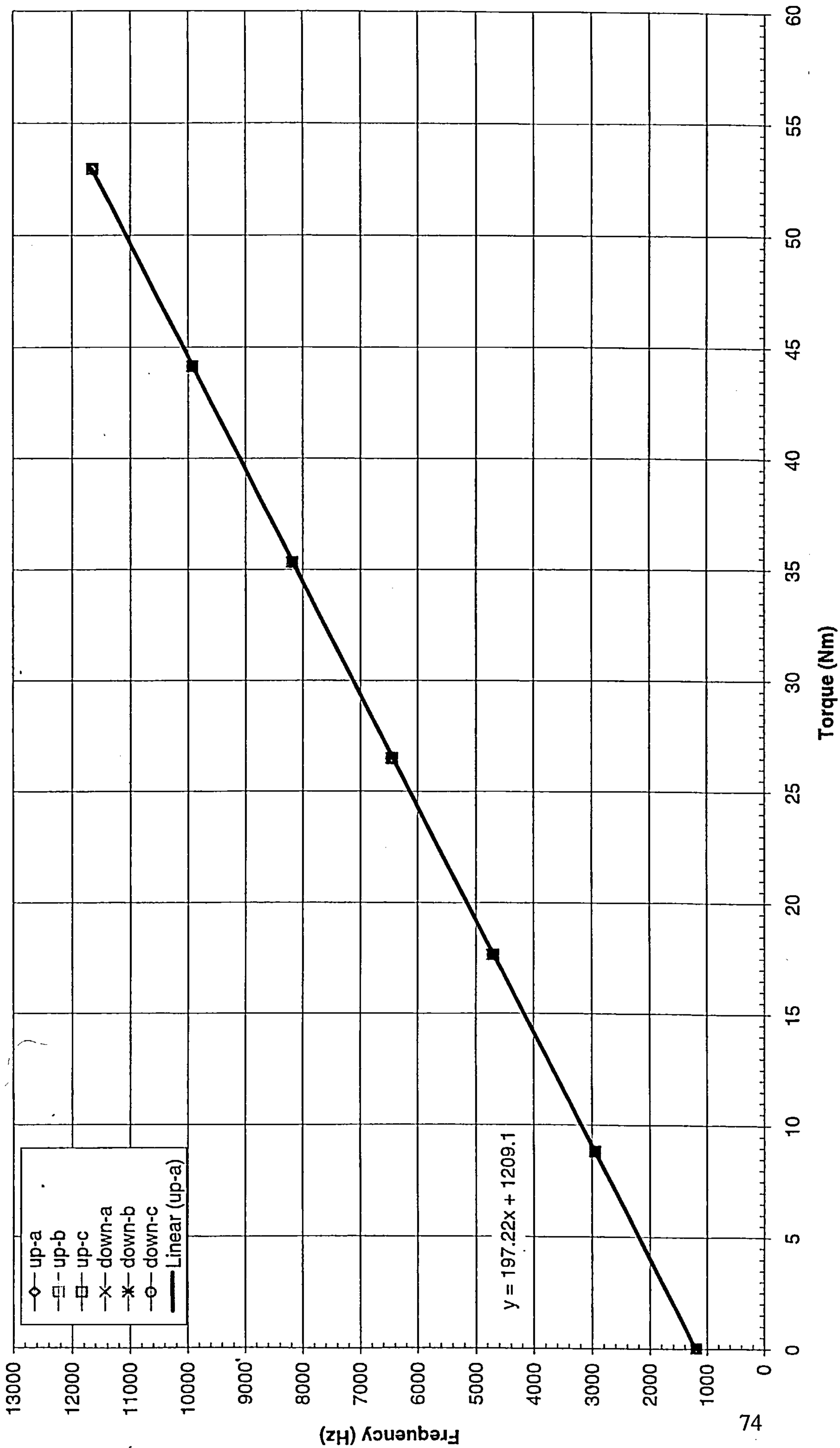
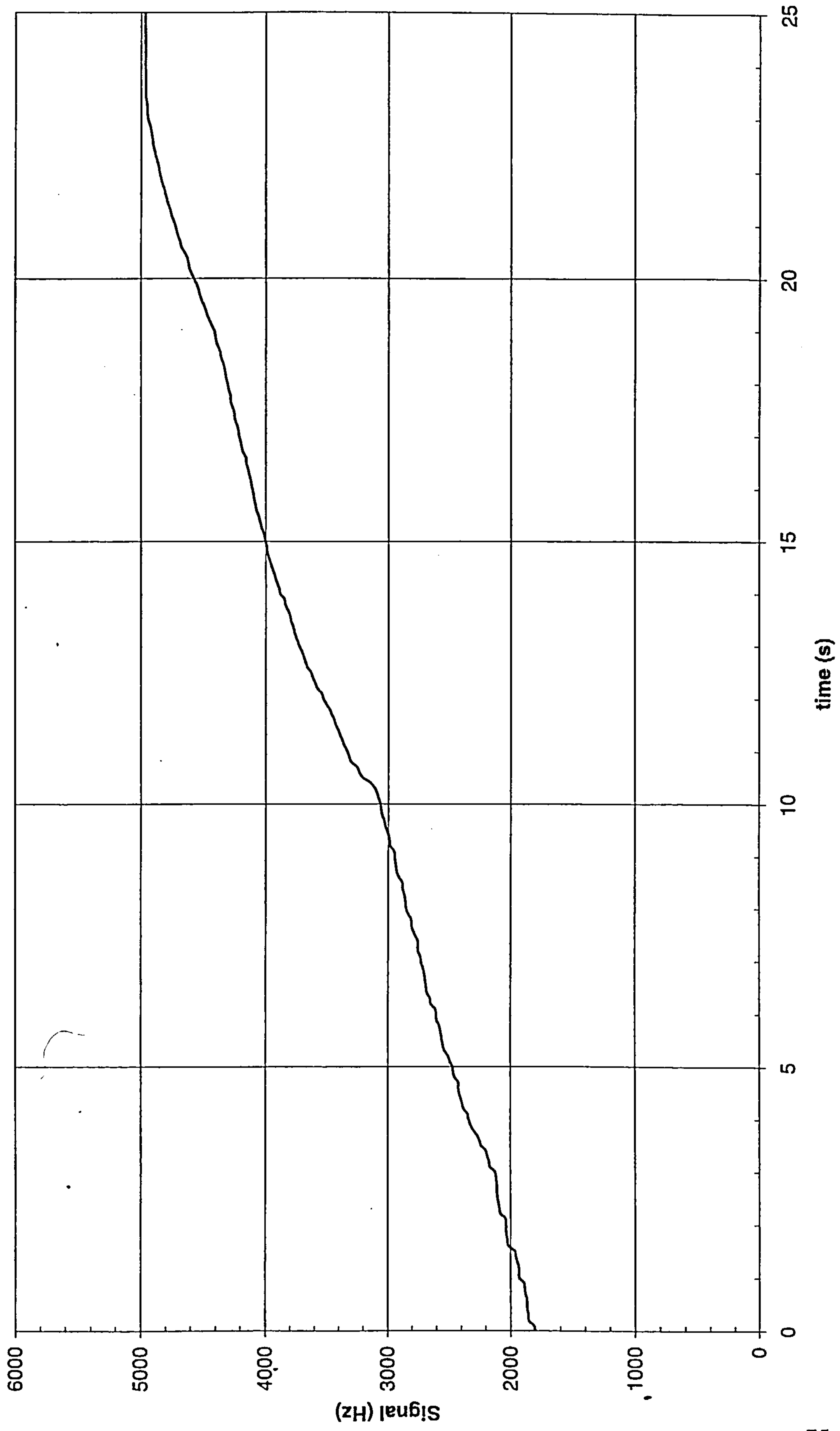


Figure 3-19: Dynamic Test of Torquemeter



### **3.6 Summary**

This chapter has described the design, test and calibration of two non-contacting torque sensors for input and output power (crank and rear sprockets) of a cycle chain drive. The sensors are designed to operate at a sampling rate of 33kHz and have a torque resolution of  $3 \times 10^{-3} \text{Nm}$ . The torque values along with the speed and data acquisition are used in the chain drive efficiency test rig described in Chapter 7.

## 4. Load Distribution Analysis

### 4.1 Introduction

This chapter presents the results of an investigation evaluating the forces present in a statically loaded bicycle chain prior to and beyond sprocket engagement. The forces have been measured and a model based on a modification of Binder's<sup>(15)</sup> GPLD is used to describe the results. One link of a length of chain was instrumented by the use of a strain gauge, and tension measurements of the chain were made as the chain was wound around a sprocket. Previous research in this area has been confined to industrial chains and sprockets<sup>(20),(18)</sup> but as pointed out in Chapter 2, the industrial chain drive system differs from that of a bicycle not only in its dimensions but also in its operation. A typical bicycle chain exhibits a high degree of lateral flexibility in order to work with the derailleur mechanism, which commonly operates at angles of misalignment of  $\pm 3^\circ$ . The following analysis compares the measured and calculated forces found in an outer link of a chain under tension for three sprocket sizes and for three angles of alignment. A further advancement on earlier work includes observing the stresses for some distance prior to engagement. This is of interest since localised bending arising from misalignment can increase or decrease the strain in the outer link plates by a substantial fraction and, furthermore, it is initiated some distance before meeting the sprocket teeth. Ultimately, these forces will affect engagement friction and hence the efficiency of the chain system.

The experiments conducted provided an insight into how the tension decreases in a chain once engaged with the sprocket. This understanding aids the calculation of bearing pressures and their duration within the chain cycle, thus allowing more

accurate modelling of forces and the determination of the corresponding magnitudes of friction losses in the system.

The distribution of chain load from the ‘tight’ to ‘slack’ side depends fundamentally on the size of sprocket, the lap (proportion of engaged teeth to the total number in the sprocket), the tooth pressure angle and the materials used. The work of Binder<sup>(15)</sup> previously described in Chapter 2 is the classical reference for research in the area of load distribution in chains and allows predictions of chain tensions using a technique known as geometric progression load distribution (GPLD). The results of experiments will be compared with the theoretical distribution of load by GPLD. This comparison was conducted to show how appropriate a model developed for industrial drives is to that of the bicycle.

To recapitulate from Chapter 2, the GPLD may be calculated using,

$$F_n = F_t \left\{ \frac{\sin \phi}{\sin(\alpha + \phi)} \right\}^n$$

In this experiment, the  $F_n$  force will be measured in one link from being equal to  $F_t$ , engaging fully with the sprocket to disengaging and becoming equal to  $F_s$ .

#### **4.2 Misalignment from out-of-plane bending**

Whilst GPLD theory is valid in the 2D movements found in most industrial applications, a model must be developed to understand the influence of bending in a third plane caused by misalignment. The following analysis is not strictly applicable to the case of when a link is fully engaged with the sprocket as in the GPLD case because of the lateral support from the tooth flank. It does, however, estimate the

bending stresses in a chain  $n$  links prior to engagement of a sprocket mounted at  $\beta$  degrees from normal inclination.

Figure 4-1 shows how the chain may be regarded as accommodating the misalignment angle  $\beta$  over  $n$  links of pitch  $p$  assuming that all of the out-of-plane (OOP) deflection is carried by whole body movements of the chain elements. If each link is regarded as carrying the same angular misalignment,  $\gamma$ , the OOP deflections at the first and second links  $x_1$  and  $x_2$  can be written:

$$\begin{aligned} x_1 &= p \sin(\beta - \gamma) \\ x_2 &= x_1 + p \sin(\beta - 2\gamma) \end{aligned} \quad \text{Eq. 4-1}$$

or, more generally for the  $n$ th link:

$$x_n = p \sum_{i=1}^n \sin(\beta - i\gamma) \quad \text{Eq. 4-2}$$

which also represents the moment arm of the chain tension  $t_0$  about point A.

The stress in the outer link from the chain tension,  $t_0$  is a function of the cross sectional area of the link plates,  $a$  and is expressed as:

$$\sigma_t = \frac{t_0}{a} \quad \text{Eq. 4-3}$$

The bending stress on the surface of the outer links  $\sigma_b$ , can be obtained from the beam bending function:

$$\sigma = \frac{My}{I} \quad \text{Eq. 4-4}$$

where  $M$  is the bending moment,  $I$  is the second moment of area of the link plates and  $y$  is their average distance, from the neutral axis of bending of the link. Calculating an average  $I$  and  $y$  value to account for the difference in geometry between the inner and

outer plates allows a general equation to be formed using Eq. 4-2 for the bending moment with  $t_0$ ,

$$\sigma_b = t_0 \frac{y}{I} p \sum_{i=1}^n \sin(\beta - i\gamma)$$

The relationship between the bending and direct stress can now be expressed as:

$$\frac{\sigma_b}{\sigma_t} = \frac{pya}{I} \sum_{i=1}^n \sin(\beta - i\gamma) \quad \text{Eq. 4-5}$$

To compare the ratio of total (or combined) tension to that purely from direct stress the term  $(1 + \sigma_b/\sigma_t)$  is used. Figure 4-2 shows values of  $(1 + \sigma_b/\sigma_t)$  calculated for a range of values of  $n$  and  $\beta$ . When  $\beta$  equals zero degrees, i.e. no bending, the total tension is simply  $\sigma_t$ , which is the case for co-planar sprockets.

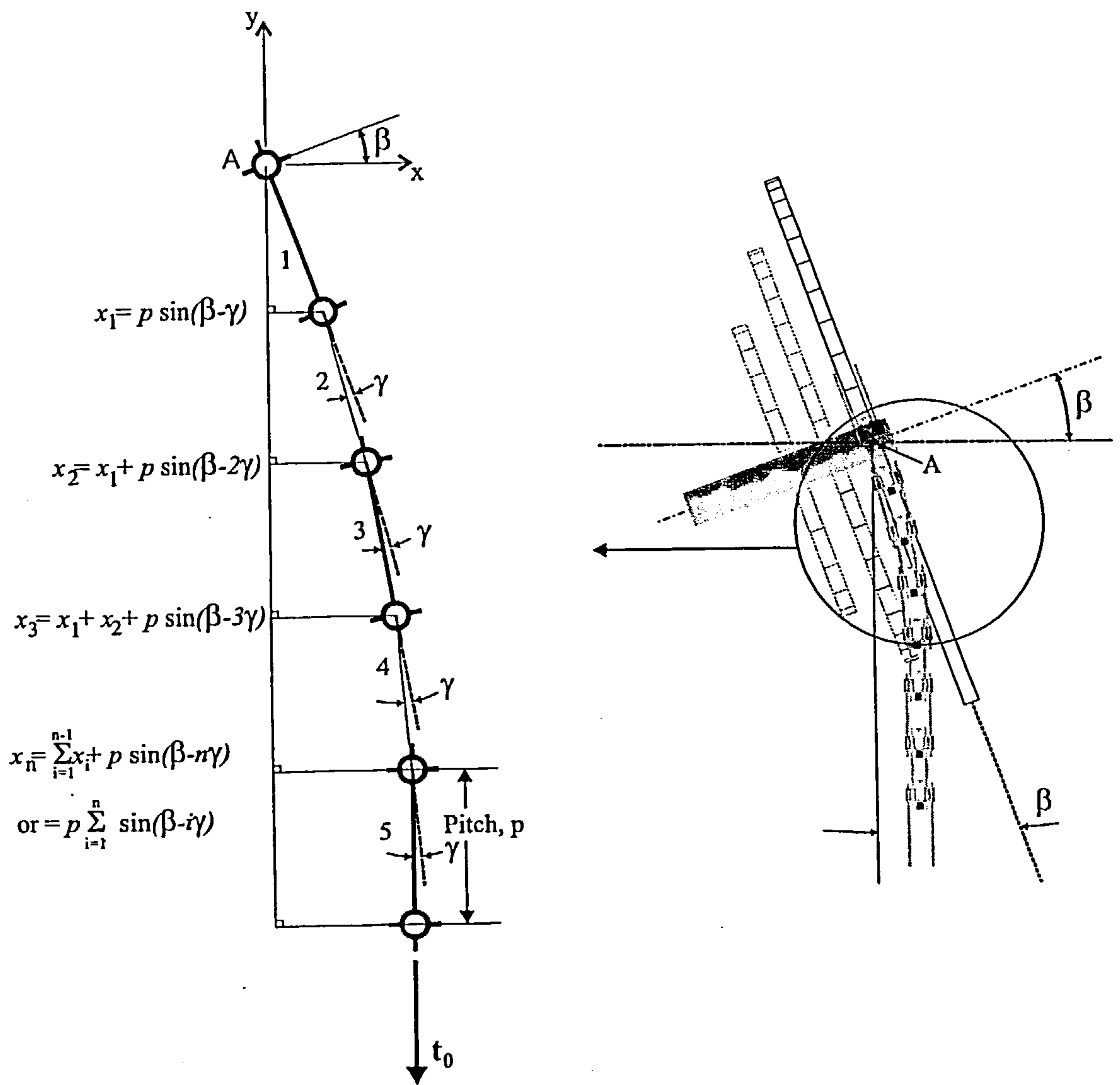
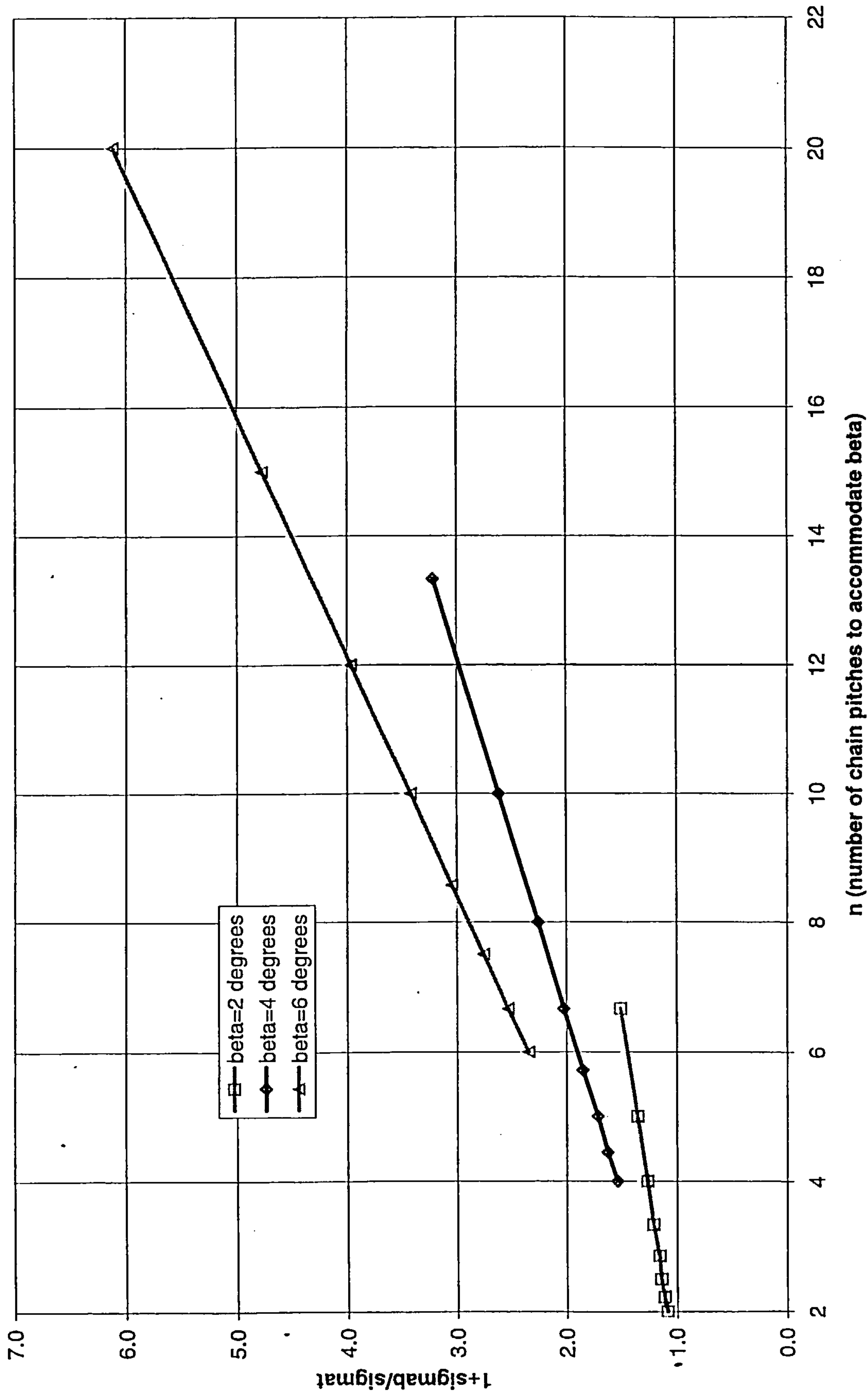


Figure 4-1: Accommodating misalignment, exaggerated chain link positions

Figure 4-2: Bending stress relative to direct stress for values of beta.



The chain dimensions used in this experiment are those from a sample chain detailed in Table 4-2. The value of  $n$  is dependent upon the value of  $\gamma$  and Table 4-1 gives the approximate number of corresponding links to cope with a total misalignment angle of  $\beta = 4$  degrees.

Angle	$\gamma$	0.5	0.6	0.7	1.0
Number of links	$n$	8	~7	~6	4

Table 4-1: Links to accommodate various angles of misalignment

Figure 4-3 represents the chain sprocket combination used for the experiments reported in this chapter where the sprocket inclination angle  $\beta$  was allowed to vary from 3.5 degrees below the horizontal ( $0^\circ$ ) to 3.5 degrees above it. The in-plane component,  $t_0\cos\beta$  generates tension in the links as described by GPLD equations<sup>(15)</sup>. However the out of plane component  $t_0\sin\beta$  contributes to the local bending of the chain outer links.

Figure 4-4 shows (in exaggerated form) the rotational and lateral displacements that a typical pair of bicycle chain links can experience. The geometric parameters  $\gamma$  and  $\delta$  may be estimated from measurements made of the chain samples, a summary of such results is shown in Table 4-2

Dimension	$C_1$	$C_2$	$C_3$	$C_4$
mm	4.1	4.1	4.4	4.7

Table 4-2: Sample chain measurements

The cumulative effect of the angle  $\gamma$  over the working length of chain is that it enables the derailleur system to accommodate non-coplanar sprockets. The maximum lateral translation  $\delta$  is simply  $C_4$  minus  $C_3$ .

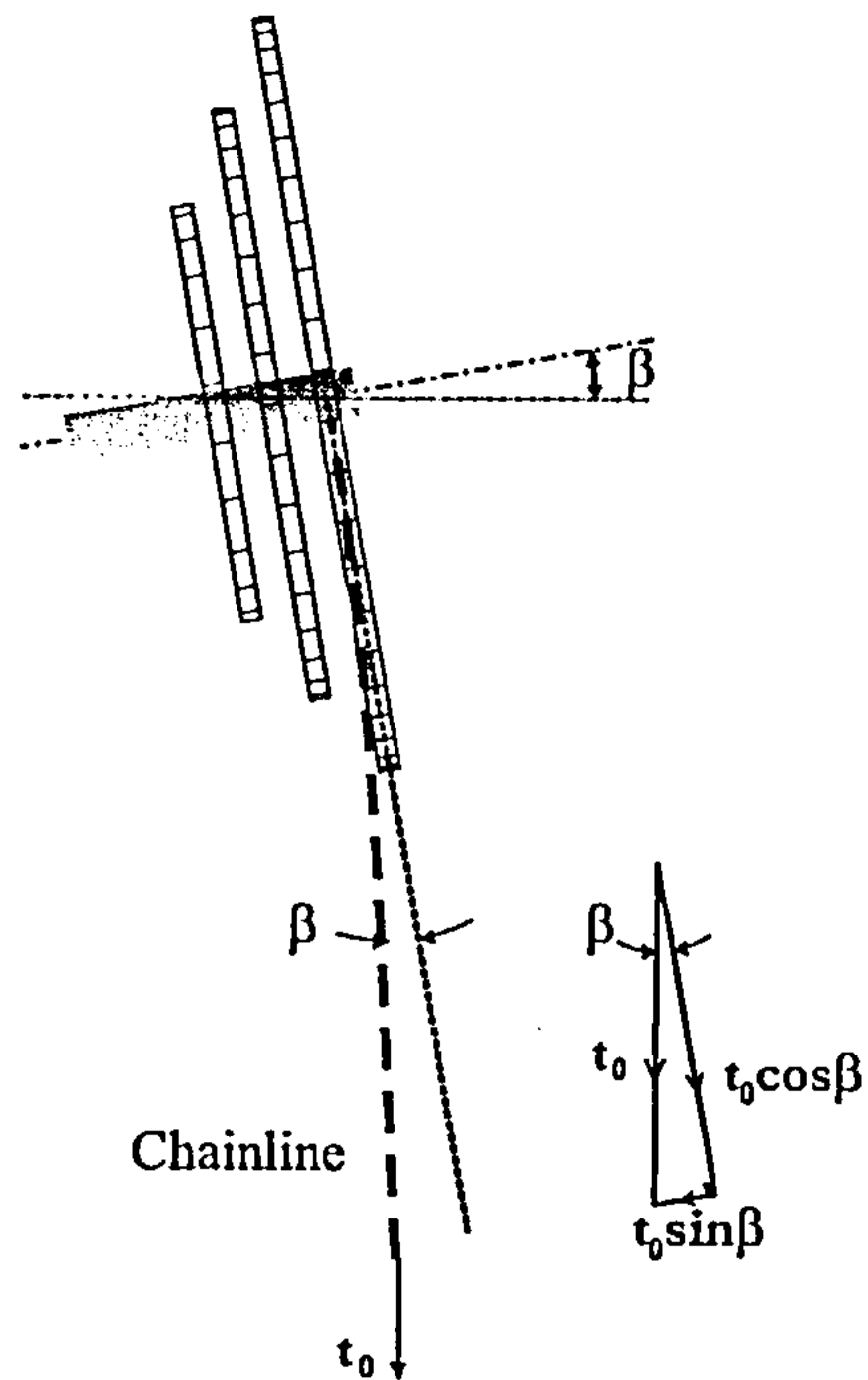


Figure 4-3: Sprockets inclined at an angle  $\beta$

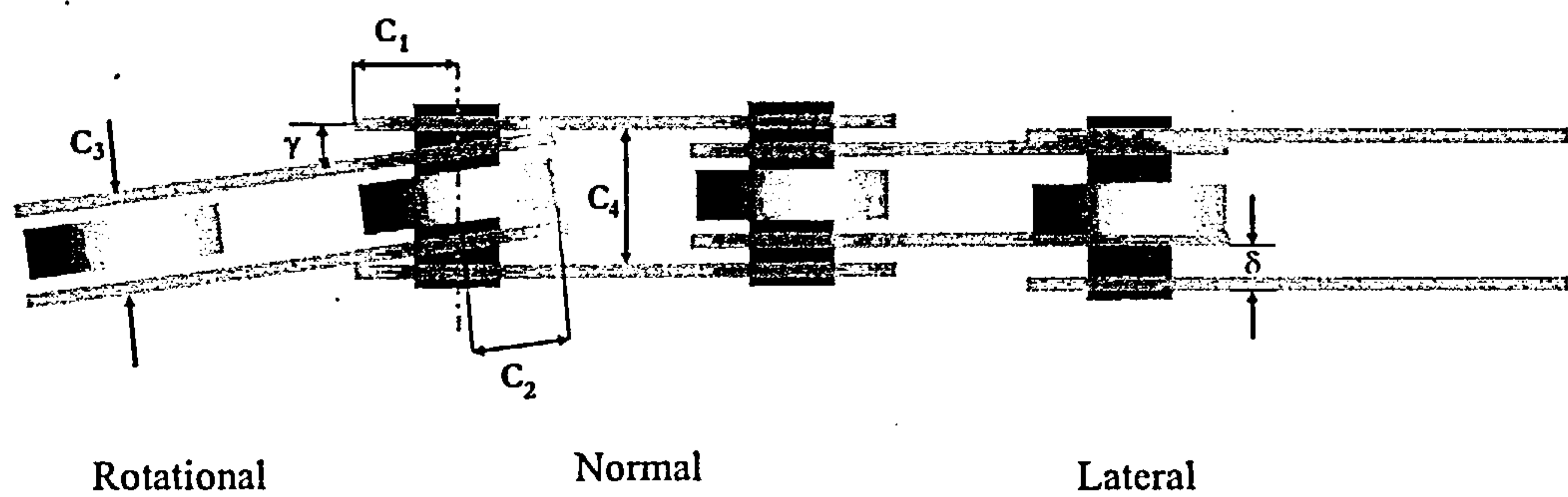


Figure 4-4: Exaggerated possible component positions

As shown in Figure 4-1, out-of-plane loading causes the chain to adopt a curved profile partly as a consequence of the bending effect of  $t_0 \sin \beta$  and partly due to the inherent flexibility of the chain offered by the various devices. The bending effect was found to be accommodated in approximately 3 to 4 chain pitch lengths when  $\beta = 4.0^\circ$ ; this was calculated by solving Eq. 4-6 for  $\gamma$ , then dividing  $\beta$  by  $\gamma$ .

$$C_4 = C_3 \cos \gamma + \sin \gamma (C_1 + C_2 \cos \gamma) \quad \text{Eq. 4-6}$$

It should be noted that the rotational movement shown in Figure 4-4 assumes that, at the time of bending, each inner link is positioned in the middle of the outer link's longitudinal axis. Additionally, the radial clearance between the inner link and the pin must be sufficient to allow the movement depicted. Failure to meet either of these criteria will result in a reduced  $\gamma$ , thus requiring more links to accommodate the overall angle of misalignment,  $\beta$ . The actual bending of the plates is assumed to be negligible. It could be interpreted that the values calculated represent the minimum number of chain links over which the misalignment will be accommodated and accordingly the maximum likely bending moments. Equally the analysis does not include any consideration of flexure of the chain components.

### **4.3 Apparatus and procedure**

Chain tension was measured with single linear strain gauges mounted to outer chain links. Connected as a quarter bridge configuration to a Measurements Group 1000 Strain Gauge Amplifier, the gauge provides a sensitive and accurate measurement of strain in the outer link without interfering with the operation of the chain. The dimensions and features of the bicycle chain do not lend themselves to having strain gauges bonded to them. Many manufacturers' links are stamped or

embossed in some way or have very little featureless, flat surface area. The opportunity to mount a gauge on the “inside” (see Figure 4-4) surface of a link as in Naji’s<sup>(18)</sup> work was precluded by the link’s construction and operation. When engaged with the sprocket, the tooth flank commonly rubs against the inner link surface; this rubbing changes to support when there is an element of misalignment between chain and sprocket. Having found suitable links for the installation, gauges (EA-06-062AQ-350) were bonded to four consecutive links, two each on opposite sides of the chain. Each gauge was operated independently, providing redundancy of measurement as the failure rate of the gauges or wires was high due to the fragile installation (see detail in Figure 4-5)

The principle and procedure of the experiment was similar to that conducted by Eldiwany and Marshek<sup>(20)</sup>. Figure 4-5 represents the test apparatus and shows how tension was imposed on the chain by gravity acting on standard laboratory masses hanging from the tight side of the chain. A thrust bearing coupling situated at the chain to wire rope junction ensured there was no torsional component of force added to the chain from rotation of the masses. The total load in the chain was 800N, which is considered representative of a cyclist’s power output of between 200-400W depending on the sprocket ratio and speed.

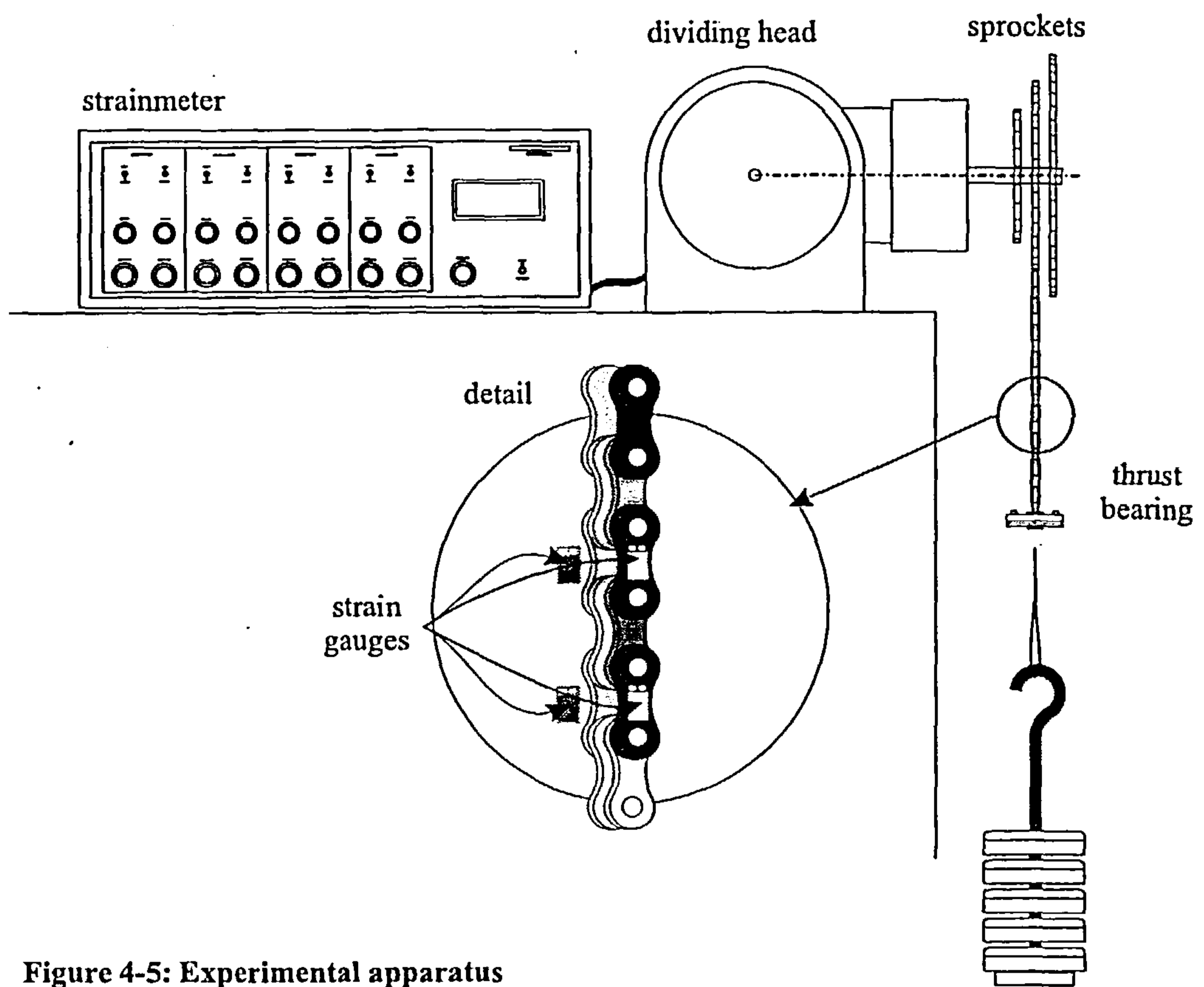


**Figure 4-5: Experimental apparatus**

To maintain a good representation of the bicycle environment, the sprockets were mounted on a five arm “spider” spigot, similar to the components found on a bicycle. Not only does this method of securing the sprockets reflect the stiffness found on a bicycle but it also ensured that sprockets were mounted concentrically and without the need to modify their stiffness. The sprocket spider was attached to a shaft using the same “Tranotorque” device as used in the chain efficiency experiment (Chapter 7), thus allowing the sharing of components and maintaining ease of installation. The shaft was held in a machine tool dividing head, which allowed easy rotation of the sprockets under load by way of a 40:1 turn ratio. A further feature of this arrangement was the ability to introduce calibrated rotation of the shaft from the horizontal plane; this was used to set the sprockets  $\pm 3.5^\circ$  from normal (vertical) operation.

Initial experiments used a Strainmeter 3000 strain gauge amplifier, the reading of which was noted manually against angular position. The rotation of the sprockets was also carried out manually and incrementally, readings being taken at every  $9^\circ$  of sprocket rotation. This, however, gave insufficient resolution to determine the transition point ( $0^\circ$ ) when the upper pin of the gauged link starts to be supported by a sprocket tooth.

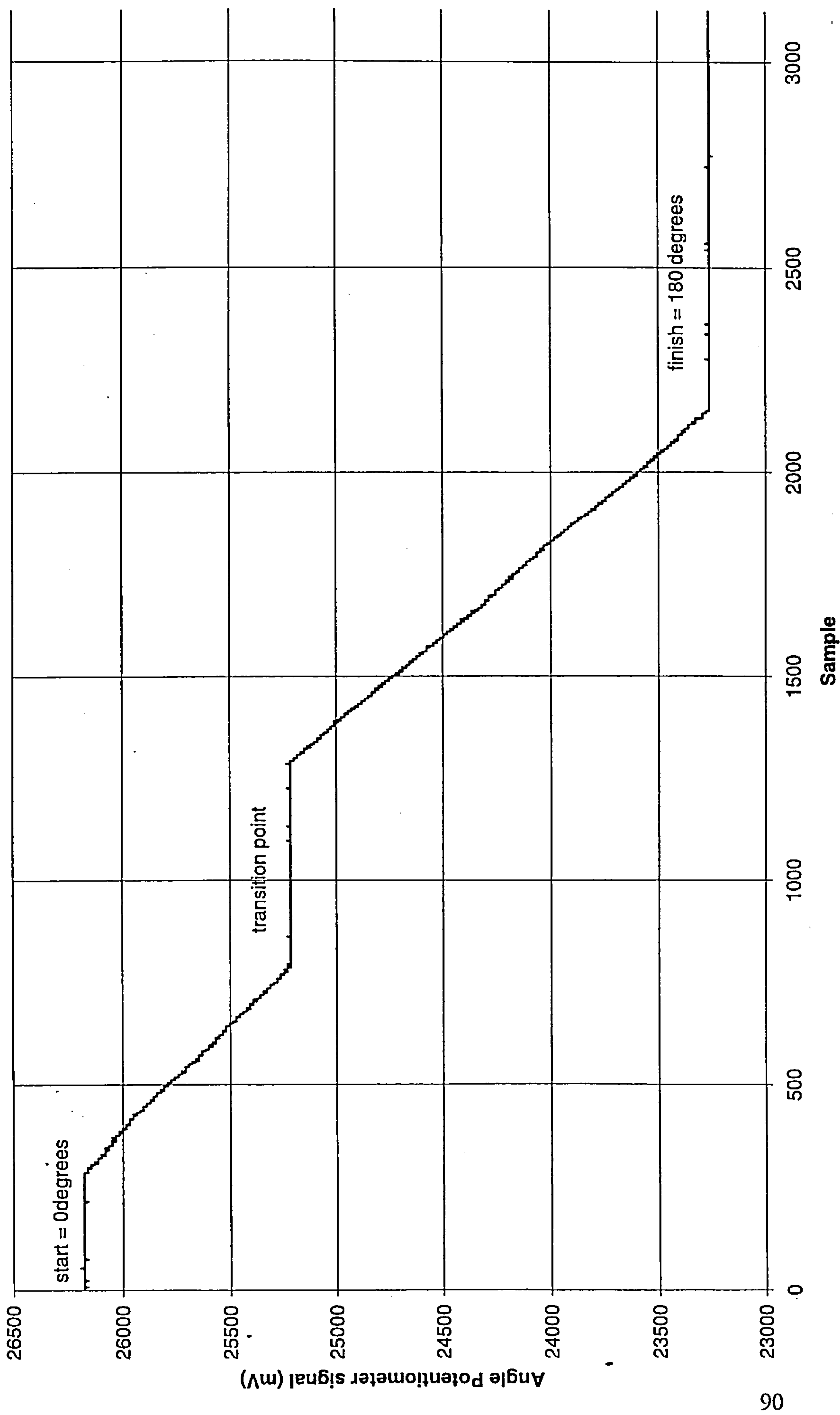
To refine the instrumentation and provide a continuous accurate measurement of angular position, a ten-turn potentiometer was connected between the shaft and the frame. The rotation of the sprockets and shaft results in a change of resistance of the potentiometer. By applying a constant voltage across the input of the potentiometer, the varying output voltage proportional to rotation could be read digitally alongside the strain. Calibration of the angular measurement was made during each

experimental run by using a dwell in the angular position of the shaft as an indicator of a datum point. For each experimental run, a delay in movement was placed at the start (9 o'clock), transition point (variable) and finish (9 o'clock again). Using the calibrated scale and operation of the dividing head, a simple calculation could yield a potentiometer-angular position relationship. A sample angular co-ordinate plot is shown in Figure 4-6. By acknowledging the delay at the transition point a  $0^\circ$  datum would then be set, negative angular values now representing a position prior to engagement. This angular co-ordinate is, of course, that of the sprocket, and not of the gauged chain link. The two are only equal when links are fully engaged for around  $180^\circ$ .

The determination of the  $0^\circ$  transition point was achieved by line-of-sight and human judgement. The angular position was noted in a trial test and marked on the dividing head temporarily. This method allowed the point to be found quickly and reliably during a test when data is being acquired. The implications of this in terms of overall experimental accuracy are discussed in Chapter 9.

In order to maintain correct operation of the chain (i.e. proper seating of links into the sprocket), a low mass counter-weight was attached to the non-loaded side of the sprocket. Without this measure, the chain may not have bedded into the sprocket, giving incorrect readings and also potentially permitting the chain to slip off the sprocket, allowing the masses to drop. Such a situation of the chain being thrown off could not only damage the strain gauge lead wires as they take the load but also the gauges themselves.

Figure 4-6: Angular Test Plot



Acquisition of data was performed using a laptop PC with a DAP data acquisition board sampling two channels at 50kHz per channel. The sampling rate provided several readings of strain for each degree of rotation, far superior to the previous method of measurement. Analysis was conducted in Matlab, the file format of which was a 2D array of strain and angular position, each recovered using the appropriate calibration. A typical record length was  $12 \times 10^6$  samples, taken over a 240s period of experiment.

#### **4.4 Results**

Figure 4-7 to Figure 4-9 represent the results of 9 experiments comprising three sets of data for each size of sprocket. For convenience, all measured strain signals (which in essence give a measure of load in the chain) are normalised relative to the strain value occurring before the gauged links engage with the sprockets. Hence a normalised strain of unity relates directly to a chain tension ratio  $t_n/t_0 = 1$ . The figures demonstrate this clearly in the regions beyond chain engagement with the sprocket i.e. for negative angles of sprocket rotation.

Binder's GPLD has been plotted alongside the experimental data to illustrate the theoretical distribution of strain (load). Here, a friction angle  $\varepsilon = 5^\circ$  (corresponding to a coefficient of friction of 0.087) has been assumed to plot the GPLD.

Figure 4-7: 28 Tooth sprocket results

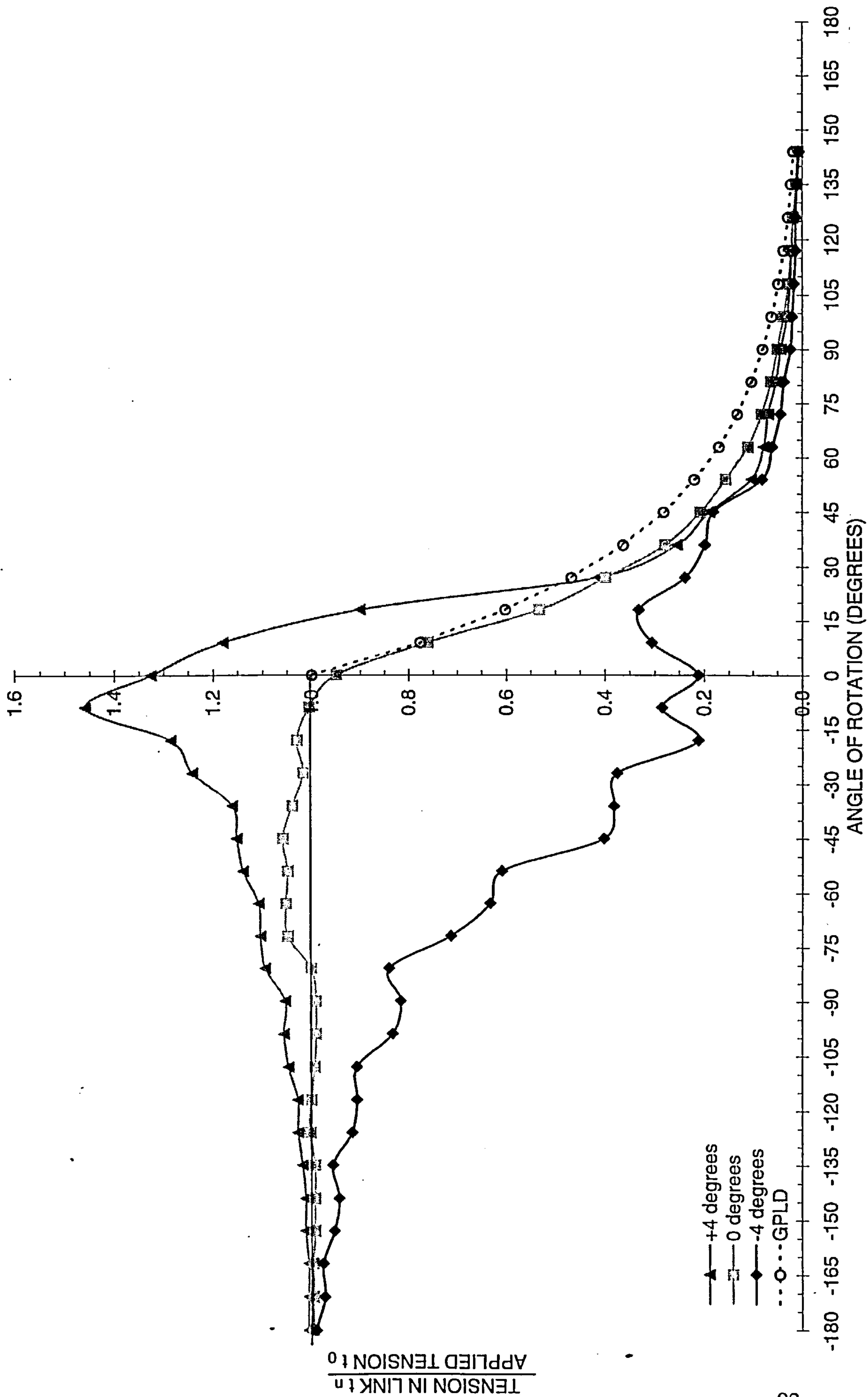


Figure 4-8: 38 Tooth sprocket results

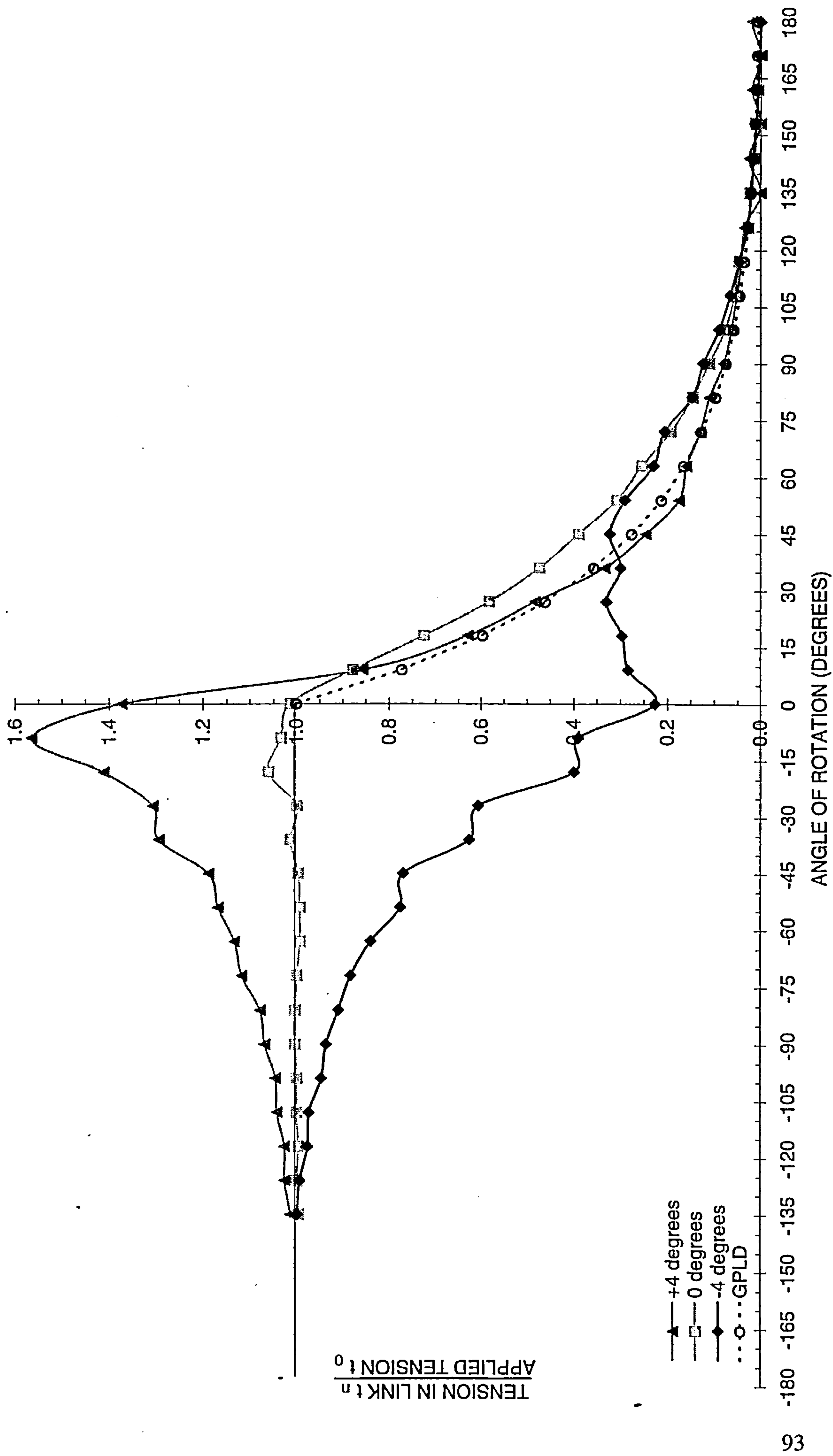
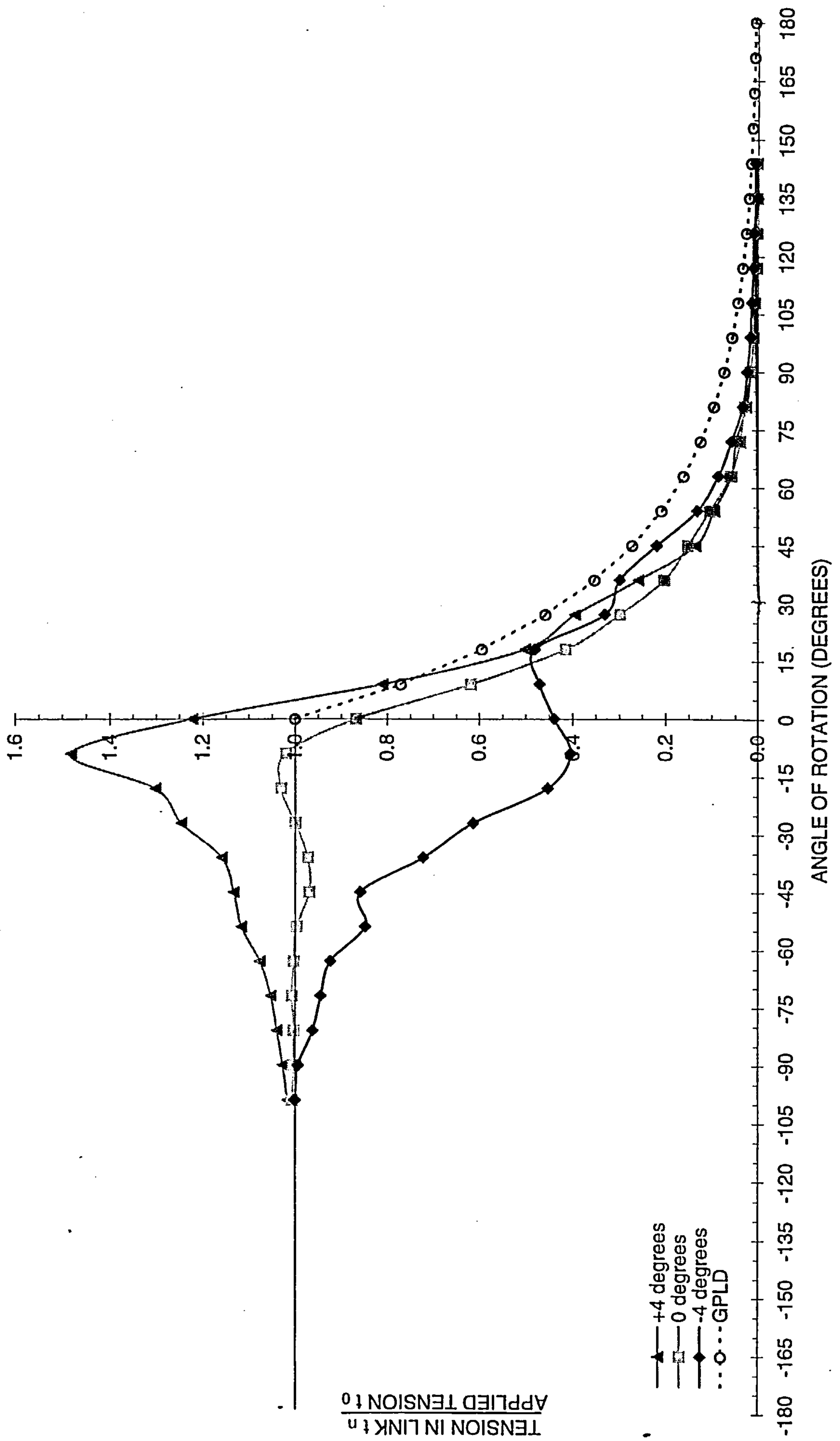


Figure 4-9: 52 Tooth sprocket results



#### 4.4.1 In-Plane Loading 0°

All three sets of data illustrate quite clearly the expected characteristics of chain load engagements, that is  $t_r/t_0 = 1$  prior to engagement followed by rapid decrease immediately after engagement, the reduction being of the order of 50% after 30° for both the 28 and 52 tooth sprockets. For both of these sprockets, the post-engagement plots compared very favourably with the GPLD, whereas the pre-engagement part for the 28 tooth sprocket dropped below unity at about 60° and remained as such up to 0° (i.e. engagement)

Strangely, the post-engagement plot for the 38 tooth sprockets did not decrease as rapidly as did the others, and remained substantially above the GPLD until around 135°

The GPLD curve is sensitive to many factors, the unknown variable in the case of these chain/sprocket experiments was the assumed friction angle. Changes in this could result in better accordance with the data. The consequences for friction losses and thus efficiency from changes to these parameters are discussed in Chapter 9.

#### 4.4.2 Out-of-plane loading +3.5°

When the chain-sprocket planes are misaligned by 3.5°, the strain in the link shows an effect common to all sprocket sizes. The link is responding to both direct tension ( $t_0 \cos \beta$ ) and tensile bending ( $t_0 \sin \beta$ ) and the combined effect increases the measured normalised strain ratio to around 1.5 at peak. The rise to the peak immediately prior to engagement commences at an equivalent angle of between 50° to 120° before the maximum. Whilst the stepped increase is common for all sizes of sprocket, the phenomenon is best illustrated by the 28 tooth sprocket. Figure 4-7

shows how the strain ratio almost instantly starts to increase at around  $-120^\circ$ ; this is equivalent to 9 chain pitches (114mm) before engagement with the sprocket. For the 38 and 52 tooth sprockets, the point at which recording commenced was a little later so that the departure of  $t_r/t_0$  from 1.0 had originated prior to taking data; despite this, the deviations are estimated to start at 8 and 7 links respectively pre-engagement.

#### 4.4.3 Out-of-plane loading $-3.5^\circ$

As expected, these results are similar in form to those for  $+3.5^\circ$  except that the links now experience compressive bending plus direct tension. Not surprisingly, the pre-engagement portions of both plots for  $+3.5^\circ$  and  $-3.5^\circ$  form an approximate mirror image when viewed along the axis where normalised strain equals 1, illustrating the contrasting effect of bending action in the outer links.

Once the chain is fully located within the sprocket, the strain rises to meet the underlying GPLD of a normally aligned chain/sprocket combination. The rate of increase in strain as the chain link returns to a normal alignment angle of operation with the sprocket is affected by the size of the sprocket. The 52 tooth sprocket exhibits the sharpest return to normal running, with a  $+3.5^\circ$  misalignment. A more gradual re-convergence to GPLD by the chain on a 28 tooth sprocket means that the  $t_r/t_0$  ratio increased very little after engagement.

#### 4.4.4 Pre-engagement Phenomenon

Although the magnitude of the deviation from normal tensile load can be predicted easily, the rate and onset of this deviation is a new observation. The design and implementation of industrial chain drive systems generally precludes their operation with any degree of misalignment. The systems found on bicycles, however,

lead to misaligned running becoming an inevitable operating condition; indeed some 80 to 90% of possible gear combinations on a derailleur system will result in operating with a element of misalignment. The construction of the bicycle chain lends itself to running under misalignment and, as such, exhibits a more exaggerated bending effect over the laterally inflexible industrial drives. The observations made of pre-engagement loads are an insight into the mixed bending/catenary working of the chain and this has implications for overall efficiency.

Due to the discrete nature of the chain, a stepping of strain is exhibited in the pre-engagement region of the load distribution plots. The stepping is most prominent in the 28 tooth sprocket but it is still discernible in the 38 and 52 tooth sprockets. The measured period of the steps is summarised in Table 4-3.

Teeth	Period Degrees	Length mm
28+	30	29.2
38+	20	26.7
52+	15	27.5
28-	28	27.7
38-	21	28.1
52-	15	27.5

Table 4-3: Step characteristics

## **4.5 Summary**

The experimental measurements of strain (load) for an aligned chain/sprocket combination during engagement agree reasonably well with Binder's GPLD predictions for the three sprocket sizes examined. In particular, the strain measurements illustrate discontinuous progression attributed to the discrete nature of the chain in the pre-engagement region.

The case of misaligned chain and sprocket produces considerable deviations from Binder prior to engagement, where the offset bending effect is very significant. After engagement, the pattern of rapid strain reduction is similar to that of the aligned case with convergence towards GPLD being evident.

## 5. Coefficient of Chain Friction

### 5.1 Introduction

The efficiency of a mechanical drive system is defined simply as the ratio of power output to power input and its experimental determination invariably involves measurement of power loss. In the case of chain drives, power loss occurs due to the presence of friction at the bearing surfaces of those components having relative movement. When there is less friction in the transmission system there is less power loss, thus the overall efficiency rises. The magnitude of the friction force present between two bodies moving relative to each other is dependent on the normal force at the interface and the coefficient of friction between the surfaces, denoted  $\mu$ . The extent to which the friction forces occur within a chain and sprocket drive system is influenced by both mechanical and geometric factors which can dictate the level of rolling and sliding action as the chain articulates during its motion. Such geometric influences exist even in a new chain/sprocket combination before wear has occurred. With a worn chain there is a greater movement of components, increasing the rolling and sliding required for the chain to conform to the sprocket, all of which increase friction.

When in operation, the chain has relative movements both within itself and with the sprockets that give rise to friction. Figure 5-1 shows the four areas of contact that contribute to the overall friction loss of the chain:

- (a) Pin and Bush: pin may slide or slip within inner bushing of adjacent link.
- (b) Bush and Roller: inside of roller may slide or slip against outer bushing surface of link – related to (c).

- (c) Roller and Sprocket: outer surface of roller may slide, slip or roll down flank of sprocket.
- (d) Inner and outer plates: inside of outer and outside of inner link will articulate, sliding will occur with misalignment and occasionally under normal alignments.

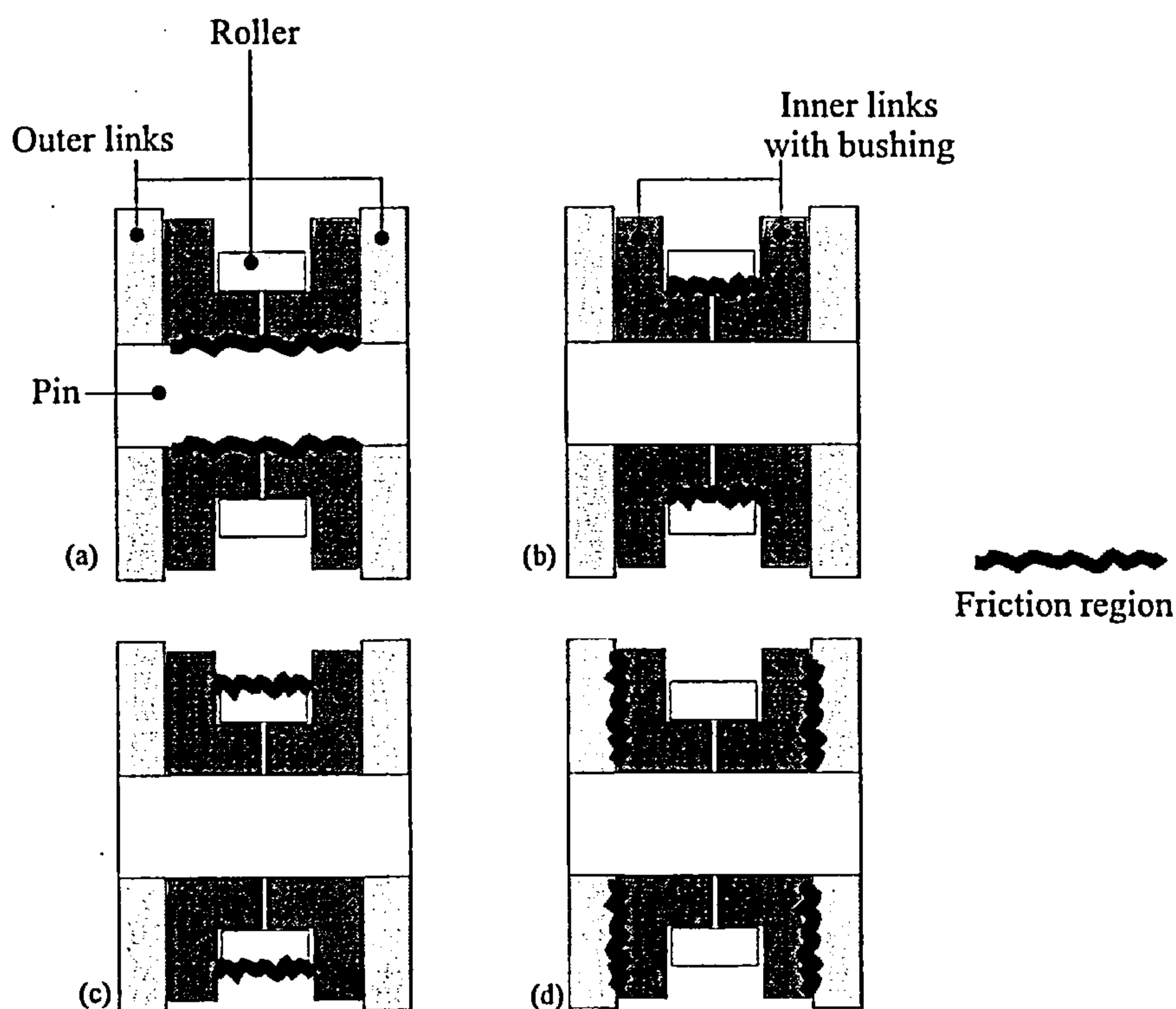


**Figure 5-1: Friction points**

A more detailed consideration of the surfaces that contribute to friction is given in Chapter 8. The largest friction forces occur in case (a) and the lowest in case (d). For a total energy loss calculation each contact point is considered, the friction force calculated and multiplied by the sliding or rolling velocities of each.

For any two surfaces in contact in a chain system, appropriate material selection and preparation can reduce the friction but, most commonly, it is reduced by use of a lubricant. Even for common metal pairs with or without the presence of a

lubricant layer there are no theoretical methods to predict the coefficient of friction. Although values for  $\mu$  can be found in many handbooks and reference texts, their origin derives almost wholly from experiment. It is a relatively simple matter to quantify  $\mu$  and several methods<sup>(51)</sup> exist to calculate it from mechanical measurements.

If it is desired to know the coefficient of friction relating to a particular material pair under specific operating conditions, then the most reliable procedure is to measure  $\mu$  experimentally in a simulated environment. If simulation is not feasible, a common alternative is to match the materials used with samples and apply a known load or torque; a transducer can then make the measurement of friction force. Several forms of measurement exist and are commonly combined with apparatus to observe the wear of components. Three general categories of friction and wear test equipment exist depending on the geometry of the actual component application:

- (i) test bodies with parallel sliding surfaces (pin-on-disc).
- (ii) contact of curved surface on a plane (cone-on-plate, cylinder-on-plate and ball-on-plate).
- (iii) contact of two curved bodies (ball-on-ball, involute-on-involute).

The results of coefficient of friction tests will serve many purposes. Comparisons can be made simply and quickly between the effectiveness of different lubricants. The functional lubricant properties can be observed over time, under different conditions and in the presence of foreign bodies. Results of coefficient of friction measurements may then be used to enhance the accuracy of theoretical efficiency calculations rather than assuming a value or approximating to corresponding data obtained from other published data. Time can be an important

experimental variable as  $\mu$  may change as the lubricant becomes adsorbed, dispersed, broken down or simply contaminated. All of these factors are of potential interest in examining performance of the chain.

Both a simulation and a sample method were used in this research, a pendulum for simulation and a pin-on-plate method as an adaptation technique. The former approach is a realistic test bench trial, the other a model test of a scaled or modified system but with the same general components. The two types of measurements are used to obtain an enhanced understanding of the friction losses in chains and, to this end, a number of chain components were examined metallographically.

## **5.2 Examination of Chain Components**

Samples of each component part of a chain were examined by a number of different methods. Observations of macroscopic form to microscopic sections allow a greater understanding of the surfaces and their interactions during chain operation.

Of most importance with respect to the origin of most frictional losses is the chain pin. *Talysurf* profiles were used to identify the distinctive wear patterns on the chain pin. A range of pins were tested from new to extensive wear showed characteristic wear patterns in two locations. The segments of the pin affected were the regions in contact with the inner bush bearing surfaces under load. Even pins that had only undergone light use of a few hundred kilometres showed some wear. With less service time, the pin wear pattern was only visible as polishing of the surface and remained undetectable by the apparatus.

Following extensive use, perhaps including some time in a non-lubricated state, deep wear scars begun to be visible. The depth of these grooves could be as

much as 0.3mm, compared to the nominal pin diameter of 3.6mm. To reduce the rate of wear some models of chain feature surface treatments in addition to the standard heat treatments.

To examine a treated pin surface a complete chain section (similar in profile to Figure 5-1) was prepared in resin and etched with Nital. The chromized layer, referred to as delta hardening by the manufacturer, is clearly visible in Figure 5-2 as an unetched layer of 30 $\mu$ m thickness is present along the outer surface of the pin. The same photograph illustrates the pin-bush interface area that accounts for the pin wear profile.

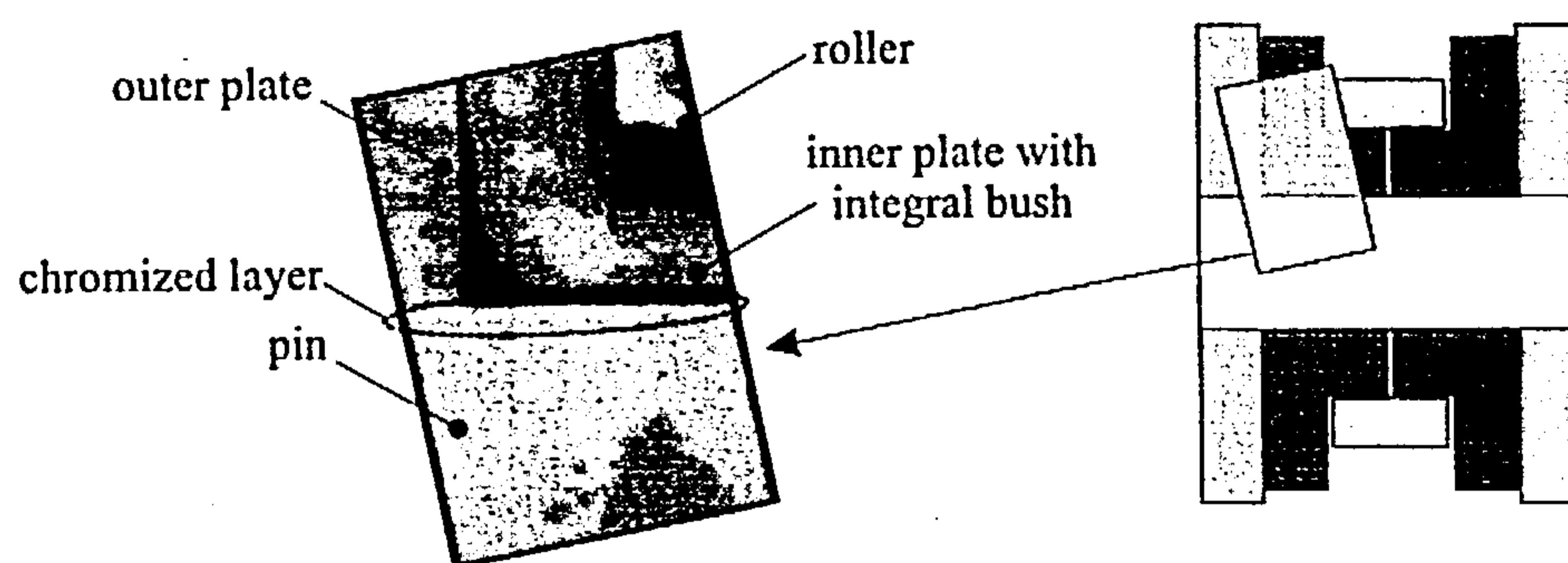


**Figure 5-2: Chain cross section**

Three models of chain, covering the spectrum of available quality, were tested primarily for pin and inner-link/bush hardness. Because of the thin layer and the profile of the chromized pin only the bulk material value could be measured. Bush hardness values of 454, 512 and 503HV were obtained, listed by increasing cost. The pin material was harder than that of the bush in all cases: 491, 603, 576HV (in order of increasing cost). The other chain components, roller and outer plates, were briefly

examined with fewer measurements made and were revealed to be within 10% of the bush hardness values.

In conjunction with the universal wear machine (UWM) coefficient of friction tests described in section 5.4 an attempt was made to quantify the wear rates of chain components. Measurements of were taken before and after the closed environment conditions of the test. The pin and bush plate materials were weighed and examined by low power microscope. No change in mass of the chain pin was discernible and no visible changes of the surface in contact were present. The plate material, however, lost 0.001% in mass despite being lubricated and only being run for 25 minutes. The changes in the plate were clearly visible as the black burnished layer was damaged, revealing the parent metal colour, Figure 5-3

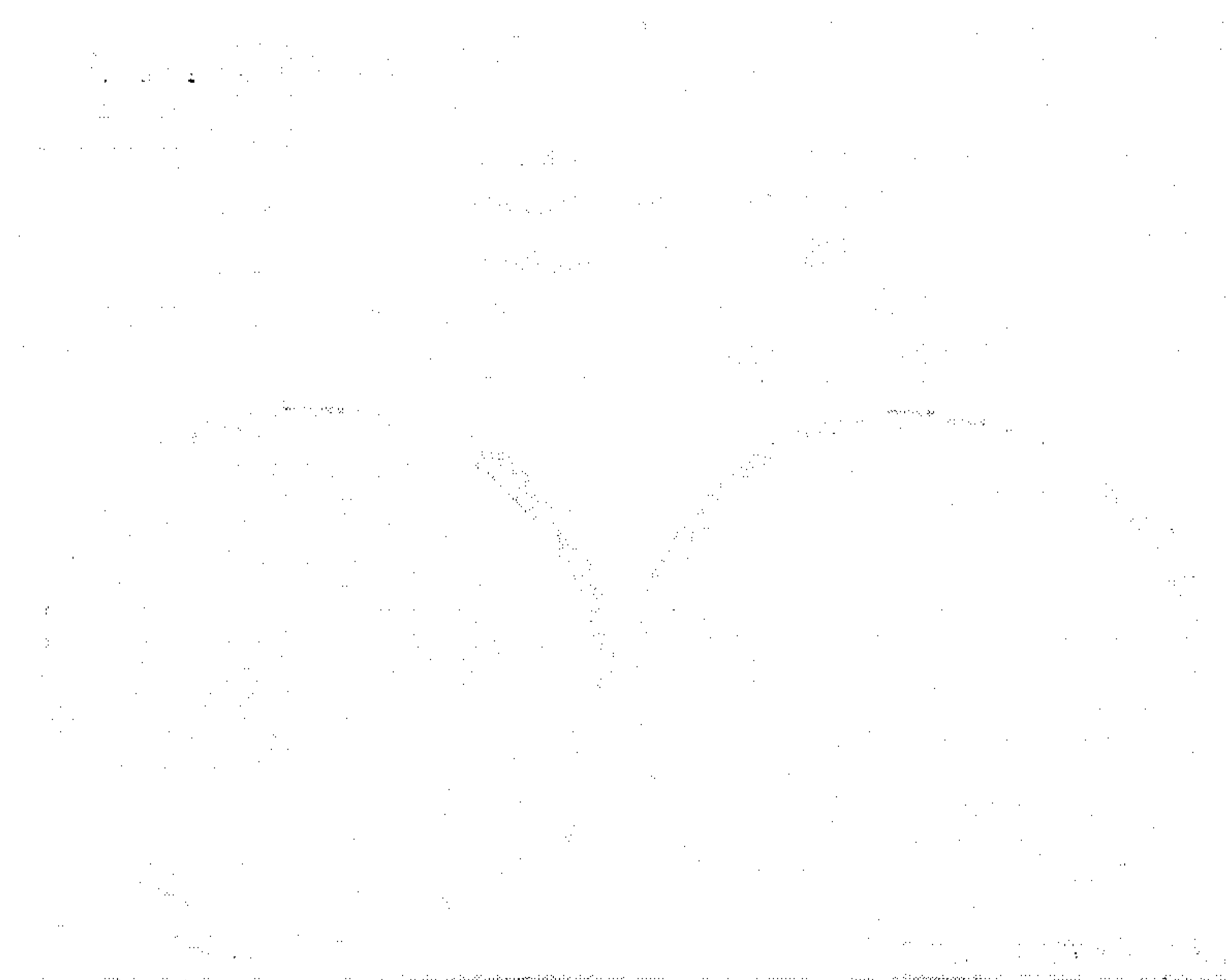


**Figure 5-3: Visible changes to chain components from wear simulation.**

### 5.3 *Pendulum Method*

The principle of operation in this experiment was to use actual cycle chain components under conditions approaching those found in practice. A pendulum was suspended by a chain link that acts as the pivot and the decay in amplitude of the swing was measured. Data can be analysed not only to produce values for  $\mu$  but also to distinguish a particular type of friction action.

Figure 5-4 shows the general arrangement of apparatus with a chain link firmly attached to a frame, allowing a second link of chain to hang vertically and freely. A load was imposed on the chain by means of masses hung from the bottom of a connecting rod attached to the second link. The masses introduce a tension in the chain thereby loading the pin-bush interface under investigation and also providing inertia permitting the pendulum motion to be achieved. The amplitude of free motion was measured by an LVDT, the signal of which was observed on an oscilloscope and recorded by a computer with a data acquisition system.

The decay of the pendulum motion over time reveals the type of friction dominating the bearing surfaces. With an exponential decay (Figure 5-6), the friction is said to be viscous suggesting the presence of a lubricating action. When the bearing surfaces are dry and devoid of lubrication the motion decays linearly (Figure 5-7) and the friction type is said to be dry or Coulombic<sup>(82)</sup>.

Figure 5-4: Pendulum test apparatus

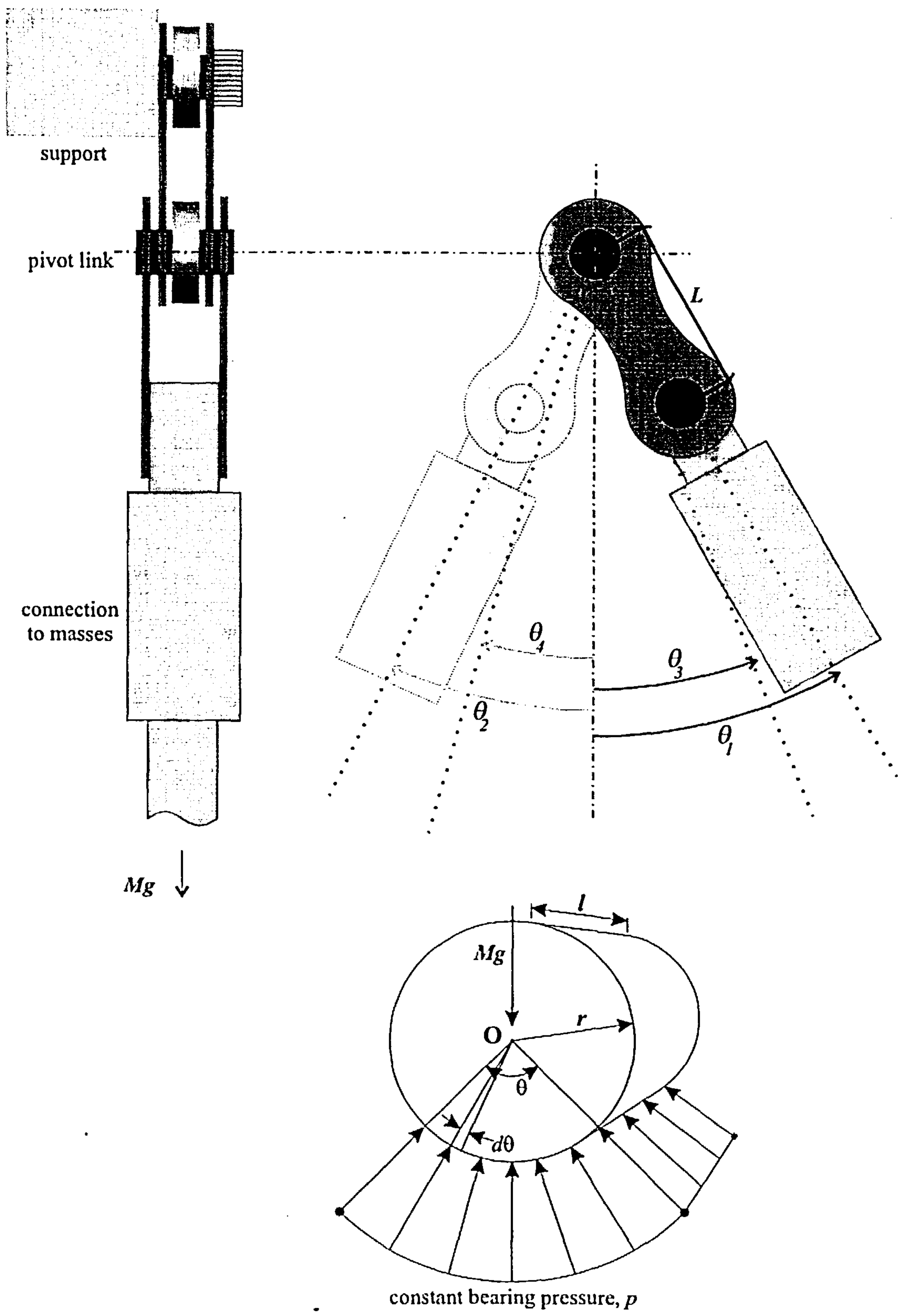
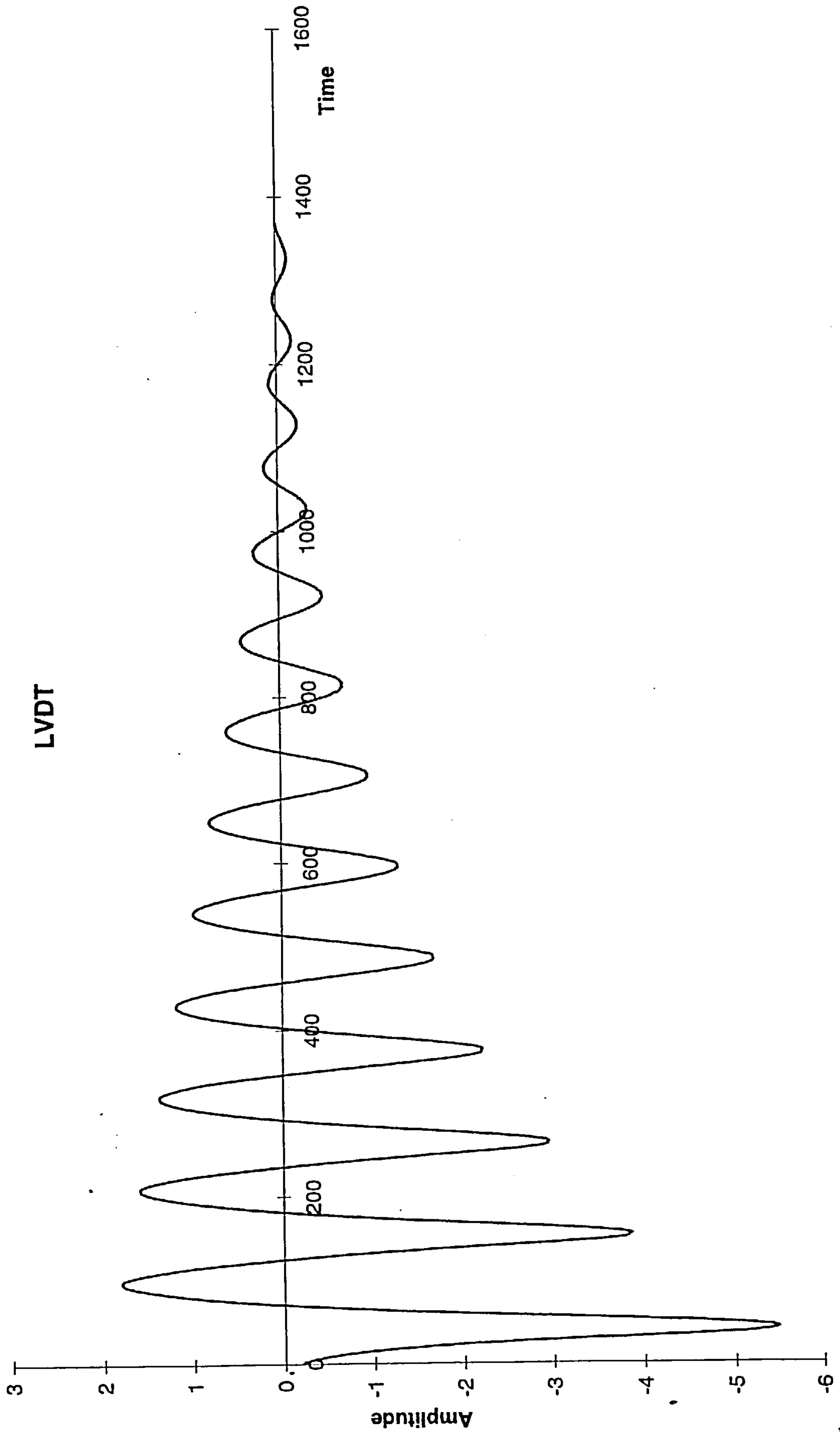


Figure 5-5: Example waveform



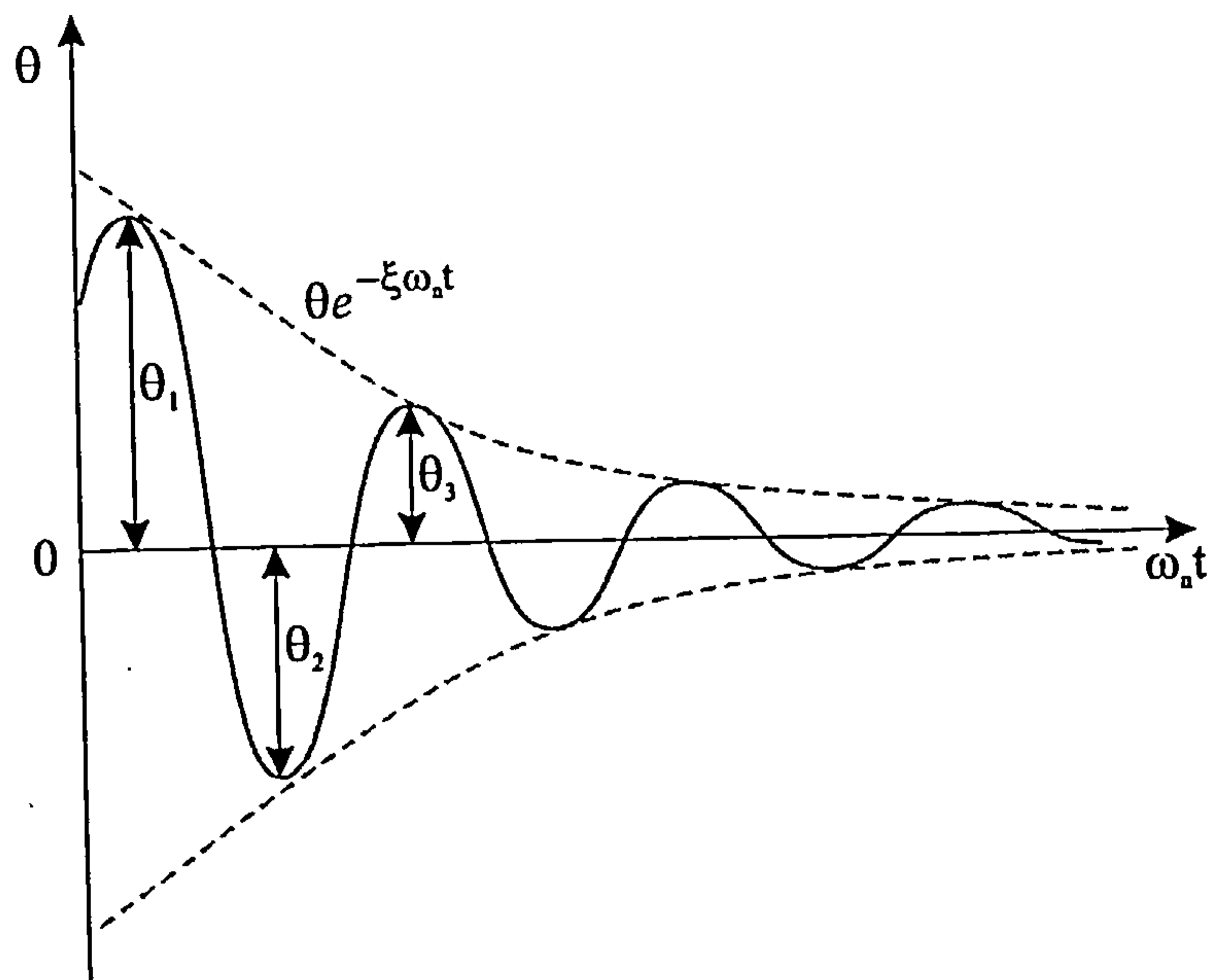


Figure 5-6: Exponential decay, viscous damping,  $\xi < 1.0$  (underdamped)

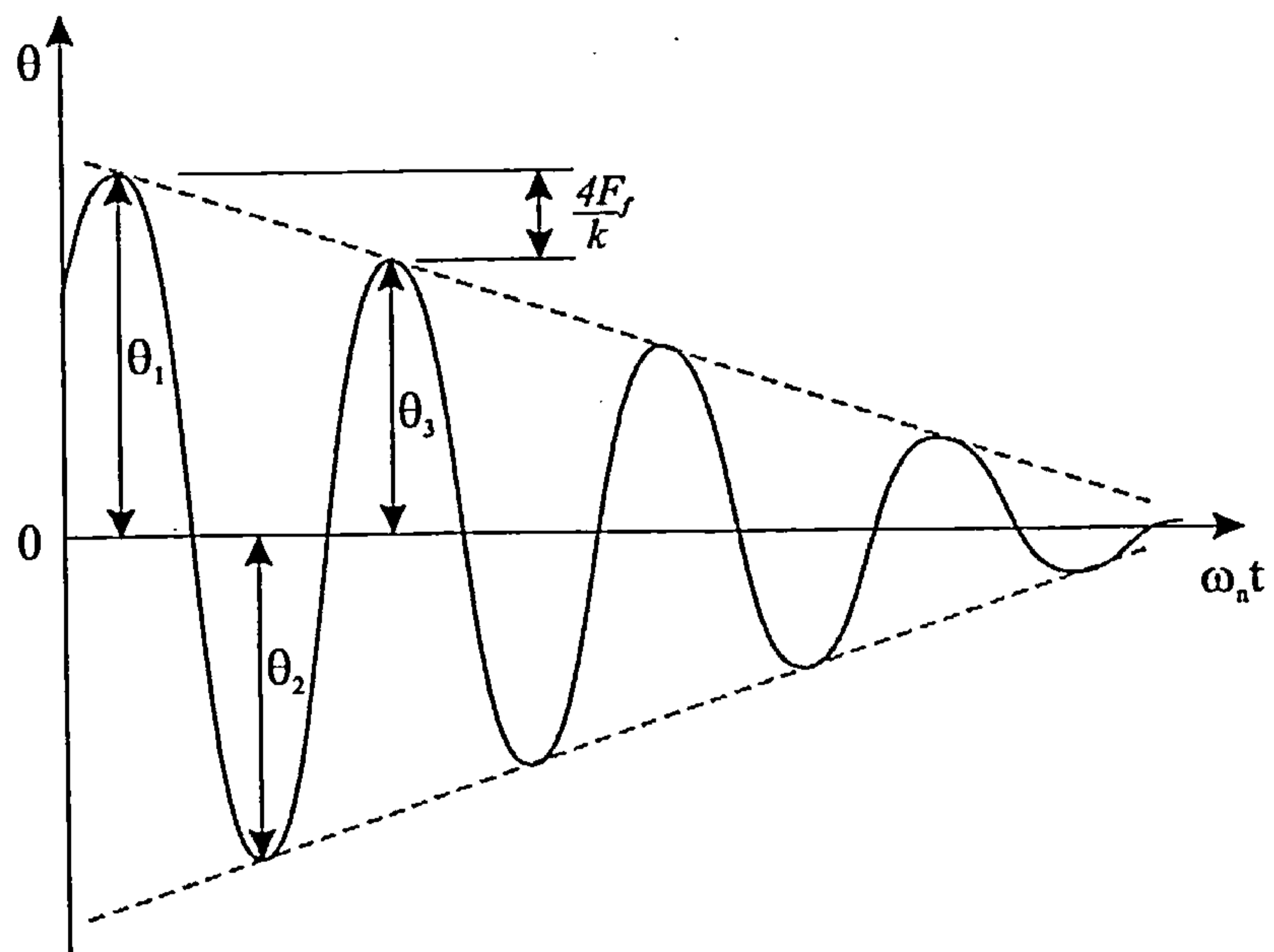


Figure 5-7: Linear decay, Coulombic damping

### 5.3.1 Estimation of $\mu$ from Pendulum Tests

Using the rig shown in Figure 5-1, a series of simple free-motion tests was conducted from which the coefficient of friction,  $\mu$ , was estimated from analysis of the LVDT signals. The pendulum was moved to a predetermined position, located by observing the position of the LVDT rod relative to the core. The LVDT rod was attached to the pendulum hanger ~35mm below the pin bearing being examined. The drag from the LVDT was measured to be  $100 \times 10^{-6}$  Nm from measurements made from an electronic balance. The LVDT signal was amplified and then either observed by an oscilloscope or recorded by a PC and data acquisition system. An example plot is shown in Figure 5-2. Values of the amplitudes of the positive peaks ( $\theta_1$ ,  $\theta_3$  etc.) were calculated and recorded. For the first 3 pairs of successive peaks e.g.  $\theta_1$  &  $\theta_3$ ,  $\theta_3$  &  $\theta_5$ ,  $\theta_5$  &  $\theta_7$  a value for the coefficient of friction was calculated. To facilitate interpretation of the results and values of  $\mu$  obtained, the tests were conducted under the following conditions:

- (i) two loads were used, 22 and 44N.
- (ii) two conditions of chain, new with no wear and an old sample with wear (~3% by length) and surface rust.
- (iii) two lubrication states, dry (with squeaking action during operation) or lubricated with an aerosol chain lubricant (*PJ-1*<sup>TM</sup>).
- (iv) with and without angular displacement ( $4^\circ$ ) from normal operation, simulating the misalignments found in derailleur gear combinations.

Use of the above parameters enabled  $\mu$  to be estimated for extreme operating conditions i.e. new/lubricated, old/dry and with or without misalignment. Half of the possible  $2^4$  combinations of variable were examined, the eight experiments being

summarised in Table 5-1. Both (new and worn) samples were cleaned chemically beforehand to ensure no contamination. The addition of lubricant to the link was done on the rig and around 0.5ml was supplied. A few minutes pause allowed the lubricant to penetrate to a good degree and the volatile ingredients to evaporate off; this was in accordance with the manufacturer's guidelines.

### 5.3.2 Analysis of results

The decaying LVDT signals were analysed using 3 separate approaches; in each case an expression for the quantity given in Table 5-1 was obtained enabling a value for  $\mu$  to be calculated. Three separate approaches have been used to determine an expression for the coefficient of friction in terms of pendulum angular displacements. This expression was then used to analyse the decaying sinusoidal LVDT signals.

#### 5.3.2.1 Energy Technique

Referring to Figure 5-1, it can be seen that the potential energy lost over one cycle, is given by:

$$\text{Potential Energy} = MgL(\cos\theta_3 - \cos\theta_1)$$

Which must equal the friction work done, from a work-energy principle. To determine the friction work component a pin bearing pressure is required. As the pin diameter so closely matches the inner bush diameter a constant bearing pressure,  $p$ , may be assumed to act over  $90^\circ$  for a length,  $l$ . Figure 5-4 illustrates how the forces act so that:

$$\int_0^{\frac{\pi}{2}} p(r d\theta) \sin\theta = Mg \quad \text{Eq. 5-1}$$

which simplifies to:

$$p = \frac{Mg}{lr} \quad \text{Eq. 5-2}$$

The frictional torque,  $T_f$  takes a similar form:

$$\int_0^{\pi} p(r d\theta) \mu r = T_f \quad \text{Eq. 5-3}$$

which can be reduced to

$$T_f = \frac{\pi}{2} \mu r M g \quad \text{Eq. 5-4}$$

using Eq. 5-2. For work done, Eq. 5-4 must be multiplied by the angular displacement of  $\theta_1 + \theta_2 + \theta_2 + \theta_3$  in one complete cycle of the pendulum. With small damping  $\theta_2 \approx \theta_3 + \frac{1}{2} (\theta_1 - \theta_3)$  so that:

$$\text{FrictionWork} = \pi \mu r M g (\theta_1 + \theta_3) \quad \text{Eq. 5-5}$$

Equating the potential energy loss to the frictional work yields an expression for a term common to all the determination methods, for the coefficient of friction:

$$\mu \left( \frac{\pi r}{L} \right) = \frac{\cos \theta_3 - \cos \theta_1}{\theta_1 + \theta_3} \quad \text{Eq. 5-6}$$

### 5.3.2.2 Viscous Technique

Considering the pendulum as a simple one-degree of freedom rotating system with viscous damping, as illustrated in Figure 5-4, the basic equation of motion applies:

$$I_0 \ddot{\theta} + c \dot{\theta} + MgL\theta = 0 \quad \text{Eq. 5-7}$$

which is a form of the more common homogeneous equation of motion<sup>(82)</sup>:

$$m\ddot{x} + c\dot{x} + kx = 0 \quad \text{Eq. 5-8}$$

The viscous technique includes the friction work done in the damping term,

$$c\dot{\theta} = \int c\dot{\theta}d\theta = \int_0^T c\dot{\theta}^2 dt \quad \text{Eq. 5-9}$$

where  $T$  is the period between oscillations and:

$$d\theta = \frac{d\theta}{dt} dt = \dot{\theta} dt \quad \text{Eq. 5-10}$$

then uses a similar energy approach as in 5.3.2.1. For a system with no damping the amplitude,  $A$  would remain constant and

$$WorkDone / cycle = \pi c A^2 \omega_n \quad \text{Eq. 5-11}$$

For a system with a small damping coefficient,  $A$  can be approximated to  $\frac{1}{2}(\theta_1 + \theta_3)$  so:

$$WorkDone / cycle = \frac{\pi}{4} c \omega_n (\theta_1 + \theta_3)^2 \quad \text{Eq. 5-12}$$

The log decrement of a free vibration is the natural logarithm of the ratio of any two successive amplitudes. It is derived from the following:

$$\frac{\theta_1}{\theta_{n+2}} = \left( \frac{\theta_1}{\theta_3} \right) \left( \frac{\theta_3}{\theta_5} \right) \left( \frac{\theta_5}{\theta_7} \right) \dots \left( \frac{\theta_{n-2}}{\theta_n} \right) = (e^\delta)^n = e^{n\delta} \quad \text{Eq. 5-13}$$

then, 
$$\delta = \ln\left(\frac{\theta_1}{\theta_3}\right) \quad \text{Eq. 5-14}$$

From Thomson<sup>(82)</sup>, when the damping ratio  $\xi$  is small the following approximation can be made:

$$\delta \cong 2\pi\xi \quad \text{Eq. 5-15}$$

where the damping ratio is defined as:

$$\xi = \frac{c}{c_c} \quad \text{Eq. 5-16}$$

From Eq. 5-8 and Eq. 5-9:  $c_c = 2I_0\omega_n$  Eq. 5-17

which yields a damping coefficient term,

$$c = \frac{\omega_n I_0}{\pi} \ln\left(\frac{\theta_1}{\theta_3}\right) \quad \text{Eq. 5-18}$$

So now the work done per cycle becomes,

$$\text{WorkDone / cycle} = \frac{1}{4} \omega_n^2 I_0 \ln\left(\frac{\theta_1}{\theta_3}\right) (\theta_1 + \theta_3)^2 \quad \text{Eq. 5-19}$$

Equating the work done with the friction work the common term can be derived as:

$$\mu\left(\frac{\pi r}{L}\right) = \frac{1}{4} \ln\frac{\theta_1}{\theta_3} (\theta_1 + \theta_3) \quad \text{Eq. 5-20}$$

### 5.3.2.3 Coulomb Technique

Coulombic damping of a system occurs when two dry surfaces are sliding relative to each other. The damping force is the product of  $\mu$  and the normal force. Using the same argument 5.3.2.1, the friction torque is taken to be  $T_f$  and changes sign each  $\frac{1}{2}$

cycle of motion. The pendulum amplitude decays linearly with time and analysis is given by<sup>(82)</sup>:

$$\theta_1 - \theta_3 = 4 \frac{FrictionForce}{k} \tag{Eq. 5-21}$$

Where  $k$  is derived from Eq.5-7 and Eq. 5-8, therefore:

$$\theta_1 - \theta_3 = 2\pi\mu \frac{r}{L} \tag{Eq. 5-22}$$

per cycle. Simple manipulation leads to the following term allowing a comparison with the previous two approaches,

$$\mu \left( \frac{\pi r}{L} \right) = \frac{1}{2} (\theta_1 - \theta_3) \tag{Eq. 5-23}$$

Table 5-1 Summarises the expressions for the coefficient of friction term for the three approaches used and numerical checks showed that all 3 were in good agreement for evaluating  $\mu$  for a typical set of low-damped LVDT signals. For example, with  $\theta_1 = 18^\circ$  and  $\theta_2 = 16^\circ$  (i.e. an amplitude decay of  $2^\circ$ /cycle) the expressions agree to within 2%.

Determination method	$\mu \left( \frac{\pi r}{L} \right)$
Energy	$\frac{\cos \theta_3 - \cos \theta_1}{\theta_1 + \theta_3}$
Viscous	$\frac{1}{4} \ln \frac{\theta_1}{\theta_3} (\theta_1 + \theta_3)$
Coulomb	$\frac{1}{2} (\theta_1 - \theta_3)$

Table 5-1: Derivation of friction coefficient term

5.3.3 Results

Table 5-2 shows a summary of successive results from the pendulum tests where the values of  $\mu$  are based on the Energy method (from Table 5-1). All three mean values for  $\mu$  are shown, calculated from three successive periods of decay.

					Coefficient of Friction Range			
Experiment	Wear	Load	Lube	Angle	(1-3)	(3-5)	(5-7)	mean
1	0	22N	yes	0	0.0036	0.0035	0.0036	0.0036
2	0	44N	yes	0	0.0019	0.0010	0.0010	0.0013
3	0	22N	no	0	0.0034	0.0034	0.0036	0.0035
4	0	22N	yes	4°	0.0095	0.0105	0.0086	0.0095
5	0	44N	no	0	0.0051	0.0051	0.0048	0.0050
6	3%	22N	no	0	0.0155	0.0155	0.0149	0.0153
7	3%	22N	no	4°	0.0095	0.0105	0.0086	0.0095
8	3%	44N	no	0	0.0162	0.0162	0.0147	0.0157

Table 5-2: Pendulum friction test results

The values of  $\mu$  differed by more than an order of magnitude and reflect the significance of the physical state of the chain and the presence of a lubricant. These two factors, representing extreme conditions of operation, were considered fairly typical of those that might be encountered in cycle chains. Since chains, both old and new, tend to have close-fitting pins the action of the pendulum pivot could be reasonably taken as rolling with little or no sliding action being present. The action of the aerosol lubricant applied to the pivot was such as to provide a state somewhere between boundary and mixed lubrication at the bearing surfaces; the penetration of the lubricant could not be determined easily.

The results indicate the trend of lower coefficients found with newer and lubricated chains. With dry, rusted or misaligned bearing surfaces the friction was higher. Strictly,  $\mu$  should be approximately constant irrespective of weight. With this test, the maximum weight was governed by the rig itself with the link supported only on one side. Had both sides of the link been attached, a bigger load could have been

used with no likely bending effects however this would require a more extensive test rig. The influence of misalignment was limited to two cases that revealed contradictory findings. In experiment 4 the coefficient of friction was around 3 times higher than its equivalent case (1). However when the chain was worn and dry (7) the change in operation angle reduced the coefficient by around 0.005 in comparison with experiment 6.

## 5.4 Pin on Plate method

This approach to determining the coefficient of friction between two surfaces is of more general applicability and test equipment is readily available. The principle of operation is to apply a known load and measure the reaction force, in this case the lateral force generated from the contact between two samples sliding relative to each other. The apparatus (Figure 5-8) permits several permutations of experiment including pin-on-disk and pin-on-plate. The closest situation to the pin and bush bearing in a chain is the pin-on-plate mode. Pin samples were placed at some distance along a pivoting loading arm with the load being applied by masses hung from the free end of the lever. The load created between the pin and plate sample is variable to suit the desired operating conditions. On a reciprocating carriage, the plate sample was clamped such that the magnitude of oscillation will ensure that the pin will remain loaded on it throughout the limits of reciprocation. The lateral force experienced by the arm was measured by a load cell transducer situated at the end of the load arm. The load cell can be interchanged with others of higher ratings to widen the operating range of loads. Knowing the normal force,  $N$ , imposed by the masses and load arm arrangement, the reaction force  $F$  allows  $\mu$  to be calculated simply by:

$$\mu = \frac{F}{N} \quad \text{Eq. 5-24}$$

Although Amonton's Law of friction states that  $\mu$  is independent of apparent area of contact between the two bodies, the pressure between them should bear some relation to the operating environment because of the unknown lubricant performance.

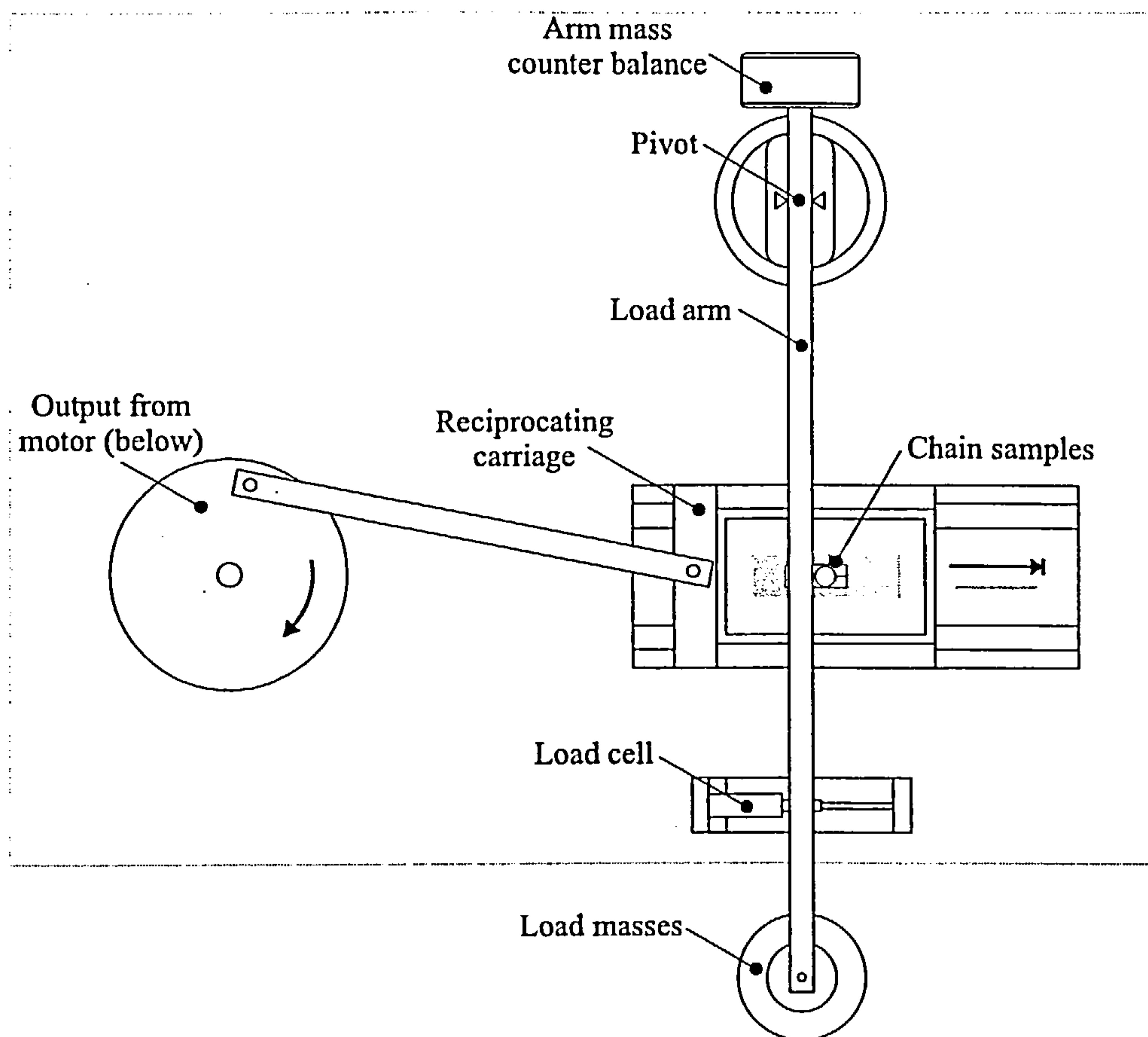


**Figure 5-8: Universal Wear Machine Apparatus**

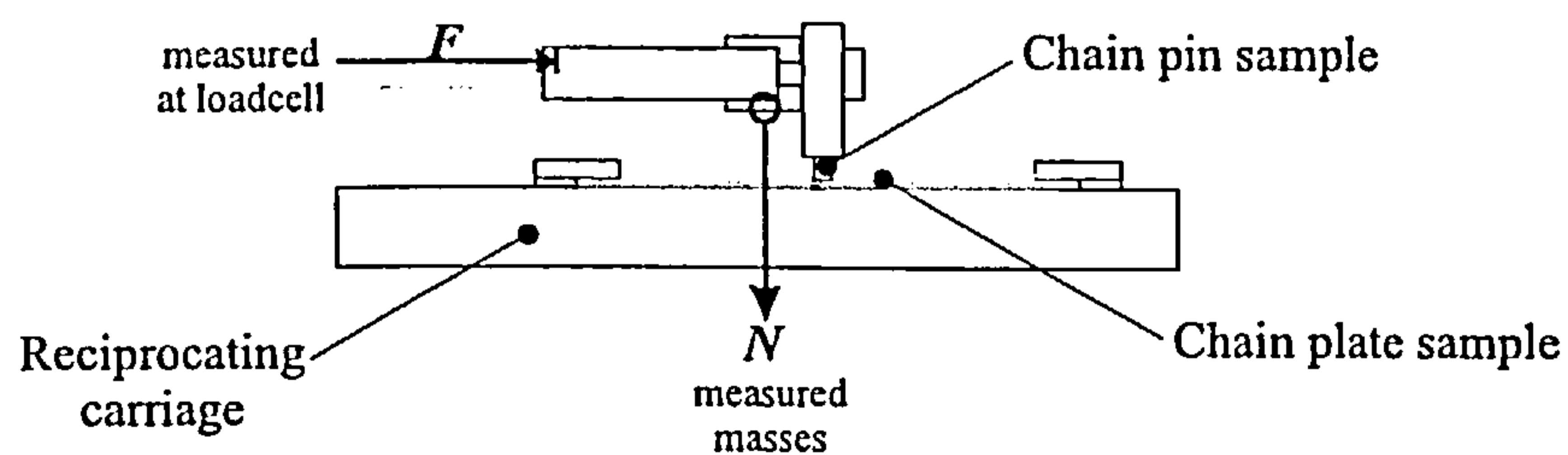


**Figure 5-9: Pin-Plate interface and forces**

The coefficient of friction can be monitored for some time and observations can be made to give an estimate of longevity. In this work tests were normally completed over a 180-minute period. The types of lubricant tested are given in Table 5-3:

Substance	Constituents
Water	H <sub>2</sub> O
Lubricant A ( <i>Triflow<sup>TM</sup></i> )	Paraffin oil, mineral spirits, corrosion inhibitor, anti-wear additives, degreaser and PTFE
Lubricant B ( <i>Finish Line X-Country lube<sup>TM</sup></i> )	Polyalphaolefin oil, IRGA lube, polybutene and BHT.
Lubricant C ( <i>Weldite<sup>TM</sup></i> multi-purpose)	Not disclosed
Lubricant D ( <i>Scottoiler<sup>TM</sup> SACI a.k.a. Rockoil 9440<sup>TM</sup></i> )	Mineral oil, anionic surfactant, corrosion inhibitor and alkanolamine/fatty acid/boric acid product.

Table 5-3: Biceri test lubricants

Of particular interest are the results of the initial tests with no lubricant, then with water added. The question of whether a non-hydrocarbon based substance such as water can provide sufficient lubricant qualities is raised by a new form of lubricant device for bicycles. If water alone cannot perform adequately, then tests can be made to evaluate its performance with a range of additives. For the mixed lubrication regime, typical substances to form an additive (extreme pressure or anti-wear) include: saturated and unsaturated fatty acids; natural and synthetic fatty acid esters; primary and secondary alcohols.

#### 5.4.1 Biceri UWM tests

The plate was a sample of link material used in the manufacture of higher quality chains. The plate originated as normal mild steel but had undergone heat treatment and burnishing. The properties of the material as received represented those found in the final chain product; of particular interest is its hardness, measured to be 503HV. Actual chain link pins were used, again supplied by a chain manufacturer. The samples were taken just before final assembly when the ends of the pins are swaged into the side plates. Because of the operation of the apparatus, the end face of the pin should be as featureless as possible as it is this surface that comes into contact with the plate. The pin hardness was measured as 576HV.

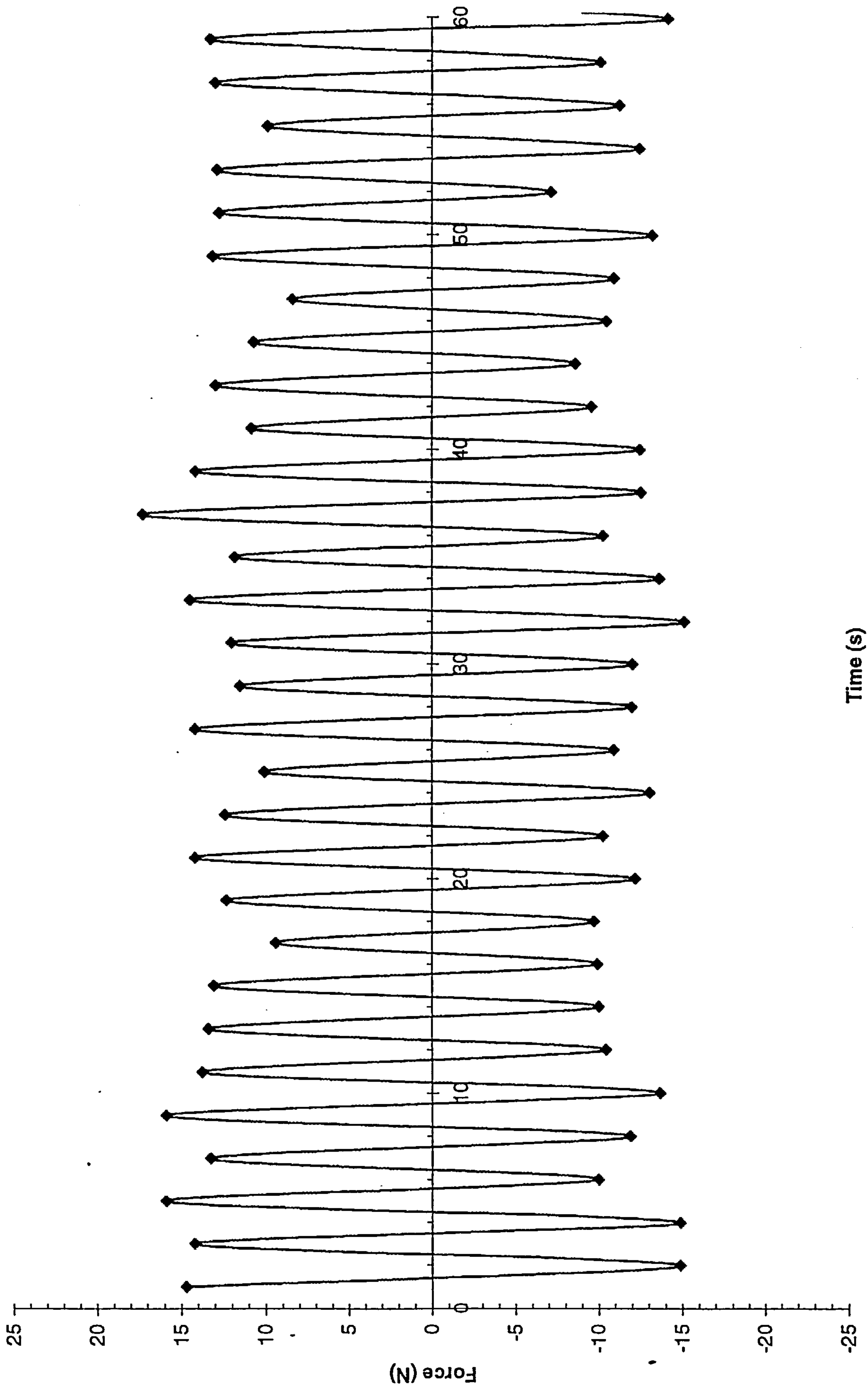
Figure 5-9 shows how the pin and plate come into contact and how a balance lever loads the pin. The load placed at the end of the lever was 5kg for dry and water tests, rising to 10kg for the oil based lubricants; this was to allow a better resolution of comparison between the similarly performing oil lubricants. Because of the limits of the force transducer (120N maximum), the loads for tests involving water were lower as the coefficient of friction is higher. The positioning of the pin with respect to the pivot results in a load of 100 to 200N on to the plate. With the pin diameter of 3.6mm, this results in a bearing pressure of 11 to 22Nmm<sup>-2</sup>. A chain in operation with 300-900N tension would experience magnitudes of pressure not much greater than this, though the actual figure may depend on the model chosen to calculate the stress. Considering a 90° contact area for the pin-bush interface (as in 5.3.2.1) a basic  $P=F/A$  relationship gives 30-100Nmm<sup>-2</sup>. Hertzian<sup>(79)</sup> stresses are of course higher, at around 200~300Nmm<sup>-2</sup>. Each test began with a new pin and a fresh area of plate; this state of materials is representative of a break-in condition where the surfaces are coming

together for the first time. This will allow any initial asperity deformation and destruction to occur. Further changes in  $\mu$  may arise from the wear debris and depending on the type of wear particle produced it, may increase or decrease. A fan positioned close to the plate was used to maintain a rapid rate of evaporation.

## **5.5 Results**

The output of the transducer was calibrated before each batch of tests. A known lateral force was applied to the arm and this reading, combined with the unloaded condition, provided enough information to calibrate the load cell and data acquisition system. The frequency of the data reading was altered depending on the duration of the test. For a short test run of 2 minutes, data was acquired at 50 or 100Hz but, for the longer tests of 60 to 120 minutes, the frequency would be 2 or 5Hz. The higher resolution scan rate was used for the shorter duration tests because of the possibility that there might be rapid changes in  $\mu$ . The reciprocating movement of the plate causes the friction force also to oscillate; a sample plot is given in Figure 5-10. To calculate  $\mu$ , the average absolute force was used, ignoring the sign. The brief time that the system was not moving, at the limits of travel, were sufficiently short not to affect the average constant friction value.

Figure 5-10: Force variation with time at the load cell for pin-on-plate tests

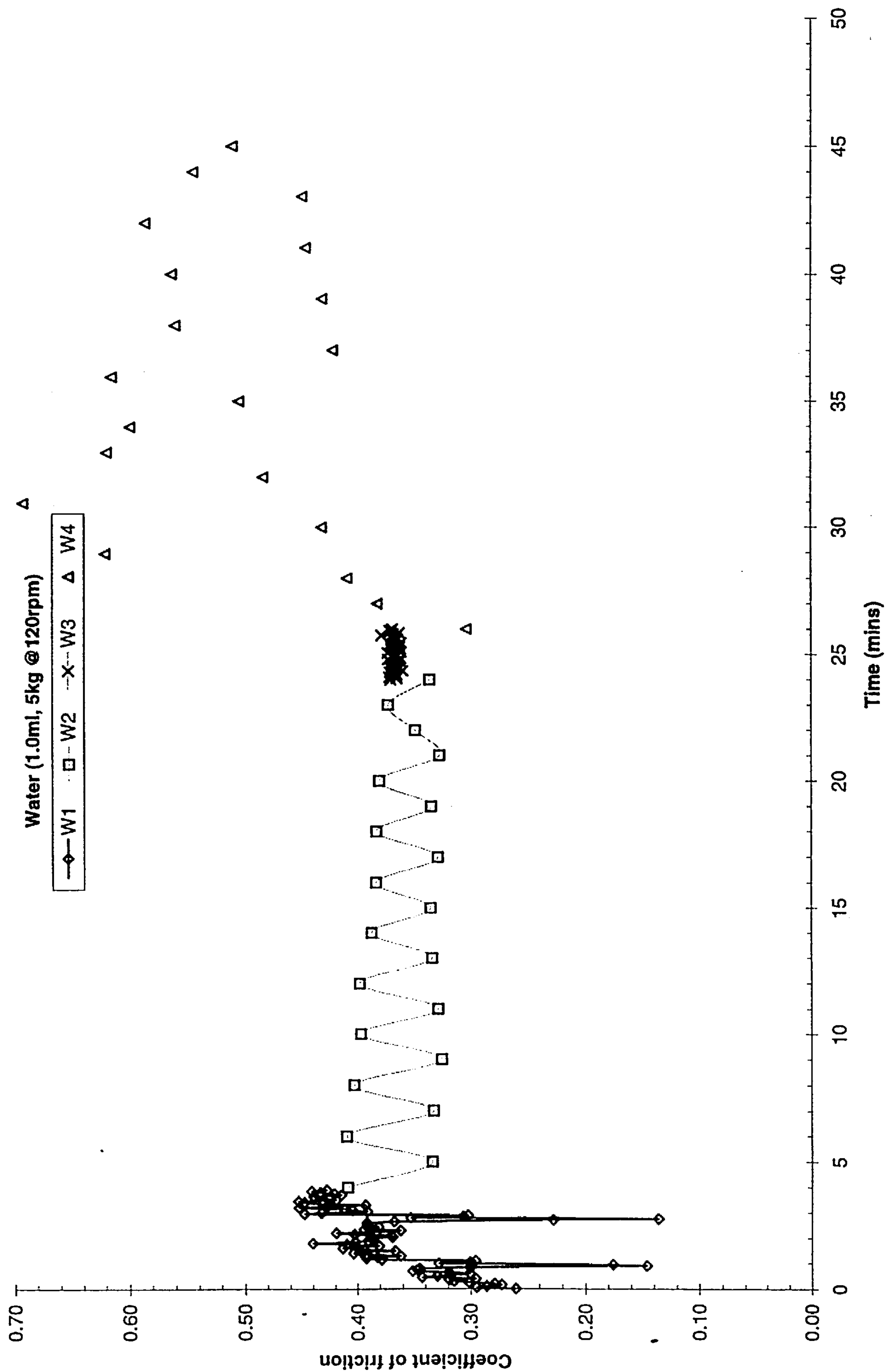


### 5.5.1 Water

The first liquid to be used as a lubricant was water. This is not an obvious choice given the spectrum of lubricants available, but was chosen to observe how it performed in comparison to a dry system and one with an appropriate or recognised lubricant. There is a suggestion from a lubricant delivery device manufacturer that water can, in some instances, perform adequately as a chain lubricant. Its performance can be enhanced by the addition of a water-soluble lubricant or surfactant based substance; the results of this combination are given in section 5.5.5.

Figure 5-11 shows how  $\mu$  varied over time with a load of 100N, with the plate reciprocating at 120 strokes per minute and an initial volume of water of 1.0ml. From an initial value of 0.30,  $\mu$  rose over the first 4 minutes (W1 in figure) to reach 0.40. Over the next 20 minutes, however, it fell slightly to around 0.36 (W2 region). The 2 minute period immediately following this (W3) used a much higher data acquisition rate and confirms the accuracy of the previous readings. For the next 20 minutes (W4) the value for  $\mu$  varied greatly, increasing to 0.70, then falling back to an average value of 0.50.

Figure 5-11: Coefficient of friction using Water as a lubricant



### 5.5.2 Lubricant A (*Triflow*)

As might be expected, this PTFE fortified aerosol lubricant provided better friction properties than water. Not only was  $\mu$  lower but it remained so with little deviation over time despite only 0.2ml being supplied. Figure 5-12 shows how  $\mu$  is maintained closely at an average value of 0.127. The duration of this test was 27mins, made up of 3 continuous sampling periods indicated by T1, T2 and T3 where the second period used a higher sampling rate.

### 5.5.3 Lubricant B (*FinishLine*)

Similar to A, this lubricant also has a PTFE additive and produces comparable results. Figure 5-13 illustrates a slight decreasing trend of  $\mu$  until 180 minutes when a small rise occurs. Overall, the average  $\mu$  was calculated to be 0.136.

### 5.5.4 Lubricant C (*Weldite*)

This lubricant represents a cheaper alternative with no PTFE additives and no claims of superior performance. The lubricant gave an average coefficient of friction of 0.140 over the 120 minute period. Although there was a slight decrease after 60 minutes,  $\mu$  then rose back to the average over the ensuing 30 minutes.

Figure 5-12: Coefficient of friction - Lubricant A

(0.2ml, 5kg @120rpm)

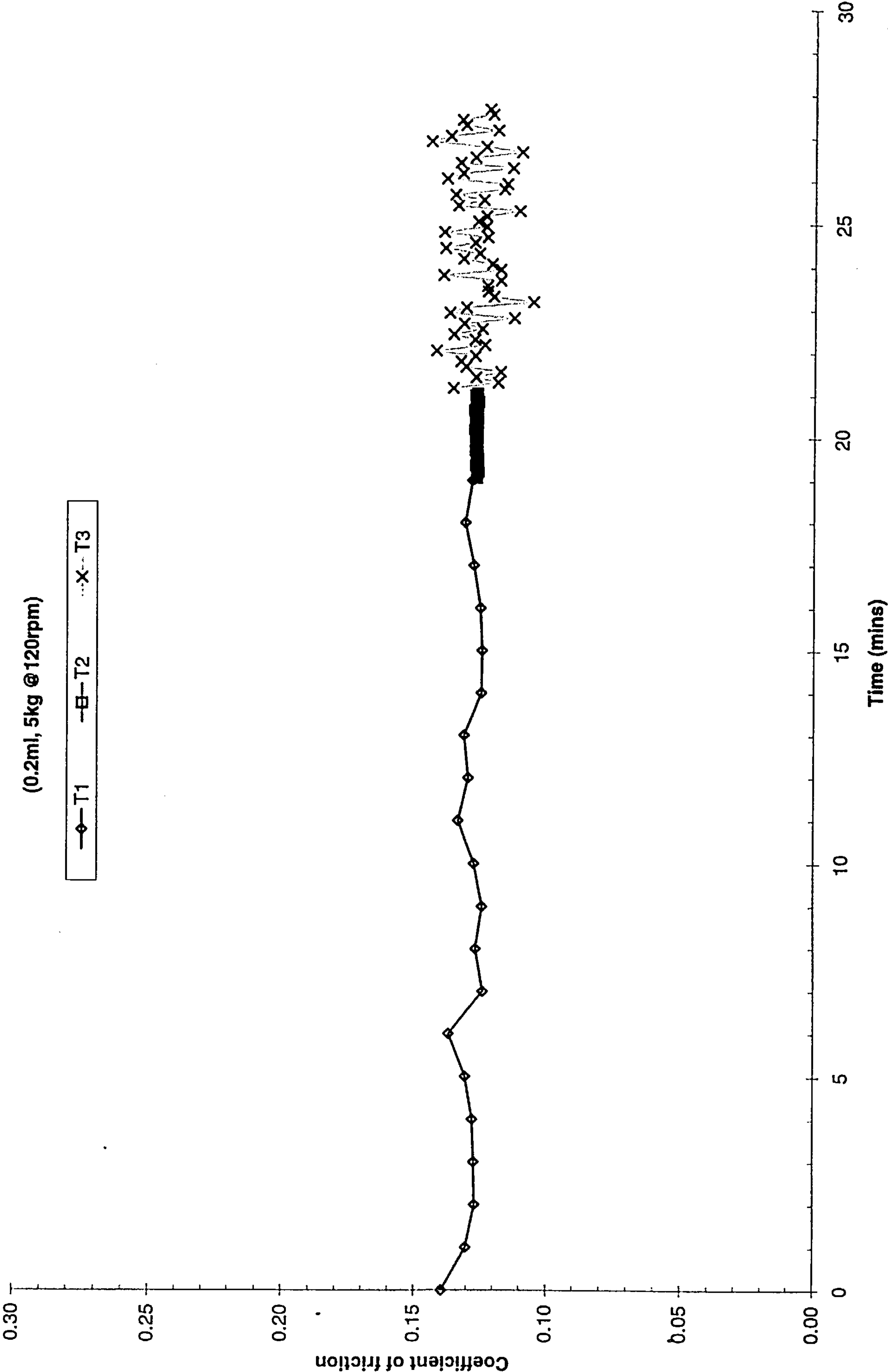


Figure 5-13: Coefficient of friction - Lubricant B

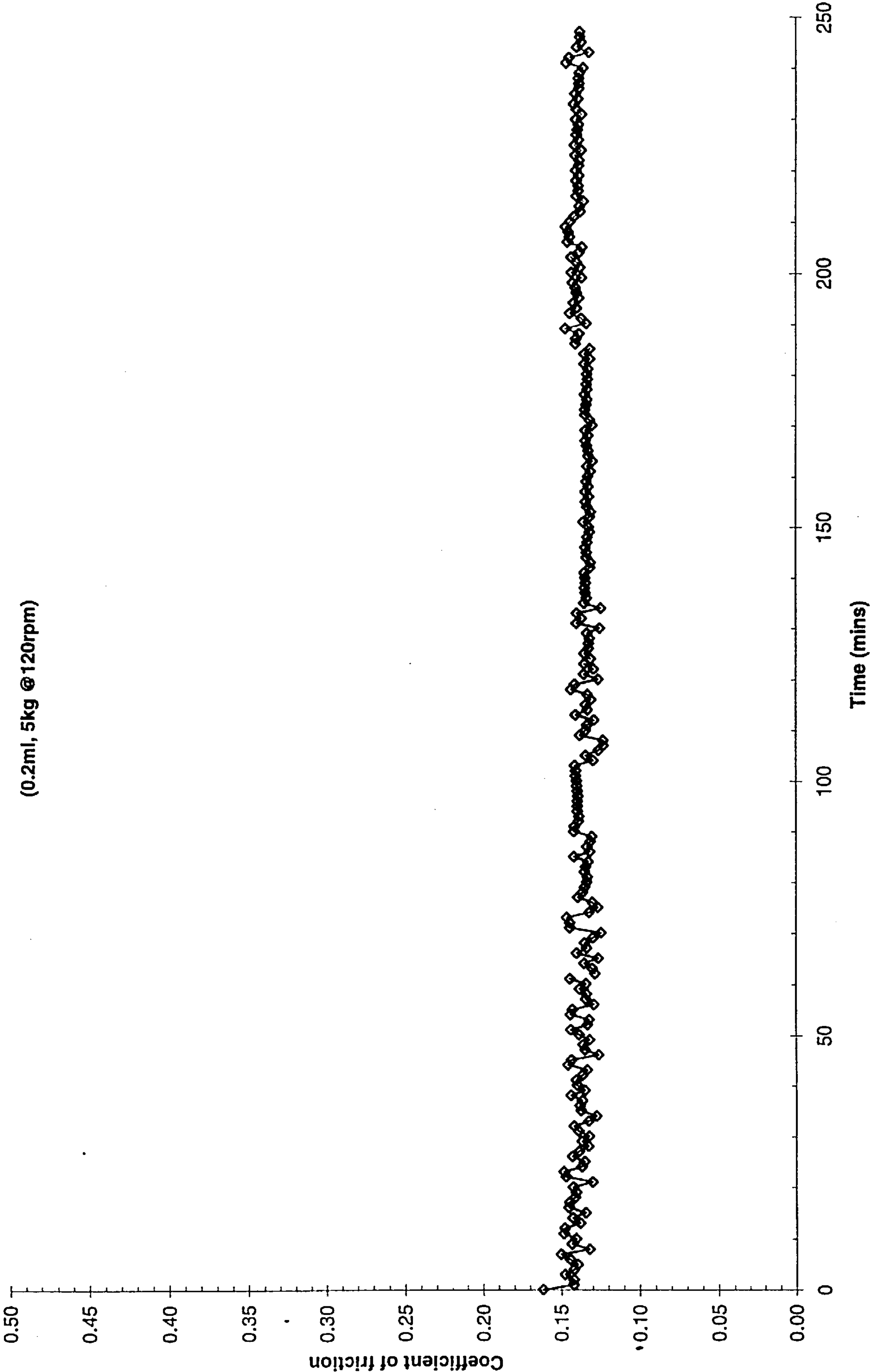
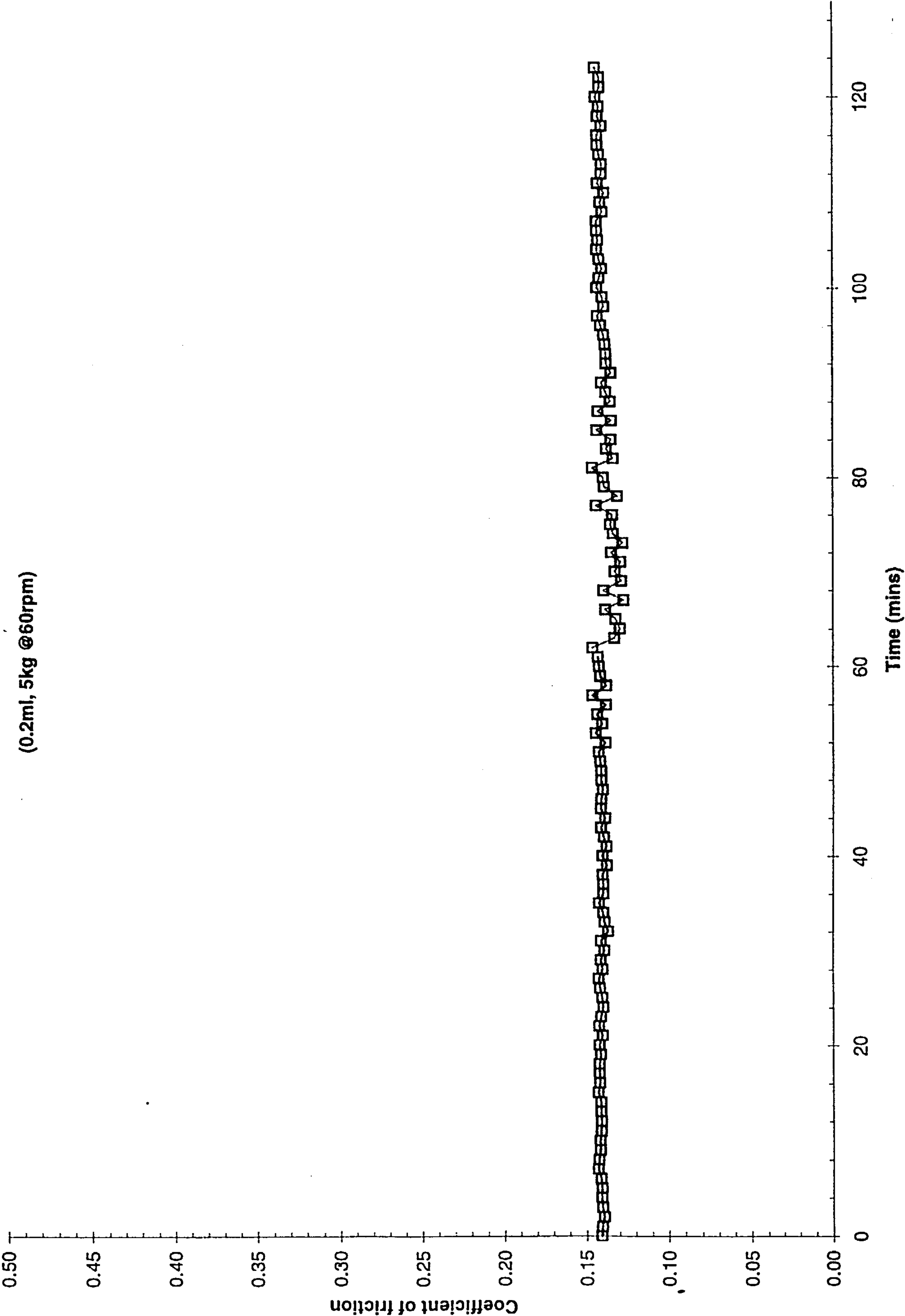


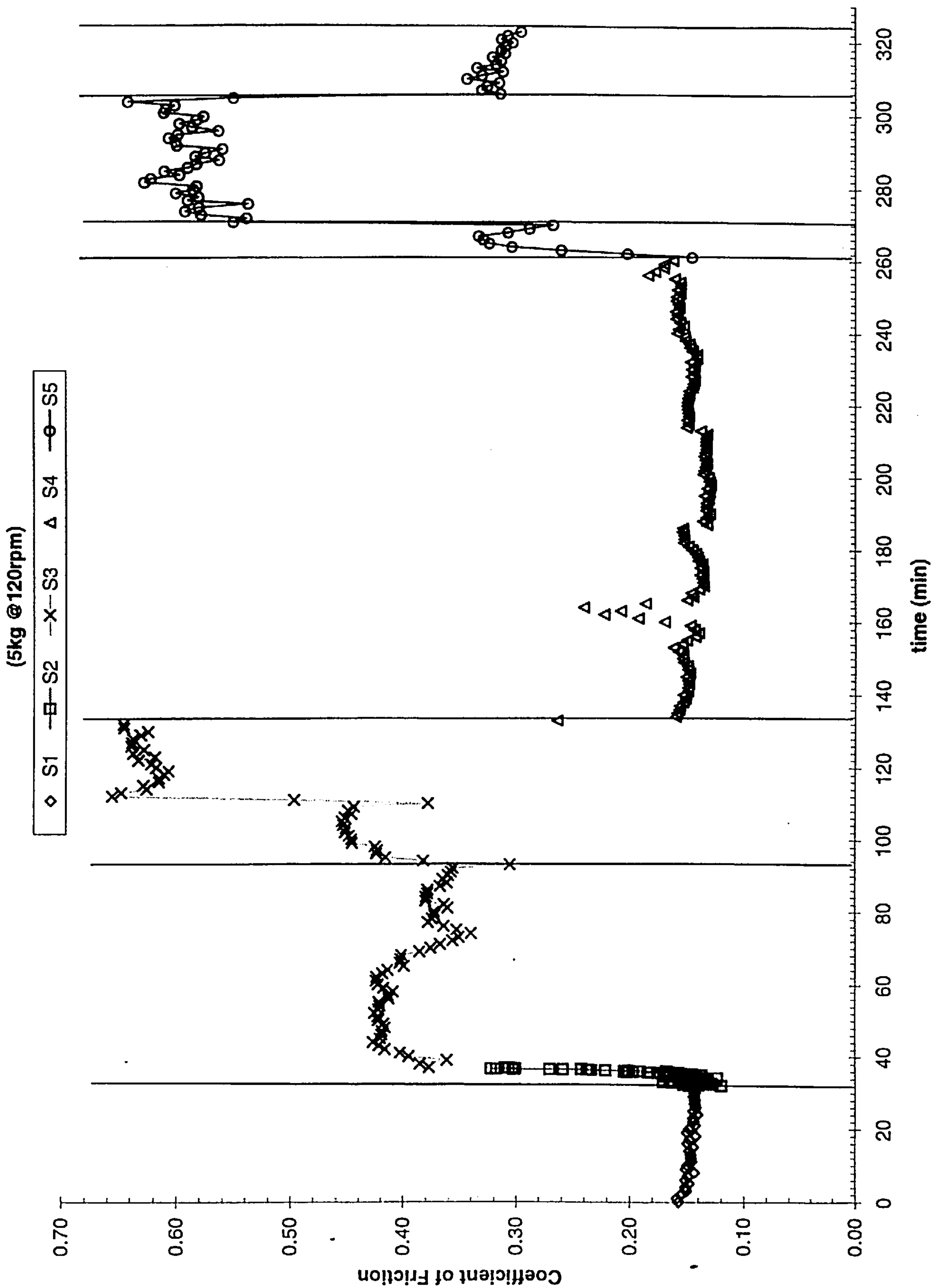
Figure 5-14: Coefficient of friction - Lubricant C  
(0.2ml, 5kg @60rpm)



#### 5.5.5 Lubricant D (Water and **SACI** combination)

At the start of this experiment 0.2ml of a 50% water and 50% SACI mixture was injected to the pin-plate interface (S1 in Figure 5-15). After 30 minutes water was added at a constant rate amounting to 15ml over the following 50 minutes (S2 and part of S3), increasing  $\mu$  to around 0.40. Excess water was then absorbed by paper towel and the plate dried, causing  $\mu$  to rise above 0.60 (remainder of S3) until another 0.2ml water/SACI combination was added at 130 minutes (S4). The mixture reduced friction to levels of those at the start and remained constant for that period (S5). 1.0ml of water was then at 260 minutes accumulated time, each time producing a change of  $\mu$  to 0.3 as shown in Figure 5-15. As the much-diluted mixture evaporated  $\mu$  rose rapidly to around 0.6, the surfaces having virtually no lubricant at all until 313 minutes when 0.2ml of water was added to the dry surface. This addition of water returned the coefficient of friction to a level close to those found with just water earlier (Section 5.5.1).

Figure 5-15: Coefficient of friction - Water/SACI combination



## 5.6 Summary

The major contribution to every loss in bicycle chain transmission arises from friction. As the chain travels around the components of the bicycle, friction occurs as surfaces roll or slide against each other. The location of the surfaces causing friction has been identified as those shown in Figure 5-1. A series of experiments determined the likely coefficients of friction at each of the occurrences of surface interaction. Observing the decay in the oscillations of a pendulum whose pivot was a chain link indicated the range of values of  $\mu$ . The difference between new, lubricated chain and worn, dry chain gave the bounds of what  $\mu$  could be in the rolling state, which was 0.001 to 0.016.

The examination of chain components under sliding conditions was done using a pin-on-plate apparatus. The data from this experiment gave higher values for  $\mu$  than in the rolling case. The performance of different lubricants was also considered, comparing no lubrication with substances such as water, surfactant soluble oil and PTFE fortified lubricants. The results showed low and stable long-term values for  $\mu$  with hydrocarbon lubricants designed for chain use. Water was shown to act as some form of lubricant, lowering  $\mu$  compared to the dry state and its performance was enhanced if it was used in conjunction with a soluble surfactant.

## 6. Lateral Force Analysis

### 6.1 *Introduction*

For a bicycle with derailleur gears, the chain alignment between front and rear sprockets can only be co-planar for as many gears as there are front sprockets. An eighteen speed bicycle will thus have a chain misaligned in 15 of the gears, equal to 89% of possible gear combinations. The effect of the misalignment leads to altered chain forces at the sprockets because of a lateral force, as was first examined in Chapter 4. The measurements presented here examine the lateral force directly from axial measurements taken by a load cell. The results confirm that, as the angle of misalignment,  $\phi$ , increases, so the lateral force also rises.

### 6.2 *Apparatus*

A rig was built to measure the lateral thrust on a shaft fitted with a six speed bicycle sprocket freewheel. The shaft was mounted in bearing blocks that allowed both free rotation of the sprocket and, using low friction linear bearings, lateral (axial) translation. Figure 6-1 and Figure 6-2 are a photograph and a schematic diagram, respectively, of the apparatus used.

A pulley wheel of equivalent diameter to a 35 toothed bicycle sprocket and into which the chain lies, was used to simulate the application of chain tension. The distance between front pulley and rear sprocket axes was 420mm, representative of the centre distances found on competition cycles. The pulley was mounted onto the rig base plate *via* two plain roller bearings housed to allow stepped lateral displacements,

thus presenting the chain at a variety of angles to the rear sprockets. Both pulley and sprocket axes were at the same height relative to the base plates and remained parallel.

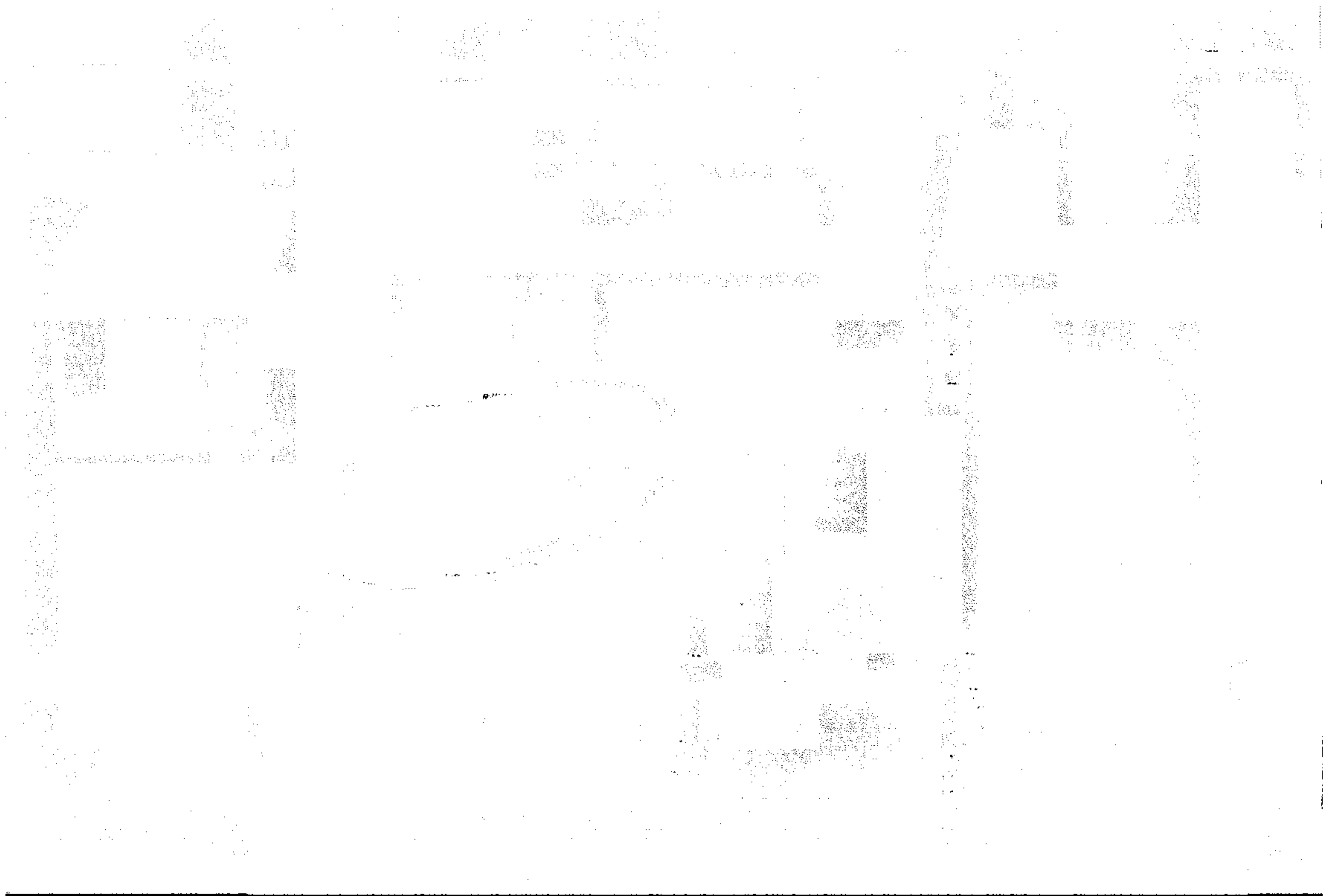


**Figure 6-1: Lateral Force photograph**

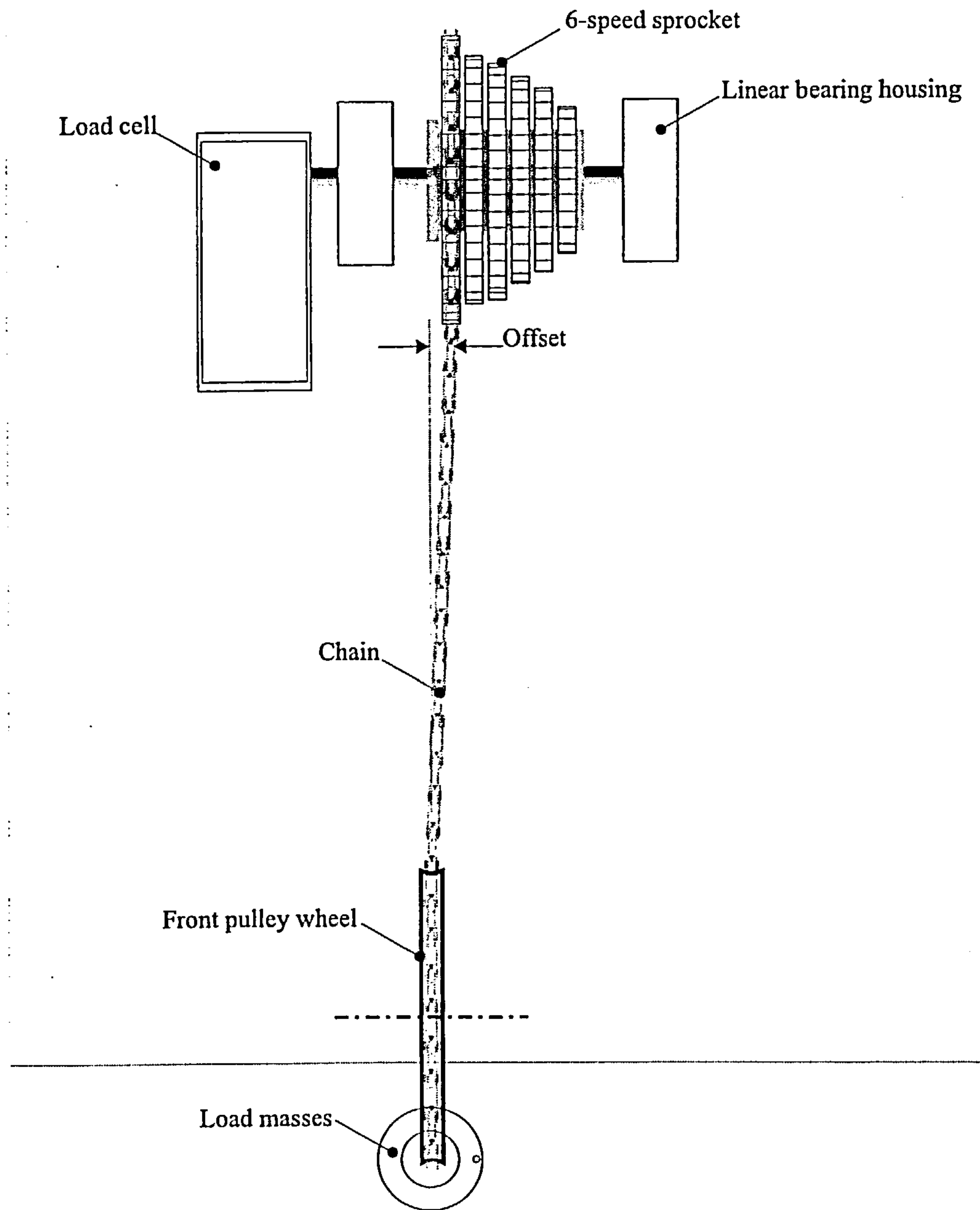


Figure 6-2: Lateral force rig (schematic)

The rear sprockets formed part of a *Shimano* freewheel with the sprocket sizes were 30, 25, 20, 17, 15 and 13 teeth. The freewheel was mounted into the axle using a threaded hub identical to those found on rear bicycle wheels, which allowed the freewheel to maintain as close to real bicycle operating characteristics as possible.

A static form of test was chosen so the chain was anchored to the base plate, just beyond the position of the front sprocket. The anchoring of the chain at some distance away from the rear sprockets allowed the angle of misalignment for the lower length of chain to affect the lateral force to a lesser degree than the top strand. The chain used for the experiment was a *SRAM* PC41, recently lubricated and previously unused, end of initial length 117 links. Masses were hung at the free end of chain, ranging from 2 to 14kg in 2kg steps, which equates to a chain reaction force at the sprocket of 20 to 140N in 20N steps. The lateral force is related to twice the chain tension, however, because the chain is under equal tension on the upper and lower halves of the sprocket.

A 2kg load cell (RS 632-736) was used to measure the lateral force. Before each test, the cell was calibrated using known masses, the load cell readings being taken manually from the power supply and display unit of the load cell system.

### 6.3 Theory

Chapter 4 introduced the concept of a lateral force component of the chain when it was engaged on a sprocket at an angle of misalignment. With a chain tension,  $T$ , and misalignment angle,  $\beta$ , the lateral force is  $T\sin\beta$ . Using Figure 6-2 as reference, the reaction force at the load cell  $R$  is defined as:

$$R = T \sin \beta = 2Mg \sin \beta$$

For a static system, a term for any frictional bearing loss would not normally be required but, because there is movement before the system is balanced, it must be considered. If stiction in the bearings is sufficiently large it would result in an increased load cell reaction force. The reading may be higher if the lateral force is weaker than the stiction force, with the initial momentum temporarily causing stiction to be overcome. Conversely, if the initial momentum of the sprocket and shaft were not sufficient, the stiction force would resist the lateral force present. To overcome this difficulty, the shaft was moved away from the load cell manually, allowing it to return to the correct position. Taking readings after each of these resets, the load revealed no indicating suggesting that stiction was not a problem at the loads and angles used.

#### 6.4 Results

The front pulley was positioned such that the least misalignment occurred when the chain was wrapped around the 30T sprocket; the angle was calculated to be 2.29°. Table 6-1 contains the calculated misalignment angles for all 6 sprockets with respect to the front pulley.

Gear	Teeth	misalignment ( $\theta^\circ$ )
1	30	2.29
2	25	3.01
3	20	3.74
4	17	4.45
5	15	5.18
6	13	5.90

Table 6-1 : Sprocket size and associated misalignment

Figure 6-3 shows the measured lateral forces as a function of applied torque for each of the sprockets. Also indicated in the figure is the value of lateral force suggested by the component of the tension introduced by the misalignment,  $T\sin\beta$ . As

can be seen, the larger sprockets show a weaker dependence with this simple model and the smaller sprockets show a stronger dependence. The reason for this variation is probably due to the fact that the sprocket diameter changes with misalignment and in an attempt to normalise for the associated vertical angle, the lateral force values were normalised with respect to the number of sprocket teeth. The resulting plot of normalised lateral force vs. misalignment (Figure 6-4) shows a family of curves which show approximately the expected sinusoidal dependence of lateral force on misalignment.

The effect of increasing load was mirrored by the lateral force measurements. Additionally, as the angle of misalignment became greater so the lateral force also rose. At the smallest misalignment angle with the 30 tooth sprocket, the lateral force remained at 2% of the applied chain tension throughout its increase.

## **6.5 Summary**

As the chain between front and rear sprockets becomes misaligned so the magnitude of lateral force rises. The loss of force to rotate the sprockets does not reduce efficiency directly because its effect is equal at the front and rear; the effect on the chain movements is where the losses occur. Friction between the inner and outer plates and with the tooth flank become greater due to the greater bearing forces from induced bending producing a non-linear relationship.

Figure 6-3: Lateral force experimental data

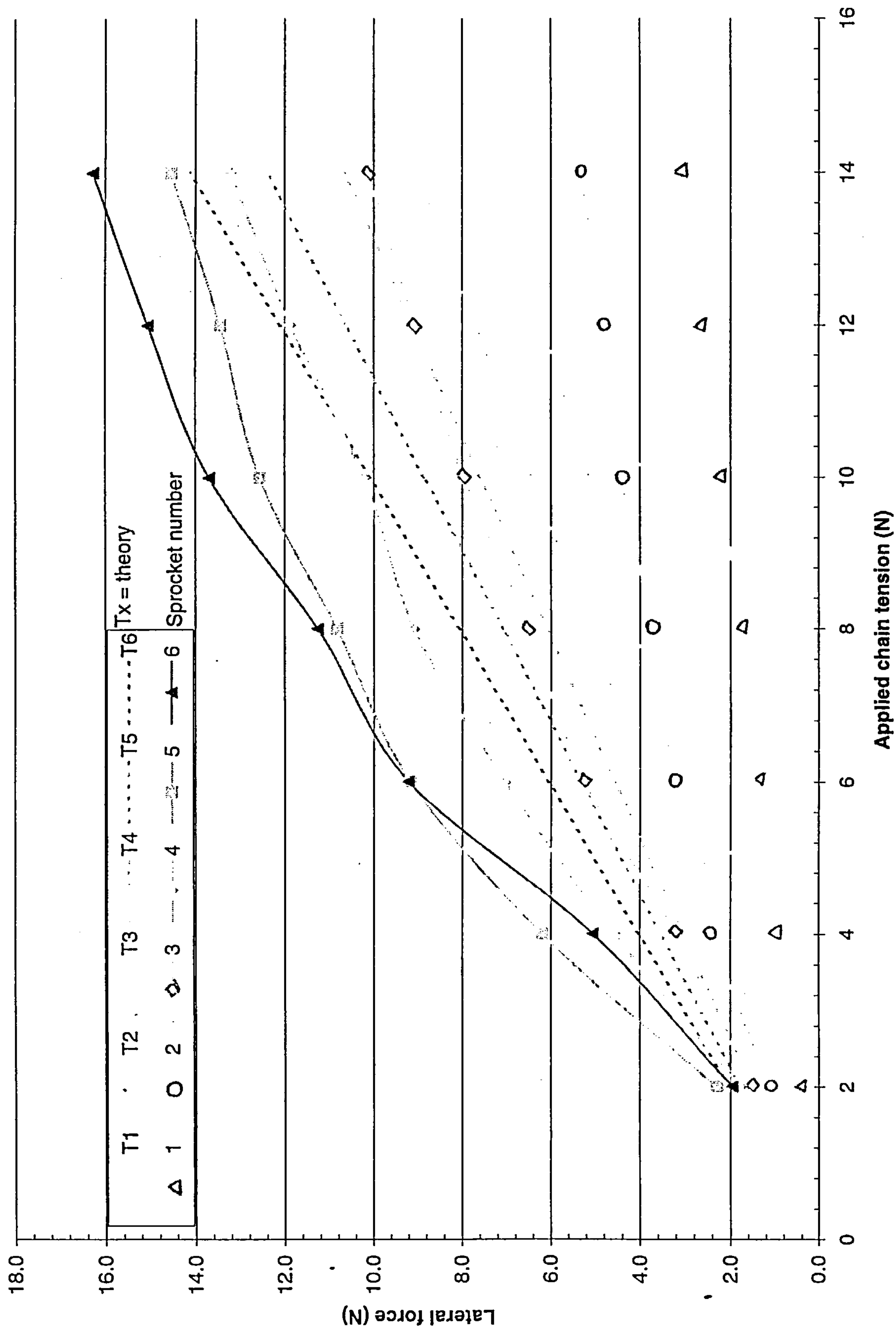
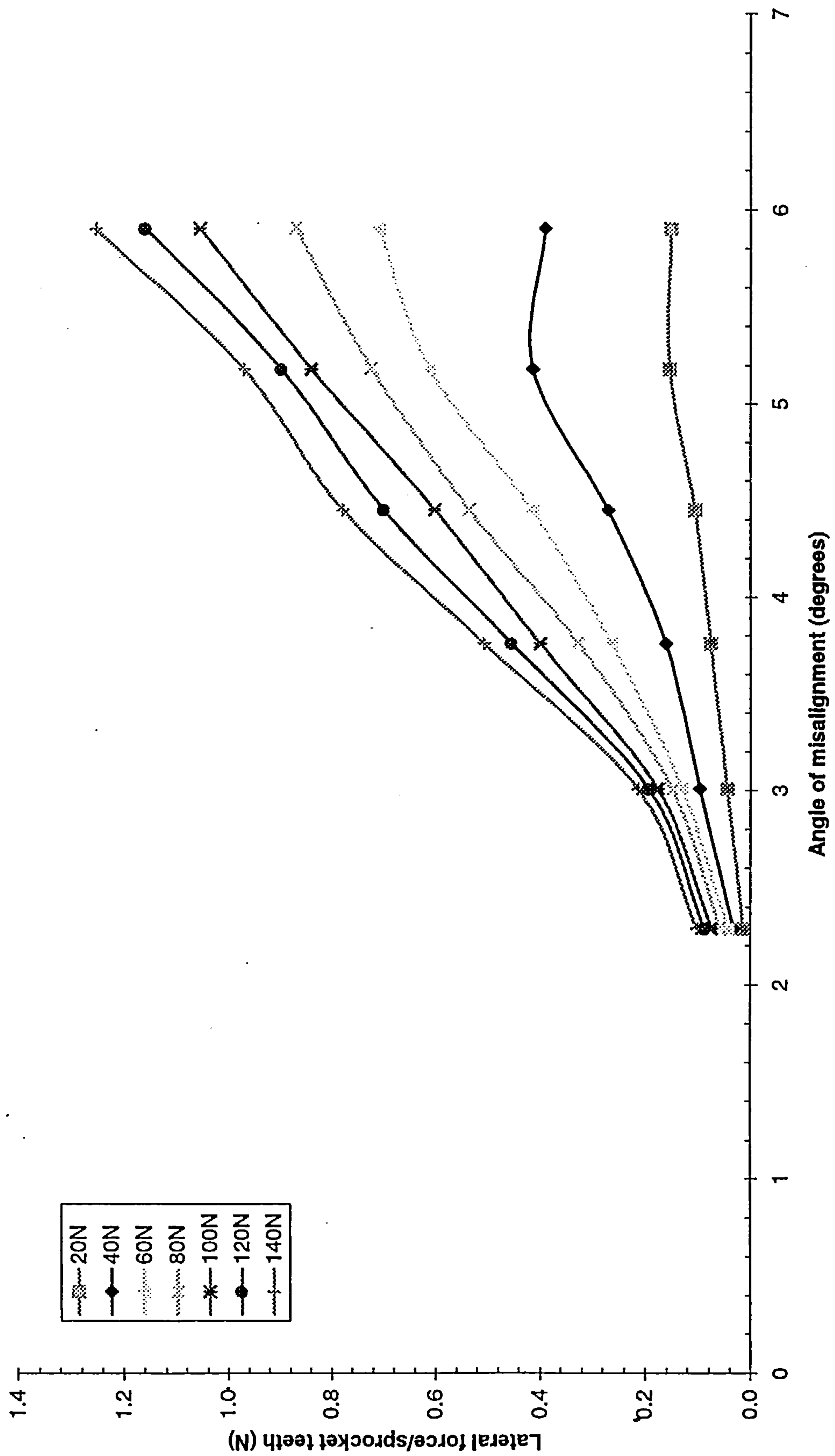


Figure 6-4: Normalised lateral force experimental data



## 7. Chain Efficiency

### 7.1 *Introduction*

This chapter carries the main experimental work for the thesis which is the measurement of chain efficiency in a simulated bicycle environment. Although experiments <sup>(11),(12)</sup> with similar purpose have been constructed several times in the past 100 years, the analysis of results and scope of experimental variables has not been comprehensive. Additionally, the accuracy of previous attempts has never been stated, perhaps because of the nature of the instruments used. Accuracy is seen as important to this work, firstly because of the relatively high efficiency involved and secondly because of the relative importance of small gains in efficiency in competition applications. By measuring chain efficiency for a wide range of parameters likely to influence chain performance, e.g. type of lubricant or degree of misalignment between sprockets, a fuller understanding of their relative importance becomes apparent. For this purpose, a design-of-experiments approach was taken using as realistic a test environment as possible.

One of the principal objectives of the test programme was to observe the effectiveness of different lubricants with respect to running time, in regard to both chain wear and transmission efficiency. For example, a cyclist may be interested more in high efficiency achieved in the short term than reduced chain wear achieved in the long term but at the expense of efficiency. Up to five variables acting simultaneously were examined to observe the changes on the efficiency by interaction, for example, a worn but lubricated chain operating at low power. To further the initial broad range of tests, an additional 6 factors were tested in isolation from normal interaction, such as

changing sprocket ratio but not accruing any associated misalignment. By detaching the dependency of such variables, the extent to which each affects efficiency can be broken down, furthering understanding of the complex chain-component interactions of the bicycle.

Traditional methods of chain maintenance and care are time-consuming and grimy. The range of available lubricants has, historically, also limited cyclists to one of the following: paraffin wax, graphited grease, a multi-purpose oil, or specialist oils with additives. The criteria for selecting a lubricant are typically longevity, ease of application and cleanliness, with high levels of transmission efficiency being of secondary importance, except perhaps to the dedicated cycle mechanic. For many cyclists, the first indication that a lubricant is failing is either squeaking or failure to change gear properly. In the competitive cycling environment, improvements to the efficiency of transmission through proper lubrication would be of great benefit whether it is from immunity from water penetration or simply longevity of lubricant effectiveness.

The resurgence in the popularity of recreational cycling in the past ten years, especially among those with higher incomes, is an acknowledged trend<sup>(83)</sup>. This, combined with technological advances, has led manufacturers of both components and lubricants to cater for a new market. The choice of lubricants now available is several times the number only a decade or two ago. The unpleasant chore of chain cleaning has been made more acceptable by a device that can be temporarily attached to the bicycle, degreasing and washing a chain quickly and simply to an acceptable degree. New technologies have also helped in producing synthetic oils and new additives to lubricants, designed not only specifically for bicycles but even for

different conditions. A popular additive present in a wide-ranging proportion is PTFE suspended in a base solution of grease, liquid or aerosol form. In short, the modern cycle user, competitor or not, is interested in the bicycle as a machine and wishes to keep it in good mechanical condition.

Whilst a commonly agreed practice for lubricating a chain was never reached when only a handful of products was available, now, with a large “lube” market, the choice can be overwhelming. Such a situation can be expected, however, due to the wide range of environmental conditions to which a modern bicycle can be subjected. Since no two cyclists adopt a common routine in regard to type of lubricant and maintenance techniques, a scientific appraisal of this aspect of bicycles is needed; this chapter provides an insight into this problem.

The design of the chain efficiency rig allows realistic cyclist power throughput, simple interchanging of cycle components and an accurate measurement of performance. Chapter 3 describes the design and testing of the two torquemeters used in this experiment, and the remainder of the components are introduced and detailed in this chapter.

Due to the large number of independent qualitative and quantitative variables, an excessive number of experimental combinations would be required to investigate every possible permutation. To reduce the number of individual experiments and increase the statistical confidence of results, an experimental design plan was devised based on a 2<sup>n</sup> approach <sup>(84),(78)</sup> and is detailed in 7.5.1.

## **7.2 Experimental apparatus and procedure**

The main elements of the apparatus were mounted on a common frame to which plates were attached. These plates in turn allowed the drive motor and shaft bearing housings to be mounted and permitted adjustments to ensure correct alignment for the three shaft axes- these features and others are shown in photographs 7-1 and 7-2, a schematic diagram in Figure 7-3 also identifies the key elements.

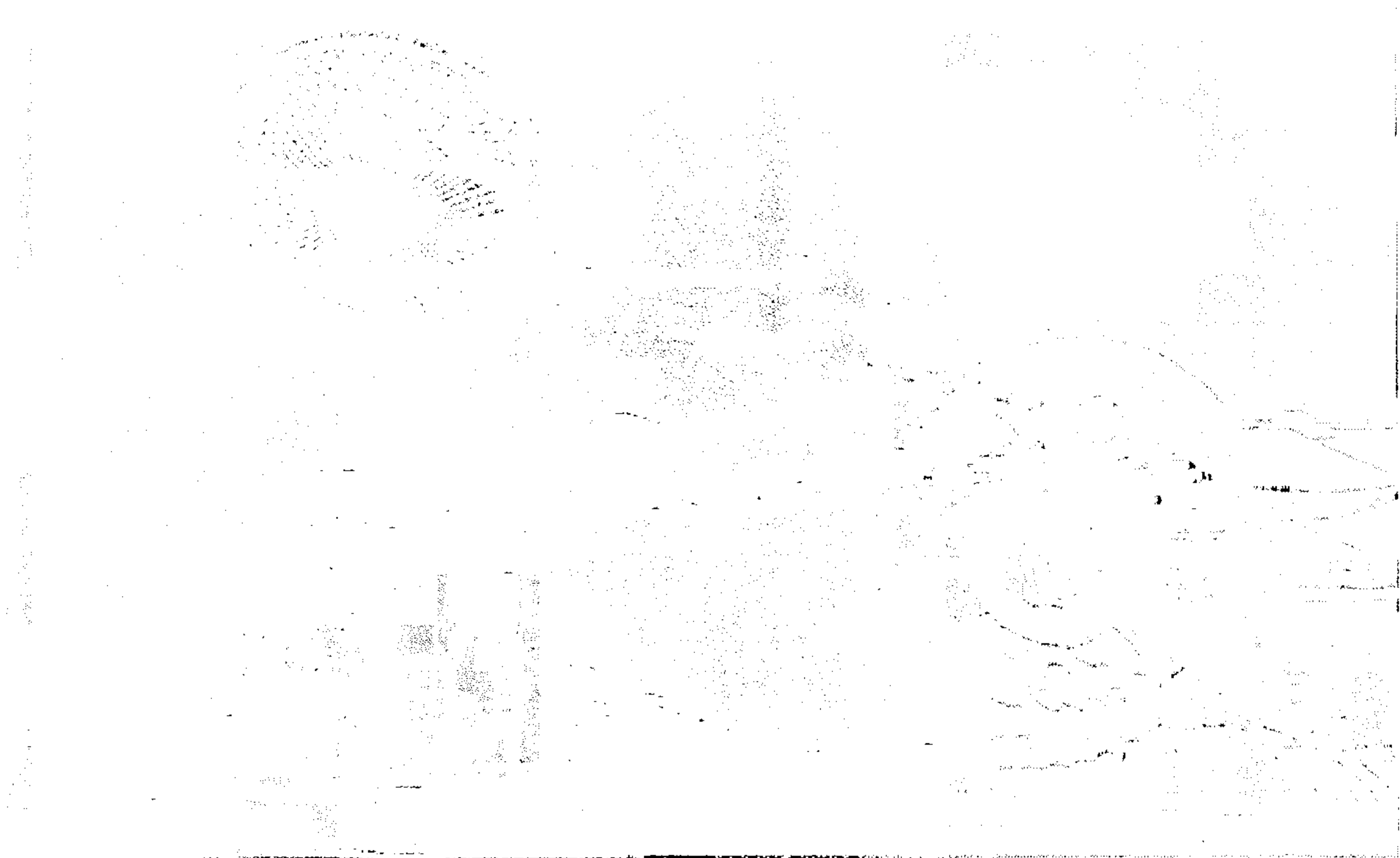


**Figure 7-1: Photograph of chain efficiency test apparatus (side)**

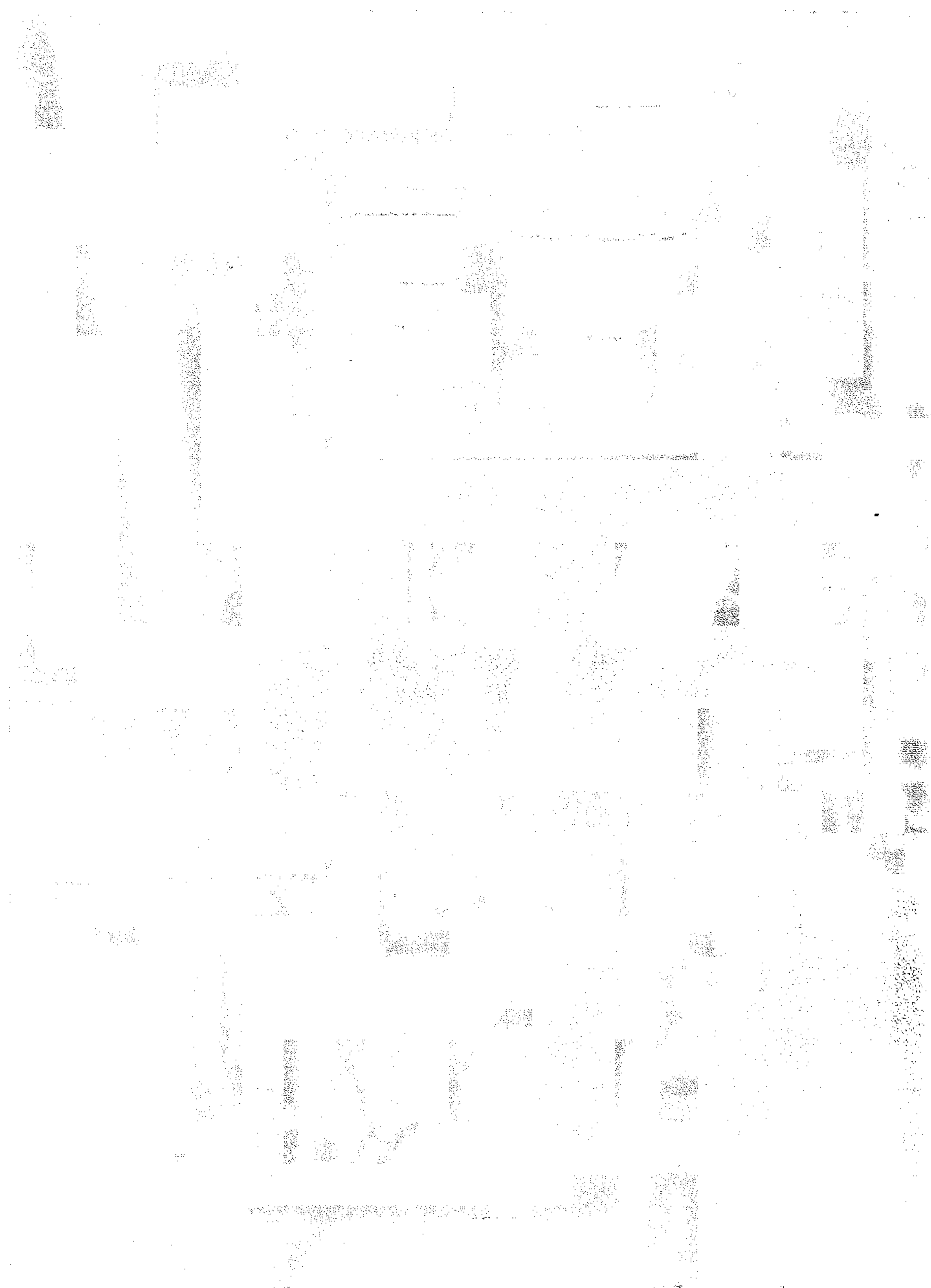


Figure 7-2: Photograph of steam efficiency test apparatus (part)

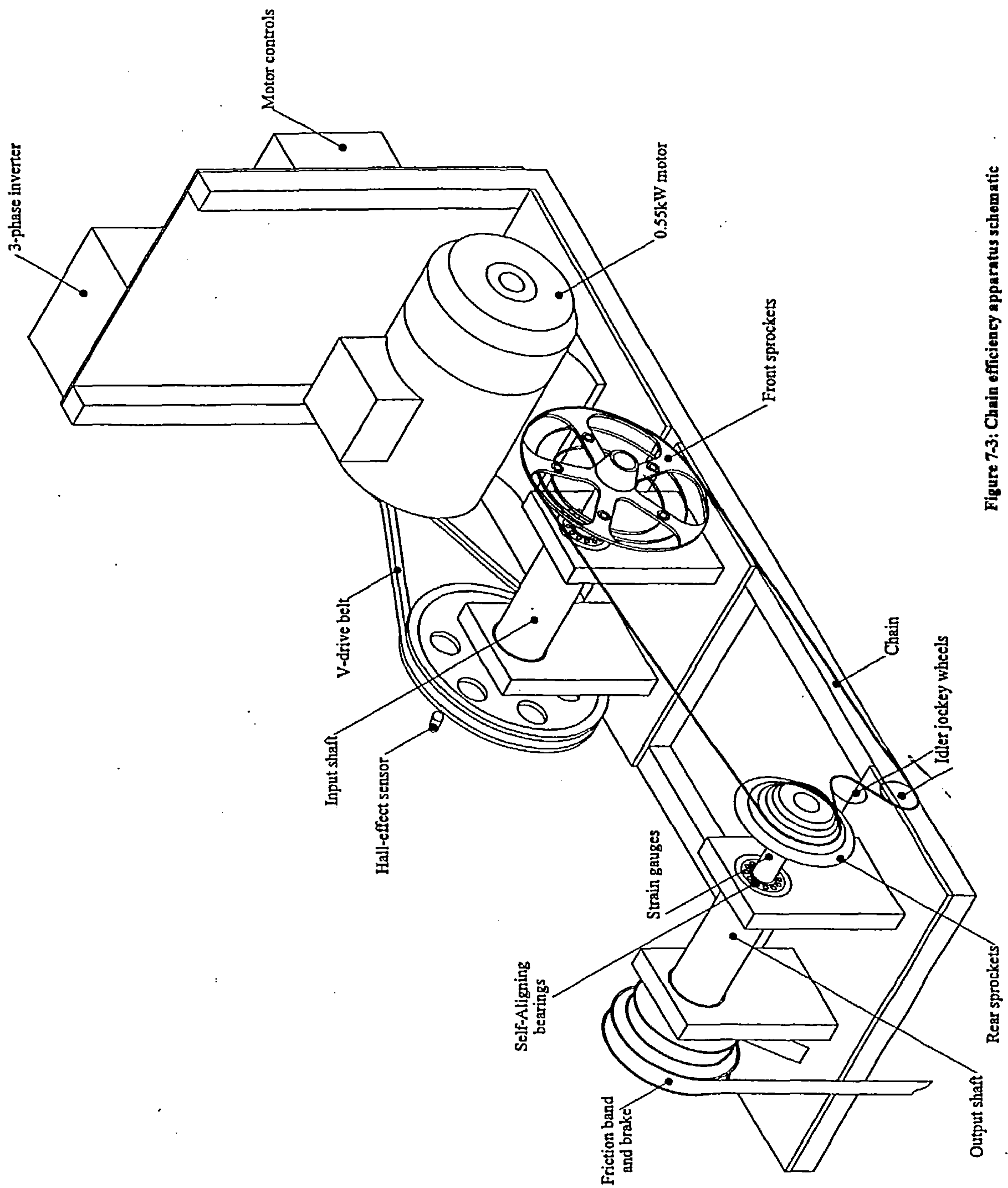


Figure 7-3: Chain efficiency apparatus schematic

The chain system was powered by a 0.55kW three-phase motor via a V-belt pulley arrangement to gear the input speeds down by 8:1.75. The motor controller allowed a fine control of speed with one direct speed adjustment and another giving a 0-100% trim of the initial speed setting, the whole giving a maximum speed of 350rpm at the front sprockets. The spacing between front and rear shafts represents the same dimension found on an average bicycle hence the chain length is also of appropriate length.

The actual speed was not calculated from the controller or motor but was measured at the end face of the input shaft resulting in a more accurate indication. A Hall-effect gear tooth sensor was positioned 1.5 mm away from the edge of a 60-tooth steel gear wheel which was affixed co-axially to the driven pulley (of the front shaft). A rare earth magnet to focus sensitivity on the ferrous tooth target enhanced the Hall-effect sensor. A square-pulse voltage was generated by the sensor with the passing of each gear tooth, and these signals could be interpreted by a frequency counter to give instantaneous revolutions-per-minute readings. During the experiments, the signal was acquired by a PC and analysed to determine the frequency and thus rpm. Fourier analysis was used to calculate the frequency of Hall-effect pulses. The sensitivity to the Fourier and filter parameters of the acquisition program to the Hall-effect signal required some performance tuning in order to obtain an accurate and reliable signal across the wide speed range used. Improper filtering would have led to brief discontinuities in the final frequency output, an example of which is shown in Figure 7-4.

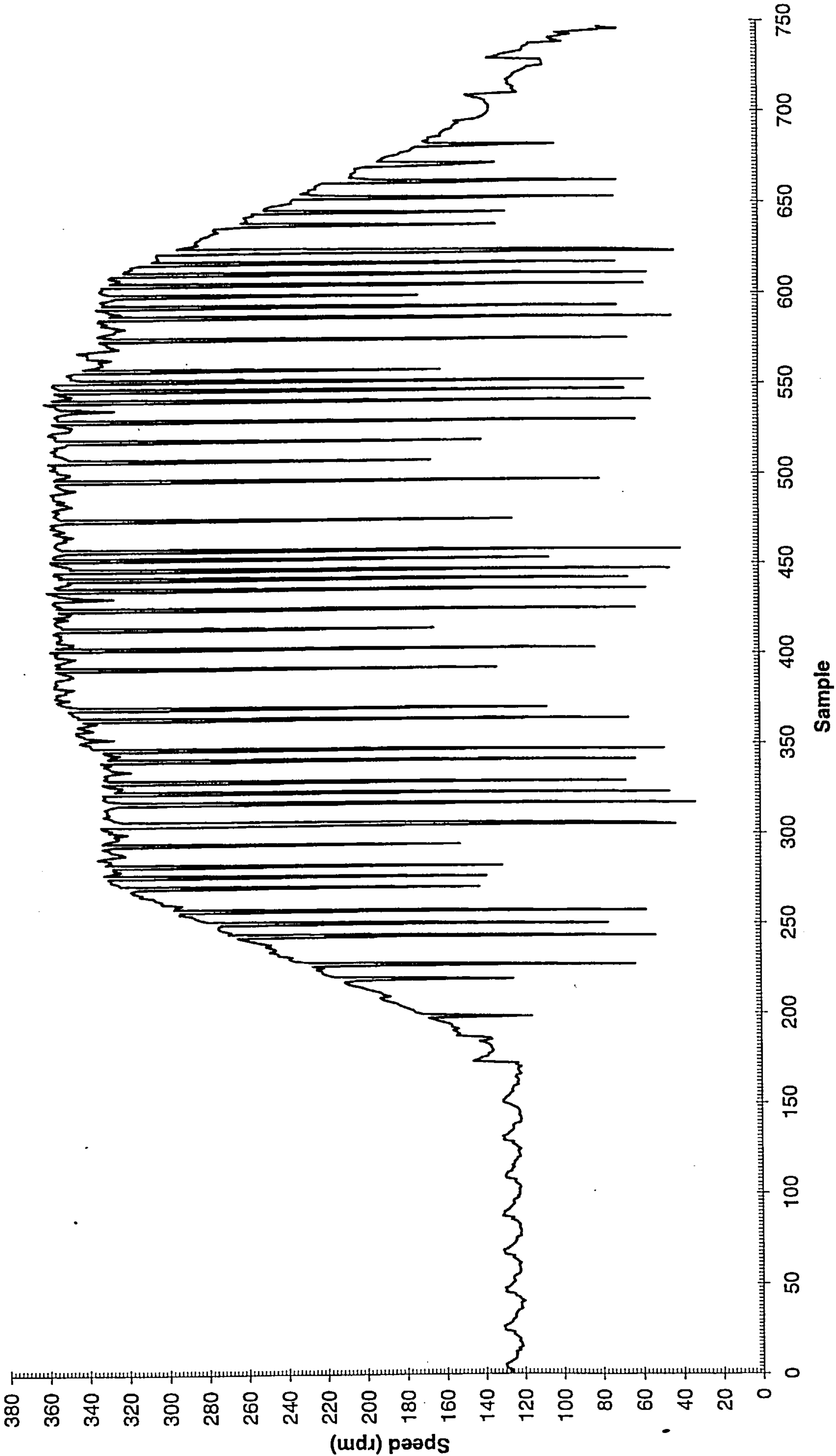
Having determined the frequency and thus the speed of the input shaft in revolutions per minute, it was then converted to radians per second yielding a value

for  $\alpha_i$ . Calculation of  $\alpha_o$ , the output angular speed, was achieved by multiplying by the gear ratio  $N_i/N_o$ . The final calculation of efficiency is simply:

$$\frac{P_o}{P_i} = \frac{T_o \alpha_o}{T_i \alpha_i} \quad \text{Eq. 7-1}$$

With the gear ratio fixed for any given run, the accuracy of the speed sensor becomes less important as both input and output torque values are affected. For absolute measurement of power, however, the speed accuracy is important. The nature of the signal tooth event meant that the accuracy is always  $\pm 1$  tooth, which equates to 1rpm. In relative accuracy terms, the faster the speed the smaller the relative error, e.g. at 50rpm, the error is 2% but at 200rpm the error only 0.5%. For efficiency calculations, the rpm signal was converted to radians per second by multiplying by  $\pi/30$ .

Figure 7-4: Frequency instability of hall effect sensor



The test parameters for the experiments can be classed as either mechanical or operational. A detailed description follows.

### 7.2.1 Mechanical Parameter Details

The mechanical parameters are those associated with the hardware and are:

- sprocket size, profile and make
- chain length, profile, state of wear, material, and manufacturer
- lubrication state, type and extent

#### 7.2.1.1 *Sprocket (front)*

Standard road-race cycles and mountain bikes are fitted with double or triple front chain rings respectively. To reflect the number and range of possibilities for front sprockets, 28, 38 and 52 toothed sizes were used. In the competitive cycling environment, a high strength (and hardness) aluminium alloy is the common choice for sprocket material and this was the choice for all four test sprockets, although not all were of the same manufacture. The profiles therefore varied from sprocket to sprocket but remained relatively simple in design.

#### 7.2.1.2 *Sprocket (rear)*

All tests were conducted on a new *Sachs*® make 8-speed set of sprockets, sized: 12, 13, 14, 16, 20, 22, 24, the ratios chosen corresponding to those used by road race cyclists. The make and model chosen was a popular one. The nature of each rear sprocket profile varies between sprockets of the same block and more markedly, between manufacturer. The reason for profile difference is to permit easier and smoother gear shifts, less damaging to the chain.

### 7.2.1.3 Chain Type

Two models of chain were examined, representing the ends of the spectrum available in the marketplace. For the standard tests and those not concerning chain make or model, the higher quality model was used. The differences between particular models are the materials, treatments used in their manufacture and slight profile alterations. The main thrust in chain design is to produce a stronger or harder wearing chain, except in the case of the PC91 that features weight saving and stress reducing outer side plates, Figure 7-5.

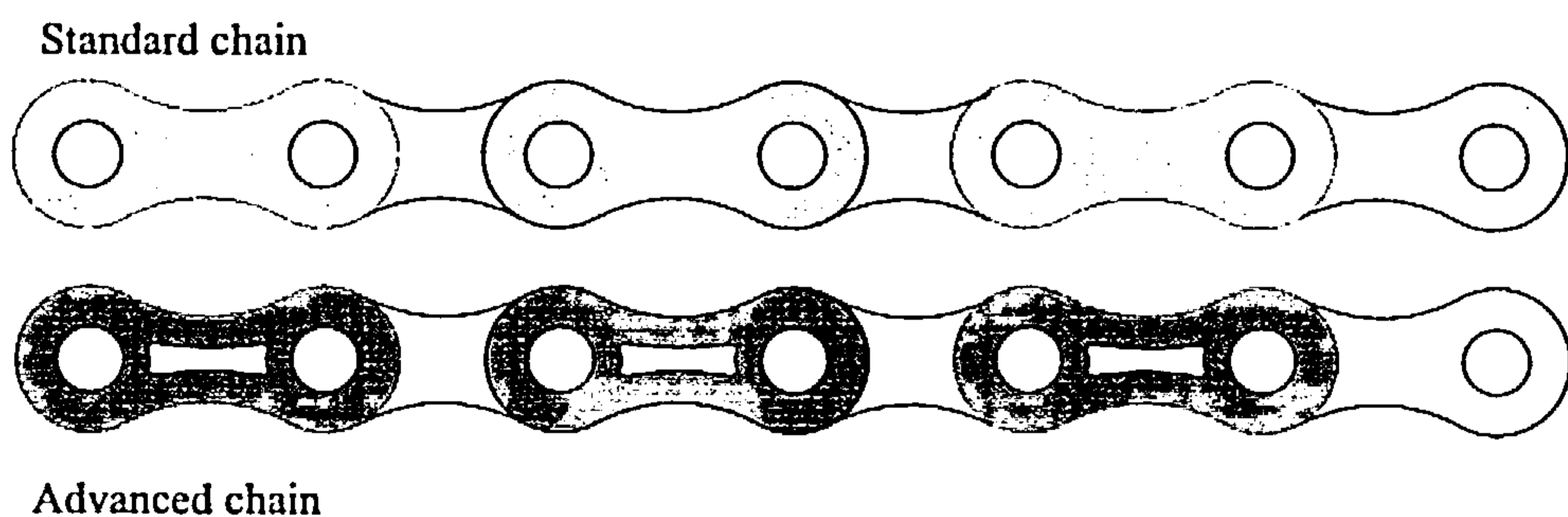


**Figure 7-5: Chain types**

Choices between one manufacturer and model of chain made by a cyclist generally centre on strength, life and reliability. No claims have been made by any one manufacturer over another to provide a more efficient chain. For this reason, all the chains came from one manufacturer which provides a range of chains all similar in profile but not material. It is possible that designs from other manufacturers, where changes are made to aid gear shifting, may produce different results.

The amount of wear a chain experiences cannot simply be quantified in terms of a number of hours usage or distance covered since the state of lubrication during that time plays too important a role. Instead, the degree of wear of the whole chain caused by the cumulative wear at pin/roller joints is measured by the overall 'stretch'

or increase in length since the new condition. A calibrated tool used by cycle mechanics performs a quick and accurate method for determining the state of wear at which chain replacement should be made. The tool has two measurement positions in which it can determine wear at either  $<0.15\%$  or  $<0.25\%$  corresponding to the limits of elongation wear for aluminium alloy or steel sprockets respectively. Exceeding wear guidelines accelerates chain wear, as sliding becomes more prevalent than rolling and thus a higher coefficient of friction results. The wear of sprocket profiles occurs at a slower rate than that of the chain in normal operating conditions. Once the sprockets are worn beyond a certain percentage, a new chain will not operate correctly as the tooth profile can no longer support the load, therefore causing jumping. The chain wear for the worn case in the experiments equalled 3%

#### *7.2.1.4 Lubricant*

The range of lubricants tested reflected the diversity in those commercially available. The lubricants chosen all had different base oils and different additives, except for PTFE, which was present in two of the four lubricants. The lubricants tested were: water, Scottoiler-SACI (surfactant corrosion inhibitor), Finish line (1), Finish line (2) and Triflow. The published compositions of these lubricants are summarised Chapter 5, although many of the active ingredients remain commercial secrets.

The amount of lubricant applied to the chain was in accordance with manufacturers' instructions and reapplied accordingly. Where no instructions were given, 1.0ml was used. A syringe positioned into the top idler sprocket of the rear derailleur was used to apply the lubricants. The time during which a lubricant operates successfully in a real bicycle environment is dependent on its ability to withstand

external environmental factors such as prevailing road and weather conditions. Simulation of these was achieved by drip feeding water into the chain at the exit point of the rear sprocket. The feed rate was controlled by adjusting a needle-in-hole metering valve, which controlled the gravity feed down a tube to the sprocket. A total of 375ml of water was supplied over several hours during which the efficiency performance was measured every 15 minutes. After this “washing” period the water was stopped to permit any recovery of the lubricant. After a further period of time the water was then supplied again, further testing the ability of the lubricant to continue performing. In total, these tests of lubricant endurance continued for up to 6 hours.

### 7.2.2 Operational effects

Besides the mechanical factors described above, a number of operational factors were examined; power throughput, rotational speed and time effects. Some of these factors (including the mechanical ones) are intimately linked and cannot be varied independently in a typical drive-train layout; a good example is gear ratio and angular misalignment between sprockets. These effects were studied separately by using the lateral positioning ability of the rig to simulate the condition.

#### 7.2.2.1 *Power*

The maximum sustainable power output of a cyclist depends greatly on the required duration and, of course, on the fitness of the subject. Top class athletes may sustain 1,200 W for a small fraction of a minute but only 400W for a period closer to an hour. Healthy, non-competing subjects would typically feature some 200-300W less than the highly trained athlete<sup>(85)</sup>. More versatile in the speed range of 50 to 120 rpm than a motor or engine; the human body can vary the power output greatly.

Limited by the 3.0A supply current of the 3-phase motor it was not possible to emulate a human within their envelope because of their high torque, low speed characteristics. The power output for the tests varied between 50 and 350 watts with an inevitable increase in speed at higher outputs, depending on the duration of test.

#### 7.2.2.2 *Speed*

Physiological, psychological and biomechanical factors contribute to the cadence of a cyclist for a given power output. Whilst a recreational cyclist could comfortably maintain 50rpm, a competitive time-trial cyclist would achieve rates as much as 120 rpm for a duration of between 20 minutes and one hour. While maximal power output is achieved at a high cadence, the most physiologically efficient movement is achieved at speeds closer to 60-80 rpm. The uniformity of the cadence is dependent to some extent on the terrain being cycled across, but, with judicious selection of gears by the cyclist, it should be possible to keep to within 10 to 15% of the optimum rate.

The specification of the motor and controller allowed a cadence simulation of speeds as low as 50rpm to an unlikely 250rpm. Whilst an experiment was in progress, the speed could be maintained to within 2% by manual adjustments of the controller.

#### 7.2.2.3 *Time*

The many types of competitive event in cycling vary in duration from minutes in a velodrome sprint to many days in an endurance competition. Somewhere in between is a typical road race which may last up to several hours for example; 5 hrs is typical for one stage of the Tour de France. Preliminary experiments indicated little deterioration in efficiency over the first hour of test at typical power throughputs,

provided there was no contamination in that time. Measurements of efficiency were taken for the whole duration of the experiment if the purpose was to examine short lived changes in the system. The monitoring time for each of the experiments as part of the 2n analysis lasted two minutes. When conducting the lubricant endurance investigations, the experiment was run for up to 6 hours with measurements made regularly for 2 minutes at a time.

### **7.3 Test procedure**

To prevent cross-contamination between tests and ensure that the components were in the same initial state for each test, a standard cleaning procedure was introduced. The first stage for heavily soiled and intricate parts was to soak in diesel and agitate with a brush. The cleaning procedure used for both front and rear sprockets was very similar. The components were first scrubbed with a small brush and a quantity of ultrasonic bath cleaning fluid. Having removed the majority of lubricant and contaminants on the surface, each tooth was then carefully wiped with acetone to ensure a dry and chemically clean surface.

Other components, and those having been washed initially in diesel, were cleaned in an ultrasonic bath filled with a solvent (*OptiClear-R™*) designed to leave no residue but remove grease, oil and wax effectively. Although no residue should be left when the chains are dried with a hot air gun, a salt like deposit was normally found. Rinsing the chains in water was not an option because of possible rusting and the uncertainty that the chain will dry fully, so the final preparation involved washing of the chain in chromatograph grade acetone, which left no residue after its evaporation which occurs quickly at room temperature. The scavenging of any water-based products within the chain was completed with the use of molecular sieves in the

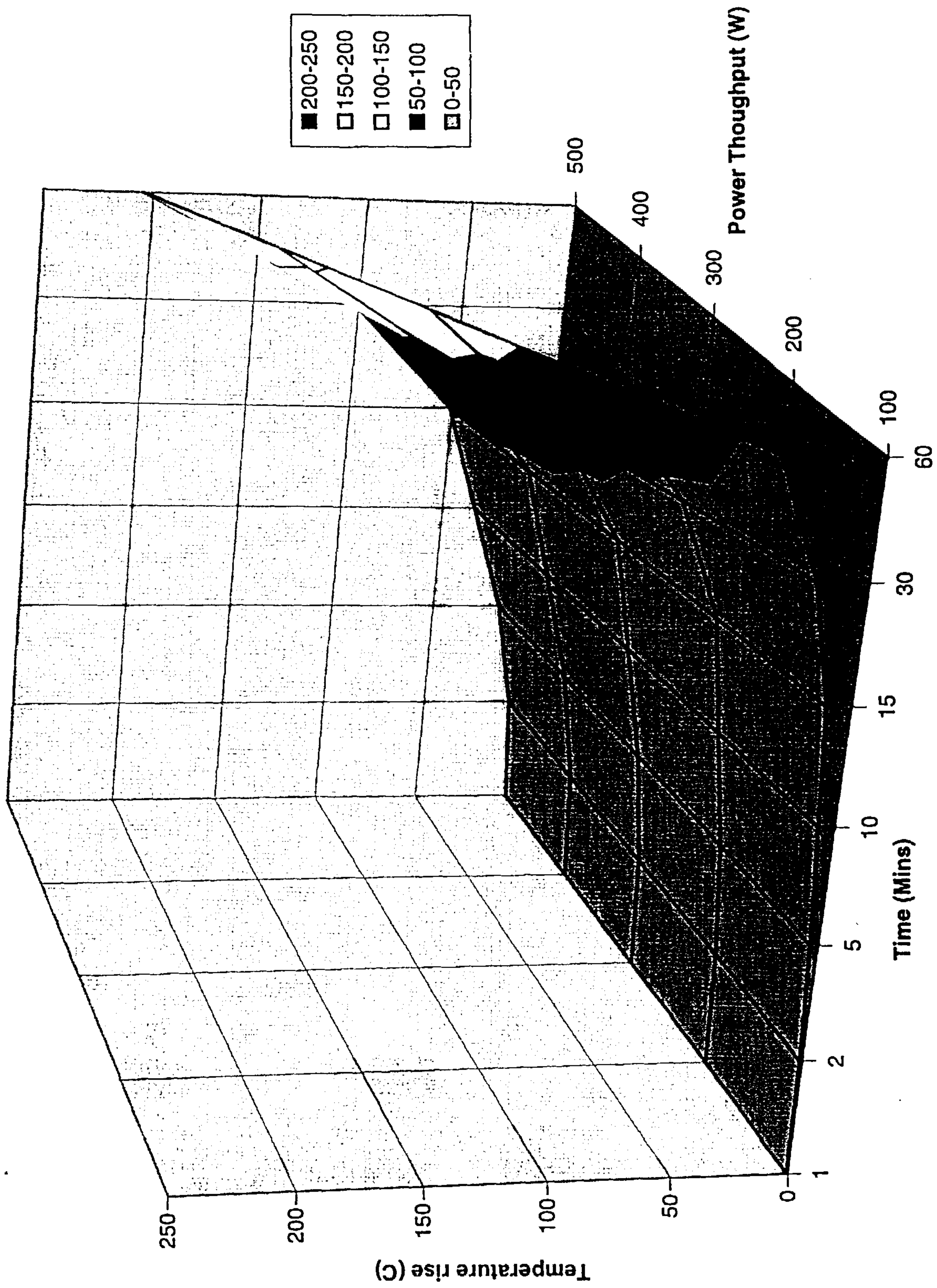
acetone bath. These micro-porous particles effectively lock away water molecules present in the solution. Once dried, the chains were stored wrapped in paper towels and normally used within 72 hours.

With all the necessary components but the chain assembled and in their test state, an initial torquemeter reading was taken. To maintain accuracy of results from the torquemeters, the chain was removed from the system to eliminate the initial tension imposed by the rear derailleur mechanism and to ensure that no loads were imposed on the sensors. The reading taken represents zero torque and was then used as part of the calibration equation to convert frequency signals back to applied torque (Chapter 3).

The next step in all tests was to set the desired speed and power parameters. The masses at the friction brake and the speed set points of the motor were adjusted to balance both speed and load to the required values. The system was run with the acquisition system operating so that real-time power readings could be made and speed readings could be made by the in-line frequency counter and displayed on the computer screen. Problems could arise at certain power/speed combinations because of the limits of the motor and controller; to monitor this, an electrical power meter was incorporated into the control of the motor to display a supply current. If the supply current exceeded 2.80A for more than a period of 30s, the controller tripped and this was initially a problem when tests were run during development. Reliable running of the system for up to 6 hours or so was possible with supply currents of up to 2.65A. Theoretical calculations (see Appendix B) were made to predict temperatures of the friction brake for a given load, shown in Figure 7-6. On tests exceeding 1 hour's duration, it was found prudent to employ a small cooling fan to

prevent the friction brake from overheating, without which the temperature could reach 100°C for prolonged heavy load conditions. The heat capacity was enhanced by the addition of a stainless steel disc, the main purpose of which was to act as an inertial damper at the brake.

Figure 7-6: Friction Brake Heating



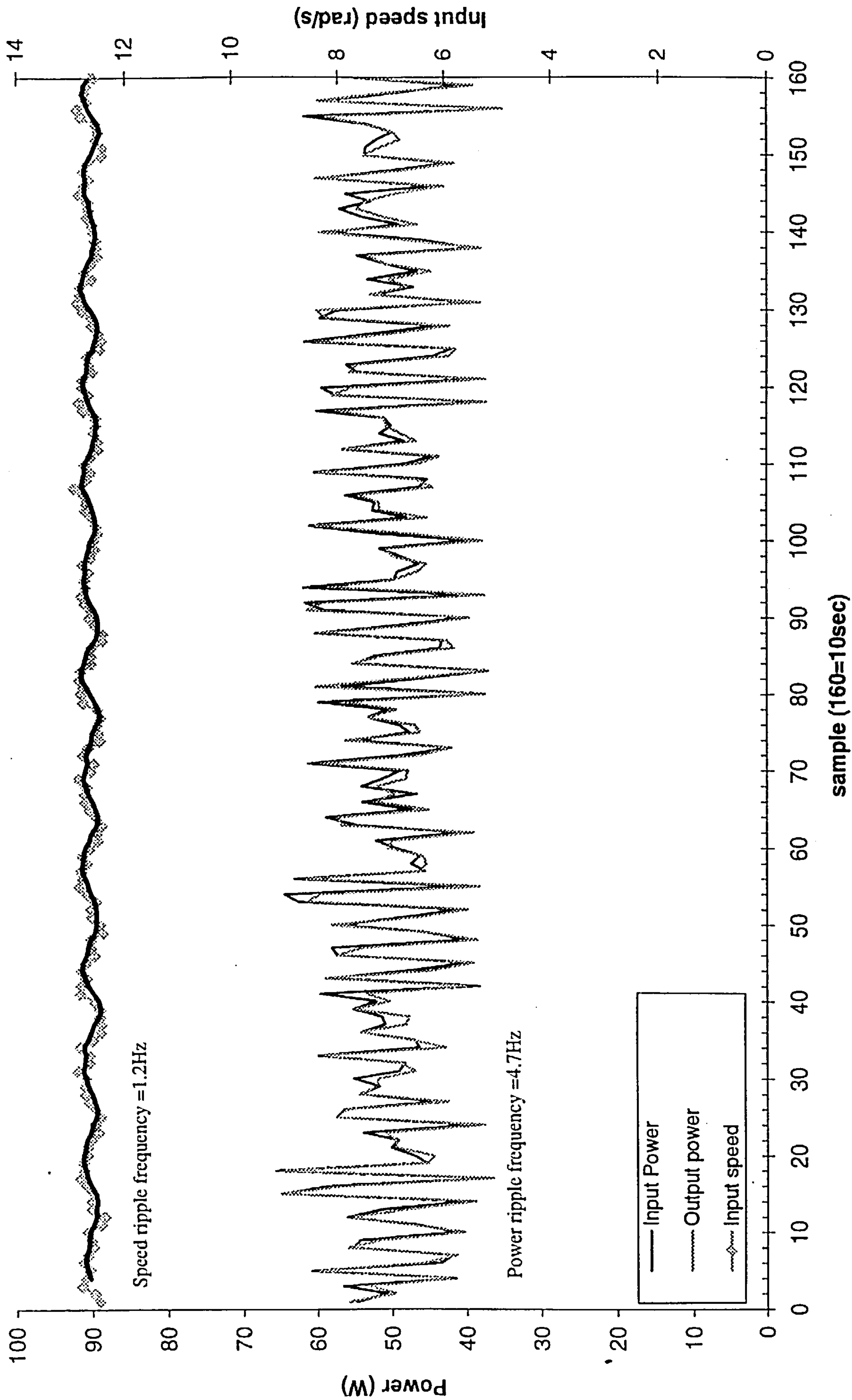
## **7.4 Procedure**

The main body of the experiments consisted of efficiency 'snap shot' acquisitions, taken over a period of 2 minutes. Figure 7-7 shows a typical plot of type two torque values and speed over the 2-minute period. The most obvious feature of the readings is that they vary by a significant amount under notionally identical conditions. The ripples of the input and output frequencies were in phase and oscillated at 4.7Hz which corresponds directly to the rear shaft rotational speed of 4.67 revolutions per second. The front sprocket speed frequency was found to be 1.2Hz, this dominant frequency does not relate to any of the rotational frequencies of the system.

When the raw data are combined to show an efficiency versus time plot the variations are amplified, leading, in some cases, to values of efficiency clearly impossible at >100%. The cyclic nature of the speed measurements can be accepted in the light of the vibrations present in chain drives, the slight imperfection in the gear teeth of the speed pick up and the non-smooth power output of the motor. To arrive at a useable efficiency value, the data is averaged over the entire period.

Figure 7-7: Sample data reading

28:12 120rpm 50W



7.5 Results

7.5.1 Combination and Solitary Effects

A factorial design approach was used to examine how the five key factors act solely and by interaction to affect chain efficiency. Each variable was used in one of two states, representative of the opposite ends of the spectrum likely to be observed in practice. Table 7-1 shows the parameters and the target high (+) and low (-) test values.

			State	
Factor	Designator	Units	-	+
Speed	a	rpm	50	200
Power	b	Watts	50	250
Sprocket ratio	c	Z <sub>1</sub> :Z <sub>2</sub>	28:26	52:12
Wear	d	%	4	0
Lubricated	e	-	No	Yes

Table 7-1: Parameter extents

The values for factors “a” and “b”, being operational factors, were targets for the experiment with the actual values sometimes being lower. The limitations of the motor controller and brake presented problems at high power, low speed combinations for example. The naming convention used for the experiments is simply a list of all parameters set to the high value, e.g. experiment “acd” has factors of speed, sprocket ratio and wear in the (+) state and all others in the (-) condition. The five variables were selected to encompass common changes possible for the cyclist and their bicycle; a 2<sup>n</sup> method leads to a total of 32 experiments, see Table 7-2.

**Table 7-2: Chain efficiency experimental parameters**

[illegible]

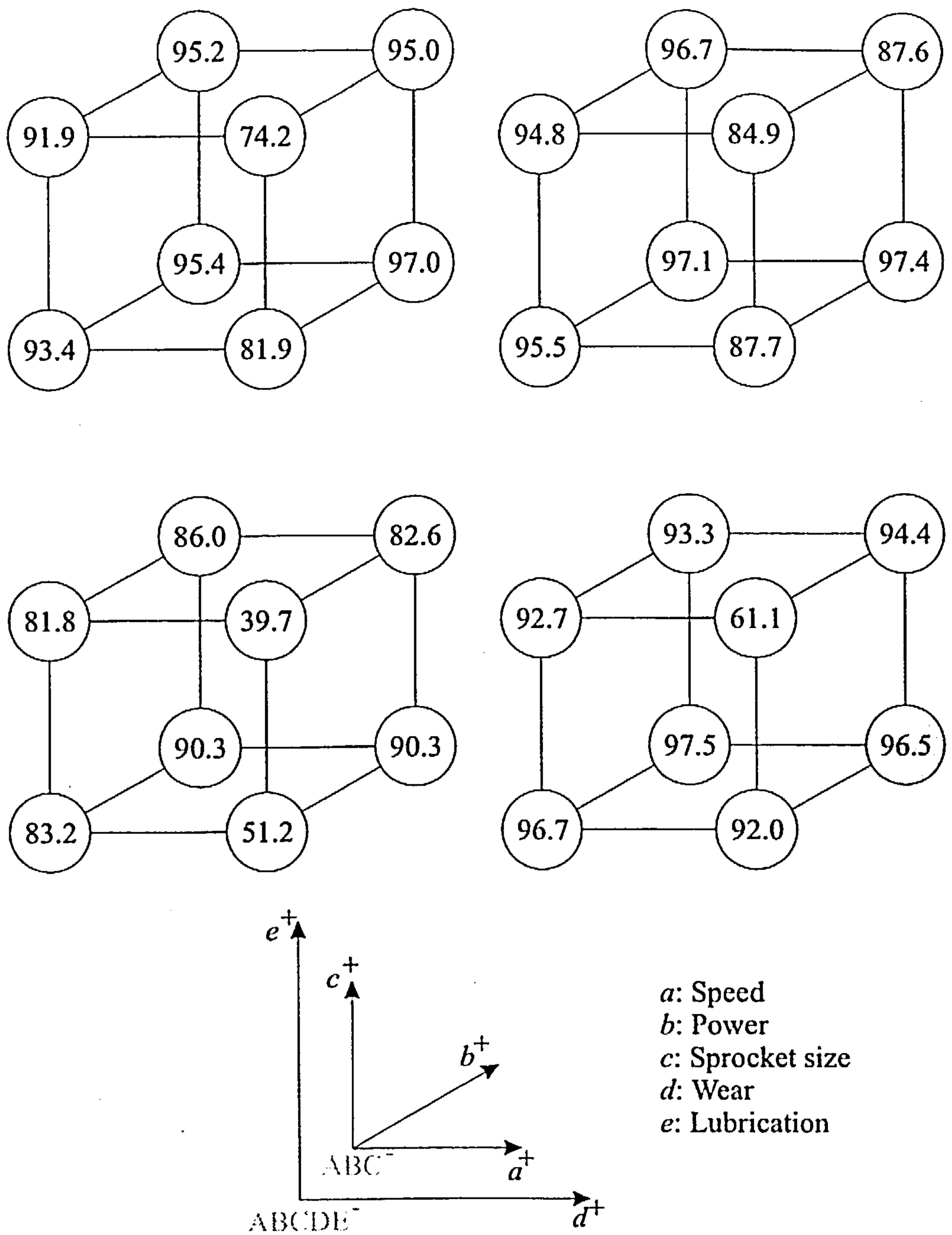


Figure 7-8: Results hypercube

The results of the 32 tests are also listed in Table 7-2. An alternative form of representation is shown in Figure 7-8, which allows easier interpretation of the data. Reinterpreting the data in this manner allows for a method of evaluating "what if?" scenarios. The "hypercube" consists of 4, 8-noded cubes arranged along two axes:  $d$  and  $e$  (analogous to  $x$  and  $y$  of Cartesian co-ordinates) representing the lubrication and wear conditions of the data. The (+) state for the  $e$  factor refers to the two upper cubes and for  $d$  the (+) state is in the two right hand cubes. Within each cube the  $a$ ,  $b$ , and  $c$  factors reflect the  $x$ ,  $y$  and  $z$  Cartesian axes, the (+) state for each is the node furthest from the lower, left hand origin of the cube. For example to compare the changing of lubrication state from the dry (-) to lubricated (+) state for an unworn chain with small sprockets at high power, high speed, two efficiencies must be found from the hypercube. Because the first efficiency is for a dry chain only the lower two cubes are considered; as the chain is unworn it must be the right hand cube. Within the cube, the efficiency must lie in the  $a$ - $b$  plane as the sprocket size is small. Refining further, with the high power, high speed combination then it is the node not collinear with either the  $a$  or  $b$  axes i.e. 96.5% (as shaded in Figure 7-8). Locating the same node in the cube above for the  $e$  (+) state the efficiency is found to be 97.4%.

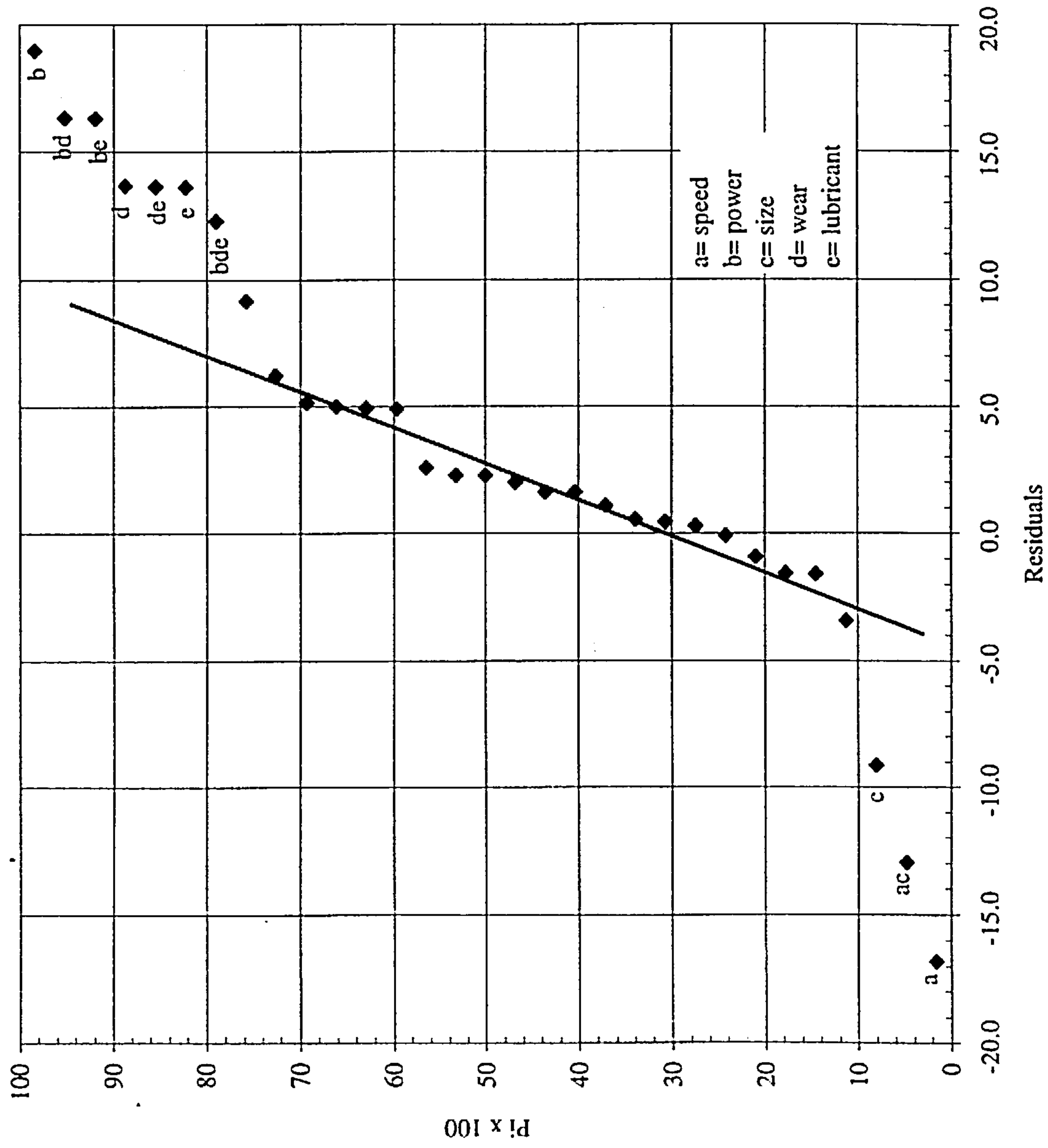
Statistical analysis of the results of a factorial experiment can be achieved by established techniques<sup>(78), (84)</sup> which use the differences between experimental combinations to isolate the effects of individual factors. The analysis identifies all the individual tests in which the states were positive and negative; deviation from the overall mean of the 32 experiments determines the extent of each factor. The quantity of data for each of the single five factors improves the confidence on its effect on the mean efficiency e.g. for the  $a$  (+) state there are 16 separate results but for  $cde$  (+) only

8 such results from which to determine a quantitative factor on the effect of chain efficiency. The examination of the residuals for the experiments allows the magnitude of their effect to be shown graphically. Points not lying along the “normal” condition constitute a more considerable effect. Those points to the right of the line represent factors that improve efficiency whilst those to the left degrade it, Figure 7-9.

The factors that produce improvements in chain efficiency were power, wear and lubricant. When these variables are in their high (+) state they improve efficiency to a greater degree than the mean effect of all the other variables. Additionally, when these positive factors are combined e.g. “bd” or “be” they show still greater improvements. The remaining two factors of the five examined show detrimental effects on efficiency when in their positive state; they were speed and sprocket ratio. Again when combined they also signify an increased negative effect. Power and speed are the most influential factors, being at opposite ends of the normal probability plot.

Having established the relative interactions between the five factors a series of further experiments were carried out to examine specific effects. First, the state of lubrication of the chain was examined in more detail with a series of experiments aimed at assessing the effects of lubricant type and longevity on efficiency. Secondly, a series of experiments were carried out specifically to assess the effect of chain operation factors such as chain tension, sprocket size, misalignment and chain length. These tests are described in the following sections.

Figure 7-9: Graphical statistical analysis



### 7.5.2 Lubricant

Four experiments were constructed to examine further some extreme states of lubrication. These states were: a completely dry chain, a dry chain "lubricated" with water only, and a chain lubricated with each of two proprietary blends. For each test the sprocket ratio was 52:13. The chain (PC91) had no measurable wear and the speed varied between 100 and 130 rpm. With these variables effectively fixed, the effect of power on efficiency was measured. Figure 7-10 shows a family of curves with the same general characteristic of low efficiency at low power input which increases and then flattens off after a certain power.

As might be expected, the dry condition exhibited the lowest performance, between 93.43% and 95.41%. When water was added to the chain, an improvement over the dry state was observed, becoming more evident as the power throughput increased. The water also had the effect of reducing the operating noise, preventing the squeaking and rattling audible with the dry condition. Not surprisingly, injecting the chain with 5ml of water, a large proportion was flung off immediately, mostly at the rear sprockets where the angular acceleration was the greatest.

The most noticeable improvement in chain efficiency over the dry state occurred when the purpose blended cycle lubricant, *Scottoiler SACI*®, was added. The lubricant increased the efficiency generally (between power ratios of 70 to 150W) by about 3%. As with the other two tests, once the power had increased to a certain load, around 150-170W, the efficiency no longer rose with increased power.

Another lubricant was examined although this was run with slightly different operating conditions. A smaller rear sprocket (12 teeth) gave rise to a slight increase in misalignment, and the input speed was slightly greater at 100-140 rpm. A different

purpose-blended cycle lubricant, *Triflow*®, was added again to a dry chain. The measured efficiency (Figure 7-11) was a little lower than for the *Scottoiler SACI* lubricant, but as indicated earlier this could have been due to a higher speed and larger sprocket ratio. Three values for efficiency are given for each power setting indicating the typical scatter of results.

### 7.5.3 Time (short term)

When measuring the efficiencies of different lubricants reported in the previous section, the system was assumed to be in a steady state condition after one minute of operation. A series of experiments was carried out to observe transient effects in lubrication using water or *Scottoiler SACI*. Efficiency measurements were started with the chain in the dry state and continued for around five minutes after addition of the lubricant. A sprocket ratio of 52:13 and a 0% wear PC91 chain were used as before. The power throughput and speed were held constant for each individual test. In all, 3 tests were carried out; one using *Scottoiler SACI* as lubricant and two using just water. On every occasion a new (dry and cleaned) chain was used.

The chain was operated in its dry state for 60 seconds before adding any lubricant and the values for efficiency are shown plotted against time in Figure 7-12. Considering the water addition at 190W and 110rpm, the initial efficiency, in the dry state, was 96.1%. Over a 20-second period 5ml of water was added and the efficiency rose to 96.6%. This peak value was maintained for around 20s and then gradually fell to reach a steady state close to 96.4%. Using water for a second time but operating at a higher power (400W) and speed (260rpm) the efficiency variations were greater. Starting with a dry chain at 96.2% efficiency the time to reach the peak was longer and the peak efficiency (97.3%) was only maintained briefly and then declined over

the ensuing minute. Centrifugal forces promoting a more rapid shredding of water and higher bearing pressures restricting the rate of fluid penetration may explain the differences, although temperatures in the bearing areas will also be higher at higher power, which may accelerate loss of water through evaporation.

A strong and sustained improvement in efficiency was exhibited by the *Scottoiler SACI* lubricant running at 160W and 110rpm. A lower, initial dry chain efficiency of 94.6% would be expected due to the low power input in comparison with the two previous tests. The increase in efficiency after addition of the lubricant was rapid and substantiated, rising to 97.5%. Once the efficiency had risen, it appeared to maintain a stable value for the remaining duration of the test.

Figure 7-10: Chain efficiency and power, various lubrication states

-- 52:13 100-130rpm 0% chain wear --

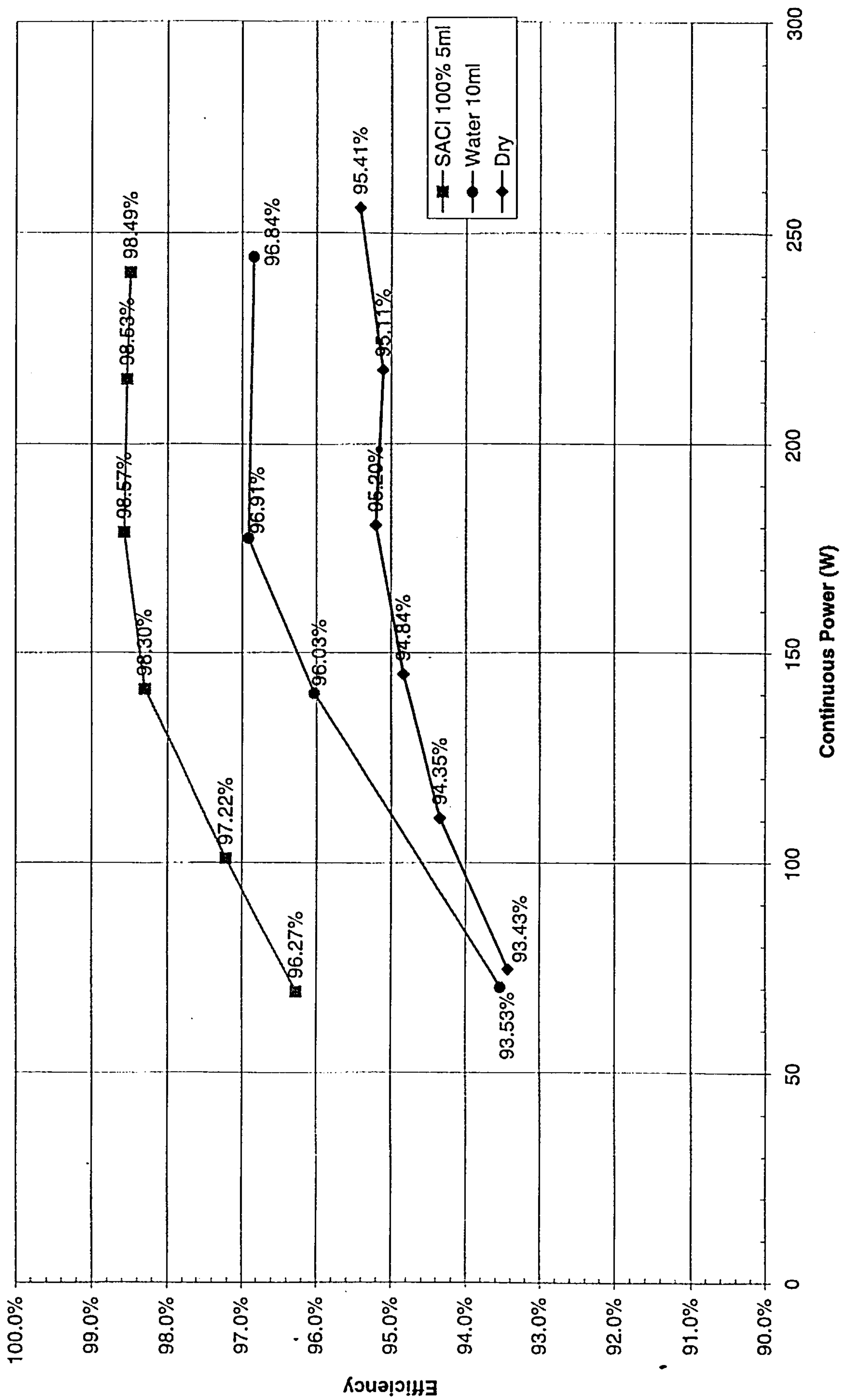


Figure 7-11: Chain Efficiency and *Triflow* lubricant  
-- 52:12 100-140rpm 0% chain wear PC91 chain --

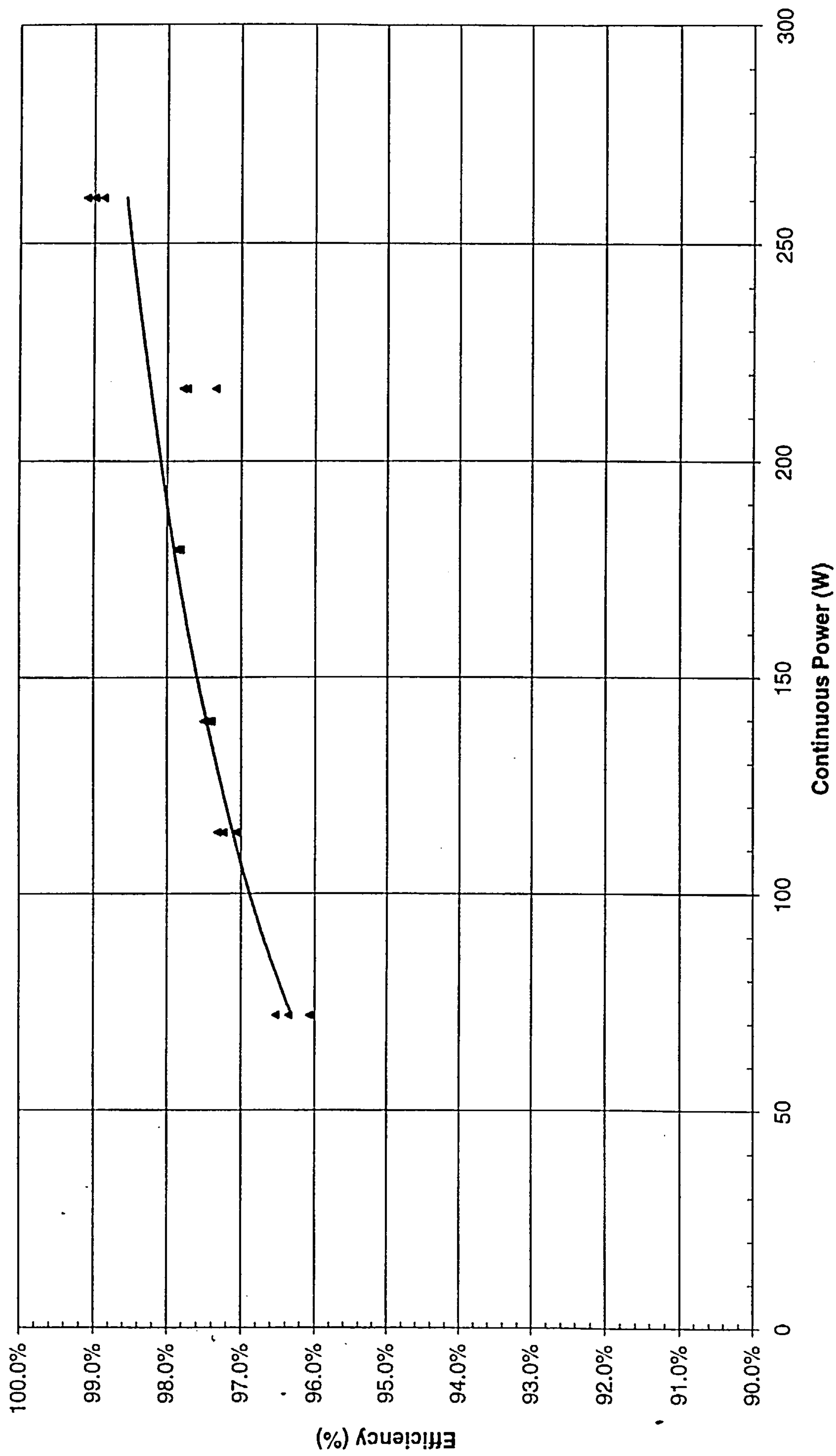
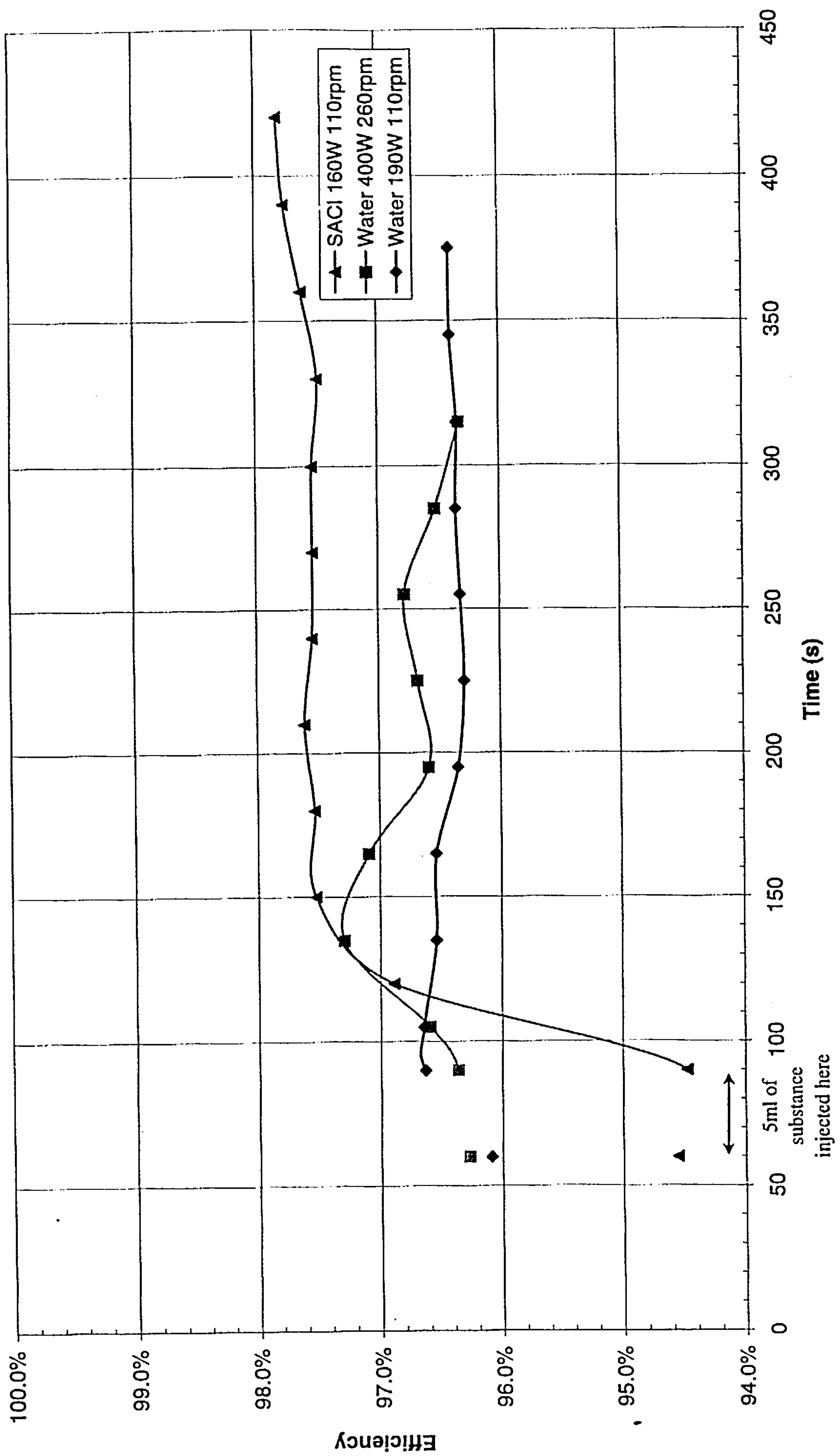


Figure 7-12: Chain Efficiency at point of lubrication injection

-- 52:13 0% wear PC91 chain --



#### 7.5.4 Time (long term)

To test the longevity and weather resistance of four lubricants in a simulated environment, water was added at a controlled rate over several hours. The addition of water to an already lubricated chain was intended to be representative of what might be experienced in road conditions during rain. The general procedure was to start with a dry chain, add 2ml of lubricant, wait for a period of around 45-60 minutes and add water (375ml) at a drip feed over 3 hours. A drying out period of an hour then follows when the water feed is stopped. Water (10-50ml) is then dripped onto the chain again at the same rate for another, shorter, period. A final drying out period of up to an hour then follows.

The *Triflow* lubricant (Figure 7-13) showed good lubrication properties and continued to work with the presence of water. On its addition to the dry chain the transmission efficiency rose from 89.8% to 96.2%. The efficiency did not suffer greatly with the water feed for the entire duration of the first period of water addition. However, once the water feed was stopped, the efficiency of the chain dropped sharply from 97.5% to 94.0% over a period of 1 hour. On reapplying water the efficiency rose again, to 95.6%. As before, when the water was turned off, the efficiency was again reduced.

The manufacturer's instructions for the *Finish Line*® (1) lubricant required two applications for maximum effect and this was evident from the results shown in Figure 7-14. Chain efficiencies rose from a dry 90% to 96.6% after the second application of the lubricant. From the start of adding water the efficiency fell gradually from 96.4% to 94.4%. Stopping the water feed appeared not to change the rate of decrease of efficiency. Re-starting the water flow however, did reduce

efficiency by a further amount from 94.3% to 92.6%. In the final period with no water addition the efficiency appeared to stabilise at around 92.3%. Overall the tolerance of lubricant to water did not suggest the lubricant would be suitable for wet conditions.

The third lubricant tested, *Finish Line (2)* showed similar characteristics to the previous test result (Figure 7-15). Peak efficiency was achieved shortly after the lubricant was applied to the chain. When water was first supplied the efficiency dropped for around 15 minutes by about 0.2%. Although a brief rise in the following 15 minutes occurred, the trend was downward for the remaining 3 hours the water was on. There was a recovery was made in efficiency when the system dried out over a 90 minute period but it then reduced as water was added for a second time. The most rapid decline in efficiency occurred during the second drying period. Again this lubricant showed less resistance to water than that of the *Triflow* lubricant.

In contrast to the previous lubricant the *Scottoiler SACI* was applied more than once, Figure 7-16. The reason for this was to simulate the way in which the lubricant is intended to be used i.e. frequent applications from an on-board supply. Because the lubricant is water-soluble and the chain became saturated with water a gradual reduction in efficiency was noticed, from 99% to 96%. Despite this trend the performance of this system was still greater than any of the other lubricants tested, not dropping below 96%. Altering the amount and regularity of *Scottoiler SACI* supplied would change the overall performance and the quantities used in the test may not be optimal.

Figure 7-13: Chain efficiency degradation with *Triflow*

-- 52:12 120rpm 200W 0% wear PC91 chain --

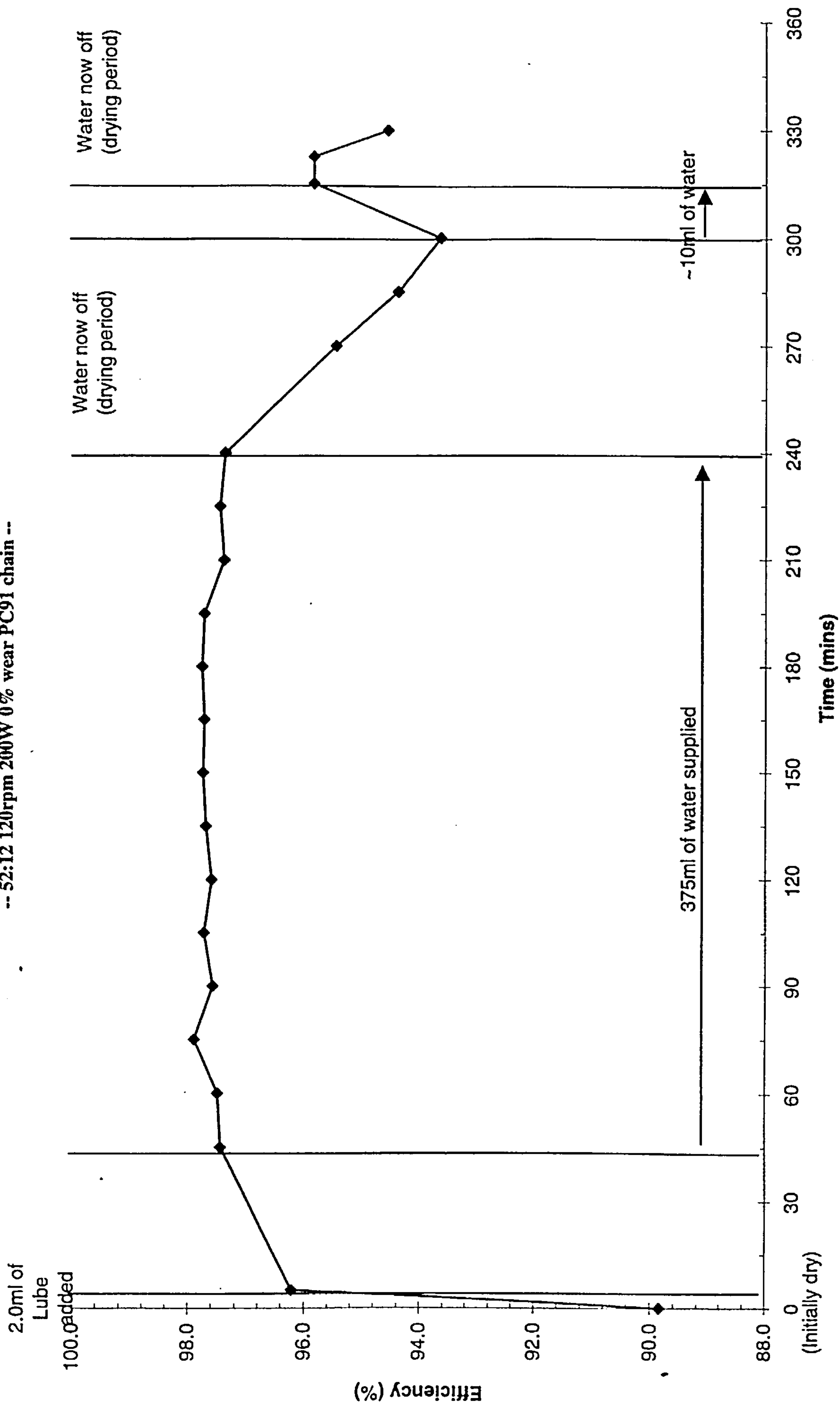


Figure 7-14: Chain Efficiency degradation with *Finish Line* (I)

-- 52:12 120rpm 200W 0% wear PC91 chain --

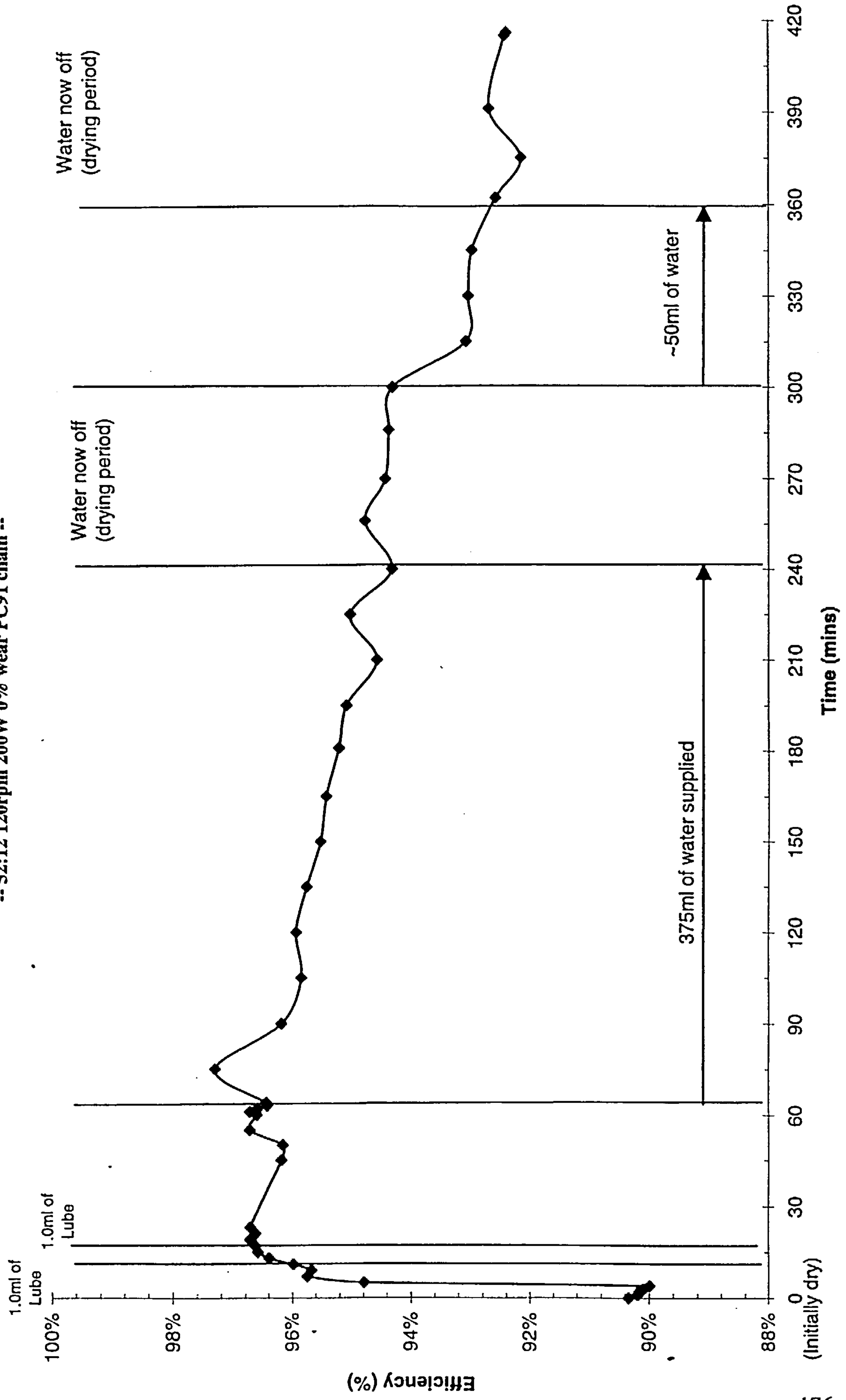


Figure 7-15: Chain Efficiency degradation with *Finish Line* (2)

-- 52:12 120rpm 200W 0% wear PC91 chain --

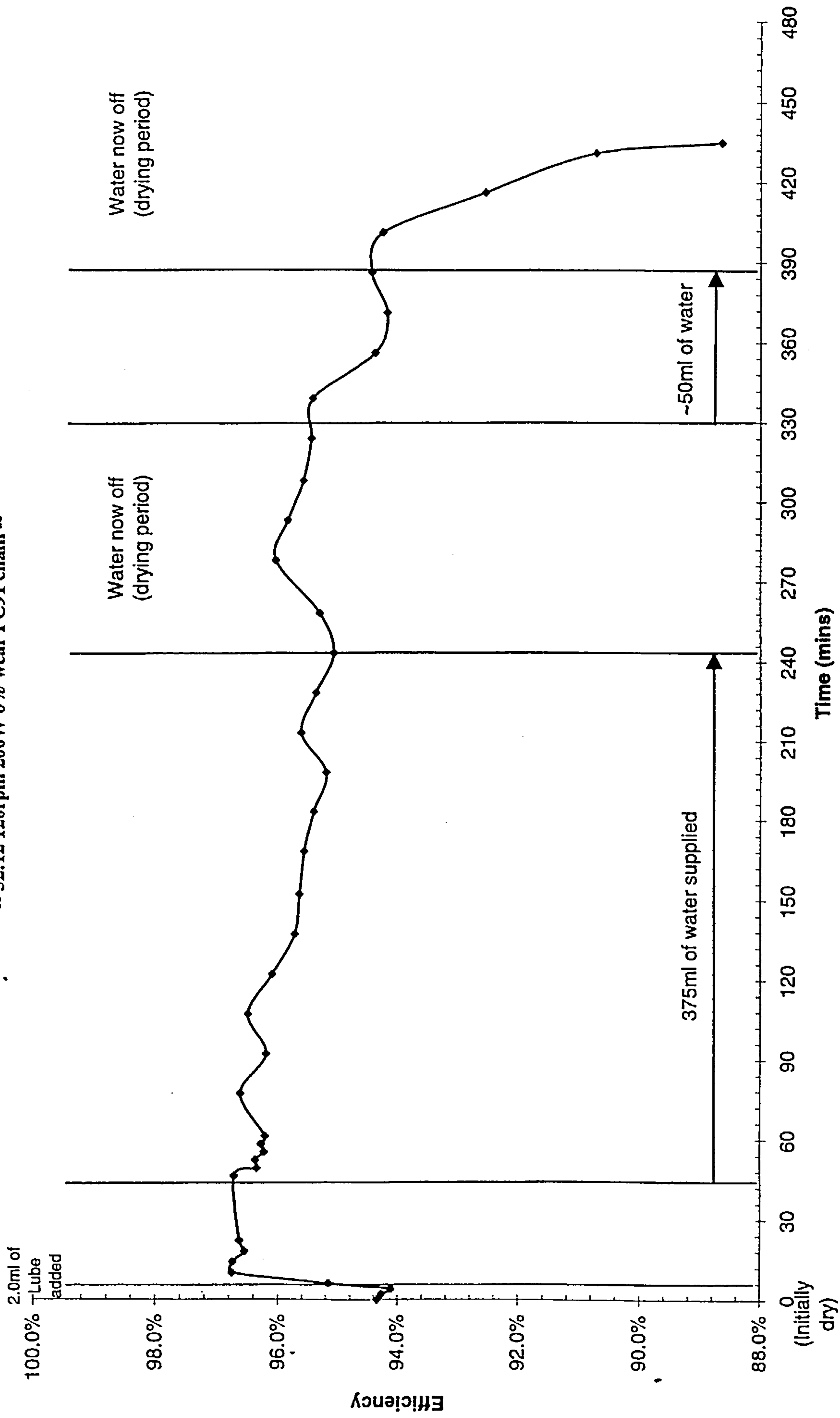
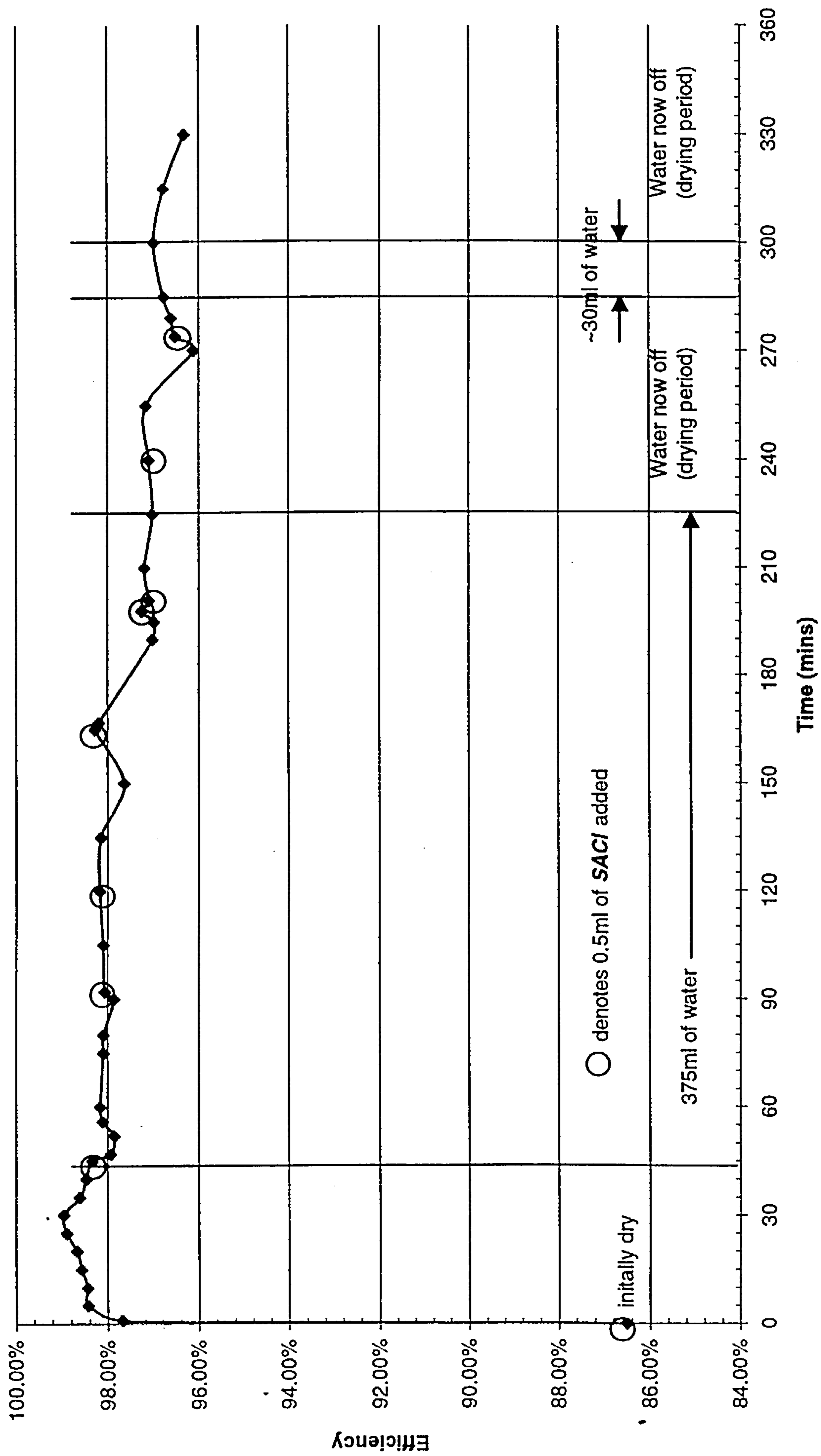


Figure 7-16: Chain Efficiency degradation with SACI  
 -- 52:12 120rpm 250W 0% wear PC91 chain --



### 7.5.5 Chain Tension

To examine the effects of chain tension on efficiency, power throughput was increased from 50W to 350W while keeping the input speed constant at 100rpm. The resulting increasing torque translates to an increase in chain tension. Three sprocket ratios were used 38:21, 38:16 and 38:12 sprocket and a recently lubricated PC91 chain.

Figure 7-17 shows the mean values of efficiency transmitted as power increases. The curve shows the expected shape of low initial efficiency, rising as the power throughput increases. The larger rear sprockets return higher efficiency values than smaller ones. This effect was first observed in 7.5.1 and will be looked at in more detail in 7.5.6 with the misalignments associated with sprocket changes removed.

To show the relationship between efficiency and tension, efficiency has been plotted against the reciprocal of tension in Figure 7-18. In order to illustrate the level of scatter for the experiment three values of efficiency are shown for each reciprocal tension value, representing three different 1-minute snap shots of data. A linear relationship was observed for all sprocket sizes, with the intercept with the efficiency axis indicating a maximum achievable efficiency. For example, examining the 38:21 data suggests a value of around 99.3% at an infinitely high chain tension. For the less efficient 38:12 set-up, the maximum suggested attainable efficiency would be 98.8%. In relation to a peak power output of a top class cyclist of 2kW, the reciprocal of chain tension would be 0.00038, all other factors remaining the same. A less powerful cyclist may produce 500W, nonetheless the range indicated in the figure illustrates that an efficiency of between 98 and 99% could be possible.

Figure 7-17: Chain efficiency and power, varying tension

-- 100rpm 0% wear PC91 chain --

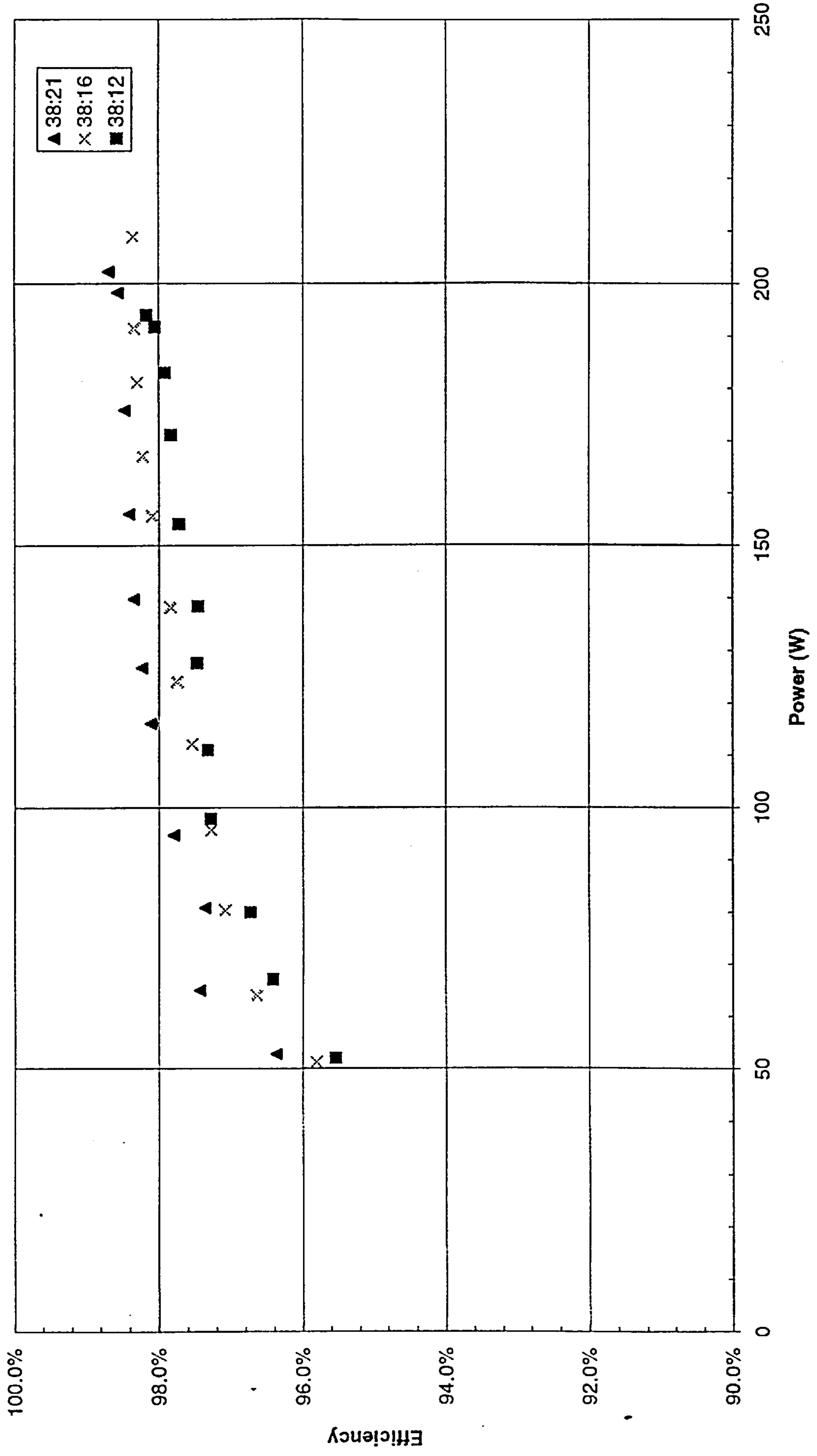
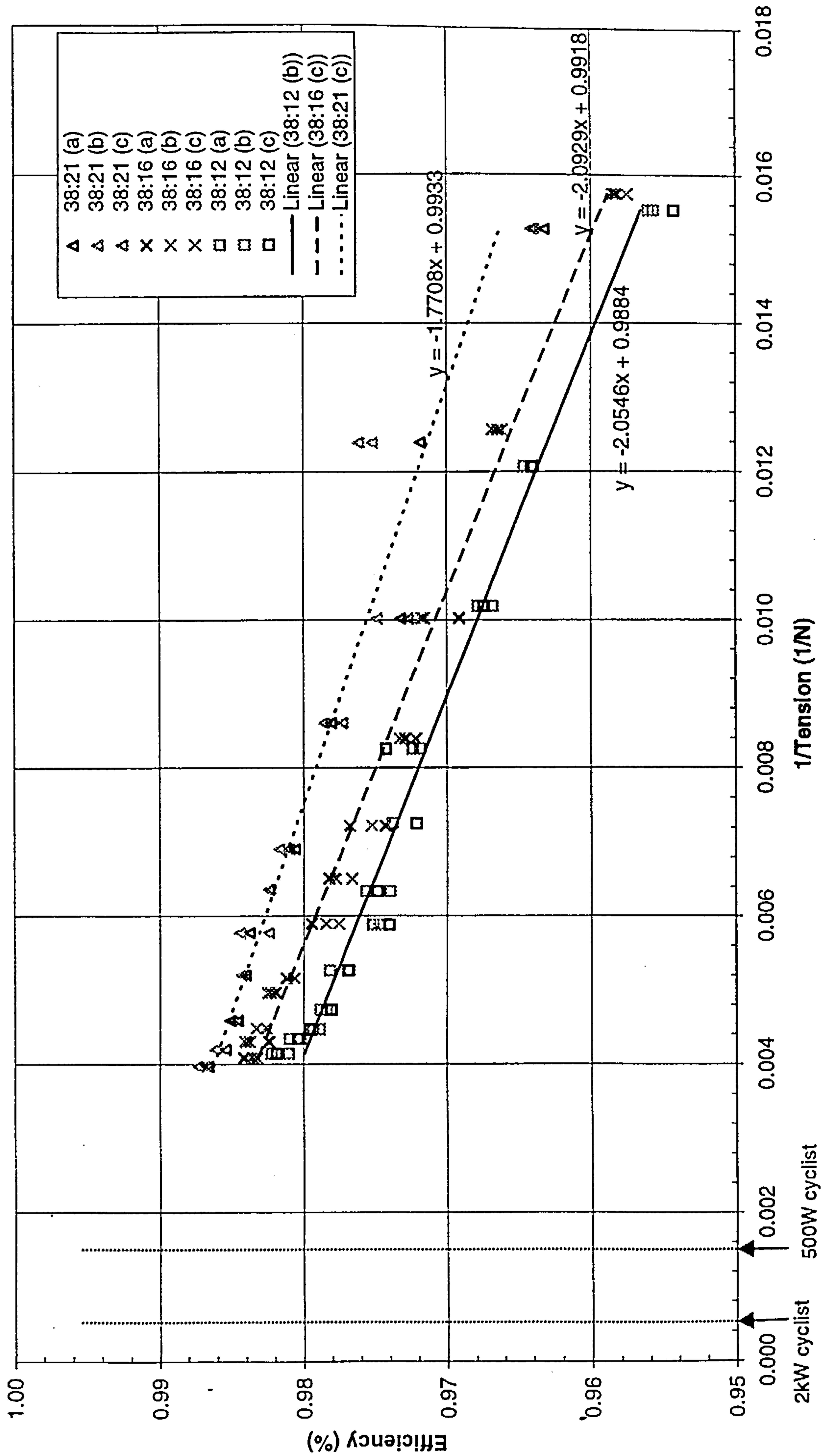


Figure 7-18: Chain efficiency and chain tension

-- 100rpm 0% wear PC91 chain --



### 7.5.6 Sprocket size

A factor inherent in the derailleur gear design is that every gear combination will have an element of misalignment, apart from a number equal to the total number of front sprockets. To isolate the effects of gear selection, two sets of experiments were conducted; those in this section cover sprocket size and those in 7.5.7 examine misalignment. In order to remove the factor of speed, sprockets were chosen to maintain a constant (within 4%) gear ratio. Finally, because changing gear ratio alters the amount of slack chain and changes slack side losses the series of tests was completed both with and without the derailleur gear mechanism in place. Manual adjustments were made to the length of the chain when operated without the derailleur to prevent excess slack chain. The chain lengths used for each sprocket and derailleur combination are given in Table 7-3 and the results are shown in Figures 7-18 to 7-20 with the letters *a*, *b* and *c* denoting the efficiency derived from 3 consecutive time snaps each of length 60s.

Figure 7-19 shows the results from a 48:21 sprocket combination operating at 130 rpm using a 0% wear, PC91 lubricated chain. The most striking feature of this graph is the high efficiency (99.56%) achieved when no derailleur is present. Furthermore, the efficiency did not change significantly despite increasing the input power from 50 to 230 watts. The results with the derailleur present are similar to other test data with a maximum plateau efficiency reached at high power.

A slightly different set of data curves is shown in 7-19 from the 38:16 sprocket combination. The non-derailleur results show high efficiency (98.7%) at low power with a slight reduction as the power increased. With the rear derailleur present the efficiency exhibited the characteristic behaviour with power.

The lowest overall efficiency performance was found with the set of smallest sprocket combinations, 28:12. The maximum attained efficiency was 98.8% without the derailleur and 98.5% with it. The results (Figure 7-21) for the non-derailleur test showed a different trend to the other sized sprockets with, the efficiency rising over the power range considered.

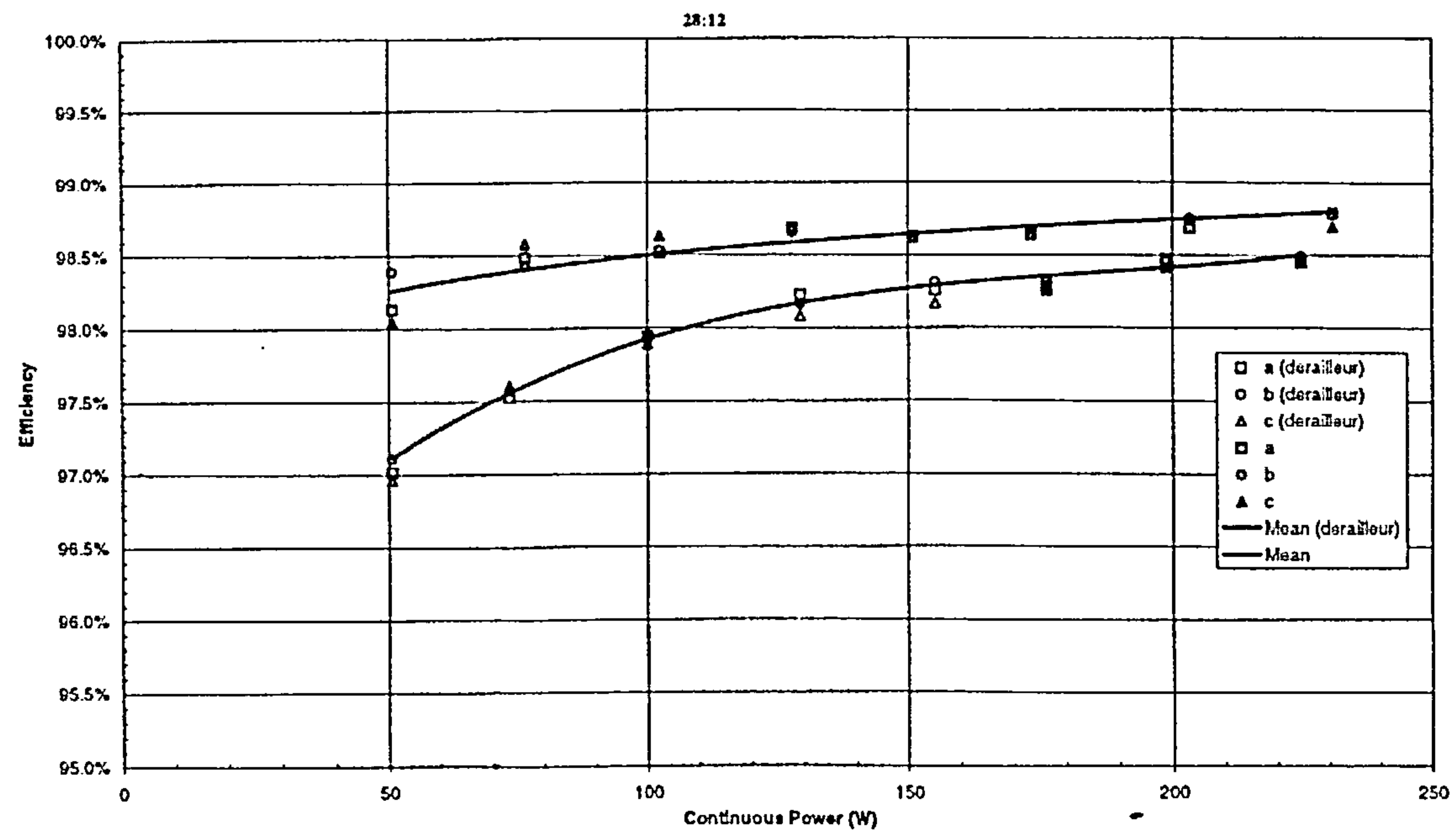
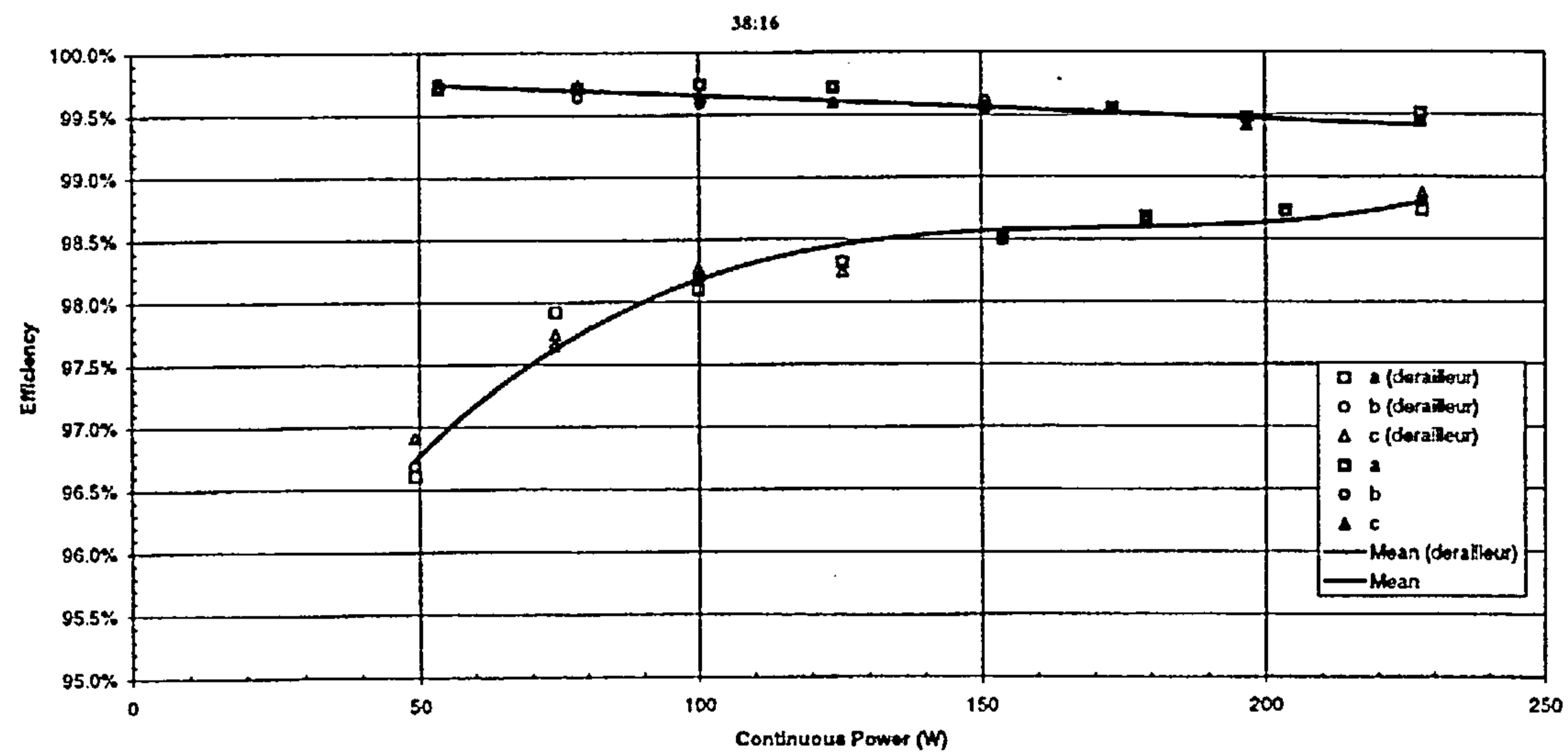
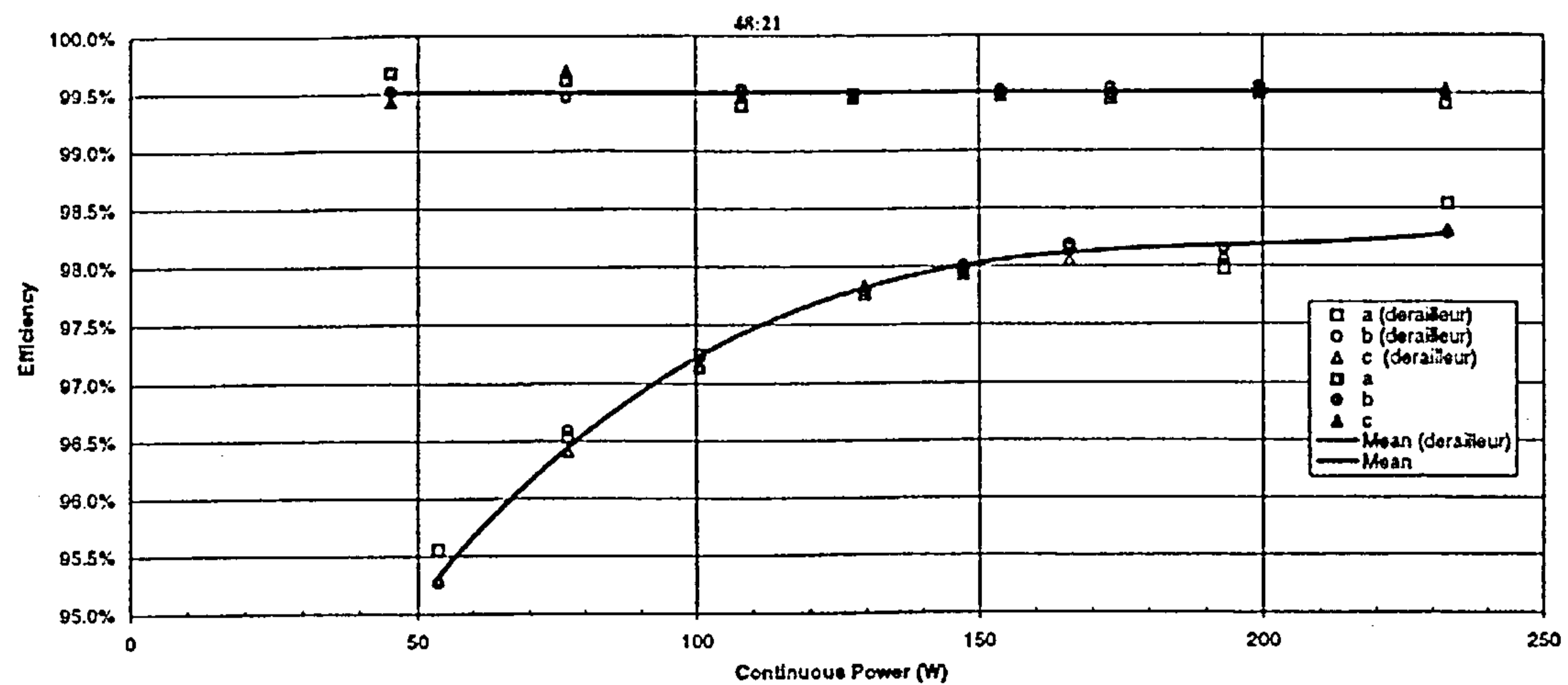
**Table 7-3 : Chain Length and Sprocket Size**

<b>Sprocket Ratio</b>	<b>Chain Length</b>		<b>Peak Efficiency</b>	
	<b>with derailleur</b>	<b>without derailleur</b>	<b>with derailleur</b>	<b>without derailleur</b>
<b>48:21</b>	114	110	98.5	99.7
<b>38:16</b>	114	102	98.8	99.7
<b>28:12</b>	108	96	98.5	98.8

Figure 7-19: Chain Efficiency and Sprocket size, 48:21

Figure 7-20: Chain Efficiency and Sprocket size, 38:16

Figure 7-21: Chain Efficiency and Sprocket size, 28:12  
-- 130rpm 0% wear PC91 chain --



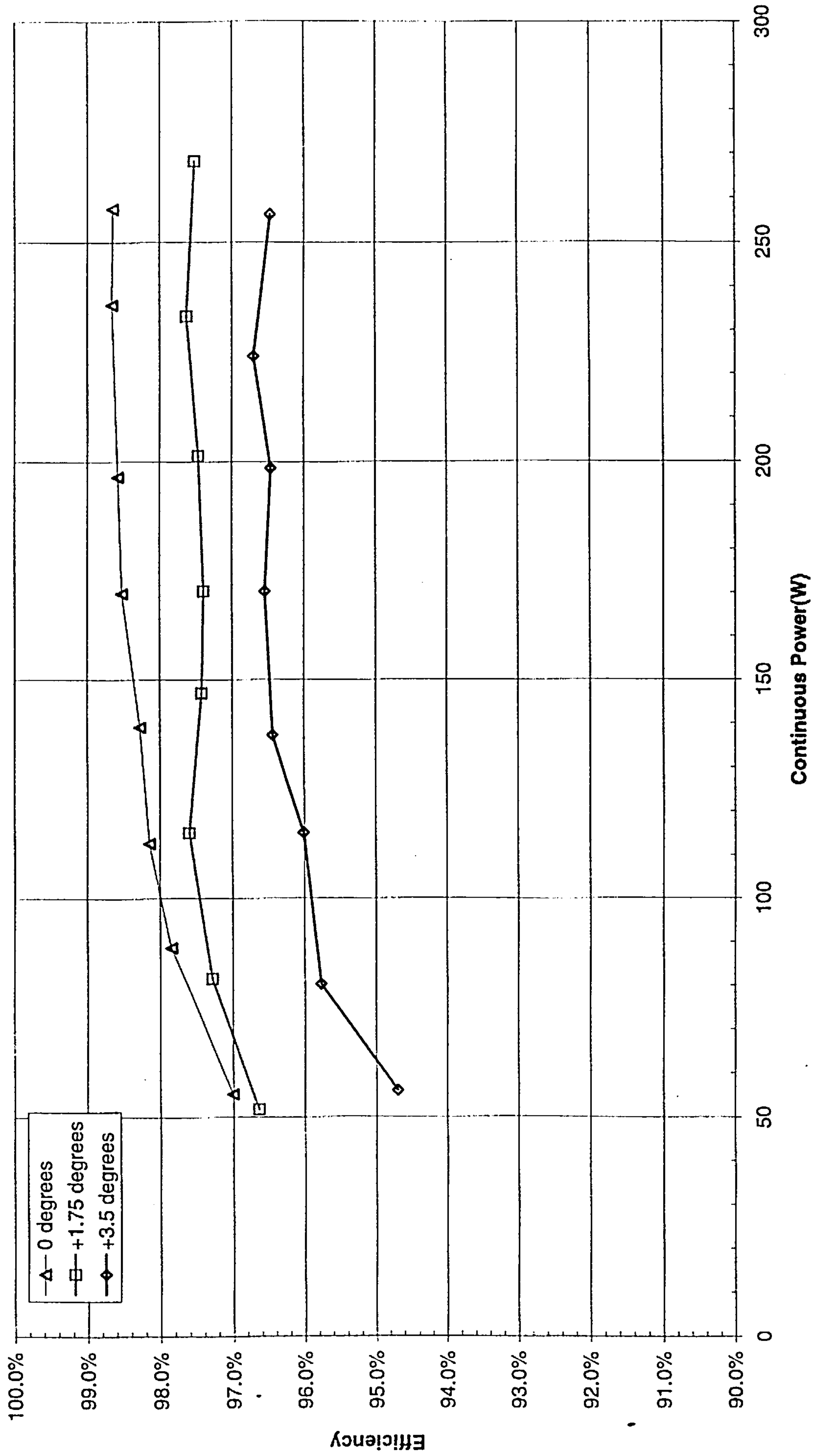
### 7.5.7 Chain Alignment

This experiment was devised to investigate in isolation the effect of alignment between front and rear sprockets. A 38:16 gear combination was chosen and operated at 120 rpm with a PC91 chain through a power range of 50-250W. To simulate the maximum misalignment achievable with a typical gear system an upper limit of  $3.5^\circ$  was set and an intermediate value of  $1.75^\circ$  was shown. Each test was also carried out with no misalignment in order to provide a datum.

The transmission efficiency versus power data is plotted in Figure 7-22. The familiar curve of the efficiency-power relationship is seen in all three cases with the curves being approximately parallel. The offset between the curves was in approximate proportion to the degree of misalignment, being about 2.3% for the  $3.5^\circ$  misalignment.

Figure 7-22: Chain efficiency and Sprocket Alignment

-- 38:16 120rpm 0% wear PC91 chain --



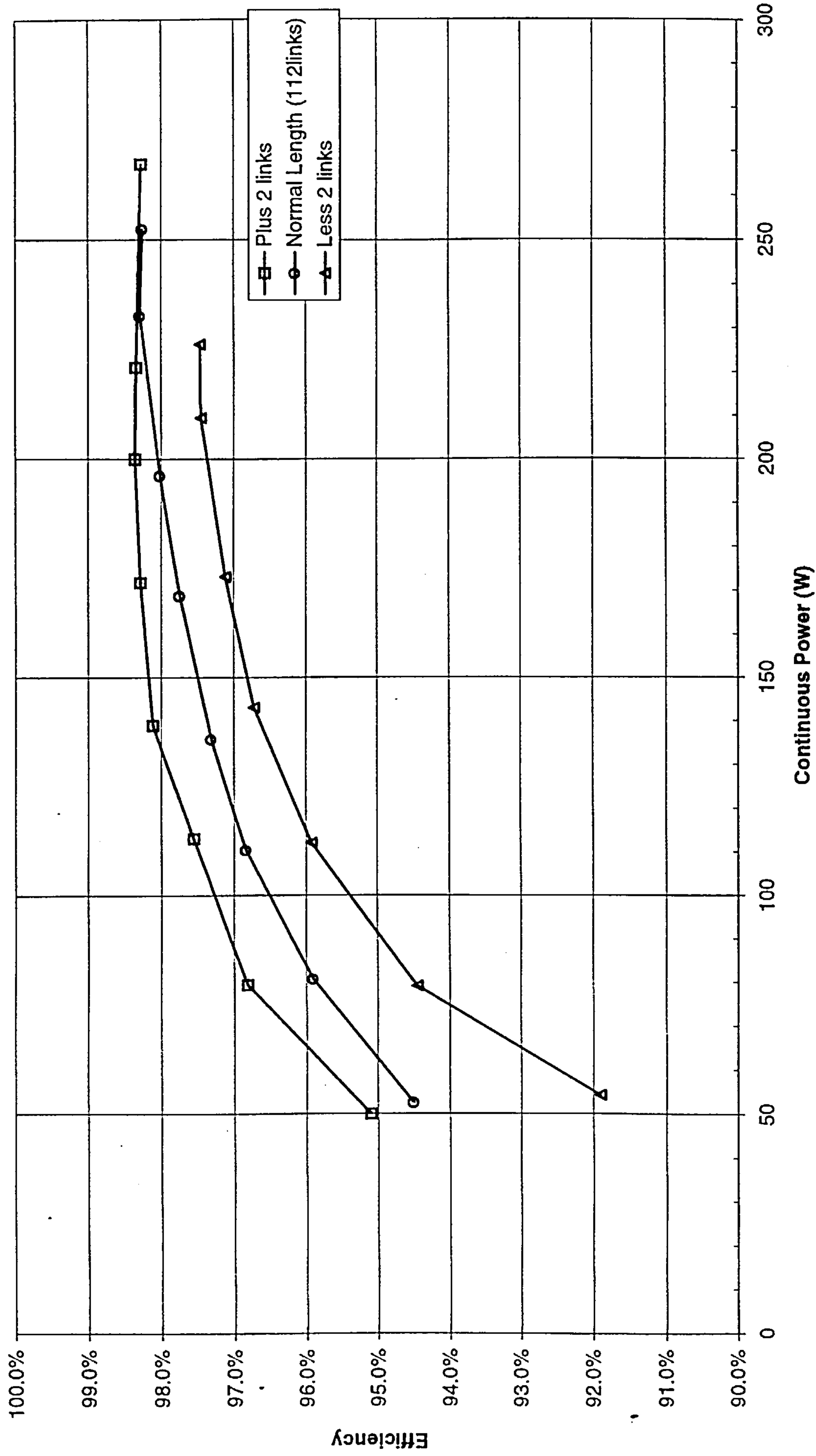
### 7.5.8 Chain Length

The last final isolated secondary effect examined was the length of chain in the drive. In order to accommodate changes in sprocket size, the excess chain length is normally accommodated by the changing geometry of the rear derailleur. A tensioning arm maintains a taut length of chain between the front and rear sprockets on the slack side and the arm moves backwards if the length of excess chain increases and vice versa. As the excess chain length increases, the chain lap also increases and the chain articulates through a greater amount. A further change also occurring is the movement arm of the derailleur and the geometry of the linkage which reduces the slack side tension when the arm is back; increasing tension the further forward it operates. This effect also affects the slack side tension from length changes when different gear ratios are used.

A 52:12 sprocket combination was used in conjunction with a lubricated 0% wear PC91 chain. The speed range varied between 110 and 130 rpm and the input power between 50 and 250W. Three chain lengths were used, based on a normal length of 112 links with two links added or removed.

The results are shown in Figure 7-23 and all showed the typical efficiency-power relationship. The effect of lengthening the chain was to increase the efficiency except at very high power levels, where it converged with the normal length of chain. Shortening the chain resulted in a drop in efficiency across the entire power range.

Figure 7-23: Chain Efficiency and Length of Chain  
 -- 52:15 110-130rpm 0% wear PC91 chain --



## 7.6 *Summary*

The multivariate analysis of power, speed, sprocket size, wear and lubricant factors has identified their relative effects on chain efficiency. An unworn lubricated chain, with large sprockets, zero misalignment and operating at high power will perform most efficiently. Smaller sprockets rotating at higher speeds will result in lower efficiency. Chain efficiency was shown to vary between 51% and 97% under the range of the above factors chosen.

An in-depth analysis of some of the variables examined in isolation revealed that chain efficiency is directly proportional to chain tension, larger sprockets improve efficiency and that the rear derailleur introduces several loss inducing parameters to the chain. The slack side tension and pressure of the derailleur mechanism was found to reduce efficiency by up to 5% at low power and 1.5% at high power throughputs in comparison with the same gear combination with no rear derailleur. Further losses are caused by misalignment between front and rear sprockets, a misalignment of  $3.5^\circ$  reducing efficiency by around 2% over the power range 50 to 250W. The length of the chain also had an effect on efficiency due to its effect on the geometry of the rear derailleur, longer lengths of chain resulting in better performance than chains with fewer links.

The effects of lubricant on chain efficiency revealed how water can act in the short term (2 minutes) as a lubricant. The ability of a lubricant to continue working whilst being diluted with water over the course of several hours was examined and it was found that some lubricants deteriorated more quickly than others. When the simulated weathering was stopped, the lubricating effect of the lubricant was invariably reduced.

## 8. Chain Mechanics and Frictional Loss

### 8.1 Introduction

Each instance of mechanical contact (sliding or rolling) of the chain and the associated interaction between component parts will now be considered with respect to the energy loss due to friction. In total, nine expressions for frictional losses are derived which together make up the overall theoretical efficiency for a bicycle chain drive. The overall efficiency expression therefore allows a separate estimate of the component losses, which is useful for discussion purposes.

### 8.2 Frictional losses – Tight side

Figure 8-1 shows a typical arrangement of a bicycle derailleur gear and chain system. As shown (shaded spots), there are 2 articulations per sprocket occurring at entry or exit, as the chain completes a full cycle around the system. Although most of the frictional losses are associated with the tight side tension ( $F_t$ ), there are not insignificant losses occurring from the slack side tension ( $F_s$ ) since the derailleur mechanism always maintains a non-zero tension around the two idler sprockets and the return span back to the driving (front) sprocket. The slack side losses are covered in 8.3

Generally, frictional losses occur wherever relative motion exists between adjacent components under a mechanical load. The following contact points were identified in Chapter 5 as sources of frictional power loss:

1. Chain pin and bush,
2. Bush and roller,
3. Chain offset.

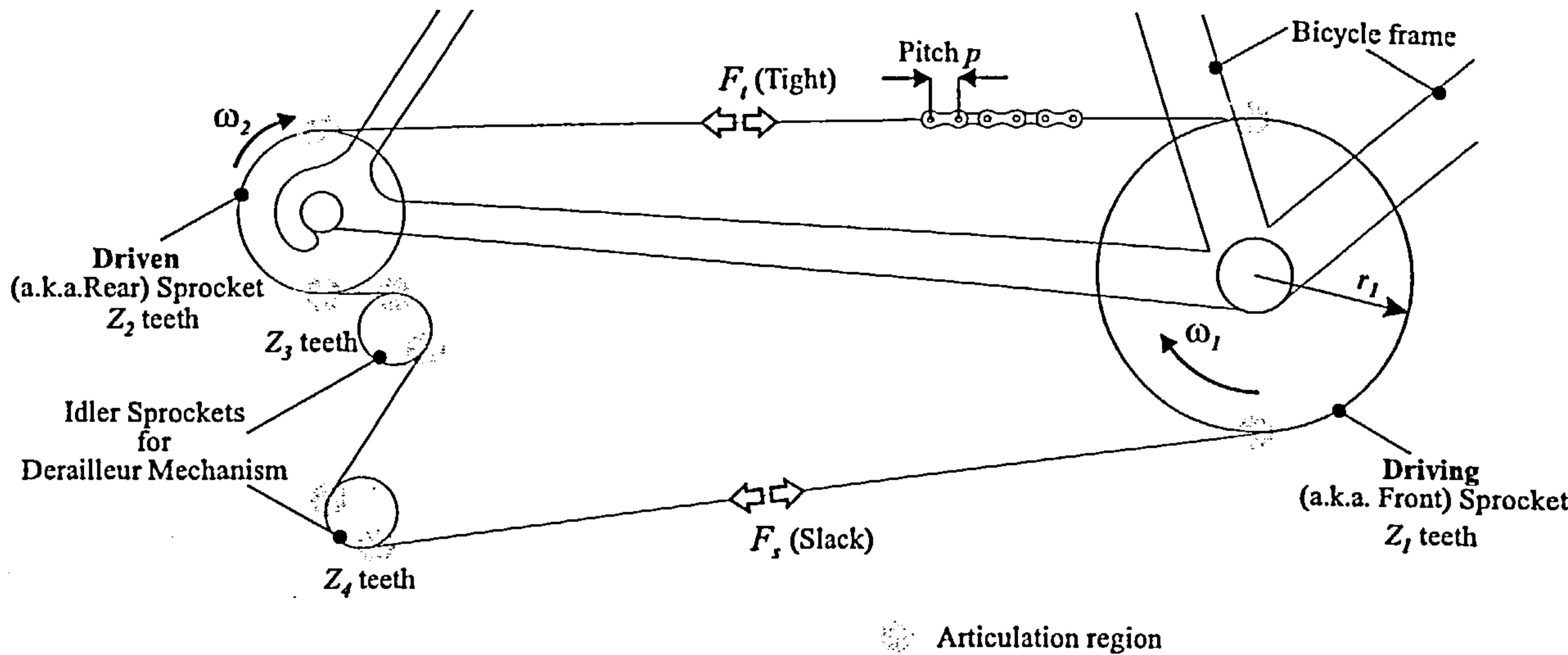


Figure 8-1: Chain arrangement on a bicycle

Fundamental analyses of chain forces and frictional losses at articulated joints have been performed by Binder<sup>(15)</sup>, Coenen and Peeken<sup>(42)</sup>, and Hollingworth and Hills<sup>(28),(39),(10)</sup>. The approach adopted here combines and extends the work of Binder and Coenen and Peeken in that the energy losses are calculated for each possible component interaction.

In analysing forces and energy losses within a chain system, it is important to distinguish between a 'pin link' and 'roller link' when these elements either enter or exit a sprocket. In the former case, relative motion or articulation takes place under constant tension (for example  $F_t$ ) whereas in the latter the force varies from the start to the end of engagement.

In the general case, frictional work may be defined as:

$$U_f = \int \bar{F} d\bar{s} \quad \text{Eq. 8-1}$$

where  $d\bar{s}$  represents the displacement over which the force  $\bar{F}$  does work.

Similarly, the rate at which frictional work is dissipated is given by:

$$P_f = \frac{d}{dt}(U_f) \quad \text{Eq. 8-2}$$

For steady-state conditions at a given rate, the frictional power loss of a chain system may be estimated by the summation of the constituent parts of  $U_f$ . Using the nomenclature in Chapter 4, the following expressions for frictional power loss are developed.

## 8.2.1 Chain Pin and Bush

### 8.2.1.1 Forward pin, pin-link

For the driving sprocket, the force between pin and bush remains constant and equal to  $F_t$ . The distance over which the force acts is the product of radius of the pin ( $d/2$ ) and the pressure angle over which the articulation occurs.

Frictional Work,  $U_{f1} = (\mu F_t) \times d/2 \times \alpha_1$

$$= \pi \mu F_t \frac{d}{Z_1}$$

The rate of doing work may be derived from the rate at which the chain completes a cycle around the entire system. The distance travelled by the complete length of chain is the product of the number of links ( $N_L$ ) and the chain pitch ( $p$ ). The time taken,  $T$ , for this length of chain to complete a cycle is the distance divided by the mean chain line pitch sprocket velocity. This velocity is the product of the angular frequency ( $\omega_1$ ) and chain line radius of curvature ( $r_1$ ), i.e.

$$T = \frac{N_L p}{\omega_1 r_1}$$

so the rate of work done by the chain is simply the reciprocal of this. Expressing the radius as its relationship with the sprocket circumference,  $\frac{Z_1 p}{2\pi}$  then,

$$\frac{1}{T} = \frac{\omega_1 r_1}{N_L p} = \frac{\omega_1 Z_1 p}{2\pi N_L p} \Rightarrow \frac{\omega_1 Z_1}{2\pi N_L}$$

thus the power loss  $P_{f1} = \pi \mu F_t \frac{d}{Z_1} \times \frac{\omega_1 Z_1}{2\pi N_L}$

$$= \mu F_t d \frac{\omega_1}{2N_L} \quad \text{Eq. 8-3}$$

For the driven sprocket however, the force between pin and bush varies between  $F_t$  and

$$F_t \frac{\sin \phi_2}{\sin(\phi_2 + \alpha_2)} \quad (\text{from Chapter 4}).$$

A precise evaluation of the mean value,  $F_{mean}$  for the tension and  $N_{mean}$  for the tooth force may be performed by a process of integration:

$$F_{mean} = \frac{1}{\alpha} \int_0^\alpha F_\theta d\theta, \quad N_{mean} = \frac{1}{\alpha} \int_0^\alpha N_\theta d\theta$$

However, since the degree of non-linearity is small, together with the articulation angle  $\alpha$ , the expressions may be represented by an arithmetic mean, as shown by:

$$F_m = \frac{F_t}{2} \left\{ 1 + \frac{\sin \phi}{\sin(\phi + \alpha)} \right\}, \quad N_m = \frac{F_t}{2} \left\{ \frac{\sin \phi}{\sin(\phi + \alpha)} \right\}$$

These expressions may be used to evaluate frictional losses at the pin-bush and bush-roller interfaces. Binder<sup>(15)</sup> also considered it sufficiently accurate to take the average force. For a driven sprocket, then, the average force is:

$$F_{m2} = \frac{F_t}{2} \left[ 1 + \frac{\sin \phi_2}{\sin(\phi_2 + \alpha_2)} \right]$$

Now the frictional work,  $U_{f2} = \pi \mu F_{m2} \frac{d}{Z_2}$

$$\text{Rate of doing work} = \frac{\omega_2 Z_2}{2\pi N_L}$$

$$\therefore P_{f2} = \frac{\mu d F_t \omega_2}{2N_L} \left[ 1 + \frac{\sin \phi_2}{\sin(\phi_2 + \alpha_2)} \right] \quad \text{Eq. 8-4}$$

Combining equations 8-3 and 8-4 gives the power loss for each forward pin over both driving and driven sprockets.

### 8.2.1.2 Rear pin, roller-link

For the driving sprocket on the roller link the analysis is similar to 8.2.1.1, the average force this time being given by:

$$F_{m1} = \frac{F_t}{2} \left[ 1 + \frac{\sin \phi_1}{\sin(\phi_1 + \alpha_1)} \right]$$

and the power loss is given by:

$$P_{f3} = \frac{\mu F_t d \omega_1}{2N_L} \left[ 1 + \frac{\sin \phi_1}{\sin(\phi_1 + \alpha_1)} \right] \quad \text{Eq. 8-5}$$

And for the driven sprocket the analysis is similar to 8-3, so that:

$$P_{f4} = \mu F_t \frac{d\omega_2}{2N_L} \quad \text{Eq. 8-6}$$

Combining 8-5 and 8-6 gives the power loss for each rear pin over both driving and driven sprockets.

## 8.2.2 Bush and roller

### 8.2.2.1 Rear roller, roller-link

If the rear roller of the roller link is now considered by using the tooth force rather than the tension force then the energy loss is:

$$P_{f5} = \pi\mu \frac{DN_{m2}}{Z_2} \times \frac{\omega_2 Z_2}{2\pi N_L}$$

where  $D$  is the roller diameter (m) and  $N_{m2}$  is the average tooth force,

$$N_{m2} = \frac{F_t}{2} \frac{\sin \alpha_2}{\sin(\alpha_2 + \phi_2)}$$

$$\therefore P_{f5} = \mu F_t \frac{D\omega_2}{4N_L} \frac{\sin \alpha_2}{\sin(\alpha_2 + \phi_2)} \quad \text{Eq. 8-7}$$

No loss occurs on the driving sprocket since there is no relative rotation between bush and roller. Hence 8-7 gives the power loss for each rear roller over both driving and driven sprockets.

### 8.2.2.2 Forward roller, roller-link

The power loss for each forward roller over both driving and driven sprockets is similar to 8.2.2.1. Here, no loss occurs on the driven sprocket since no relative motion occurs between bush and roller, and so

$$P_{f6} = \mu F_t \frac{D\omega_1}{4N_L} \frac{\sin \alpha_1}{\sin(\alpha_1 + \phi_1)} \quad \text{Eq. 8-8}$$

### 8.2.3 Chain offset

Due to the nature of the derailleur system, both driving and driven sprockets will be co-planar for only one position or gear ratio. Other ratios require that a degree of offset will be necessary, a condition accommodated by the inherent flexibility of the chain. Figure 8-2 illustrates a typical layout with an overall offset angle  $\beta$ . This offset produces a lateral force  $F_t \sin \beta$  that results in frictional contact between the inner and outer link plates during articulation at the sprockets. The frictional component of the inner plates rubbing against the tooth flank is not considered in this analysis.

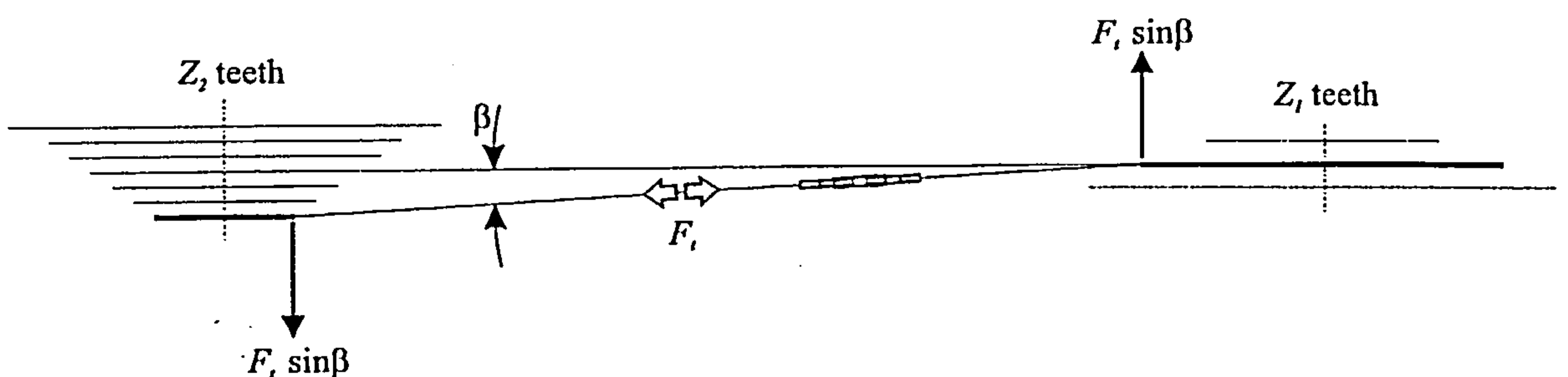


Figure 8-2: Chain misalignment

As in the previous sections, distinction between a pin link and roller link during articulation is made in order to cater for variations in the force causing the

offset contact and therefore friction between link plates. Figure 8-3 shows a schematic of the forces generated as a result of chain offset between driver and driven sprockets. It is assumed that link *A* is fully engaged with the driven (rear) sprocket (and parallel to its plane) while link *B* is just short of engagement and carrying tension  $F_t$ . The angle of misalignment  $\gamma$  between *A* and *B* is dictated by the geometry and manufacturing tolerances of the chain links. It is seen that edge contact between the inner and outer plates occurs at points 1 and 2, giving rise to forces  $F_1$  and  $F_2$ .

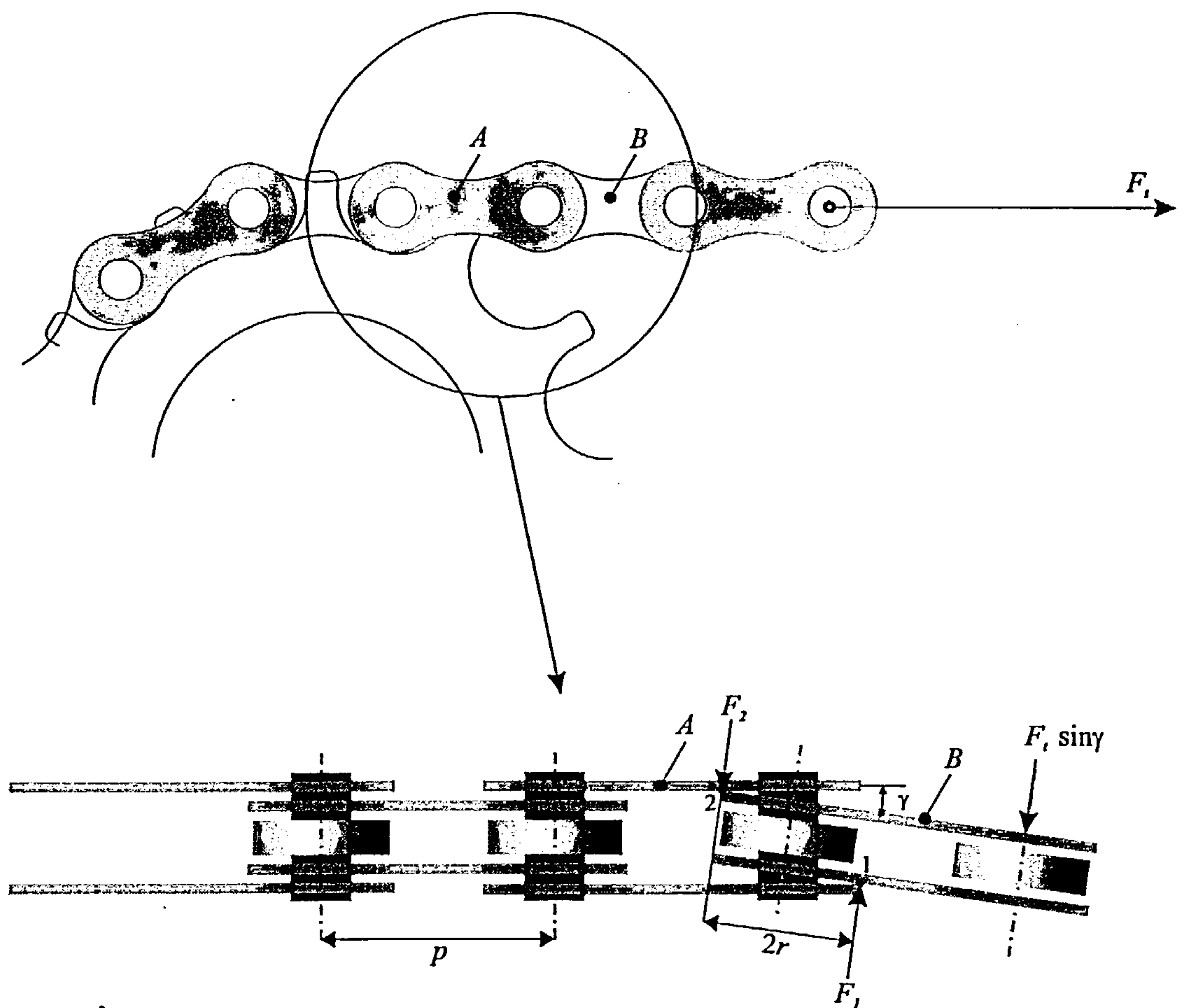


Figure 8-3: Offset forces schematic

Analysis of the forces acting on link  $B$  yields:

$$\begin{aligned} F_1 &= \frac{1}{2} F_t \sin \gamma \left( \frac{p}{r} + 1 \right) \\ F_2 &= \frac{1}{2} F_t \sin \gamma \left( \frac{p}{r} - 1 \right) \end{aligned} \quad \text{Eq. 8-9}$$

Where  $p$  is the chain pitch and  $r$  is the radius at which  $F_1$  and  $F_2$  act during articulation of link  $B$ . Expression 8-9 relates to the pin link case where the basic tension  $F_t$  remains constant. For the roller link case, this force is variable and must be replaced by the average force  $F_m$  where:

$$\begin{aligned} F_{mi} &= \frac{F_t}{2} \left[ 1 + \frac{\sin \phi_i}{\sin(\phi_i + \alpha_i)} \right] \\ \text{i.e.} \quad F'_1 &= \frac{1}{2} F_{m1} \sin \gamma \left( \frac{p}{r} + 1 \right) \\ F'_2 &= \frac{1}{2} F_{m2} \sin \gamma \left( \frac{p}{r} - 1 \right) \end{aligned} \quad \text{Eq. 8-10}$$

As in previous sections, the rate of doing work is given by  $\frac{\omega Z}{2\pi N_L}$  and the distance over which forces  $F_1$ ,  $F_2$ ,  $F'_1$  and  $F'_2$  operate is  $r\alpha$ . Hence considering frictional losses on the tight side only, the power loss for chain offset may be expressed:

$$P_{f7} = \frac{\mu_s r \alpha_1 \omega_1 Z_1}{2\pi N_L} (F_1 + F_2 + F'_1 + F'_2) + \frac{\mu_s r \alpha_2 \omega_2 Z_2}{2\pi N_L} (F_1 + F_2 + F'_1 + F'_2)$$

now substituting in 8-9 and 8-10,

$$P_{f7} = F_t \frac{p}{r} \sin \gamma \left\{ 1 + 1 + \frac{\sin \phi_1}{2 \sin(\phi_1 + \alpha_1)} + \frac{\sin \phi_2}{2 \sin(\phi_2 + \alpha_2)} \right\} \times \left\{ \frac{\mu_s r \alpha_1 \omega_1 Z_1}{2\pi N_L} + \frac{\mu_s r \alpha_2 \omega_2 Z_2}{2\pi N_L} \right\}$$

$$\text{or, } P_{f7} = \frac{F_t \mu_s p \sin \gamma}{2\pi N_L} (\omega_1 \alpha_1 Z_1 + \omega_2 \alpha_2 Z_2) \left\{ 2 + \frac{\sin \phi_1}{2 \sin(\phi_1 + \alpha_1)} + \frac{\sin \phi_2}{2 \sin(\phi_2 + \alpha_2)} \right\} \text{Eq. 8-11}$$

### 8.3 Frictional Losses – Slack Side

The previous expressions 8-3 to 8-9 estimate the frictional power loss  $P_f$  due to the effects of tight side tension  $F_t$ . The slack side tension  $F_s$ , although less than  $F_t$ , still has an effect on the overall losses of the chain drive system. Between the exit from the driving sprocket and the entry to the driven sprocket, the tension also operates on the idler sprockets that form the derailleur mechanism.

If it is assumed that the gear mechanism maintains a constant tension  $F_s$  around the idler sprockets 3 and 4 (Figure 8-1) then additional expressions may be written to account for the losses associated with the slack side.

#### 8.3.1.1 Idler sprockets

In the derailleur system both idler sprockets have the same number of teeth (typically 11) i.e.  $Z_3 = Z_4$  and  $\omega_3 = \omega_4$ . Since there is neither a driver nor driven sprocket the analysis can be made simpler by considering an average force that operates at all 4 articulations of the chain. The following expression accounts for all idler sprocket friction losses arising from interaction with the chain (i.e. ignores bearing losses):

$$P_{f8} = 4 \times \left\{ \frac{\mu d F_s \omega_3}{2 N_L} \left[ 1 + \frac{\sin \phi_3}{\sin(\phi_3 + \alpha_3)} \right] \right\} + 2 \times \left\{ \frac{\mu D F_s \omega_3}{4 N_L} \left[ \frac{\sin \alpha_3}{\sin(\alpha_3 + \phi_3)} \right] \right\}$$

$$\therefore P_{f8} = \frac{\mu F_s \omega_3}{N_L} \left[ 2d \left\{ 1 + \frac{\sin \phi_3}{\sin(\phi_3 + \alpha_3)} \right\} + \frac{D}{2} \left\{ \frac{\sin \alpha_3}{\sin(\alpha_3 + \phi_3)} \right\} \right] \quad \text{Eq. 8-12}$$

### 8.3.1.2 Driver & Driven Sprockets

Losses occur at exit from the driving and entry to the driven sprockets, both at tension  $F_s$ . Using previous expressions, an expression may be obtained for the remaining sources of power loss.

$$P_{f9} = \frac{\mu F_s d \omega_1}{2N_L} + \frac{\mu F_s d \omega_2}{2N_L} \left[ 1 + \frac{\sin \phi_3}{\sin(\phi_2 + \alpha_2)} \right] + \frac{\mu F_s d \omega_1}{2N_L} \left[ 1 + \frac{\sin \phi_1}{\sin(\phi_1 + \alpha_1)} \right] + \frac{\mu F_s d \omega_2}{2N_L} \\ + \frac{\mu F_s d \omega_2}{4N_L} \left\{ \frac{\sin \alpha_2}{\sin(\alpha_2 + \phi_2)} \right\} + \frac{\mu F_s d \omega_1}{4N_L} \left\{ \frac{\sin \alpha_1}{\sin(\alpha_1 + \phi_1)} \right\}$$

## 8.4 Transmission Efficiency

$$\text{Efficiency, } \eta, \text{ is defined as: } \eta = \frac{\text{Input Power} - \text{Losses}}{\text{Input power}} = 1 - \frac{P_{Loss}}{P_{Input}}$$

Since the expressions for power losses  $P_{f1}..P_{f9}$  are per link, they must be multiplied by  $N_L/2$  to give the total loss, noting that the total number of links  $N_L$  is evenly divided between pin links and roller links

$$\therefore P_{Loss} = \frac{N_L}{2} \sum_{i=1}^9 P_{fi}$$

Given that the nominal power input is defined as:

$$P_{Input} = (F_t - F_s) \frac{D_1 \omega_1}{2}$$

and the mean line circumference for the front sprocket may be expressed as  $Z_1 p = \pi D_1$

then:

$$P_{Input} = F_t \left( 1 - \frac{F_s}{F_t} \right) \frac{\omega_1 Z_1 p}{2\pi} \quad \text{Eq. 8-13}$$

Combining the expressions for power input and overall efficiency,

$$\eta = 1 - \frac{\pi N_L \sum_{i=9}^9 P_{fi}}{\omega_1 Z_1 p F_t \left( 1 - \frac{F_s}{F_t} \right)} \quad \text{Eq. 8-14}$$

To evaluate the final expression for chain efficiency a series of estimations must be made for some of the parameters. The pressure angle,  $\phi$ , for the bicycle sprockets may be assumed to be calculated using the ASA method,  $\phi = 35^\circ - \frac{120^\circ}{Z}$ . A further general assumption may be made that this profile is similar for all sizes of sprocket. For the numerical estimates of efficiency used in Chapter 9, the pressure angle was taken to be  $31.8^\circ$ . The measurements of rolling and sliding coefficients of friction were used to suggest values of  $\mu$  at 0.004 (from Table 5-2) and  $\mu_s$  at 0.50 (from 5.5.1) accordingly. The  $N_L$  term for the number of links cancels on full expansion of equation 8-14. For the bicycle chain the pitch standard is 12.7mm. Finally an estimate of  $F_s$  is also required which varies between make, model and length of chain used; a value of 20-40N is appropriate estimated from spring balance measurements.

Upon evaluation of each individual frictional power loss, its contribution to the overall loss may be calculated. The pie chart in Figure 8-4 provides a visual indication for a typical cycle component usage (250W, 52:12, 80rpm). The largest components,  $P_{f2}$  and  $P_{f4}$  account for 63% of the total power loss.

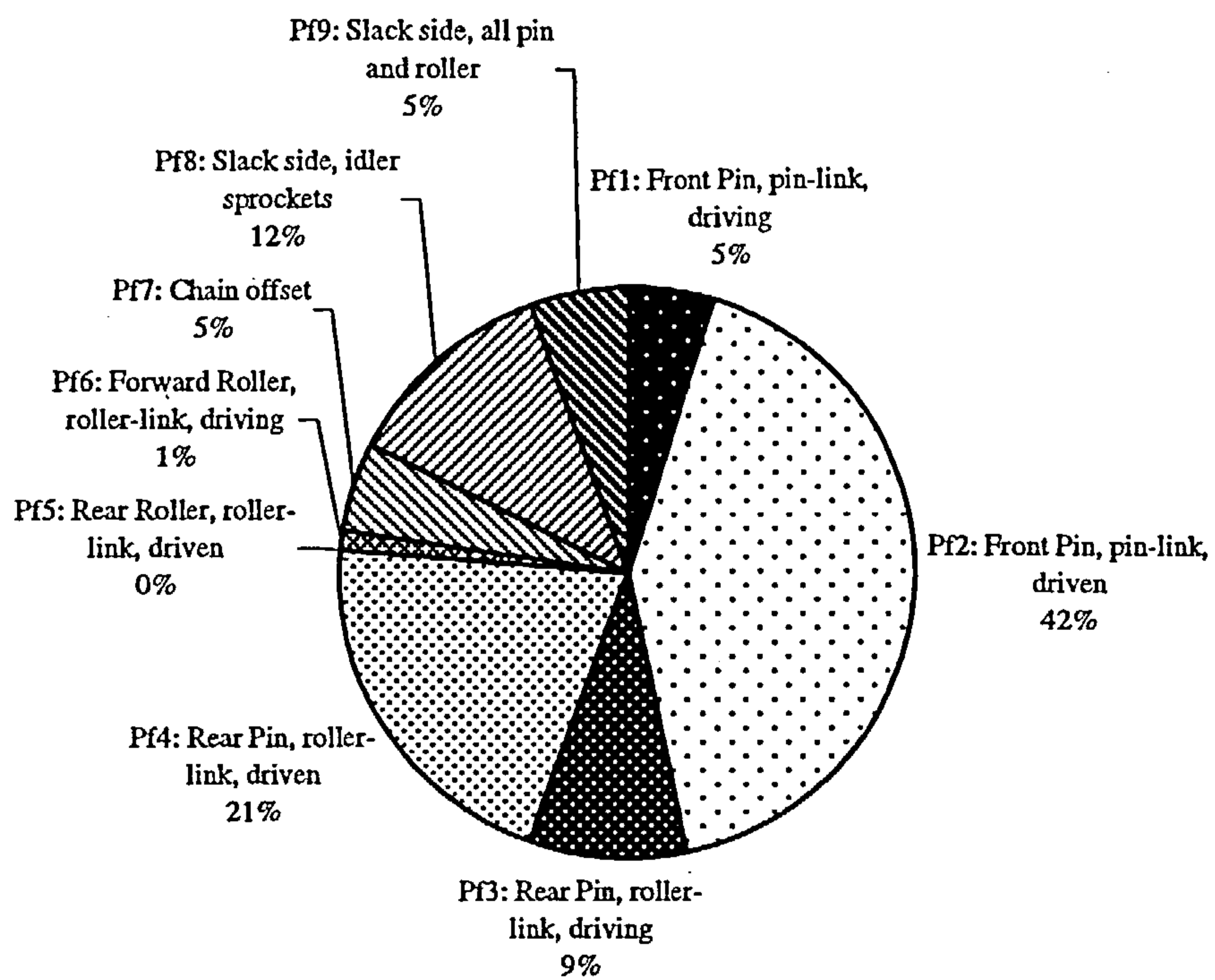


**Figure 8-4: Power Loss Constituents of Total Friction Component Modelling**

## **9. Discussion**

### **9.1 *Introduction***

This chapter examines the measurement of chain efficiency, secondary chain movements and the characteristics of chain efficiency in the light of the previous chapter, with a view to identifying the optimal gearing and lubrication strategy for competition applications. Because the accuracy of determination of efficiency is so important, the instrumentation and design of the apparatus used to measure chain efficiency is considered first. The quality of measurements is compared with others and possible improvements to the test rig will also be discussed. The analysis of the results from experiments in chain efficiency (Chapter 7) will be reviewed in conjunction with the analysis developed in Chapter 8 and the results of the ancillary experiments (Chapters 4, 5 and 6).

### **9.2 *Instrumentation and Measurement***

The popularity of the chain in its use as a power transfer medium stems primarily from its efficient drive transmission characteristics. In order to measure the small percentage of power loss an instrumentation system must have a good degree of accuracy. To measure further subtle changes in efficiency requires highly accurate and sensitive apparatus. With two independent torque measurements used to determine efficiency, their resultant data are divided by each other, compounding the error in the system. The consequences of errors are examined in Appendix A where it is shown that the errors in measurement of torque, efficiency and power are respectively, 0.13%, 0.26% and 0.175%. One potential uncontrolled source of error is the ripple in speed measurements (Figure 7-7). Since the source of this ripple could not be traced

and its fundamental frequency was unattributable to the chain drive system, it has been assumed the angular velocity is constant under given experimental conditions and the mean value used. All power data used for charting an analysis was time averaged as a matter of course.

If a loss only measurement were required, a different approach would have been taken, such as the four square principle. In such an approach the same level of accuracy could be attained more easily because only a single measurement of the power required to overcome the system losses is necessary. An in-line torque measurement system was chosen to return the most accurate readings of shaft power. Measuring anywhere else than on the sprocket itself would require estimations of such factors as bearing loss.

Traditional in-line torque transducing methods such as slip rings and FM telemetry were costly solutions that had recognised limitations with respect to the quality of data returned. The alternative methods offered commercially were also cost prohibitive and either had no proven record of performance or required an element of bespoke design necessary for their implementation.

By combining traditional methods of strain measurement with a novel data transmission system, the benefits of accuracy and low cost would be met. The most appropriate solution was found to be the use of strain gauges of transducer quality mounted on the shafts in such a manner as to measure pure torque (with bending effects cancelled). Strain gauges require only electronics and it was possible to employ high quality but inexpensive discrete components to achieve transmission and amplification.

The transfer of the torque signal was based on the frequency modulation principle used by FM radio and an infrared (IR) link converted the voltage signal to frequency pulses of IR emission. The collection of these signals by a matched photodiode required little electronic complexity and resulted in no loss of signal integrity. After testing at each design stage the static and dynamic capabilities of the torquemeter system were established with it when fully installed on the test rig.

When calibrating the strain gauges, differences from the actual load were noted near the limit of torque of the system. These differences were manifest as a slight hysteresis in the load-unload curve and were attributed to creep in the mechanical system. The effect was reproducible and could therefore be accounted for in the recorded efficiency data. Because the gauge factor remained constant and the zero offset had the potential to drift, it was possible to accommodate this in the pre-test calibration procedure. For tests running at high load for long periods, such as the lubrication endurance test, the system was operated for around 15 to 20 minutes beforehand to 'condition' it for use. Calibration values for the front and rear shafts were noted before and after all experimental runs to ensure that any drift was within an acceptable amount. The acceptable difference between pre- and post-experiment zero readings depends on the exactness required of the data or data trend. As an example, for experiments observing large (in relative terms) changes in efficiency such as dry to lubricated state of chain, variation in calibration constants of 0.5% would be acceptable. For tests when small, subtle changes are expected the tolerance may be less than 0.1%. Typically, variations for the rear torquemeter were around 0.15% and for the front 0.25%.

The source of the zero drift may originate from the system electronics or from the strain gauge adhesive and shaft material characteristics. The strain gauge manufacturer claims that, while the shaft may exhibit positive creep under certain load conditions, so the gauge possesses negative creep and in a typical case the two cancel each other. The levels of such micro creep phenomena are not normally discernible unless the detection method is sensitive to greater than one part in a thousand (0.1%). The torquemeter instrumentation developed here is has a resolution of similar magnitude.

In industrial applications of strain gauges as transducers, the matching of micro creep between components and gauge is achieved by a two-stage process<sup>(86)</sup>. Micro creep measurements are made (with a neutral gauge) of the component by applying a load over a period of time. With this data, a selected gauge with corresponding compensation can be used. This development process of a transducer would be a refinement to the approach taken in the manufacture of the two transducers used in the chain efficiency apparatus. The minor problems with strain gauge drift did not compromise the accuracy of the system because of the effect could be nulled by the refitting of calibration data post acquisition. However improvements could be made elsewhere to enhance the torquemeter as a piece of instrumentation.

The manipulation of the strain gauge amplifier output and its interfacing with an acquisition system involved several steps and, although this was adequate for the purpose, a more convenient method is possible. If the analogue voltage output at the bridge amplifier could be digitised 'on-shaft' with a 16 bit A/D converter, then no further bench-side manipulation of data would be required. The digital signal could be sent directly to a high-speed serial port on a computer, for example, eliminating the

need for PC hardware and associated programming development time. The transmission of the digital data could be performed using a recognised infrared standard, IrDA. Communicating data with IrDA at speeds of 2Mbps would provide a fast and easily interfaceable transmission medium as the IrDA standards are commonly utilised in laptop PCs or can feature as an inexpensive desktop peripheral. The use of this communication standard would also allow bi-directional transfer of data. Rather than using manual potentiometers to adjust the offset and gain of the strain gauge bridge, signals from a host PC could control these parameters by software and microprocessor control. By implementing the IrDA standard's requirement of buffering, the integrity of the data could be assured.

Again, whilst adequate for the present purposes, the manipulation of the data once within a host computer could also be improved by enhancing the software. The current programme displayed speed, power and efficiency in real-time, but further parameters may also be calculated. With such a system, it would be possible to set up more realistic longer term simulations with splash, grit and other road conditions and the energy losses could be shown in an accumulated manner to reflect the 'real' losses experienced by a cyclist over a period of time. Statistics could also be produced to show the quality of data or the variations in efficiency occurring. For long-term tests it would be desirable to incorporate an improved data logging procedure in which snapshots could be taken and filed at predetermined intervals. Output from a computer could control the speed or power input allowing a program of varying power input over the course of a test. Outputs from a computer could control the speed or power input allowing a program of varying power input over the course of a test. Implementing a control loop such as this would lessen the demands on the operator

that is required to balance speed or load through the duration of an experiment if the efficiency changes.

In comparison with other published works on bicycle chain efficiency (11),(12),(13),(42),(28),(45),(14) where no suggestion for the accuracy of the experiment has been made, the data from the instrumentation used in this work was found to have an error bound of 0.2%. Not only is the accuracy likely to be in excess of previous works but the quality of the data with respect to realistic simulations of chain use and the wide range of parameters covered is also greater; statistical analysis of the combination factors is also novel. A summary of the range of conditions considered by this work is given below, Table 9-1.

Factor	Range
Speed	60-200rpm
Power	50-450W
Rear sprockets	12-32 teeth
Front sprockets	28-52 teeth
Lubricant	dry, water, 4 proprietary
Misalignment	0-3.5°
Wear	0-5%
Chain length	96-114 links
Time	5s-5hrs

Table 9-1: Chain efficiency factors examined

### 9.3 Sensitivity of chain efficiency to combined factors

The factorial design of experiment detailed in Chapter 7 offered a sensitivity analysis for chain operation parameters not only in isolation but also in combination. High speed and small sprocket size were found to reduce efficiency in comparison to the overall mean value of 32 experiments. High power, no wear and a lubricated chain improved the chain transmission efficiency. Figure 7-10 shows the 5 test parameters

and combinations can be seen lying to the left, on, or to the right of, the normal distribution line.

In the combination analysis, speed and power were considered as separate parameters despite their both being related to applied torque. They were simply chosen as easily controllable and measurable operational effects. However, in the experiments repeated in 7.5.5, chain tension is varied, which is directly related to torque. The results of these separate experiments help explain why power and speed appear at opposite ends of the sensitivity spectrum, since chain efficiency was found to be inversely proportional to the reciprocal of chain tension. With the relatively low chain tensions of 25 and 32 N found in the (ac) and (c) conditions the respective measured efficiencies of 40% and 51% can now be explained. The tension in the chain directly affects the bearing pressures and thus the frictional losses would be expected to be proportional to this factor.

Chain wear is an inevitable feature of the bicycle in its use. The rate at which it occurs varies greatly and is linked to the lubricant used and the environment; these factors are considered further in section 9.8. Experiments (bd), (d) and (de) revealed that the highest efficiencies occur with 0% wear. With a worn chain the reduction in efficiency was of lower magnitude than the other factors examined. Another factor seen to improve efficiency is the presence of a lubricant, (e) although this was to be expected from its purpose of reducing friction.

Taken individually the results from the sole factors of speed, power, sprocket size, wear and lubricant may not seem surprising. The factors of speed and power may not be considered as something particularly controllable to a cyclist. They are operational factors that are dictated by the body and the cyclist's competitive strategy,

if one exists. In essence, a cyclist would not be prepared to pedal slower or increase their physical power output for what amounts to very small gains in efficiency. With respect to the magnitude of effect on efficiency, it is equally beneficial to have a 0% worn chain as it is a lubricated chain. Combining these two factors did not further improve efficiency. The observations of the effect of sprocket size on chain efficiency revealed that using smaller sprockets was the most detrimental to efficiency of the non-torque related factors. The size results will be discussed in the next section.

Further to individual parameter effects, the 32 experiments as a whole illustrate the realistic combined effects present with a bicycle on the road. Previously the magnitude of individual effects could only be estimated and for combined effects the estimate of efficiency would become even less accurate.

#### **9.4 Chain Efficiency and Sprocket Size**

Although first suggested by Barr in correspondence to Mack<sup>(11)</sup> as a factor affecting chain efficiency, it was Burgess<sup>(14)</sup> who first completed an experiment proving that larger sprockets provided better efficiency with a new, greased chain under a realistic static loading of 6 to 60Nm. Using this knowledge in cycling strategy is not a simple matter. As an example, consider a cyclist pedalling at 80 rpm in a gear combination of 52:13 and a power output of 200W. The cyclist then starts to go up an incline and changes gear to 52:16. Assuming that the operational factors of cadence and power output remain constant, three mechanical factors change, the most obvious of which is that the rear sprocket is now 16 teeth rather than 13. However, there is now an altered chain alignment angle, which, in this particular case is around  $1.5^\circ$  (from  $0^\circ$  before). Finally, the length of slack side chain is reduced, which alters the

angle of rear derailleur in turn changing the slack side tension. The effects of chain alignment and slack side tension are covered independently in the following sections.

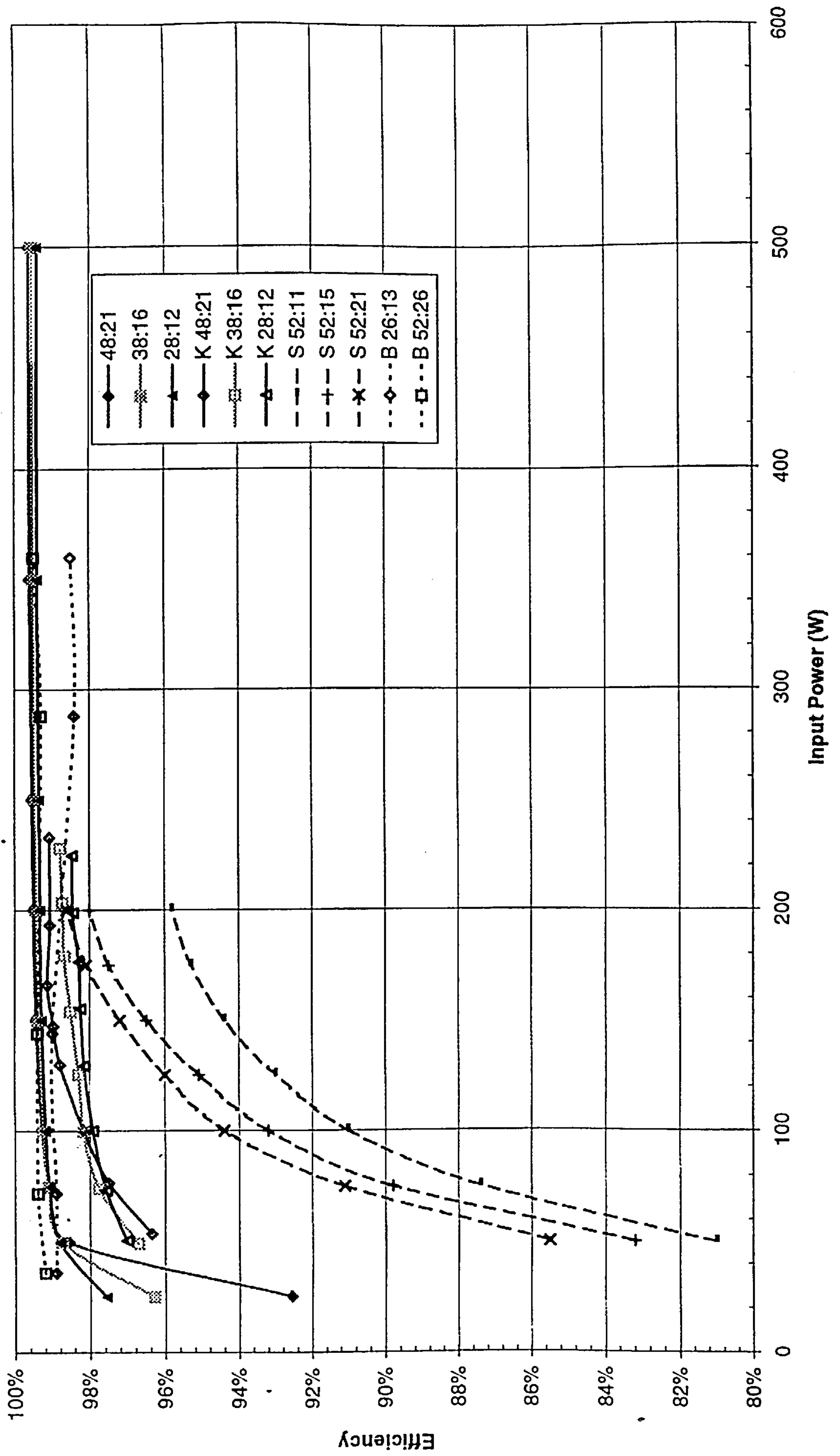
To eliminate the effects of alignment in the current sprocket size experiments, the rear shaft was adjusted laterally so that the front and rear sprockets were co-planar. To compensate for the slack side tension, the length of chain was adjusted and more significantly, the rear derailleur was removed entirely. By maintaining the front to rear sprocket ratio between each of the 3 gear combinations tested, the effect of speed and therefore chain tension differences were removed.

Whilst the work of Burgess<sup>(14)</sup> used pseudo-static analysis to test the sprocket size and chain efficiency hypothesis, the results in this work (shown in 7-18, 7-19 and 7-20) represent a true dynamic analysis. Using the theory developed in Chapter 8 and using calculated values for the pressure angle and coefficient of friction, a set of efficiency curves can be generated. Figure 9-1 shows the calculated efficiency for three typical gear ratios and the data (suffixed by 'K') from the experiment detailed in 7.5.6. The difference in efficiency from high to low ratio is generally quite small (around 0.3%) except at lower power inputs (around 25W) although it should be noted that, in this region, it is the smaller sprockets that have a higher efficiency than larger combinations; this was also observed during the experimentation. The general form of increasing efficiency with power input, eventually saturating at higher power input is observed with both measured and calculated results.

Comparison of form is also possible with the data plotted from the works of Burgess<sup>(14)</sup> and Spicer<sup>(45)</sup> in Figure 9-1. Although neither of the experimental data sets are compatible, observations can still be made of the trends. The data from Spicer (suffixed by 'S') is from a constant speed (60rpm) experiment in which different

sprocket sizes were tested. The data agrees with Burgess's hypothesis of larger sprockets improving efficiency and the trends matches those found in this work. The work of Burgess concerned static tests but if an assumed rotational speed of 60rpm is applied to the data, an indication of a dynamic test can be made. Very little variation of results occurred in the Burgess data (suffixed by 'B'), seemingly independent of power. This is due to the lack of rear derailleur in the experiment and the results are comparable in form to the data presented in Figure 7-19 to Figure 7-21 for the no derailleur case and Figure 9-2 for the 0N slack side tension predictions.

Figure 9-1: Theoretical and experimental chain efficiency at various sprocket sizes



## 9.5 *Slack-Slide Tension*

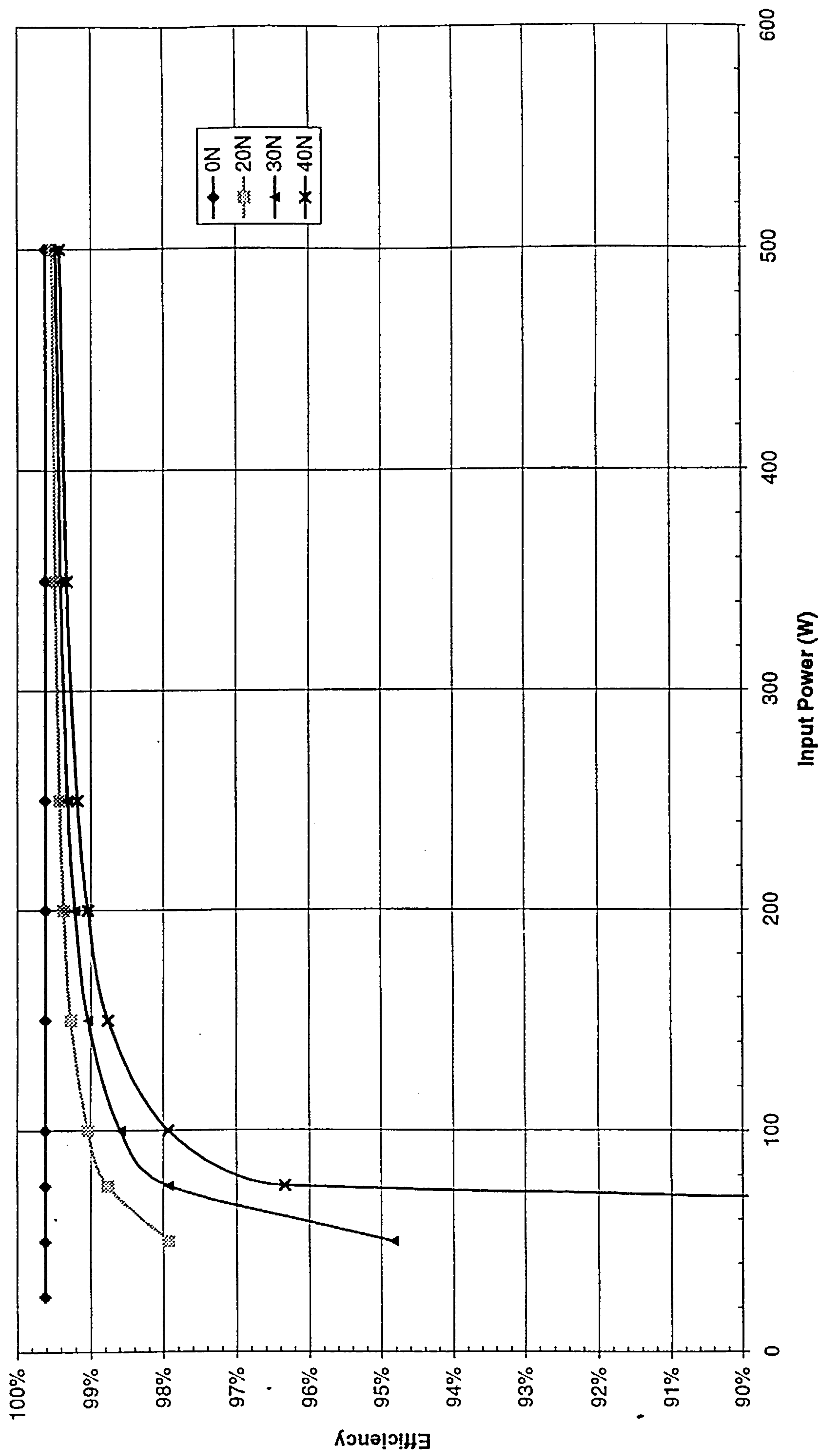
The results of the sprocket size experiment discussed in the previous section highlighted the dramatic effect of removing the rear derailleur. For example, results from the 48:21 ratio Figure 7-19, show the chain efficiency to be 99.5% throughout the power range when no derailleur is present, whereas a variation from about 95% to 99% is seen under the same conditions with the derailleur present. The mathematical model summarised in Equation 8-12 can be used again to help explain this phenomenon. Figure 9-2 shows plots of theoretical efficiency varying slack-side tension across a wide range of power input using the same assumed values of pressure angle and coefficient of friction. With no slack side tension, all slack-side losses become zero, and this is effectively what occurs when no rear derailleur is used, which is in good accord with the measured data. For comparison, the data from Figure 7-19 showed that the efficiency did not vary from around 99.5% when the power was increased. To observe the sensitivity of the theoretical efficiency to the magnitude of slack-slide tension, three values were used. The results indicate that, the larger the tension, the less efficient the entire chain power transfer becomes as increased amounts of friction work are done at the exit and entrance to the main sprockets and also at the idler wheels. The tension imposed by the rear derailleur varies between make and model, typically in the 20-40N range.

The result of changing the length of chain (Figure 7-23) was to alter the angle of the rear derailleur arm and thus the slack side tension. Although the absolute values for chain efficiency using the mathematical model are 1-2% higher than those measured, the same with power and with tension is observed. The difficulty in

estimating chain tension and the effect of idler sprocket bearing losses may account for the difference between predicted and measured results.

**Figure 9-2: Theoretical chain efficiency and slack-side tension**

**52:12 110rpm (no misalignment)**



## 9.6 Sprocket alignment

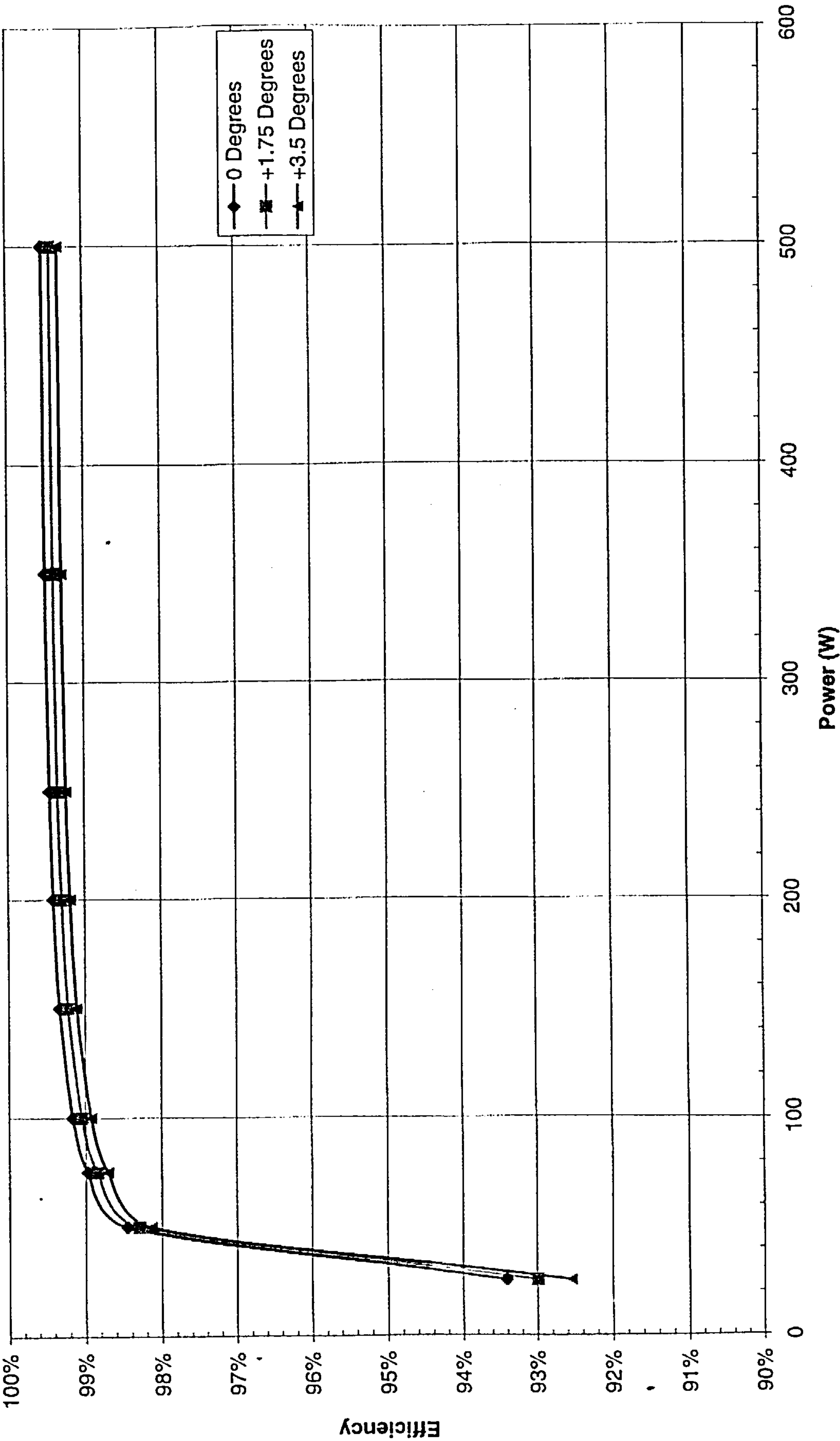
The last of the three effects of changing gear is now considered, that of misalignment between front and rear sprockets. From the experimental data (Figure 7-22) it was seen that, when the chain is running perfectly aligned, it returns the best efficiency and deviations from this degrade it. In the worst case, when the angle of misalignment was 3.5 degrees, the chain was 2% less efficient than the (well) aligned chain over the entire power range.

Modelling chain misalignment requires a number of parameters to be set. Although the overall angle of misalignment ( $\beta$ ) between front and rear sprockets may be judged from the axis centre distances and lateral offset, this is not sufficiently accurate for the purpose of determining the forces within the chain. Chapter 4 introduced the first known experimental study of chain misalignment and it was observed how the chain link plates underwent sharp changes in loading several links before sprocket engagement. In the modelling of this, an individual link to link angle of misalignment was proposed, denoted  $\gamma$ . Using this same principle of accommodating  $\beta$  within  $n$  links each with  $\gamma$  misalignment, the frictional losses can be modelled.

Considering the cases where  $\beta = 0, 1.75$  and  $3.5$  degrees, and is accommodated within 4 links, Figure 9-3 represents the theoretical efficiency for the power range of 25 to 500W with the same sprocket ratio and speed used in the experimental study. The spread of efficiency values between different alignments was around 0.3% for the model compared with 2% observed. Also, the absolute efficiency values are somewhat higher for the model than the measured values.

The results of the load distribution analysis in 4.4.2 illustrated how the chain tension can exceed the nominal chain tension by 50% at the critical point when inner and outer plate rubbing occurs. The energy lost at this interface proves to be considerable at low input power, reflected by the low calculated efficiency in the theoretical data. The discrepancy between efficiencies at higher powers may be due to tooth flank and inner plate rubbing. This was not a factor accounted for in the power loss equations of Chapter 9 as the sprocket and chain interactions under tension and bending become complex and difficult to model. The axial effects of misalignment forces were measured, reported in Chapter 6 revealing that there was perhaps a non-linear relationship between lateral and chain tension force.

Figure 9-3: Theoretical chain efficiency and alignment  
38:16 120rpm



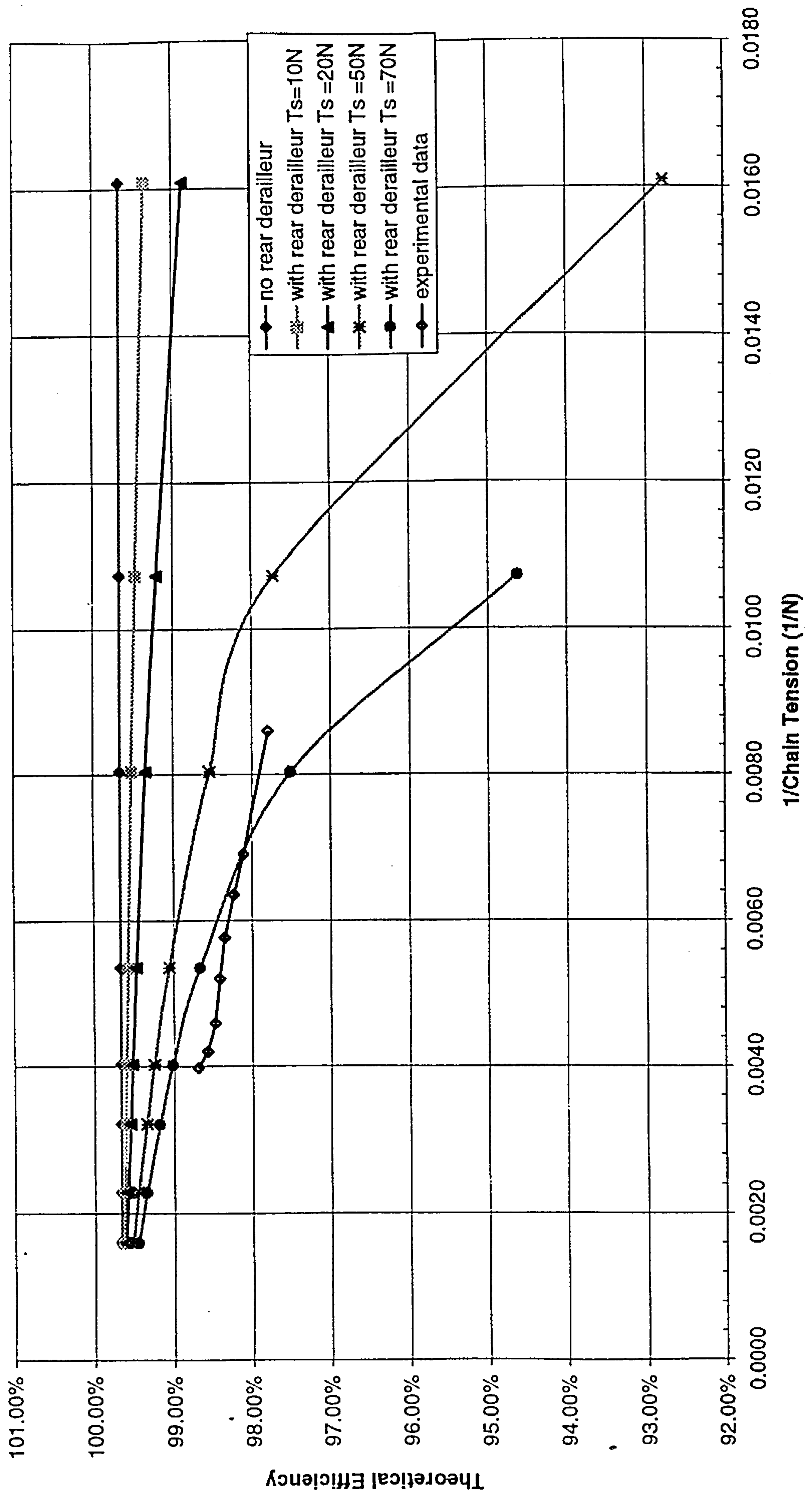
## **9.7 Chain Tension (*tight side*)**

The results of chain tension variation were reported in 7.5.5, where it was shown that the measured efficiency decreased approximately linearly with the reciprocal of chain tension. In an attempt to reproduce these results with the mathematical model, Figure 9-4 was derived from three settings of slack side tension.

As can be seen, the effect of chain tension on efficiency is strongly dependent on slack side tension. When there is no slack-side tension, the efficiency is high and is independent of chain tension. Closest agreement between the measured and modelling data sets occurs with the larger of modelled slack-side tensions (e.g. 50N), although the theory still predicts a higher achievable efficiency. Linear extrapolation of the measured data to infinitely high tension suggests that a maximum value of 99.4% could be achieved. With the model all data sets tend towards the line for zero slack side tension, as the tight side tension becomes very large. The maximum efficiency suggested by this extrapolation is in the region of 99.6%, close to the extrapolation of measured data.

Figure 9-4: Theoretical Chain Efficiency and Chain Tension

38:21



## 9.8 Lubrication

Generally speaking, the efficiency of lubricated chain is around 3% higher than a dry one in transferring continuous power in the range of 50 to 250 Watts, Figure 7-11. In a competitive environment it may be assumed that all chains would start in the best-lubricated, unworn state. The duration for which this ideal state exists is highly dependent on factors such as the weather and surface conditions and the type and amount of lubricant chosen. For short events, it may be that the efficiency of the chain remains constant. However, if the competition passes for some time through wet roads, or worse, muddy tracks, then it is very likely that power will be lost through lubricant failure and significant chain contamination and a little wear may occur in extreme events such as the Tour de France. Such conditions are encountered more frequently in mountain bike races where the demand for a well and continuously lubricated chain is greater.

The effectiveness of different lubricants under sustained water ingress was found to vary substantially. It was found (Figure 7-13) that the *Triflow* lubricant maintained an unaffected high efficiency of 97.5% for 200 minutes under sustained dripping water. The performance of two other lubricants (*FinishLine* 1 and 2) in identical conditions was not as good, efficiency declining by around 1% in both cases. Some other interesting observations were made after the water supply was halted. The two lubricants that had gradually returned reducing efficiency values showed either an improvement or at least a cessation in the decline of efficiency for the duration of the first drying period. In contrast to this, the initially better performing lubricant showed a drop, eventually by 3.5% after an hour's drying.

The responses to wetting and drying suggest that the effect of water is not simple, acting in some cases simply to disperse the lubricant. To examine the effect further the water supply was activated and then deactivated for a second time. During the second drying period all the excess water disappeared, perhaps also taking with it any emulsified lubricant, depending if the water was lost mechanically or by evaporation. In the case of the *Triflow* the reapplication of water increased the efficiency by around 2% in a short time. Removal of the water supply after this, again reduced the system's efficiency, thereby reaffirming that the *Triflow* worked reasonably well in conjunction with the water.

Supplying water for the second time to the *FinishLine* products showed a similar 1% reduction in efficiency, confirming the lubricant's intolerance to water. This effect was similar to the first decrease in efficiency but sharper because of a reduced amount of lubricant active on the chain. The final drying period after six hours of running produced different effects between the two *FinishLine* lubricants. After an hour of no water supply, the *FinishLine* (1) chain efficiency had not decreased appreciably. However the *FinishLine* (2) showed a marked reduction of 6.5%. After such an extensive duration of test it is difficult to establish whether time or the presence of water was the main factor for this lubricant.

The short-term benefits of chain lubrication by various substances are illustrated in Figure 7-12. Although the water and surfactant corrosion inhibitor (*SACI*) are not as sophisticated as the lubricants examined in the endurance tests, their use can still be important in on-board lubricant devices as a solution to the long-term uncertainty of chain efficiency in an environmentally dynamic situation. One proposed cycle product uses a water-soluble *SACI* mix both to clean and lubricate the chain

whilst the cyclist is moving. The performance of *SACI* and water as lubricant is shown in Figure 7-10, indicating also that water alone can perform, to some degree, the role of a lubricant. This effect was also perhaps observed in conjunction with the *Triflow* lubricant and water test (7.5.4). The short-term longevity of water alone however (Figure 7-12), indicated that it should either be supplied continuously or in conjunction with an additive. For longer-term benefits the regular application of the mixture should maintain an adequate efficiency, depending on external environmental factors. The volume of lubricant mix required is likely to be several times greater than that used with more conventional lubricants and the mass of this would be added to the mass of the bicycle. The overall effect is still beneficial for the user of such a system in terms of energy exerted. The performance of *SACI* in long term usage with a water supply examined in 7.5.4 revealed that an on-board system could maintain an efficiency above 96% for nearly three hours with the aggregate addition of 5ml. This performance could be tuned to meet environmental conditions and has the ability to achieve higher efficiencies than any other current lubricant system.

## **9.9 Summary**

It was found that accurate high-resolution measurements could be made of dynamic chain efficiency using the specially designed torque transducers. The accuracy performance of the transducers at 0.2% surpassed that of commercial products and was of much lower cost. The results of many chain efficiency experiments suggest that operating with large sprockets, new chains, high tension and no misalignment can enhance the performance of the chain drive system. Around 17% of losses are associated with the slack side tension and so maximum performance can be achieved with the removal of the rear derailleur. However, this must be considered

against the widely recognised benefits of the mechanism that allows the cyclist's physiological efficiency to be maintained. To sustain high chain efficiency frequent lubrication in arduous environmental situation is recommended. The theory developed in Chapter 8 gives trends in accord with the measurements thereby confirming the location and action of the friction losses within the chain.

## 10. Conclusions

This thesis embodies an extensive and detailed investigation of the bicycle chain. The limitations of previous studies on industrial chains have been overcome to provide an insight with specific application to the bicycle and associated derailleur gear system. A model, which indicates how the efficiency of chain power transfer is affected by mechanical and operational parameters, has been suggested. The successful implementation of a novel, low-cost, high accuracy torque transducer was central to the acquisition of wide ranging experimental data leading to evaluation of transmission efficiency. Secondary experiments were devised to investigate the forces present in a chain subject to articulation and misalignment, together with determination of the coefficient of friction of chain components. Using the information gleaned from mathematical modelling and the empirical analyses, a more efficient chain usage strategy was suggested.

Quoting a generic value for bicycle chain efficiency can be both misleading and incorrect unless the conditions pertaining to its use and operation are precisely defined. The frequently cited Whitt and Wilson<sup>(9)</sup> reference of 98.5% is neither correct nor wrong. Undoubtedly the chain may achieve this value at some point but it is equally likely to fail to meet it, as it is to exceed it.

One unique feature of the bicycle chain on a typical competitor road or mountain bicycle compared with an industrial chain is the rear derailleur. Although this mechanism serves the cyclist well with up to 27 gear combinations to maximise human efficiency, it gives rise to frictional losses accounting for up to 22% of the total. For up to 90% of the gear combinations chain misalignment with the front and rear sprockets occurs and this can reduce efficiency by 2.5%. For all gear ratios with a

derailleur gear, a varying amount of non-zero slack slide tension is present and this has its greatest effect on efficiency, where it can account for up to 4% losses.

Larger sprockets improve efficiency by 1 to 2% whilst chain wear and poor lubrication degrade it by 2 to 8%. To maintain high physiological performance a cyclist attempts to sustain a constant cadence. Whilst in this mode of constant cadence and assuming no change of gear, a change in gradient or wind resistance would affect the tension in the chain. Increases to chain tension offer a 1% to 2.5% improvement in efficiency.

It was found that the lubricant and lubrication strategy could also affect the performance of a chain. In certain conditions a simulation of prolonged heavy rain showers revealed wide variations in chain efficiency, in some cases returning it to a value characteristic of a dry chain of below 90%. A successful choice of lubricant and method of application can provide a sustainable high efficiency of 96% to 98% over several hours providing up to a 4% advantage over other competitors. In the competitive cycle environment any improvements, no matter how small, are always welcomed as the winning margins of races or world records are slight themselves.

## References

1. Conwell, J. C., Johnson, G. E., and Peterson, S. W., "Design and construction of a machine to evaluate the forces in roller chain drives", International Power Transmission and Gearing Conference ASME, New York, 703-709. 1992
2. Hill, R. D. "Design & Development of the LotusSport Bicycle". *Proceedings of the Institution of Mechanical Engineers, Part D: Journal of Automobile Engineering* vol 207(4), 285-294 (1993).
3. Kidd M. D. "Bicycle Chain Efficiency". BEng thesis (ME4-021-95), Dept. Mechanical Engineering, University of Edinburgh. 1995.
4. Hopkins, M. W., Principe, F. S., and Kelleher, K. J., "Beyond materials: Du Pont's aerodynamic bicycle wheel", Advanced Materials - The Challenge for the next Decade - 35th International SAMPE Symposium Anaheim, CA, 947-959. 1990
5. Kubomura, K., Tsuji, N., Kimura, H., Maikuma, H., Herai, T., and Yamamura, K., "Lightest composite monocoque bicycle frame", National Sampe Symposium and Exhibition (Proceedings) 2 edition, 2216-2223. 1990
6. Wang, E. L. & Hull, M. L. "Model for determining rider induced energy losses in bicycle suspension systems". *Vehicle System Dynamics* vol 25(3), 223-246 (1996).
7. Hull, M. L., Wang, E. L. & Moore, D. F. "Empirical model for determining the radial force-deflection characteristics of off-road bicycle tyres". *International Journal of Vehicle Design* vol 17(4), 471-482 (1996).
8. Burgess, S. C., Stolarski, T. A., and Karp, S. "An accelerated life test for bicycle freewheels". *Measurement Science and Technology* vol 1, 1-8 (1990).
9. Whitt, F. R. & Wilson, D. G. "Bicycling Science". McCullagh, J. C.(ed.), MIT Press, Cambridge, Massachusetts 1982.

10. Hollingworth, N. E. and Hills, D. A. "Theoretical efficiency of a cranked link chain drive". *Proceedings of the Institution of Mechanical Engineers, Part C: Mechanical Engineering Science* vol 200(C5), 375-377 (1986).
11. Mack, G. D. "Tests of the Efficiency of the Bicycle". *Transactions of the ASME* vol XVIII(May), 1067-1071 (1897).
12. Carpenter, R. C. "The Efficiency of Bicycles". *Engineering* , Aug 19th-Aug 26th (1898).
13. Keller, J. "Der Wirkungsgrad im Fahrrad Antrieb". *Radmarkt* (12), 71-75 (1983).
14. Burgess, S. C. "Improving cycling performance with large sprockets". *Sports Engineering* vol 1(2), 107-114 (1998).
15. Binder, R. C. "Mechanics of the Roller Chain Drive". Prentice-Hall, Englewood Cliffs, NJ, 1956.
16. Conwell, J. C., Johnson, G. E., and Peterson, S. W., "Experimental investigation of the forces in a link side plate during normal operation of a roller chain drive", International Power Transmission and Gearing Conference ASME, New York, 711-715. 1992
17. Naji, M. R. & Marshek, K. M. "Analysis of sprocket load distribution". *Mechanism & Machine Theory* vol 18(5), 349-356 (1983).
18. Naji, M. R. and Marshek, K. M. "Experimental determination of the roller chain load distribution". *Journal of Mechanisms, Transmissions, and Automation in Design* vol 105(3), 331-338 (1983).
19. Eldiwany, B. & Marshek, K. "Experimental load distributions for double pitch steel roller chains on polymer sprockets". *Mechanism and Machine Theory* vol 24(5), 335-349 (1989).
20. Eldiwany, B. & Marshek, K. "Experimental load distributions for double pitch steel roller chains on steel sprockets". *Mechanism and Machine Theory* vol 19(6), 449-457 (1984).

21. Stamets, W. K. "Dynamic Loading of Chain Drives". *Transactions of the ASME* vol 73 (July), 655-665 (1951).
22. Kin, Y. and Dubrovsky, R., "New power transmission chain design", ASME Design Automation Conference, Cincinnati ASME, New York, NY, USA, 107-114. 1985
23. Naji, M. R. and Marshek, K. M. "Effects of the pitch difference on the load distribution of a roller chain drive". *Mechanism and Machine Theory* vol 24(5), 351-362 (1989).
24. Kim, M. S. and Johnson, G. E., "Mechanics of roller chain-sprocket contact: a general modelling strategy", International Power Transmission and Gearing Conference ASME, New York, 689-695. 1992
25. Naji M. R. "On timing belt & roller chain load distributions". PhD thesis, University of Houston. 1981.
26. Naji, M. R. and Marshek, K. M. "Analysis of roller chain sprocket pressure angles". *Mechanism and Machine Theory* vol 19(2), 197-203 (1984).
27. Murray, M. J. and Canfield, T. R., "Modeling a flexible-link power transmission system", International Power Transmission and Gearing Conference ASME, New York, 723-728. 1992
28. Hollingworth, N. E. "Four-square chain wear rig". *Tribology International* vol 20(1), 3-9 (1987).
29. Ross, M. O. and Marshek, K. M. "Four-square sprocket test machine". *Mechanism and Machine Theory* vol 17(5), 321-326 (1982).
30. "Manual of Mechanical Power Transmission". Parry, E. L.(ed.), Trade & Technical Press (Power Transmission) Ltd., 1936.
31. "Mechanical Drives". Smith, E. A.(ed.), Morgan-Grampian (publishers) Ltd., Kent 1970.

32. "CRC handbook of lubrication : theory and practice of tribology, Volume I : Application and Maintenance". Booser, E. R.(ed.), CRC Press, Florida 1983.
33. Deutschman, A. D. "Machine design theory and practice". Collier Macmillan, London 1975.
34. Patton, W. J. "Mechanical Power Transmission". Prentice-Hall, London 1980.
35. Vogwell, J. "Component Selection: Chain Drives". Prentice Hall, 1994.
36. Wilson, B. "Roller chain lubrication". *Industrial Lubrication and Tribology* vol 48(4), 4-5 (1996).
37. Wright, J. L. "Getting the most from chain drives". *Machine Design* vol 65, 74-76 (1993).
38. Peeken, H. and Coenen, W. "Influence of oil viscosity and various additives on the wear of roller chains". *Wear* vol 108(4), 303-321 (1986).
39. Hollingworth, N. E. and Hills, D. A. "Forces in a heavy-duty drive chain during articulation". *Proceedings of the Institution of Mechanical Engineers, Part C: Mechanical Engineering Science* vol 200(C5), 367-374 (1986).
40. Kidd D. E. Cycle chain efficiency tests, Strathclyde University. 1991.
41. Hollingworth N. E. "Wear studies of a heavy-duty drive chain". PhD thesis, Trent Polytechnic. 1986.
42. Coenen, W. & Peeken, H. "Wirkungsgrad von Rollenkettengeräten unter besonderer Berücksichtigung des Schmierungszustandes". *Antriebstechnik* vol 24(11), 56-61 (1985).
43. Charnock, G. F. "The Mechanical Transmission of Power". Crosby Lockwood, London, 1933.
44. McKay, R. F. "The Theory of Machines". Longman, London, 1920.

45. Spicer, J. B., Ehrlich, M. J., Bernstein, J. R., Richardson, C. J. K., Fukuda, M., and Terada, M. "Efficiency and Energy Loss Location in Bicycle Chain Drives". *submitted to Transactions of the ASME* (1999).
46. Fichtel & Sachs. Internal Report: Versuchs-Bericht Nr. 5162. 1987.
47. Radcliffe, S. J. "Wear mechanisms in unlubricated chains". *Tribology International* vol 14, 263-269 (1981).
48. Rabinowicz, E. "Friction and Wear of Materials". Wiley, New York, 1995.
49. Challen, J. M., Kopalinsky, E. M., and Oxley, P. L. B., "Asperity deformation model for relating the coefficients of friction and wear in sliding metallic friction", Proceedings of the IMECHE International Conference: Tribology - Friction, Lubrication and Wear Fifty Years On, London. 957-964. 1987
50. Zhou, R. S., Cheng, H. S. & Mura, T. "Micropitting in rolling and sliding contact under mixed lubrication". *Journal of Tribology, Transactions of the ASME* vol 111(4), 605-613 (1989).
51. Williams, J. A. "Engineering Tribology". Oxford Science Publications, 1994.
52. Cameron, A. "Basic Lubrication Theory". pp. 170-174 Longman, London, 1971.
53. Radchik, V. S. & Kotlyar, Y. J. "About joint deformations of asperities and the destruction of rough surfaces during friction". *Tribology Transactions* vol 37(4), 871-875 (1994).
54. Sherrington, I. & Smith, E. H. "Modern measurement techniques in surface metrology: part i: stylus instruments, electron microscopy and non-optical comparators". *Wear* vol 125(3), 271-288 (1996).
55. Hamrock, B. J. "Fundamentals of Fluid Film Lubrication". NASA, 1991.
56. Tripp, J. H., Houpert, L. G., Ioannides, E., and Lubrecht, A. A., "Dry and lubricated contact of rough surfaces", Proceedings of the IMECHE International

Conference: Tribology - Friction, Lubrication and Wear Fifty Years On, London.  
MEP, 71-79. 1987

57. Azarkhin, A. & Richmond, O. "On friction of ploughing by rigid asperities in the presence of straining. upper bound method". *Journal of Tribology, Transactions of the ASME* vol 112(2), 324-329 (1990).
58. Black, A. J., Kopalinsky, E. M., and Oxley, P. L. B. "An investigation of the interaction of model asperities of similar hardness.". *Wear* vol 153, 245-261 (1992).
59. Dakshina Murthy, H. B., "An Analysis of Boundary Lubrication Considering Conditions of Dynamic Equilibrium", Mixed lubrication and lubricated wear proceedings of the 11th Leeds-Lyon Symposium Tribology held in Bodington Hall, The University of Leeds, England 4-7 September 1984 Dowson, D., Butterworths, 81-88. 1984
60. Kingsbury, E. P. "The heat of adsorption of a boundary lubricant". *ASLE Transactions* (3), 30-35 (1960).
61. Kingsbury, E. P. "Some aspects of the thermal desorption of a boundary lubricant". *Journal of Applied Physics* (29), 888-892 (1958).
62. Bowden, F. P. & Tabor, D. "The Friction and Lubrication of Solids". Oxford, 1950.
63. Lansdown, A. R., "Lubricants", Proceedings of the IMECHE International Conference: Tribology - Friction, Lubrication and Wear Fifty Years On, London. MEP Ltd., 365-378. 1987
64. Bowden, F. P. "Friction, An Introduction to Tribology". pp. 117 Heinemann Educational, London, 1974.
65. Hutchings, I. M. "Tribology: Friction and Wear of Engineering Materials". pp. 58-77 Edward Arnold, 1992.

66. Sorensen, F. and Petersen, H. J. S. "Nonsolvent based lubrication of machine elements". *Lubrication Engineering* vol 50(1), 63-64 (1994).
67. James, R. W. "Strain-gage misalignment errors - a special case of interest". *Experimental Techniques* vol 12(6), 28-29 (1988).
68. Gindy, S. S. "Force and torque measurement, a technology overview. part I - force". *Experimental Techniques* vol 9(6), 28-33 (1985).
69. Gindy, S. S. "Force and torque measurement, a technology overview: part II - torque". *Experimental Techniques* vol 9(7), 9-15 (1985).
70. Buchele D. R. "Optical Torquemeter". Patent number (3196675). 1965. US.
71. Marker bands allow simple shaft torque measurement. *Eureka on Campus* , 8-8. 1996.
72. Asson, K. M. & Dunn, P. F. "Compact dynamometer system that can accurately determine propeller performance". *Journal of Aircraft* vol 29(1), 8-9 (1992).
73. Spooncer, R. C., Heger, R. & Jones, B. E. "Non-contacting torque measurement by a modified moiré fringe method". *Sensors and Actuators, A: Physical* vol 31(1-3 pt3), 178-181 (1992).
74. Rudd, R. E., Kline, B. R., Hoff, F. G. & Spillman, W. B. J. "Fiber optic torquemeter design and development". *ISA Transactions* vol 28(2), 19-23 (1989).
75. Garshells, I. J., Whitney, K., and May, L., "Development of a non-contact torque transducer for electric power steering systems", *Sensors and Actuators SAE*, Warrendale, PA, USA, 173-182. 1992
76. Shelley, T. "Acoustics sense torque at low cost". *Eureka*(September), 48-49 (1993).

77. Hall, D. A., Wang, H. W., and Lonsdale, A., "Torque measurement by means of a SAW resonator", *Sensors VI: Technology, Systems and Applications* Grattan, K. T. V. and Auggousti, A. T., IOP Publishing, UK, 201-206. 1993
78. "The systematic experiment". Gibbings, J. C.(ed.), Cambridge University Press, 1986.
79. Roark, R. J. "Roark's Formulas for Stress and Strain". 1989.
80. Boylestad, R. L. & Nashelsky, L. "Electronics: a survey of electrical engineering principles". Prentice-Hall, New Jersey, 1996.
81. De Sa, A. "Principles of Electronic Instrumentation". Edward Arnold, New York, 1990.
82. Thomson, W. T. "Theory of Vibration with applications". pp. 17-49 Prentice Hall, 1999.
83. Market Report: "Bicycles". Howitt, S. 8th ed. 1999. London, Key Note.
84. Montgomery, D. C. "Design and Analysis of Experiments". pp. 228-353 Wiley, 1999.
85. Kyle, C. R. "Energy and Aerodynamics in Bicycling". *Clinics in Sports Medicine* vol 13(1), 39-73 (1994).
86. Dawsey J. Spring Element Creep in Transducers. 1999. Measurements Group.

## Appendix A: Error analysis

### Torquemeter Instrumentation

The measurement of the torque is based on a number of transductions and transformations: strain gauge amplifier, voltage-to-frequency converter, data acquisition card, fast Fourier transform. From manufacturers data sheets, the linearity of the strain gauge amplifier, v-to-f converter and data acquisition system were found to be 0.001%, 0.001% and 0.002% respectively. The error associated with the FFT conversion can be estimated to be 0.025%. Since each acts as a multiplication, the cumulative error of torque to PC based frequency signal is the sum of these errors, i.e. 0.065%. The calibration of the torquemeter involved applying masses known to within 0.0001%. Only the multiplying constant is of importance here because the instrument was zeroed immediately prior to operation. The error in the torquemeter calibration constant is therefore the sum of the previous signal error and the mass error as the lever arm length is fixed. Thus the total calibration error is 0.0651%

In operation, a measurement is made and is multiplied by the calibration factor and so the total mechanical torque to PC based signal torque is the addition i.e.  $0.0651+0.065=0.131\%$

### Chain Efficiency

Chain efficiency,  $\eta$  may be defined as:  $\eta = \frac{T_o}{T_i} \times \frac{\alpha_o}{\alpha_i}$  where  $T_i$  and  $T_o$  are the input and

output shaft torque in Nm and  $\alpha_i$  and  $\alpha_o$  are the input and output angular velocities in radians/s. The input and output rotations are determined by the number of teeth of the

two sprockets ( $Z_1$  and  $Z_2$  for input and output) such that,  $\alpha_o = \frac{Z_1}{Z_2} \alpha_i$

Therefore the efficiency becomes:  $\eta = \frac{T_o}{T_i} \times \frac{Z_1}{Z_2}$

As there is no error in the counting of sprocket teeth then,

$$\frac{\Delta\eta}{\eta} = \frac{\Delta T_o}{T_o} + \frac{\Delta T_i}{T_i} = 0.13\% + 0.13\% = 0.26\%$$

For example, with a 52:12 sprocket arrangement, a measured input torque of 22.5Nm and output torque of 5Nm the efficiency is 0.96296 or 96.296%±0.125%

## Power

The determination of power requires an angular velocity to be known. The error associated with  $\alpha_i$  is similar to the errors of the torque meter in that the signal must be acquired and processed by an FFT thus the error is 0.02%+0.025% = 0.045%.

Input power,  $P_i$  is simply  $T_i \times \alpha_i$  i.e.  $\frac{\Delta P_i}{P_i} = \frac{\Delta T_i}{T_i} + \frac{\Delta \alpha_i}{\alpha_i} = 0.13\% + 0.045\% = 0.175\%$

## Appendix B: Heat calculations of friction brake system

Assuming that all shaft output power is absorbed by the friction brake, then the temperature rise can be estimated by calculating the energy supplied over a given period of time. Assuming no thermal gradients, the temperature rise can be obtained using the following relationship,  $Q = Cm\Delta T$  where  $Q$  is the energy supplied (J),  $C$  the specific heat capacity (J/kg/°C),  $m$  is the mass (kg) and  $\Delta T$  the temperature rise in degrees Celsius. The total mass is a combination of the following: 5.76kg of aluminium and 7.50kg of steel for which the specific heat capacities are known to be 900 and 480 J/kg/°C respectively. The energy supplied is simply the product of power (W) and duration (s).

e.g. the temperature rise of the complete mass whilst running at 300W for 5 minutes

$$\text{is: } \Delta T = \frac{300 \times 5 \times 60}{(900 \times 5.76) + (480 \times 7.50)} = 10.2^\circ\text{C}$$